



AFRL-RQ-WP-TR-2017-0149

TRANSITION ON HYPERSONIC VEHICLES WITH CROSSFLOW

Roger Kimmel, David Adamczak, and Matthew Borg

**Hypersonic Sciences Branch
High Speed Systems Division**

**Joseph S. Jewell
Spectral Energies, LLC**

**Thomas J. Juliano
Notre Dame University**

**Matthew Tufts
Ohio Aerospace Institute**

**NOVEMBER 2017
Interim Report**

**DISTRIBUTION STATEMENT A: Approved for public release.
Distribution is unlimited.**

See additional restrictions described on inside pages

**AIR FORCE RESEARCH LABORATORY
AEROSPACE SYSTEMS DIRECTORATE
WRIGHT-PATTERSON AIR FORCE BASE, OH 45433-7542
AIR FORCE MATERIEL COMMAND
UNITED STATES AIR FORCE**

REPORT DOCUMENTATION PAGE

*Form Approved
OMB No. 0704-0188*

The public reporting burden for this collection of information is estimated to average 1 hour per response, including the time for reviewing instructions, searching existing data sources, gathering and maintaining the data needed, and completing and reviewing the collection of information. Send comments regarding this burden estimate or any other aspect of this collection of information, including suggestions for reducing this burden, to Department of Defense, Washington Headquarters Services, Directorate for Information Operations and Reports (0704-0188), 1215 Jefferson Davis Highway, Suite 1204, Arlington, VA 22202-4302. Respondents should be aware that notwithstanding any other provision of law, no person shall be subject to any penalty for failing to comply with a collection of information if it does not display a currently valid OMB control number. **PLEASE DO NOT RETURN YOUR FORM TO THE ABOVE ADDRESS.**

1. REPORT DATE (DD-MM-YY) November 2017			2. REPORT TYPE Interim		3. DATES COVERED (From - To) 01 July 2015 – 01 July 2017		
4. TITLE AND SUBTITLE TRANSITION ON HYPERSONIC VEHICLES WITH CROSSFLOW			5a. CONTRACT NUMBER In-house				
			5b. GRANT NUMBER				
			5c. PROGRAM ELEMENT NUMBER 61102F				
6. AUTHOR(S) Roger Kimmel, David Adamczak, and Matthew Borg (AFRL/RQHF) Joseph S. Jewell (Spectral Energies, LLC) Matthew Tufts (Ohio Aerospace Institute) Thomas J. Juliano (Notre Dame)			5d. PROJECT NUMBER 3002				
			5e. TASK NUMBER				
			5f. WORK UNIT NUMBER Q1FN				
7. PERFORMING ORGANIZATION NAME(S) AND ADDRESS(ES)					8. PERFORMING ORGANIZATION REPORT NUMBER AFRL-RQ-WP-TR-2017-0149		
Hypersonic Sciences Branch High Speed Systems Division Air Force Research Laboratory, Aerospace Systems Directorate Wright-Patterson Air Force Base, OH 45433-7542 Air Force Materiel Command United States Air Force			Spectral Energies, LLC 5100 Springfield Street Suite 301 Dayton, OH 45431-1261				
Department of Aerospace and Mechanical Engineering University of Notre Dame 107 Hessert Laboratory Notre Dame, IN 46556			Ohio Aerospace Institute 5100 Springfield Suite 308,Beavercreek, OH 45431				
9. SPONSORING/MONITORING AGENCY NAME(S) AND ADDRESS(ES) Air Force Research Laboratory Aerospace Systems Directorate Wright-Patterson Air Force Base, OH 45433-7542 Air Force Materiel Command United States Air Force					10. SPONSORING/MONITORING AGENCY ACRONYM(S) AFRL/RQHF		
					11. SPONSORING/MONITORING AGENCY REPORT NUMBER(S) AFRL-RQ-WP-TR-2017-0149		
12. DISTRIBUTION/AVAILABILITY STATEMENT DISTRIBUTION STATEMENT A: Approved for public release. Distribution is unlimited.							
13. SUPPLEMENTARY NOTES PA Case Number: 88ABW-2017-5244; Clearance Date: 24 October 2017							
14. ABSTRACT This interim technical report summarizes technical activity on AFRL 6.1 laboratory task LRIR 15RQCOR102 during fiscal year 2017. The objective of this task is to better understand boundary layer transition in hypersonic flowfields with spanwise nonuniformity. Several advances were made under this task during FY17. The HIFiRE-5b flight data were analyzed. Wind tunnel tests were conducted at angles of attack and yaw representative of flight, and computations were carried out for the flight conditions. Also, analysis of cones at angle of attack, as tested in the AFRL Mach 6 high Reynolds number wind tunnel, was also conducted. The effects of angle of attack and yaw angle on crossflow transition on the test bodies were quantified. Multiple transition effects arising from crossflow modes, attachment-line and centerline traveling instabilities were identified. These transition mechanisms were identified by their peculiar transition patterns and behaviors in flight, wind tunnel and computations. Generally, the Parabolized Stability Equations were effective in predicting crossflow and attachment line transition behavior.							
15. SUBJECT TERMS boundary layer transition, hypersonic, flight test							
16. SECURITY CLASSIFICATION OF:			17. LIMITATION OF ABSTRACT: SAR		18. NUMBER OF PAGES 161	19a. NAME OF RESPONSIBLE PERSON (Monitor) Roger L. Kimmel	
a. REPORT Unclassified	b. ABSTRACT Unclassified	c. THIS PAGE Unclassified	19b. TELEPHONE NUMBER (Include Area Code) N/A				

<u>Section</u>	<u>Page</u>
List of Figures	iii
List of Tables	vi
Acknowledgments.....	1
1. Summary	2
2. HIFiRE-5b Flight Overview	3
2.1. Background and Experimental Overview	3
2.2. Vehicle	3
2.3. Trajectory and Vehicle Attitude.....	10
2.4. Transition Phenomenology	15
2.5. Comparison to Ground Test.....	22
2.6. Conclusions	25
3. HIFiRE-5b Attitude Determination	27
3.1. Pressure Distribution RMS Analysis and Comparison with CFD	27
3.2. Comparison with Differential Pressures	31
3.3. Conclusions	33
4. HIFiRE-5b Heat Transfer	35
4.1. Pre-Flight Ground Tests and Computational Analyses.....	35
4.1.1. Instrumentation	35
4.2. Data Reduction Methodology	36
4.2.1. Calculation of Heat Flux from Thermocouple Data.....	36
4.2.2. Transition Assessment.....	38
4.2.3. Non-dimensionalization.....	38
4.3. Heat Flux and Transition Results	39
4.3.1. Presentation Format	39
4.3.2. Streamwise Transition Variation	39
4.3.3. Spanwise Variation of Heat Flux and Transition	43
4.3.4. Comparison to CFD Results	47
4.3.5. ‘Contour’ Plots.....	49
4.4. Conclusions	49
5. HIFiRE-5 at Angle of Attack and Yaw.....	54
5.1. Experimental Overview	54
5.2. Quiet Flow.....	58
5.2.1. 0° Angle of Attack.....	58
5.2.2. Effect of Stationary Crossflow on Traveling Vortices	64
5.3. Angle of Attack.....	65
5.3.1. Background	65
5.3.2. Global Heat Flux Measurements.....	66
5.4. Noisy Flow	75
5.4.1. Zero angle of attack	75
5.4.2. Non-zero Angle of Attack.....	77
5.5. Summary and Conclusions.....	81
6. HIFiRE-5b Post Flight Testing	83
6.1. PCB Sensors	103

6.2.	Preliminary Evidence of Secondary Instability of Stationary Crossflow Vortices	105
6.3.	Summary and Conclusions.....	107
7.	PSE Analysis of Crossflow Instability on HIFiRE-5b Flight Test	109
7.1.	Computational Methods	109
7.2.	Flow Conditions	111
7.3.	Stability Characteristics.....	116
7.3.1.	Second Mode	116
7.3.2.	Stationary Crossflow.....	118
7.3.3.	Centerline	122
7.4.	Summary and Conclusions.....	122
8.	Analysis of Windward Side Hypersonic Boundary Layer Transition on Blunted Cones at Angle of Attack.....	125
8.1.	Background	125
8.2.	Reference Experiment.....	127
8.2.1.	Model Geometry	127
8.2.2.	Freestream Conditions	127
8.3.	Methods.....	128
8.3.1.	Computational Grid	128
8.3.2.	Computational Methods.....	129
8.3.3.	Crossflow Instabilities	130
8.3.4.	Overexpansion	132
8.4.	Entropy Swallowing.....	133
8.5.	Stability Results.....	135
8.5.1.	Effects of Entropy Swallowing on Transition	137
8.6.	Conclusions and Future Work.....	143
	List of Acronyms, Abbreviations, Symbols.....	144
	References.....	147

<u>List of Figures</u>	<u>Page</u>
Figure 2-1 HIFiRE-5 stack.....	6
Figure 2-2 Elliptic cone geometry and coordinate system.....	7
Figure 2-3 HIFiRE-5 payload, including nosetip detail (dimensions in mm).	8
Figure 2-4 HIFiRE-5 nosetip detail. Dimensions in mm.....	9
Figure 2-5 Peak thermocouple roughness.....	10
Figure 2-6 Descent Mach and unit Reynolds number histories.....	11
Figure 2-7 Pressure history, $\phi=0$, $x=800$ mm.	12
Figure 2-8 Payload spin derived from measured pressure.....	13
Figure 2-9 Angle of attack and yaw angle derived from surface pressures.....	14
Figure 2-10 Angle of attack derived from pressure and from GPS/IMU	15
Figure 2-11 Leading edge temperature histories.	16
Figure 2-12 Leading edge transition symmetry	16
Figure 2-13 Centerline transition	17
Figure 2-14 Detailed temperature history for thermocouple 131, $x=550$ mm, $\phi=0^\circ$	18
Figure 2-15 Centerline temperature, heat transfer and angle of attack.....	18
Figure 2-16 $\phi=45^\circ$ transitional heat transfer and yaw angle.....	19
Figure 2-17 $\phi=45^\circ$ heat transfer history sampled on payload orientation.	20
Figure 2-18 Phase-locked heat transfer disturbances, $\phi=45$ deg.	21
Figure 2-19 Effect of transducer bandwidth on measured centerline transition location.	22
Figure 2-20 Transition Reynolds numbers at three streamwise locations	24
Figure 2-21 Noisy and quiet wind tunnel transition compared to flight transition.....	25
Figure 3-1 Angle of attack (α) and yaw (β) results for descent.	29
Figure 3-2 Detail of angle of attack (α) and yaw (β) results for the descent portion of the trajectory from the interpolation/RMS minimization routine compared with the IMU/GPS values.	30
Figure 3-3 FFT magnitude response for descent α and β derived from IMU and RMS, $t = 514$ to 518 s.....	31
Figure 3-4 Peak FFT magnitude response for descent α and β derived from pressure-difference RMS in 2 s moving windows, $t = 505$ to 519 s.....	32
Figure 3-5 Descent α and β derived from RMS pressure compared with normalized centerline and leading edge differential pressures.....	33
Figure 4-1 Layout of thermocouples, heat-flux gauges, and pressure transducers on HIFiRE-5b flight vehicle.....	36
Figure 4-2 Front- and back-face thermocouple temperature measurements. $x = 600$ mm, $\phi = 90^\circ$	37
Figure 4-3 Heat flux calculated from thermocouple data. $x = 600$ mm, $\phi = 90^\circ$	37
Figure 4-4 Heat transfer non-dimensionalization and Rex scaling for sensor at $x = 0.40$ m, $\phi = 45^\circ$	39
Figure 4-5 Heat transfer on the leading edge ($\phi = 90^\circ$).....	40
Figure 4-6 Heat transfer on the centerline ($\phi = 0^\circ$).	42
Figure 4-7 Streamwise profiles of earliest transition onset. The legend is common to both subfigures.	42
Figure 4-8 Streamwise profiles of transition location.	43
Figure 4-9 Spanwise profiles of earliest transition onset.....	44

Figure 4-10	Spanwise profiles of transition location.....	45
Figure 4-11	Heat-flux history, $x = 0.4$ m	46
Figure 4-12	Comparison of experimental and computational heat flux, $x = 0.4$ m	48
Figure 4-13	Surface temperature. $M = 7.7\text{--}7.9$	51
Figure 4-14	Global heat-flux distribution. $M = 7.7\text{--}7.9$	52
Figure 4-15	Boundary-layer state. Prior to transition onset = blue, after transition onset = red. $M = 7.7\text{--}7.9$	53
Figure 5-1	Photograph of model.....	55
Figure 5-2	Leading edge near $x = 50$ mm.....	56
Figure 5-3	Schematic of pressure-sensor locations. The dashed red line denotes approximate field of view of IR camera.	58
Figure 5-4	Heat flux for increasing Re , quiet flow	60
Figure 5-5	Transition Reynolds numbers	61
Figure 5-6	PSDs for $\alpha = 0^\circ$, quiet flow	62
Figure 5-7	Wave properties for various Re at sensor group 3	64
Figure 5-8	Wave properties at sensor groups 2-6	64
Figure 5-9	Heat flux for increasing Re , quiet flow	66
Figure 5-10	Heat flux for changing angle of attack, quiet flow, $Re \sim 12.8 \times 10^6/\text{m}$	67
Figure 5-11	Transition locations for changing angle of attack, quiet flow, $Re \sim 12.8 \times 10^6/\text{m}$	68
Figure 5-12	PSD for sensor 10 at $\alpha=0^\circ, 1^\circ, 2^\circ$, and 4° . $Re=12.9 \times 10^6/\text{m}$	70
Figure 5-13	Wave angle and phase speeds for $\alpha=0^\circ, 1^\circ$, and 2° . $Re=8.6 \times 10^6/\text{m}$, sensor group 4	71
Figure 5-14	ΔN vs. Re_x for various α	72
Figure 5-15	Growth rates	74
Figure 5-16	Heat flux for increasing Re , noisy flow	76
Figure 5-17	PSDs for a) constant $Re=7.0 \times 10^6/\text{m}$ and b) constant sensor number 4	77
Figure 5-18	Heat flux for changing angle of attack, noisy flow, $Re=7.9 \times 10^6/\text{m}$	79
Figure 5-19	PSD for sensor 9 and $\alpha=0^\circ, 1^\circ, 2^\circ$, and 4° . $Re=7.9 \times 10^6/\text{m}$. (a) Dimensional (b) Non-dimensional.....	80
Figure 6-1	Schematic of pressure-sensor locations. The dashed red line denotes approximate field of view of IR camera.	85
Figure 6-2	Model orientation, looking upstream at the back of the model. Instrumented quadrant is shown in red. The arrows depict the direction of the component of the freestream velocity perpendicular to the model longitudinal axis.....	87
Figure 6-3	α sweep, quiet flow. $Re=9.6 \times 10^6/\text{m}$	88
Figure 6-4	Re_{tr} for α sweep, quiet flow, $Re=9.6 \times 10^6/\text{m}$	89
Figure 6-5	α sweep, noisy flow. $Re=3.1 \times 10^6/\text{m}$	91
Figure 6-6	Transition Re for α sweep, noisy flow, $Re=3.1 \times 10^6/\text{m}$	92
Figure 6-7	β sweep, quiet flow, $Re=9.6 \times 10^6/\text{m}$	94
Figure 6-8	Transition Reynolds number for β sweep, quiet flow, $Re=9.6 \times 10^6/\text{m}$	95
Figure 6-9	β sweep, noisy flow, $Re=3.1 \times 10^6/\text{m}$	97
Figure 6-10	Heat flux for mixed (α, β) combinations, quiet flow	99
Figure 6-11	Transition Re for mixed (α, β) pairs, quiet flow	100
Figure 6-12	Mixed (α, β) Combinations, noisy flow	101
Figure 6-13	PSDs for sensor K19, quiet ow, $Re=9.6 \times 10^6/\text{m}$	103

Figure 6-14 PSDs for sensor PCB3 (solid) and PCB8 (dashed), α sweep, noisy flow	104
Figure 6-15 PSDs of PCBs possibly showing secondary instability	107
Figure 7-1 LST vs. LPSE Stationary Crossflow N-Factors.....	110
Figure 7-2 Full Scale HIFiRE5 $t = 514.8$ s, $0^\circ \alpha, 0^\circ \beta$, Stationary Crossflow N-Factors	110
Figure 7-3 Full Scale HIFiRE5 $t = 514.83$ s, $0^\circ \alpha, 0^\circ \beta$, Stationary Crossflow N-Factors (LST)	112
Figure 7-4 Contours of Mach Numbers, In-Flight Conditions, $1^\circ \alpha, 0^\circ \beta$,	114
Figure 7-5 Contours of Mach Numbers, BAM6QT Conditions, $0^\circ \alpha, 0^\circ \beta$,	115
Figure 7-6 Contours of Mach Numbers, Wind Tunnel Conditions, $0^\circ \alpha, 0^\circ \beta$,	116
Figure 7-7 Second Mode N-Factor Envelope, Flight Conditions, $1^\circ \alpha, 0^\circ \beta$,	116
Figure 7-8 Flight Conditions, $1^\circ \alpha, 0^\circ \beta$, Estimated Second Mode Transition Location	117
Figure 7-9 Second Mode N-Factor Envelope, Wind-Tunnel Conditions, $0^\circ \alpha, 0^\circ \beta$	118
Figure 7-10 Flight Conditions, $0^\circ \alpha, 0^\circ \beta$, Stationary Crossflow N-Factors	118
Figure 7-11 Flight Conditions, $1^\circ \alpha, 0^\circ \beta$, Stationary Crossflow N-Factors	119
Figure 7-12 Wind-Tunnel Conditions, Stationary Crossflow N-Factors.....	119
Figure 7-13 Flight Conditions, $1^\circ \alpha, 0^\circ \beta$, Preliminary Estimated Transition Locations - Stationary Crossflow Only.....	120
Figure 7-14 Flight Conditions, $1^\circ \alpha, 0^\circ \beta$, Preliminary Estimated Transition Locations.....	120
Figure 7-15 Flight Conditions, $1^\circ \alpha, 0^\circ \beta$, Preliminary Estimated Transition Locations, Experimental in Green	121
Figure 7-16 Wind-Tunnel Conditions, Preliminary Estimated Transition Locations.....	121
Figure 8-1 Cartoon of grid topology	128
Figure 8-2 Comparison of PSE and LST N-Factors, 5% Bluntness, 5 AoA, Re = 30 M/m.....	130
Figure 8-3 Sample Crossflow N-Factors Along 90 Ray, 5% Bluntness, 5 AoA, Re = 60 M/m	131
Figure 8-4 2nd Mode Windward N-Factors 5% Bluntness, 5 AoA, Re = 30 M/m	132
Figure 8-5 2nd Mode Windward N-Factors 5% Bluntness, 5 AoA, Re = 30 M/m	132
Figure 8-6 CFD Calculated Swallowing Distance	135
Figure 8-7 Computed 2nd Mode Transition Location (LST) Windward Plane.....	137
Figure 8-8 Windward 2nd Mode N-Factors, 1% Bluntness, Re = 30 M/m	139
Figure 8-9 Windward 2nd Mode N-Factors, 5 AoA, Re = 30 M/m	139
Figure 8-10 Windward 2nd Mode N-Factor Envelopes, Re = 30 M/m	140
Figure 8-11 Contours of Unit Reynolds Number (Windward Plane)	141
Figure 8-12 Non-Dimensional Transition (Style of Stetson).....	142
Figure 8-13 Swallowing Distance vs. Predicted Transition.....	143

List of Tables	Page
Table 2-1 Summary of Flight Vehicle Roughness and Steps	9
Table 4-1 Leading-edge transition onset	40
Table 4-2 Centerline transition onset.....	41
Table 5-1 Instrumentation locations and notation	57
Table 5-2 R_{tr} for $\alpha = 0^\circ$	61
Table 6-1 Instrumentation Locations	84
Table 6-2 Model Attitudes Tested	86
Table 7-1 Grid Resolution Figures	111
Table 7-2 Nominal in-flight flow parameters	112
Table 7-3 Nominal Flow Parameters - Wind Tunnel (BAM6QT)	113
Table 8-1 Cone Geometry Parameters	127
Table 8-2 Nominal Flow Parameters - AFRL High Reynolds Number Facility	127
Table 8-3 Grid resolution figures.....	129

Acknowledgments

This work was supported by the Air Force Office of Scientific Research under Laboratory Research Initiation Request 15RQCOR102. Prof. Steven Schneider of Purdue University supplied test time in the Purdue Quiet Tunnel Ludwieg Tube and provided valuable discussions.

The authors would like to thank Dr. Chau-Lyan Chang for the use of the LASTRAC and LASTRAC3D stability suite, as well as for lending expertise in troubleshooting its use. Computational resources were provided and supported by the DoD HPCMP. Drs. Nicholas Bisek, Ryan Gosse, and Timothy Leger (AFRL/RQHF) provided support and expertise in the use of DoD HPC Systems, as well as the US3D flow solver. Dr. Matthew Lakebrink provided helpful advice on troubleshooting stability calculations. Alex Moyes provided useful discussions on stability characteristics of HIFiRE 5 geometry.

1. Summary

This interim technical report summarizes technical activity on AFRL 6.1 laboratory task LRIR 15RQCOR102 during fiscal year 2017. The objective of this task is to better understand boundary layer transition in hypersonic flowfields with spanwise nonuniformity. Several advances were made under this task during FY17. The HIFiRE-5b flight data were analyzed. Wind tunnel tests were conducted at angles of attack and yaw representative of flight, and computations were carried out for the flight conditions. Also, analysis of cones at angle of attack, as tested in the AFRL Mach 6 high Reynolds number wind tunnel, was also conducted. The effects of angle of attack and yaw angle on crossflow transition on the test bodies were quantified. Multiple transition effects arising from crossflow modes, attachment-line and centerline traveling instabilities were identified. These transition mechanisms were identified by their peculiar transition patterns and behaviors in flight, wind tunnel and computations. Generally, the Parabolized Stability Equations were effective in predicting crossflow and attachment line transition behavior.

This report is compiled from previously published abstracts and conference papers. Section 2 appeared as Ref. 1, section 3 as Ref. 2, section 4 as Ref. 3, section 5 as Ref. 4, section 6 as Ref. 5, section 7 as Ref. 6, and section 8 as Ref. 7.

2. HIFiRE-5b Flight Overview

2.1. Background and Experimental Overview

The HIFiRE-5a mission launched 23 April 2012 from Andoya, Norway.^{8,9,10} HIFiRE-5a was a two-stage vehicle. The second stage failed to ignite, preventing the payload from attaining hypersonic speeds.

Despite the failure of the HIFiRE-5a second stage, the payload acquired supersonic transition data. However, since this did not satisfy mission objectives to acquire hypersonic transition measurements, a new payload, essentially identical to the first, was constructed and flown at Woomera, Australia, on 18 May 2016. This mission was entirely successful. Some minor anomalies occurred, including a short dropout of the GPS system and drift in the IMU. However, these missing data were easily reconstructed using complementary instrumentation. The cold-gas thruster system successfully oriented the payload for a low AoA reentry. During the reentry transition process, AoA was less than two degrees.

With the exception of several sensors that were damaged during installation, all primary science instrumentation functioned throughout the flight. Surface thermocouples revealed boundary layer transition under supersonic conditions during ascent and hypersonic conditions during descent, and were used along with aeroshell backface thermocouples to derive heat transfer. Lower bandwidth surface pressures were recorded and used to reconstruct the payload attitude. Higher bandwidth pressures, recorded at up to 60 kHz, recorded the transition process with high temporal resolution. High bandwidth Vatell heat transfer gauges sampled at 2 kHz also recorded transition with high temporal resolution.

Three types of transitional lobes occurred on the vehicle. One occurred on the centerline, due presumably to traveling instabilities that grew in the unstable, inflected centerline boundary layer. Another lobe occurred midway between the centerline and leading edge. Transition here was presumed to be due to crossflow instability. Both of these transition mechanisms had been predicted prior to flight and observed in wind tunnels. A third transitional lobe appeared on the payload leading edge. This transition mechanism had been predicted,^{11,14,12} but had only been observed anecdotally in one experiment.¹³

This section presents an overview of the HIFiRE-5b flight and some general conclusions regarding transition during the hypersonic flight phase. Although supersonic data were obtained on ascent, this section focuses on the primary mission, the hypersonic descent portion of the flight.

2.2. Vehicle

The HIFiRE-5 configuration was described in a prior paper.¹⁴ The configuration consisted of a payload mounted atop an S-30 first stage¹⁵ and Improved Orion¹⁶ second stage motor, shown in Figure 2-1. The term “payload” refers to all test equipment mounted to the second stage booster, including the instrumented test article and additional control and support sections situated between the test article and the second stage motor. The test article consisted of a blunt-nosed elliptic cone of 2:1 aspect ratio, 0.86 meters in length. The payload remained attached to the second stage throughout flight. The vehicle was spun at a low rate to reduce trajectory dispersion. Cant-angle on the first and second-stage fins caused the vehicle to spin passively. Because of this, the payload was rolling throughout the entire trajectory.

The elliptic cone configuration was chosen as the test-article geometry based on extensive previous testing and analysis on elliptic cones.^{17,18,19,20,21,22,23,24} This prior work^{17,18,19} demonstrated that the 2:1 elliptic cone would generate significant crossflow instability at hypersonic flight conditions and potentially exhibit leading-edge transition. Figure 2-2 illustrates the elliptic cone geometry and coordinate system.

Figure 2-3 presents a dimensioned drawing of the payload, including nosetip detail. The half-angle of the elliptic cone test article in the minor axis (x - y) plane was 7° , and 13.8° in the major axis. The nose tip cross-section in the minor axis was a 2.5 mm radius circular arc, tangent to the cone ray describing the minor axis, and retained a 2:1 elliptical cross-section to the stagnation point. The elliptic cone major axis diameter was 431.8 mm at the base, and the cone overhung the 355.6 mm diameter second-stage booster in the yaw (x - z) plane. A section with minimal instrumentation blended the elliptical cone cross-section into the circular booster cross section. A cylindrical can containing GPS, antennas and other equipment resided between the transition section and the Orion booster. The cylindrical section incorporated four small finlets for material tests.²⁵

The HIFiRE-5b nosetip construction was identical to that of HIFiRE-5a. The nosetip consisted of an iridium-coated TZM (titanium-zirconium-molybdenum) tip, followed by a carbon-steel isolator, a stainless steel joiner, and an aluminum frustum. Figure 4 illustrates the nosetip construction. Small backward facing steps were intentionally placed at the nosetip joints to accommodate differential thermal expansion, with the intent that during descent these steps would have closed to present a smooth external surface. A re-analysis during design of HIFiRE-5b indicated that the HIFiRE-5a step height requirements had been higher than necessary, and the required heights were accordingly reduced for HIFiRE-5b. The steps were measured using a Mitutoyo Surftest SJ-301 profilometer in two sessions, one during a pre-flight assembly test, and another after the vehicle was assembled at the range. Both measurement sets were essentially identical. Results are summarized in Table 2-1, which shows the arithmetic average roughness (R_a) and the maximum and minimum peak-to-valley step heights, P_t . With the exception of the joiner-aluminum joint, all steps were near the desired step height, as noted in Table 2-1. The maximum measured joiner-aluminum step was 200 μm , versus a desired 50 μm height. The nosetip assembly was recovered intact after flight. It showed no signs of melting or other thermal degradation.

The 20 mm thick aluminum frustum that served as the primary instrumented surface was constructed from two clamshell-like panels and two leading edges, described in a prior reference.¹⁴ One side of the payload, the 0° to 90° and 270° to 360° quadrants, was reserved for transition measurement and was devoid of fasteners. The other side of the payload contained countersunk bolts that fastened the closeout panel to the leading edges. This side also contained a small closeout in the nosetip assembly that permitted final assembly of the nosetip (Figure 4). All countersinks were filled flush to the vehicle outer surface with Permatex[®] Ultra-Copper[®] RTV gasket compound prior to flight. Prior tests in the NASA Langley 20-inch Mach 6 wind tunnel and HIFiRE-5a flight results demonstrated that roughness-induced transition from these fasteners would not propagate to the instrumented side of the payload.²⁶

The primary aerothermal instrumentation for HIFiRE-5 consisted of Medtherm Corporation coaxial thermocouples. Type T (copper-constantan) thermocouples were installed in aluminum portions of the aeroshell and Type E (chromel-constantan) were installed in the steel portions. The Medtherm coaxial thermocouples were finished flush with the vehicle surface. These

thermocouples were dual-junction thermocouples with one junction at the cone external surface, and the other on the backface. Kulite® pressure transducers measured local static pressures. Several pressure transducers 180-deg apart on the vehicle were operated in differential mode to measure differential pressures to aid in attitude determination. Other Kulite® transducers were sampled at up to 60 kHz to measure high-frequency pressure fluctuations.

The thermocouples presented minimal surface roughness. In some cases, the thermocouples were over-worked during the procedure to bring them flush with the aluminum surface, resulting in minor depressions, especially on the $\phi=90^\circ$ and 270° rays. The $\phi=90^\circ$ ray presented greater surface irregularities than the $\phi=270^\circ$ ray, as illustrated in Figure 2-5. However, this did not result in any discernible difference in transition Reynolds number between the two rays, as detailed in Section 2.4.

With one exception, instrumentation on HIFiRE-5b was identical to HIFiRE-5a. The Schmidt-Boelter heat transfer gauges on HIFiRE-5a were replaced with Vatell HFM heat transfer gauges, based on the good performance of these instruments on HIFiRE-1. These gauges possessed a higher frequency response than the Schmidt-Boelters they replaced.

The 0° - 90° quadrant of the test article was the primary instrumented surface. It contained thermocouple rays at $\phi=0^\circ$, 45° and 90° . In addition, three x -stations in this quadrant, $x=400$, 600 and 800 mm, were instrumented with thermocouples at closely spaced angular locations. The other quadrant on the smooth side of the test article, 270° to 360° , served as a secondary instrumented surface. It contained the Kulite® pressure transducers and a limited amount of thermocouples to provide a symmetry check of the primary instrumentation quadrant.

Each payload sensor was routed to one of twenty six sensor collection boards. The sensor collection boards amplified and filtered the signal as required for each sensor type, and typically each board could accept 16 sensors. Each sensor collection board was then routed (in pairs) to a distributed flight computer developed under the HIFiRE program using a Texas Instruments DSP along with auxiliary circuitry to handle functions like analog-to-digital conversion, serial data interfaces, telemetry input/output and digital input/output. The Flight 5 payload utilized 13 DSP flight computers grouped (groupings of 5,4,4) into three separate telemetry streams. The sensor data from the sensor collection boards was then converted to digital data using the DSP analog-to-digital conversion circuitry in groups of 32 channels and then packaged into a telemetry stream. Each of the three telemetry streams was then transmitted off board using S-band transmitters with a PCM telemetry scheme. The Flight 5 vehicle utilized the three telemetry streams each at a data rate of 8.33Mbits per second to transmit the data. This was then recorded from various ground stations during the flight.

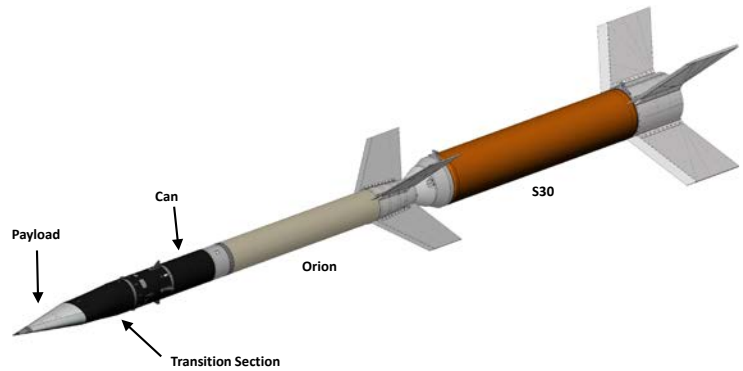


Figure 2-1 HIFiRE-5 stack.

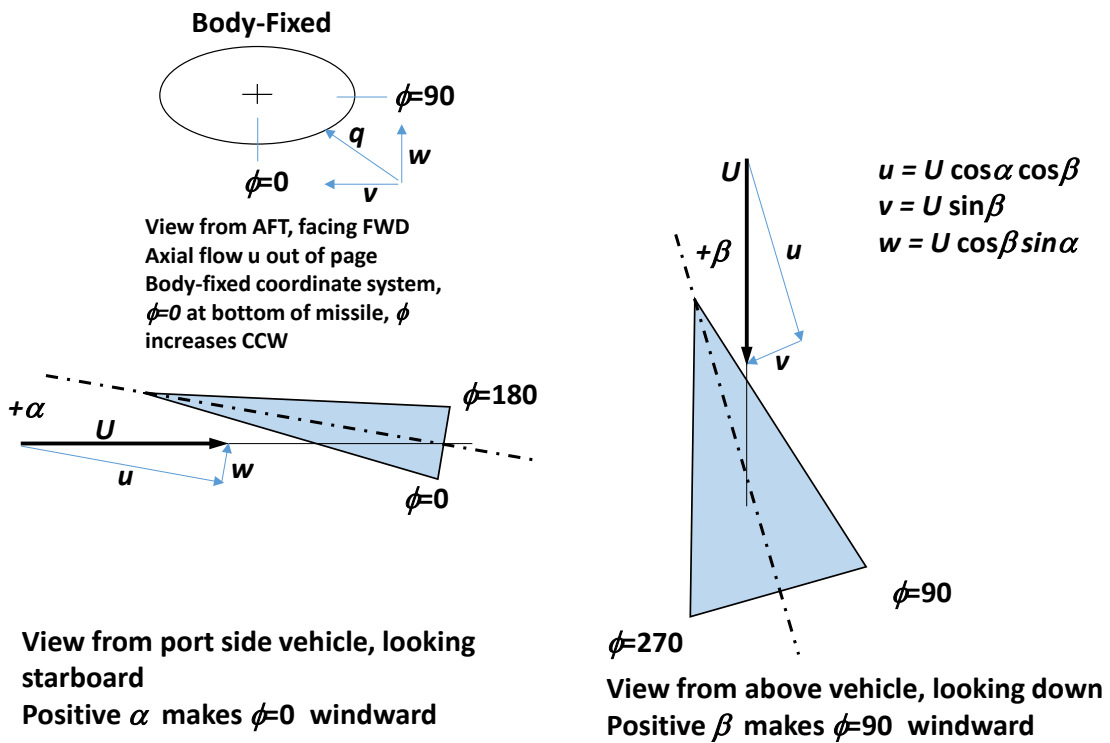
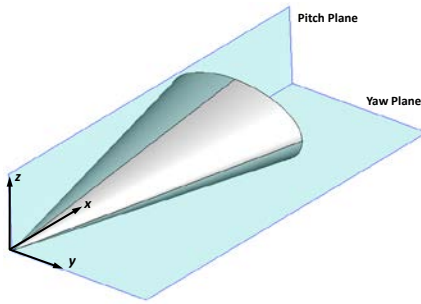


Figure 2-2 Elliptic cone geometry and coordinate system.

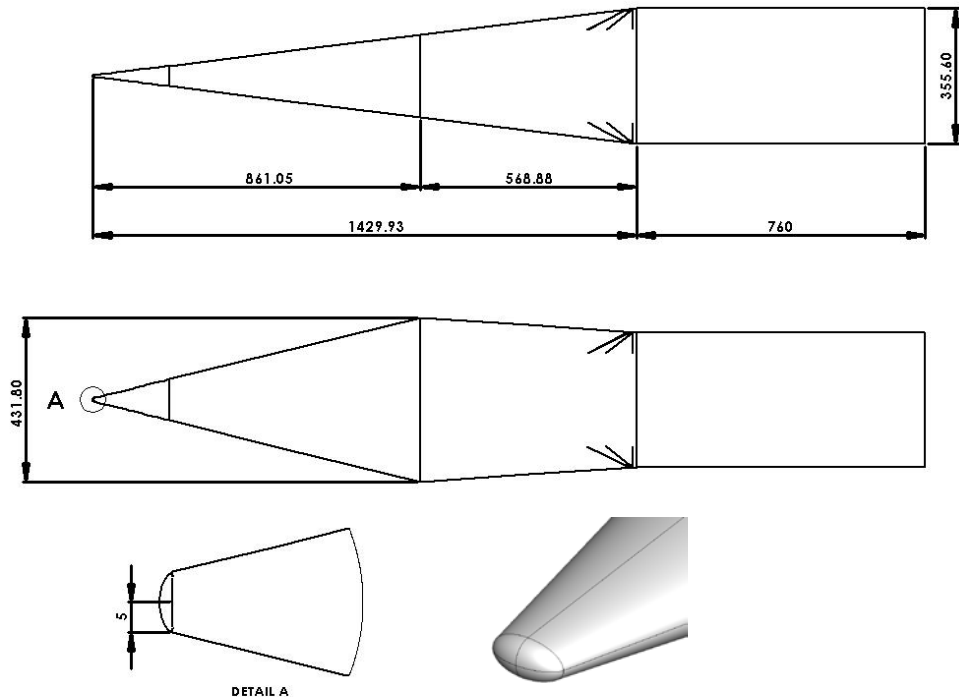


Figure 2-3 HIFiRE-5 payload, including nosetip detail (dimensions in mm).

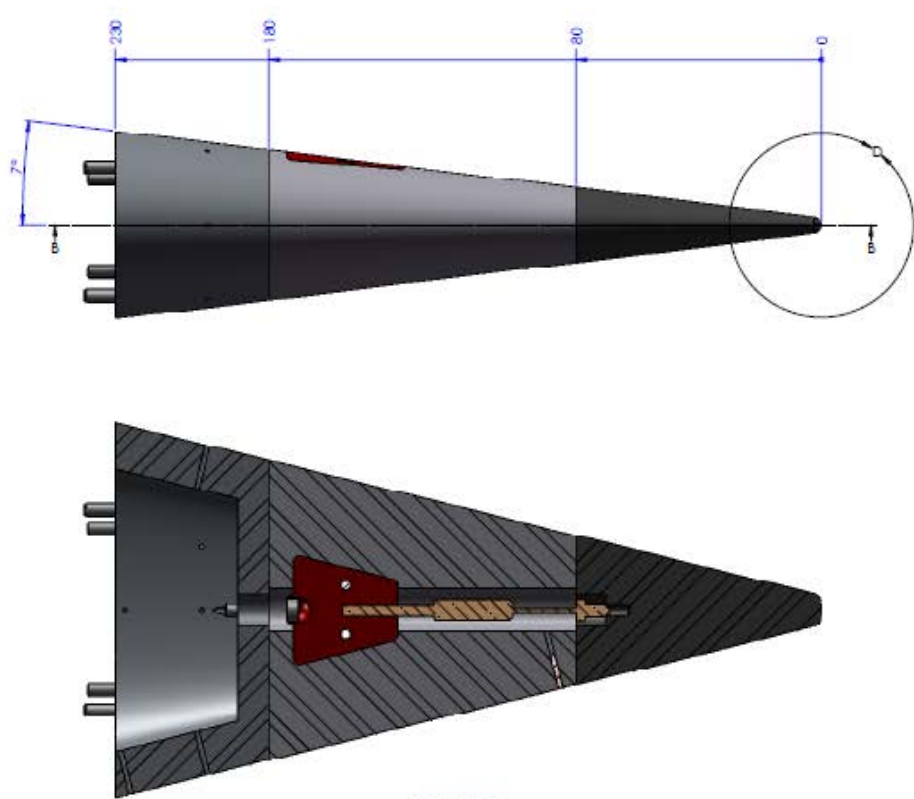


Figure 2-4 HIFiRE-5 nosetip detail. Dimensions in mm.

Table 2-1 Summary of Flight Vehicle Roughness and Steps

Roughness		Joint Steps			
Piece	Ra	Joint	Pt Min	Pt Max	Desired Cold Step
Nosetip	33	Nosetip-Isolator	1200	2500	1600
Isolator	39	Isolator-Joiner	2600	4500	3200
Joiner	49	Joiner-Cone	2200	8100	2000
Cone	32				
All dimensions microinches					

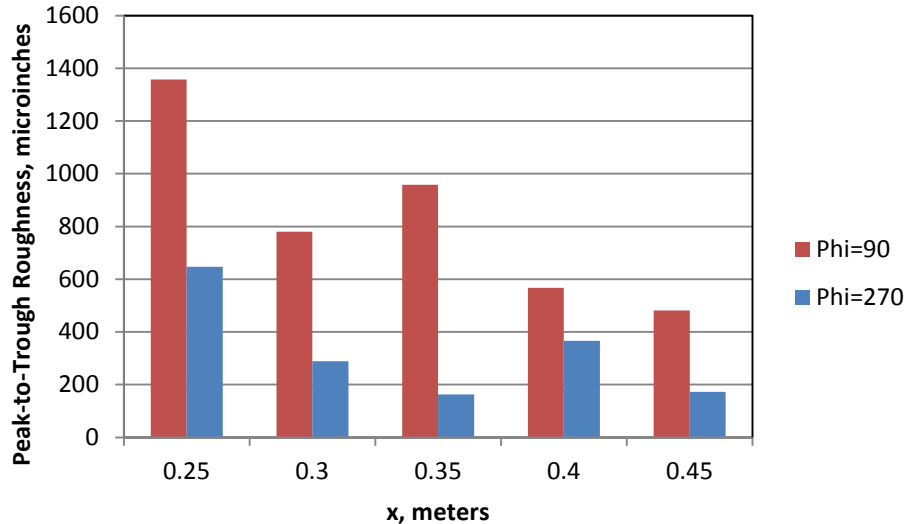


Figure 2-5 Peak thermocouple roughness

2.3. Trajectory and Vehicle Attitude

The HIFiRE-5b flight was, for the most part, nominal with two exceptions. The GPS dropped out at the beginning of second stage burn, and the IMU suffered some drift and bias shift in acceleration data. GPS functionality was restored near apogee, but IMU drift remained throughout flight. The exoatmospheric “bang-bang” orientation maneuver successfully oriented the vehicle to the nominal flight path angle for reentry. Apogee was slightly lower than nominal however, leading to a slightly lower than expected flight path angle. This deviation from the planned trajectory led to a small residual AoA during reentry. The vehicle yaw and angle-of-attack underwent damped oscillations until the vehicle departed from stable flight at $t=520$ s. By this time, the payload was almost fully turbulent and the experiment had ended.

Due to the GPS dropout and IMU drift, the post flight trajectory reconstruction was a bit more involved than previous flights. The GPS dropped out for the majority of the ascent phase, and with the IMU drift, there were no reliable data to use for the ascent altitude profile. In order to determine the ascent altitude profile, it was decided to try to use the raw IMU acceleration and gyro rates along with the initial launch conditions to integrate the trajectory over time. A process was created in Matlab using a 4th order Runge Kutta trajectory integration method, and a suitable ascent profile was generated by matching what GPS data was obtained on ascent along with a radar track from ascent.

For the reentry portion of the flight, the GPS provided the altitude versus time profile. The ascent and reentry profile were then merged to provide a full trajectory versus time for post flight analysis. Some additional work is ongoing to utilize Kalman filtering methods to help understand the IMU output deviations.

The HIFiRE-5 Mach number and freestream unit Reynolds number histories for a portion of the descent are graphed in Figure 2-6. The stated Mach and Reynolds numbers are estimated to be accurate to within 2% and 3%, respectively, driven largely by uncertainty in the altitude. The time-period in Figure 2-6 extends approximately from the beginning of the transition process, at the back of the payload, to the end of transition on the leading edge near the tip. Although the

most upstream leading edge thermocouples were still laminar at $t=520$ seconds, the rest of the payload was turbulent. Mach number varied slightly throughout the test window from $M=7.7$ to $M=7.9$. During the same period, freestream unit Reynolds number increased from about 2.5×10^6 to over 23×10^6 per m. During this period the average aluminum frustum temperature under laminar flow was about 100 deg C, +/- 10 C depending on time and location. This equated to a highly-cooled wall condition with $T_w/T_0 \sim 0.1$. Temperatures measured on the steel joiner were up to 100 deg C higher.

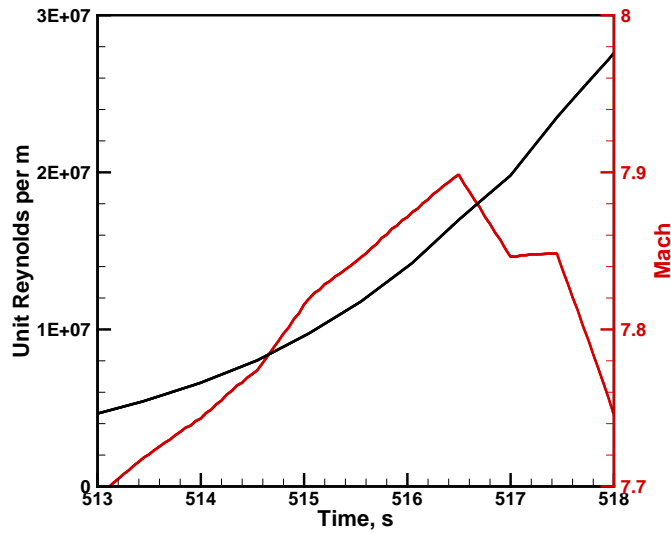


Figure 2-6 Descent Mach and unit Reynolds number histories.

Figure 2-7 illustrates pressure measured on the aft centerline of the vehicle. The mean pressure increased with time of course, as the altitude decreased. A small sinusoidal ripple was superimposed on the mean pressure, due to the combination of vehicle spin and AoA. Since the payload centerline was not coincident with the flight path vector, a single transducer like this continuously oriented from windward to leeward, and back again.

Measured pressures permitted reconstruction of the vehicle spin and instantaneous attitude, relative to the velocity vector. Figure 2-8 shows the direction of payload spin, reconstructed from measured pressures on the centerline and leading edge.

Analysis of additional pressure sensors permitted a full reconstruction of the payload orientation time history. Figure 2-9 illustrates AoA and yaw during transition. The two attitude angles varied sinusoidally as the vehicle rolled. Generally, they were 90° out of phase, so that peak AoA corresponded to zero yaw, and vice versa. This relationship is not exact, but close enough to understand the payload motion and its effect on transition. During the period illustrated, the payload AoA and yaw damped from about 1.5° at the beginning of transition to about 0.5° near the end of transition.

Vehicle attitude was also derived using the onboard GPS and IMU, as described in Ref. 8. Since the GPS and IMU both suffered from the anomalies cited above, the pressure-derived vehicle attitude was preferred over the GPS/IMU method. Nevertheless, comparison of the two methods provides some insight into the difficult problem of determining errors for the vehicle attitude. Figure 2-10 compares AoA obtained from the two methods. The overall time histories of vehicle attitude derived from GPS/IMU were similar to those derived with the pressure method. The GPS/IMU method give slightly higher amplitudes of AoA and yaw, and peak times slightly displaced from those derived from the pressure method. Peak attitude angles derived using the GPS/IMU combination were up to 0.8 degrees higher than those derived from pressures. The times of maximum attitude angles varied up to about 20 ms between the two methods. An error of $\pm 0.8^\circ$ and an uncertainty of 20 ms probably represents a conservative error estimate in the payload attitude. With a payload spin period of about 200 ms, a 20 ms timing error equates to 36 deg error in roll angle.

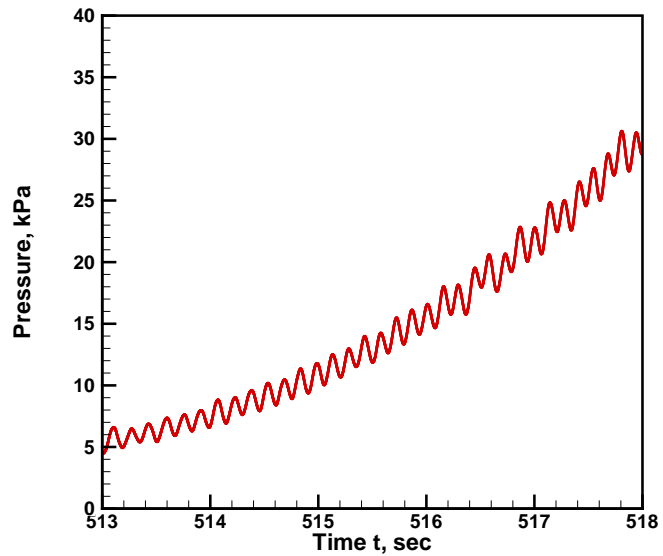


Figure 2-7 Pressure history, $\phi=0$, $x=800$ mm.

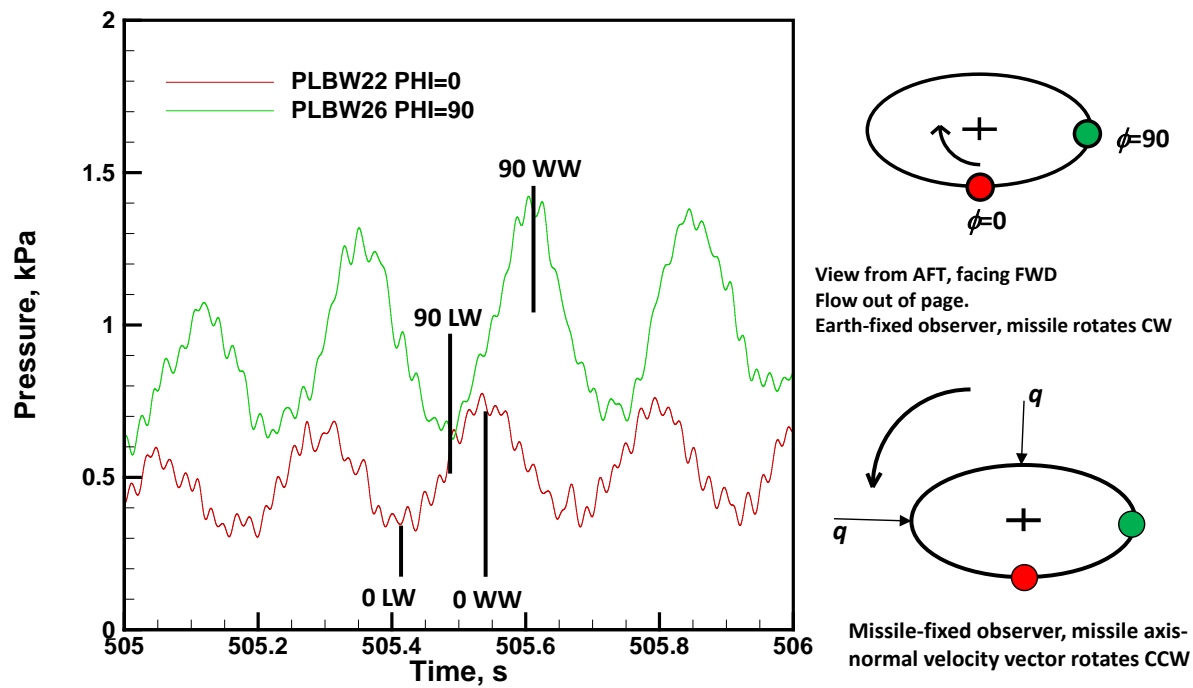


Figure 2-8 Payload spin derived from measured pressure

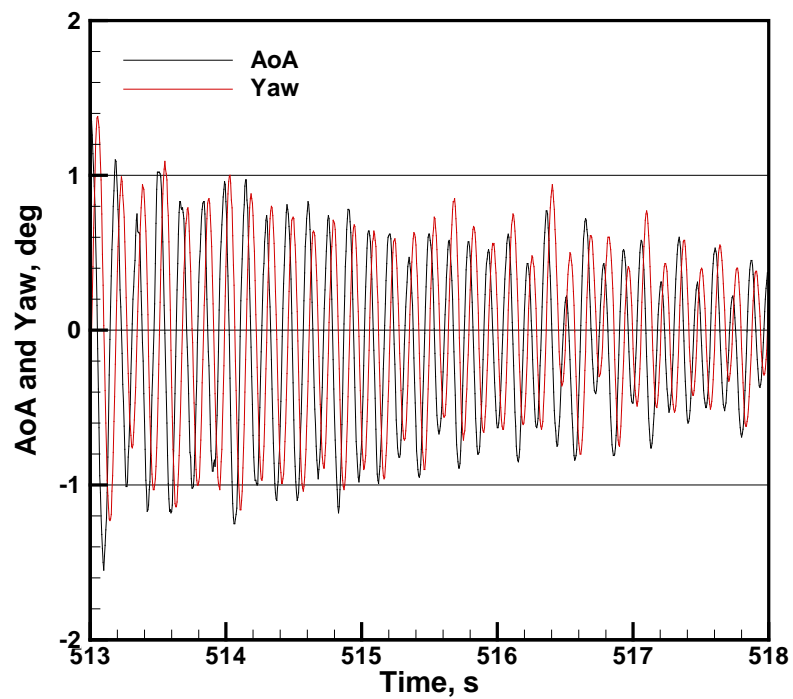


Figure 2-9 Angle of attack and yaw angle derived from surface pressures.

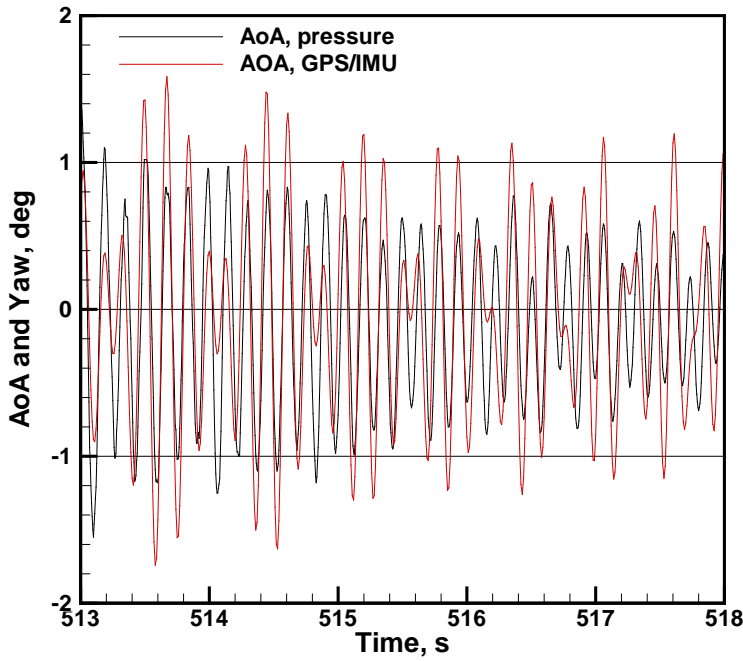


Figure 2-10 Angle of attack derived from pressure and from GPS/IMU

2.4. Transition Phenomenology

Raw temperature data are examined first to illustrate the data quality and overall transition features. Figure 2-11 illustrates leading-edge temperature histories. Boundary layer transition manifested as a sharp increase in the slope of the temperature history (for example, the $x=800\text{mm}$ curve at $t=514$ seconds). Flattening of the temperature curves after $t=518$ seconds was due to saturation of these channels and was non-physical. The thermocouple at $x=200\text{mm}$ saturated at $t=518\text{ s}$ without undergoing transition (outside range of Figure 2-11). The Figure 2-11 temperature-time histories show an orderly transition progression from the back to the front of the vehicle. There was no evidence of “flashing” of the transition front, as is typical for tripped transition,⁸ indicating a likely smooth-body transition.

The Figure 2-12 data support this supposition, showing good left-right symmetry in the leading edge transition. It is unlikely that, if leading edge transition had been provoked by roughness, that it would have been symmetric. Transition due to nose joint roughness on both HIFiRE-1 and HIFiRE-5a was asymmetric.^{8,27}

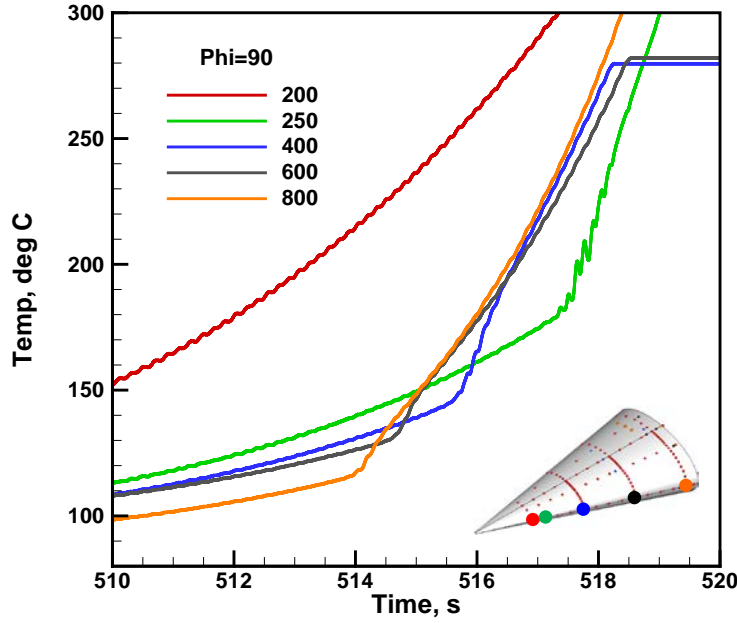


Figure 2-11 Leading edge temperature histories.

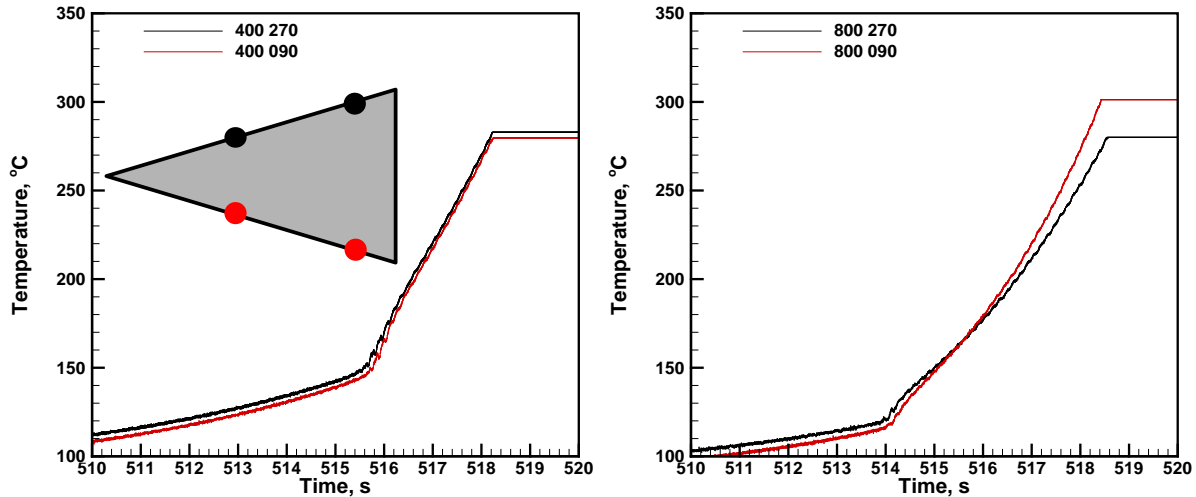


Figure 2-12 Leading edge transition symmetry

Temperature-time histories in Figure 2-13 illustrate transition on the payload centerline. Although the slope change produced by transition was not as sharp as it was for the leading edge, it was still identifiable. Similar to the leading edge, the transition progressed in an orderly fashion from the back to the front of the payload as unit Reynolds number increased.

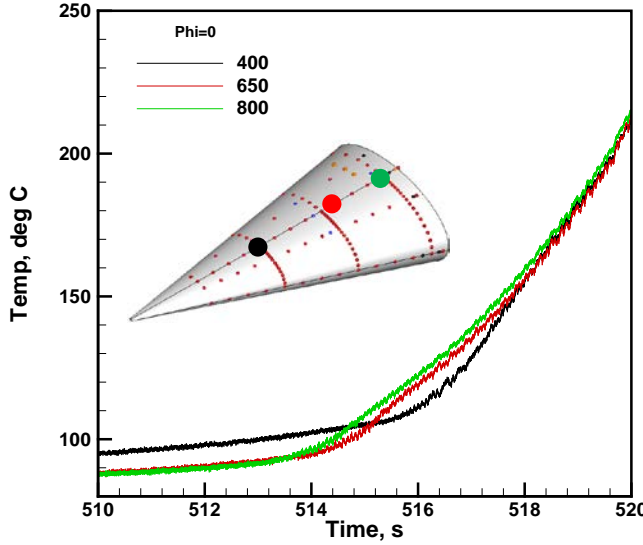


Figure 2-13 Centerline transition

Close examination of the centerline temperature histories show an increase in temperature fluctuations during transition. Figure 2-14 shows low-amplitude fluctuations of about 10 Hz, or about twice the payload spin rate, on the centerline at $x=550$ mm, for $t < 514.7$ s. Larger-amplitude fluctuations began at about $t = 514.7$ s, coincident with an increase in the slope of the mean temperature, which is taken as an indication of transition.

Comparison of the temperature time histories to heat transfer rates revealed the source of the temperature fluctuations of Figure 2-14. Prior to transition, these fluctuations occurred as streamwise hot streaks near the payload centerline convected over the sensors as yaw varied due to vehicle spun. After transition began, the oscillations were due to a combination of this effect, plus a time-periodic breakdown of the boundary layer to turbulence. Centerline breakdown began first on the windward side of the vehicle (positive AoA), then shortly after that on the leeward side (negative AoA). Figure 2-15 illustrates the close correlation between the payload AoA and the transitional heat transfer.

Heat transfer near the shoulder of the model at $\phi=45^\circ$ also showed a periodic transition progression. Figure 2-16 shows heat transfer and yaw angle for a two-second period during transition at the $\phi=45^\circ$ location. Yaw angle is presented, rather than AoA, since wind tunnel experiments showed that the shoulder area transition was more closely correlated with yaw. Figure 2-16 shows that transition occurred at this location at positive yaw angle, when this region was yawed into the wind. This transition behavior was consistent with that observed on the HIFIRE-5b model in the Purdue $M=6$ quiet wind tunnel⁵ and on a 4:1 elliptic cone test at CUBRC.¹³

The effect of yaw angle on transition may be quantified by selecting heat transfer histories based on payload orientation. Figure 2-17 illustrates the effect of the payload yaw angle on transition at $\phi=45^\circ$. Transition at this location for positive yaw (windside) occurred at $t=514.2$ seconds, compared to 515.6 seconds for negative yaw (leeside). These times correspond to transition

Reynolds $Rex=3.9 \times 10^6$ and 6.6×10^6 , respectively. The effect of AoA on transition at this location was much less.

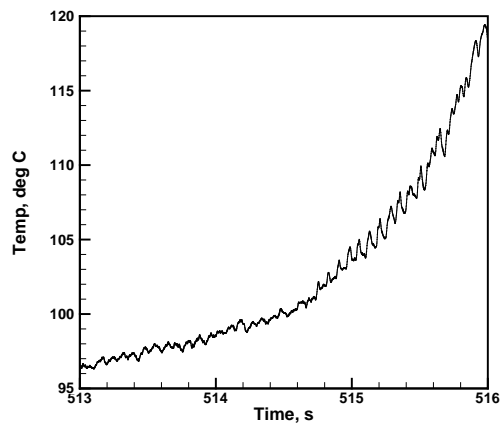


Figure 2-14 Detailed temperature history for thermocouple 131, $x=550$ mm, $\phi=0^\circ$.

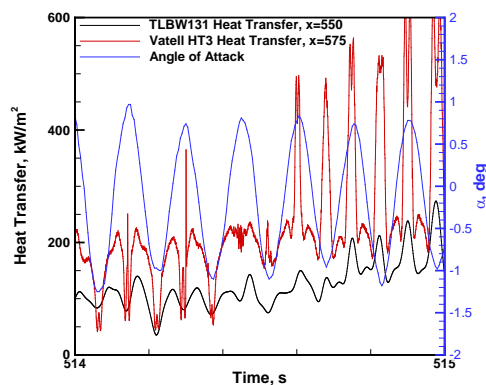


Figure 2-15 Centerline temperature, heat transfer and angle of attack

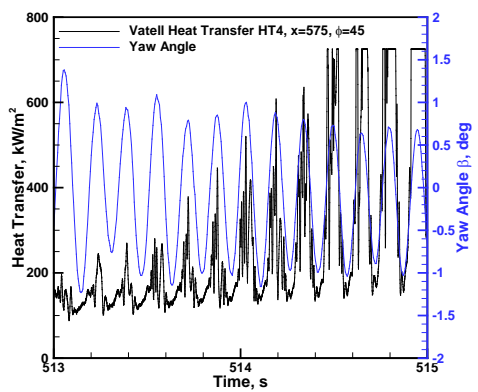


Figure 2-16 $\phi=45^\circ$ transitional heat transfer and yaw angle

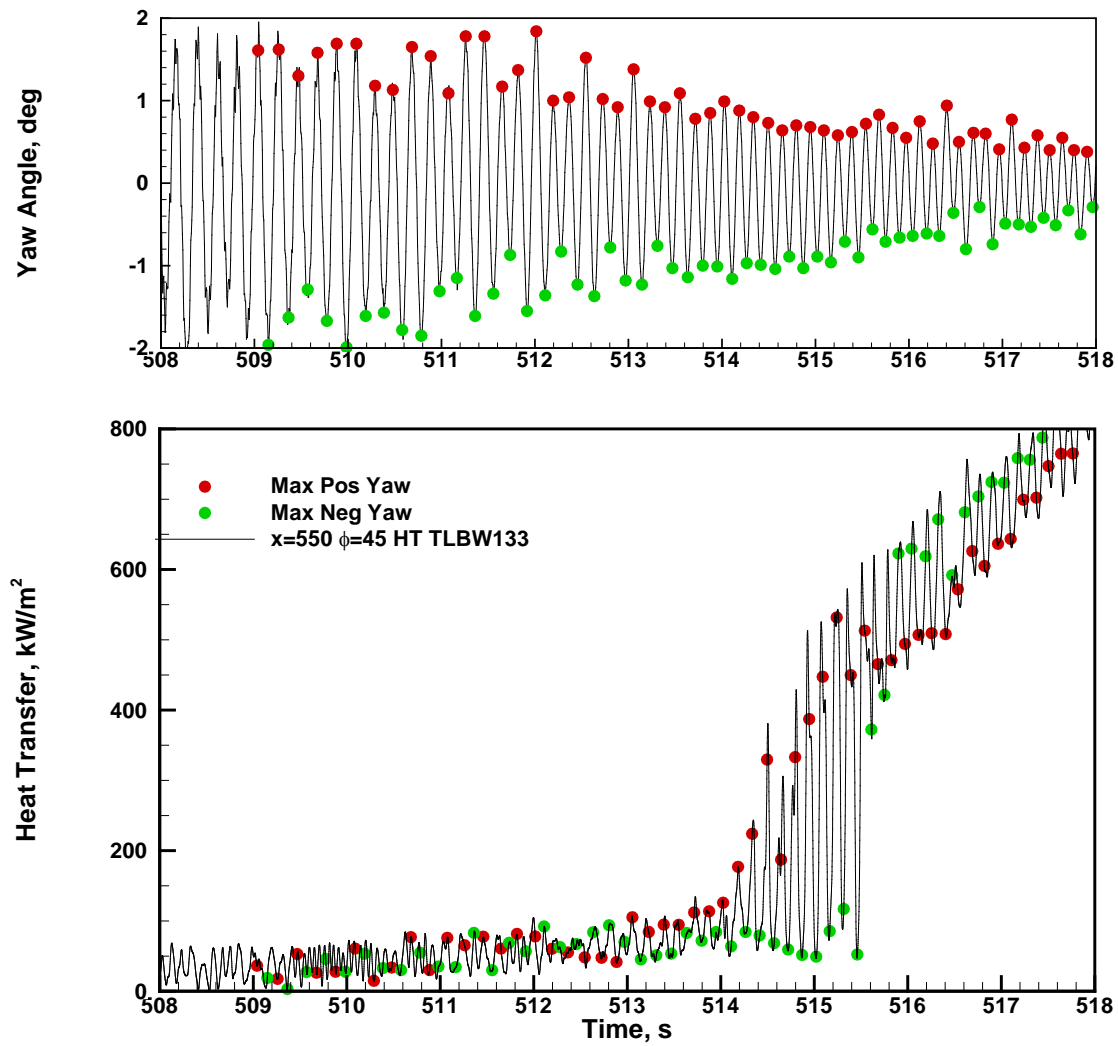


Figure 2-17 $\phi=45^\circ$ heat transfer history sampled on payload orientation.

Prior to transition, heat transfer disturbances appeared at the $\phi=45^\circ$ location when this area was yawed into the wind. These disturbances were somewhat repeatable during each roll cycle, and grew in amplitude with time. Figure 2-18 shows how these disturbances, measured using Vatell gauge HT4, were phase-locked to some extent with the vehicle attitude. In this case, the centerline pressure minimum was used to determine the start time of each cycle, rather than the pressure-derived AoA, since the pressure minimum provided a better alignment of the heat transfer features. The fixed alignment of these features is congruent with a body-fixed disturbance, perhaps crossflow vortices that convected over the transducer. Figure 2-18 also illustrates how these disturbances attained maximum amplitude when the transducer was yawed into the wind, similar to the behavior of crossflow vortices observed in the Purdue Mach 6 quiet wind tunnel.⁵

Generally, the $\phi=45^\circ$ region was most sensitive to the payload orientation, with the $\phi=0^\circ$ region being slightly less sensitive. Transition in the leading edge region was relatively insensitive to payload orientation. The $\phi=90^\circ$ and 270° locations transitioned almost simultaneously within one roll period, as shown in Figure 2-12.

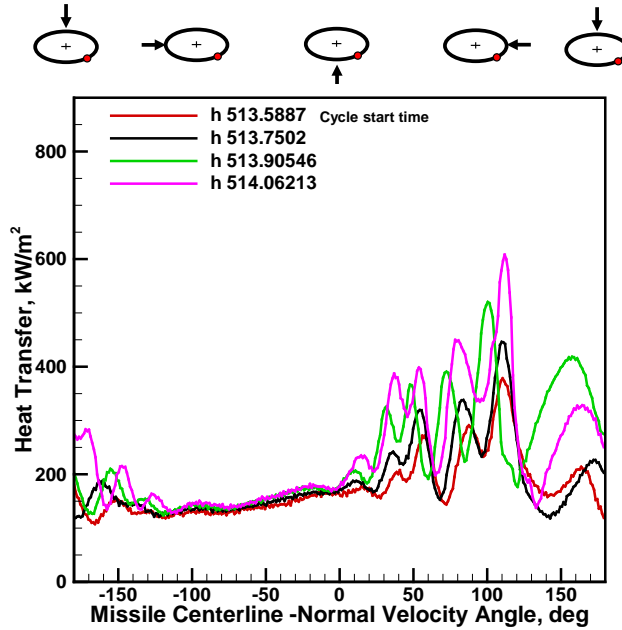


Figure 2-18 Phase-locked heat transfer disturbances, $\phi=45$ deg.

It is well-known that the type of instrument used to indicate transition affects the measured transition Reynolds number. Higher-frequency transducers are able to resolve small turbulent fluctuations that are filtered out by lower-bandwidth transducers. These more sensitive transducers tend to yield lower transition Reynolds numbers compared to lower bandwidth transducers. Figure 2-19 illustrates this effect. Figure 2-19 shows transition measured on the centerline by a Medtherm coaxial thermocouple, a Vatell heat transfer gauge and a Kulite pressure transducer. The Medtherm gauge was sampled at 400 Hz, the Vatell at 2 kHz, and the Kulite at 100 kHz. The Kulite transducer began to show small noise spikes as early as $t=512.24$ s at $Rex=3\times 10^6$. The Vatell gauge responded slightly later, showing short heating spikes at $t=514.14$ s, ($Rex=4\times 10^6$). The coaxial thermocouple responded last, at $t=514.75$ s, or $Rex=4.8\times 10^6$. During the period $512.24 < t < 514.75$, maximum AoA and yaw varied from about 1.5° to 1.0° . Since the bulk of the transition data reported in this and companion papers were derived from thermocouples, they are biased somewhat to higher transition Reynolds numbers compared to lower bandwidth transducers.

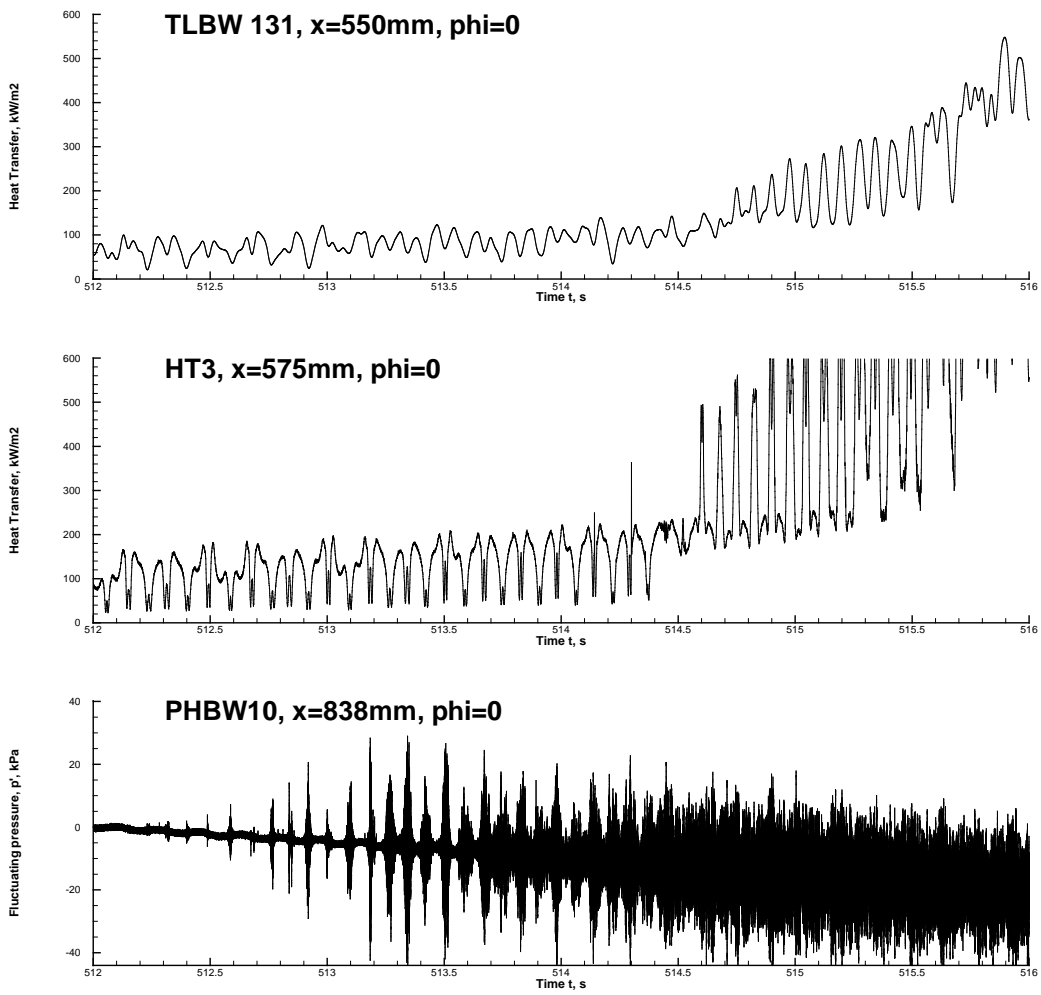


Figure 2-19 Effect of transducer bandwidth on measured centerline transition location.

2.5. Comparison to Ground Test

Temperature histories from all transducers were synthesized into maps of the transition location in ϕ - Reynolds space. Figure 2-20 (Ref 3) shows transition Reynolds number as a function of spanwise location, at three different x -stations. This figure clearly shows three transitional lobes emanating from (top-to-bottom in figure) leading edge, shoulder ($\phi=45^\circ$) and centerline. This transition pattern is similar at each x -station. For each of the lobes, the transition Reynolds number varies less than 10% with streamwise location. In the two regions of delayed transition (centered near $\phi=25^\circ$ and 70°), the transition Reynolds number and the azimuthal location of maximum transition delay is more variable. In this figure, beginning of transition was taken as the first departure of heating from laminar levels. No effort was made to discriminate the transition location based on the payload attitude. For this reason, the transition Reynolds numbers shown in Figure 2-20 are biased to the most unstable payload orientations for each particular transducer. In particular, transition near the $\phi=45^\circ$ region is more representative of the condition where that side is yawed into the wind.

At present, there is no wind tunnel test directly replicating flight conditions. There are several wind tunnel tests of HIFiRE-5 at Mach 6 and 7, and a sharp 2:1 elliptic cone at M=8. None of these tests replicated flight T_w/T_0 , which is suspected to be a significant difference. Wall-cooling destabilizes second-mode instabilities, but reduces crossflow Reynolds number.²⁸ HIFiRE-5 was tested at Purdue University, under quiet and noisy flow conditions, and at NASA LaRC, under noisy flow. The sharp 2:1 elliptic cone was tested at M=8 under noisy conditions at AEDC VKF-B. Limited qualitative infrared imaging data were obtained at Mach 7 at CUBRC. Despite the dissimilarities among these tests and flight conditions, some general conclusions may be drawn regarding HIFiRE-5 transition in the wind tunnel versus flight.

First, the centerline transition occurred at a relatively low Reynolds number in flight, as expected. In all previous ground tests, the centerline transition was dominated by the strongly inflected velocity profile here, making the boundary layer susceptible to traveling instabilities. Flight centerline transition occurred at $Re_x \sim 4.5 \times 10^6$. This is contrasted with HIFiRE-1 zero AoA transition at M=5.3, which took place at $Re_x \sim 10^7$.

Second, for the wind tunnel cases, centerline transition under noisy flow occurred at much lower Reynolds numbers (1×10^6 or less) than in flight (approximately 4.5×10^6). Figure 2-21 compares quiet and noisy wind tunnel transition to flight transition. Centerline quiet-flow transition occurred at a Reynolds number of about 3.2×10^6 , much closer to the flight value. This transition Reynolds number decrement due to tunnel noise, a factor of 3-4, is comparable to that seen for HIFiRE-1 at zero AoA and $5 < M < 6$. The transition decrement for HIFiRE-1 at these conditions was a factor of approximately two.

Third, the distinct lobe near $\phi=45^\circ$ occurred in flight and quiet wind tunnel flow, but generally not in noisy flow at zero AoA. The presence of this lobe appears to be a function of wind tunnel noise. In noisy flow, transition Reynolds number as a function of azimuthal location displayed a monotonic increase from low Reynolds number on the centerline to a higher Reynolds number on the leading edge. The transition front indentation near $\phi=25^\circ$ observed in quiet wind tunnel flow and in flight did not appear under noisy flow. LST calculations and wind tunnel tests indicate that transition near $\phi=45^\circ$ is crossflow-dominated. Conventional wisdom is that stationary crossflow transition is not strongly affected by wind tunnel noise, unlike traveling instabilities. A likely supposition for the difference between quiet/flight and noisy conditions is that under noisy flow, transition on the centerline is promoted so far forward that it spreads laterally and contaminates outboard transition, so that the crossflow lobe is not easily observed under noisy flow. It should be noted that the CUBRC $M=7$ tests were different from the LaRC and VKF-B tests, in that the CUBRC tests appeared to show a distinct crossflow lobe at low Reynolds number.

A fourth observation is that the flight case shows a distinct leading-edge transition lobe that was not seen in LaRC or Purdue tests. Leading edge transition did not occur in the Purdue wind tunnel under quiet flow. Under noisy conditions in both tunnels, no distinct leading edge transition lobe occurred. Transition occurred on the leading edge, but it was the most downstream transition location on the model. Under noisy flow, leading edge transition appeared to arise from spanwise contamination from adjacent turbulent regions. In the LaRC tests, leading edge transition occurred at $Re_x \sim 3.7 \times 10^6$, compared to about 4.5×10^6 in free flight. It appears that the leading edge transition was not as severely affected by wind tunnel noise as the HIFiRE-5b centerline transition or the HIFiRE-1 axisymmetric cone transition. This result is somewhat reminiscent of the behavior of the HIFiRE-1 windward side transition when that test

article was at angle of attack. In this case, windward transition Reynolds numbers in noisy flow were comparable to or even exceeded flight transition Reynolds numbers. At least part of this difference was ascribed to the higher wall cooling experienced by the flight vehicle.²⁹

An exception to these ground-test results for leading edge transition was the temperature-sensitive paint images obtained at CUBRC at about $M=7$.¹³ In this study, at least one image seemed to show a leading edge transition lobe where transition occurred at Reynolds numbers nearly identical to or lower than centerline transition.

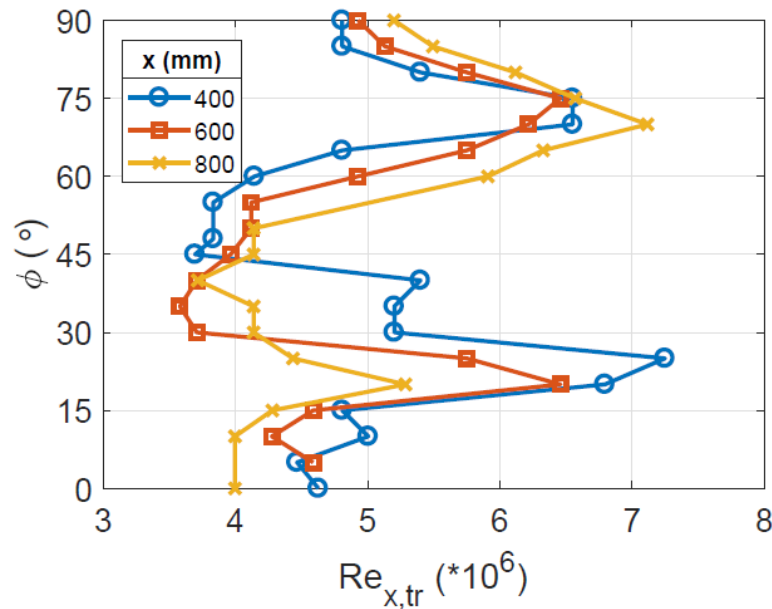


Figure 2-20 Transition Reynolds numbers at three streamwise locations

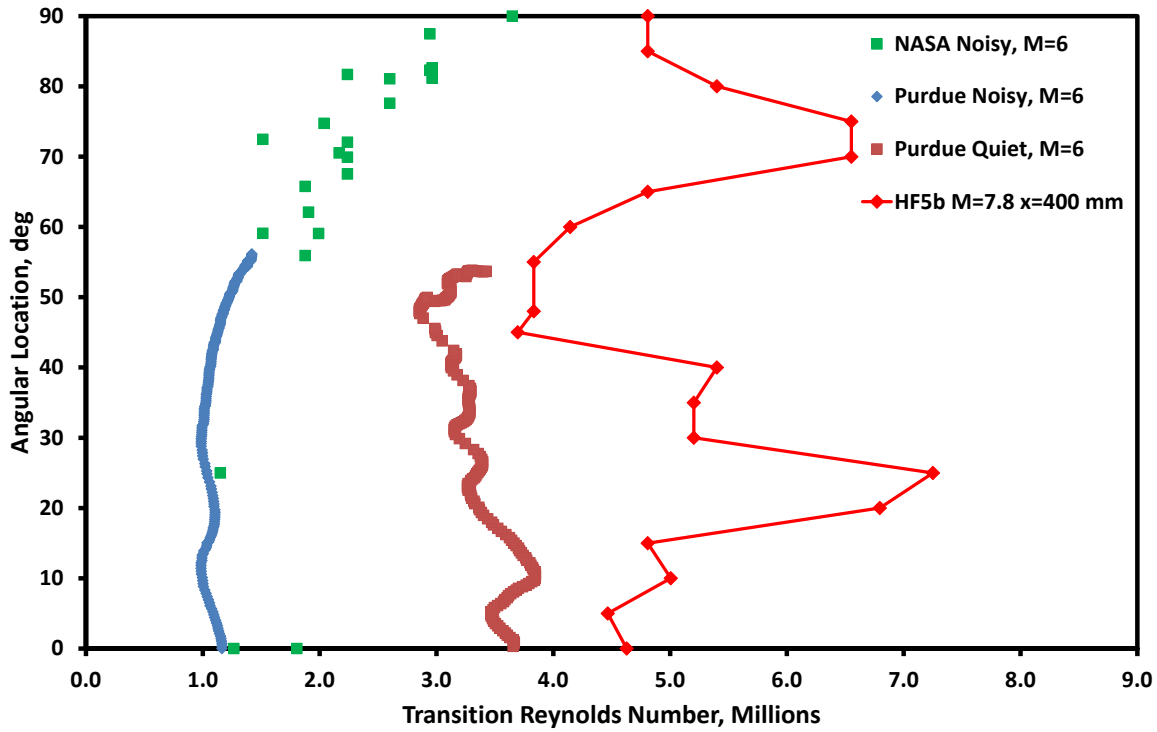


Figure 2-21 Noisy and quiet wind tunnel transition compared to flight transition.

2.6. Conclusions

The HIFIRE-5b mission was fully successful in gathering hypersonic transition on an elliptic cone configuration. The following observations may be made regarding the flight and ground test data:

1. The multi-lobe transition pattern observed in ground test, arising from second-mode instabilities on the centerline and crossflow instabilities near the $\phi=45$ location, was observed in flight. In addition, a third transitional lobe centered on the payload leading edge was observed in flight. This transition mechanism, presumably due to second mode instability, could not be resolved in quiet flow in ground test, but might have been evident in M=7 tests performed at CUBRC.
2. The difference in transition Reynolds number between flight and noisy ground test was most pronounced near the centerline. Outboard regions showed transition at a higher Reynolds number in flight than in ground test, but the differences were not so pronounced here.
3. Transition occurred on the payload at low, but not negligible AoA and yaw. During the passage of the transition front over the vehicle during reentry, AoA and yaw decreased from about 1.5° to about 0.5° . This yaw angle produced a measureable effect on transition. AoA had a lesser effect. The $\phi=45^\circ$ region was most sensitive to yaw angle. Positive yaw angle (sensor into the wind) resulted in a lower transition Reynolds number. Near $\phi=45^\circ$, this effect resulted in transition Reynolds numbers that varied from 3.9×10^6 (yawed into the wind) to 6.6×10^6 (yawed away from the wind).

4. Leading edge transition was relatively insensitive to the model orientation. Measureable differences in roughness existed between the $\phi = 0^\circ$ and $\phi = 270^\circ$ leading edges, but these were not enough to create any difference in the transition Reynolds number between the two leading edges. Transition on the leading edge, as well as the rest of the body, proceeded in a gradual and orderly manner, with no “flashing,” thus indicating an untripped transition.
5. Multiple sensors gave consistent indications of transition, although higher bandwidth instrumentation indicated transition at lower Reynolds numbers than lower bandwidth thermocouples.

In summary, the HIFiRE-5b experiment represents a very well-controlled and well-documented case to calibrate ground test and transition prediction.

3. HIFiRE-5b Attitude Determination

The HIFiRE-5b vehicle flew a ballistic trajectory, with no active attitude control. The elliptic cone test article remained attached to the second stage booster at all times, and relied on aerodynamic stability to minimize angle of attack. The payload spun to minimize trajectory dispersions. Since the payload was generally at some small angle of attack and spinning, any given point on the payload showed an oscillatory angle of attack and yaw (or equivalently, total angle of attack and roll) relative to the wind. Since the transition location is a function of vehicle attitude, it is important to determine accurately both the attitude and the time-dependent transition location. The analysis in this section closely follows methods developed for attitude determination of the HIFiRE-5a flight.¹⁰

Calculations provide both an assessment of measured and computed quantities, and a means of reconstructing the flight. Analysis of the HIFiRE-5a flight compared measured data to heating and pressure estimates, as well as computational fluid dynamics (CFD) results for attitude determination^{10, 30} and similar work has been used to derive flight attitude where Global Positioning System (GPS) information is unavailable, such as during Martian atmospheric entry,³¹ and combined with inertial measurements to improve accuracy.³² Computed pressures may then be used to back-calculate the vehicle attitude to establish a check of the attitude measured by the on-board inertial measurement unit (IMU) and GPS. The method for determining vehicle attitude from GPS and IMU was described in a prior paper.⁸ Flight angle of attack and yaw information is also used to inform predicted laminar and turbulent heat transfer levels for boundary layer transition determination.³ Since both the GPS and IMU suffered minor anomalies during the HIFiRE-5b flight, the pressure-derived vehicle attitudes took on added significance.

3.1. Pressure Distribution RMS Analysis and Comparison with CFD

Computations³³ were performed at five values of α and β (-2.0°, -1.0°, 0.0°, 1.0° and 2.0°) for flight Mach numbers between 7.7 and 8.0, which correspond to the period at t=513–518 s during the reentry portion of the HIFiRE-5b flight. These conditions were chosen, on the basis of preliminary trajectory estimates, to bracket the attitude and Mach number range during transitional flow during reentry. Both laminar and turbulent conditions were calculated. Surface pressures did not show tangible differences between laminar and turbulent cases. The two planes of symmetry of the vehicle were exploited where possible to reduce the number of necessary calculations.

Comparison of measured to computed pressures provided a method for assessment of vehicle attitude independent of the IMU and GPS. While 15 flight pressures at multiple locations were used for attitude determination in HIFiRE-5a,¹⁰ an attitude assessment scheme involving 4 transducers equally spaced by 90° in ϕ was found to be essentially equivalent and computationally more efficient, and is used in the present analysis. The method relied on finding the vehicle attitude that minimized the RMS difference between measured and computed pressures. A similar approach, utilizing a matrix of CFD solution points, has recently been used for the implementation of FADS algorithms for reconstructing the Mars Science Laboratory entry, descent, and landing trajectory.³¹ The RMS difference is defined as

$$\tilde{p} = \frac{1}{p_\infty} \left[\frac{1}{4} \sum_{i=1}^4 (p_{\text{CFD}} - p_F)_i^2 \right]^{\frac{1}{2}} \quad (3.1)$$

To reduce the effect of transducer drift, all pressure signals are re-zeroed during post-processing for the exoatmospheric portion of the flight, prior to reentry.⁵

Kulite pressure transducers measured local static pressures. Additionally, several pressure transducers were operated in differential mode to measure differential pressures 180 degrees apart on the vehicle to aid in attitude determination. The differential transducers are examined separately in Section 3.2.

Since it was infeasible to perform multiple CFD solutions at various α , β combinations, discrete combinations of α and β were calculated at freestream Mach numbers between 7.7 and 8.0. These Mach numbers bounded the reentry flight case of interest. These CFD cases were interpolated in Mach number to estimate computed pressures (and heat transfer) at intermediate Mach numbers using the Matlab gridded interpolant with six control variables (M , Re , α , β , φ and x) as described in Porter et al.³³

The process as described in Jewell et al.¹⁰ was repeated at 0.005 s intervals for $508 \leq t \leq 520.5$ s. Figure 3-1 shows vehicle attitude derived from pressure and IMU/GPS, and the minimum RMS between measured and computed pressures for the ascent case. Trajectory times approximately corresponding to the computed CFD cases ($514 \leq t \leq 518$ s) are indicated by vertical dashed lines. Although the amplitudes of dominant IMU/GPS-derived cyclic α and β oscillations early in the descent are larger than those derived from pressure data, the mean values agree extremely well. A higher variation was expected at early times in the reentry trajectory, when pressures were low. Prior to $t=510$ s, atmospheric pressure was less than 1% of the payload pressure transducer range. The oscillation frequency agrees well between both data sets. Both analysis methods show attitude variations damping with time. Figure 3-2 is a detail of the portion of the reentry trajectory analyzed, simulated, or computed in the accompanying papers,^{1, 2, 10, 11} where the best agreement is obtained. Trajectory times approximately corresponding to the computed CFD cases ($514 \leq t \leq 518$ s) are indicated by vertical dashed lines. In all cases, results were linearly interpolated from 0.2° intervals output from the Matlab griddedInterpolant, and no significant difference was found in the angles computed from pressure signals smoothed over moving 0.005, 0.01, or 0.02 s windows.

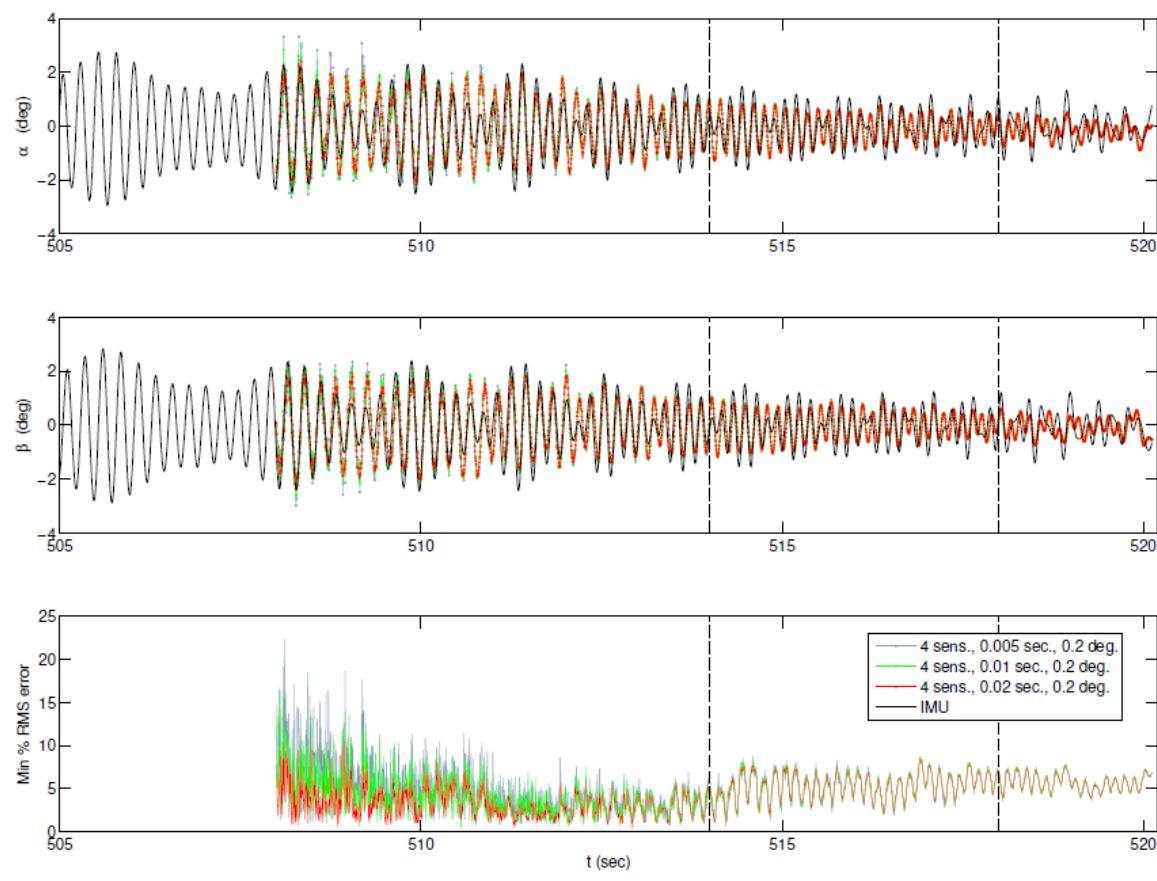


Figure 3-1 Angle of attack (α) and yaw (β) results for descent.

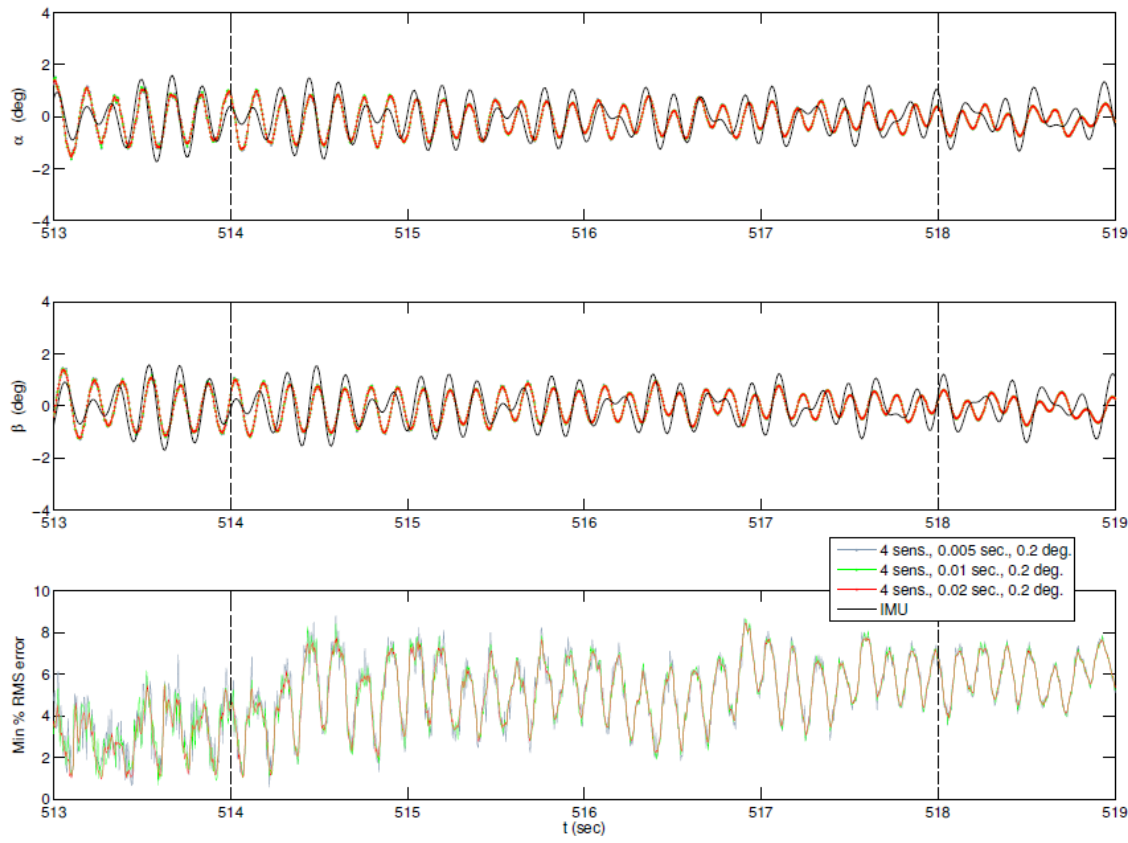


Figure 3-2 Detail of angle of attack (α) and yaw (β) results for the descent portion of the trajectory from the interpolation/RMS minimization routine compared with the IMU/GPS values.

The RMS deviation between measured and computed pressures is less than 8% for $t \geq 512$ s.

The oscillation frequencies were examined by means of fast Fourier transforms performed using the Matlab fft function. The descent signals were analyzed for $t = 514 - 518$ s, the range containing the target Mach and Reynolds numbers, and the results are depicted in Figure 3-3). While both the pressure-difference RMS and IMU/GPS signals have a peak just below 7 Hz, and a smaller peak between 3 and 4 Hz, the IMU/GPS signal also has a large peak near 5 Hz which is not seen in the pressure-difference RMS signal. This is qualitatively similar to the spectra for the descent of HIFiRE-5a,4 where both the pressure difference RMS and IMU signals had a peak just below 1 Hz and near 3 Hz, but only the IMU signal had a strong peak at 2 Hz. The source of the persistent ~ 5 Hz peak in the IMU/GPS signals is unknown, as was the source of the persistent ~ 2 Hz peak in the IMU/GPS signals from HIFiRE-5a, but neither was observed on any of the differential pressure traces examined for HIFiRE-5a or HIFiRE-5b.

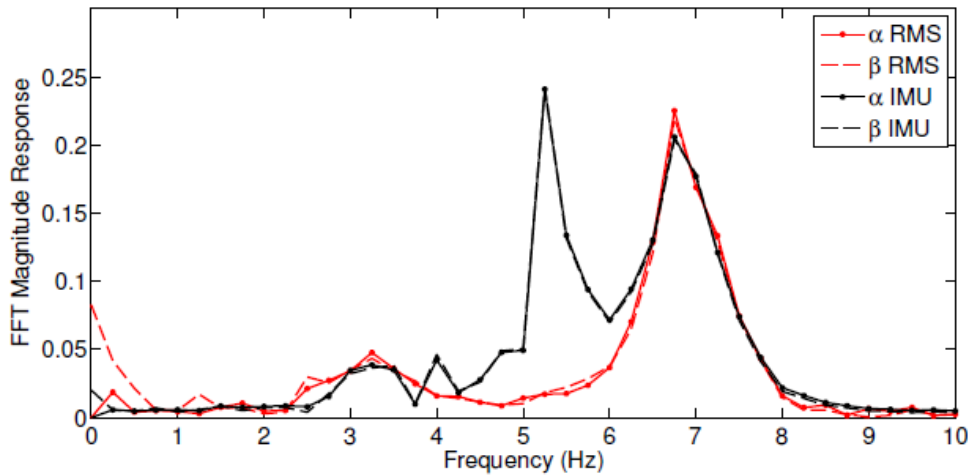


Figure 3-3 FFT magnitude response for descent α and β derived from IMU and RMS, $t = 514$ to 518 s.

The oscillation frequencies were also examined with FFTs performed over 2 s moving windows, and these results are presented in Figure 3-4. The oscillation frequencies of both α and β roughly double over the examined period, and the α and β peaks are identical within the uncertainty of the FFT, which is 0.5° due to the relatively small window size.

3.2. Comparison with Differential Pressures

Two differential pressure transducers were examined to qualitatively confirm the surface-pressure RMS computed angles of attack and yaw from $t = 514$ to 518 s. Transducer PLBW29D is located on the centerline (major axis) at $\varphi = 0^\circ$, and primarily sensitive to angle of attack, α , and Transducer PLBW25D is located on the leading edge (minor axis) at $\varphi = 90^\circ$, and primarily sensitive to yaw, β . Figure 3-5 presents differential pressure measurements, normalized by freestream pressure from the best estimated trajectory, from the descent phase of the HIFiRE-5b flight. Axis scales were chosen to make the normalized differential pressure traces approximately coincident with the angle traces. The assumption is that the differential pressure is linearly correlated with alpha and beta, which is reasonable over the small range of α , β and M considered. The normalized differential pressures agree substantially with the RMS-derived attitude results in terms of frequency and relative magnitude in both phases of the flight, which further confirms the reliability of the pressure-RMS method.

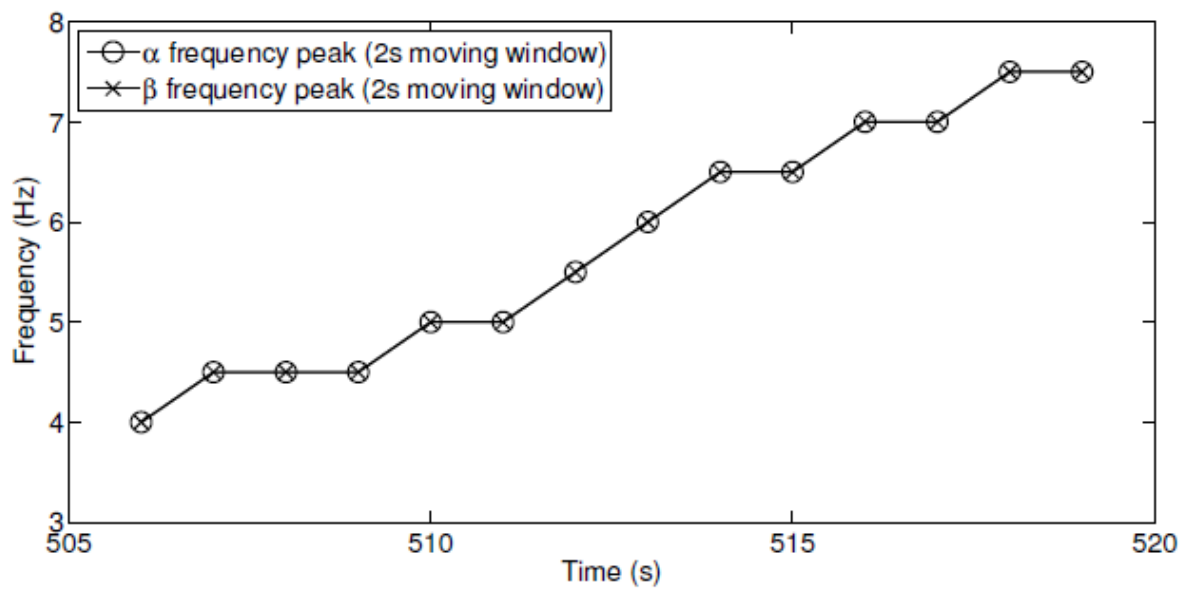


Figure 3-4 Peak FFT magnitude response for descent α and β derived from pressure-difference RMS in 2 s moving windows, $t = 505$ to 519 s.

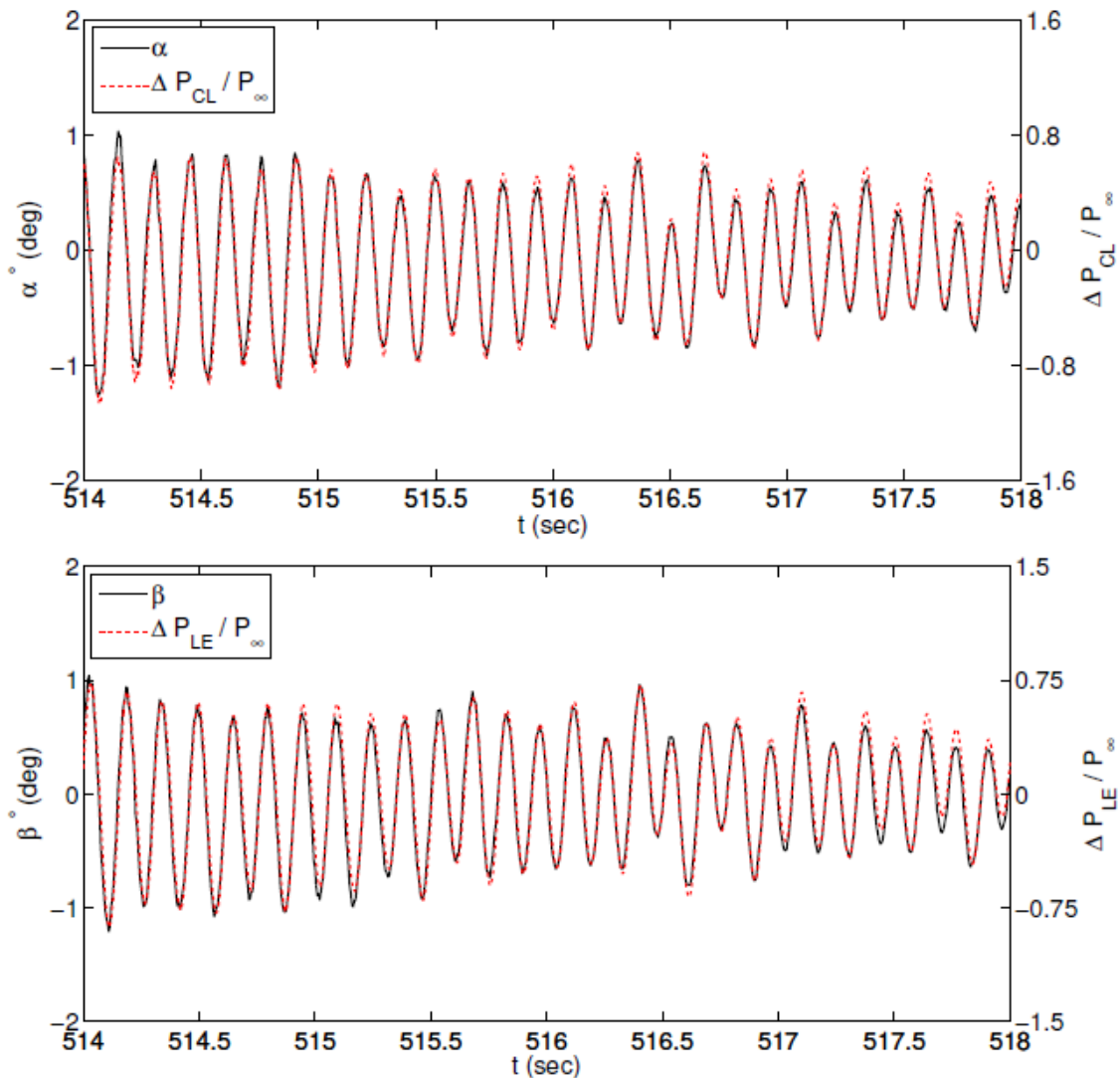


Figure 3-5 Descent α and β derived from RMS pressure compared with normalized centerline and leading edge differential pressures.

3.3. Conclusions

It has been demonstrated that normalized pressure CFD results may be used to infer angle of attack and yaw from a set of four pressure transducers distributed over the body of the HIFiRE-5b flight test article. Interpolations in Mach number have been correlated with the inertial measurement unit results for α and β from the flight, with excellent agreement for the reentry portion of the trajectory. Although attitudes derived from both methods agree well, the pressure-derived attitudes are preferred for data analysis, since both the IMU and GPS suffered anomalies during flight. The calculated α and β also agree well with differential pressure transducer measurements. The vehicle was found to increase in oscillation rate over the course of its descent from about 4 Hz to 7.5 Hz. Further work to characterize the effect of the attitude on heat transfer rates both laminar and turbulent and comparison with measured heat transfer rates will be pursued based on these results. One recommendation is that to extend the method's utility to a

wider range of altitudes, high and low-range pressure transducers could be incorporated on the payload.

4. HIFiRE-5b Heat Transfer

4.1. Pre-Flight Ground Tests and Computational Analyses

An important aspect of the overall HIFiRE program is the series of ground tests that preceded the flight tests in order to aid in model design and instrumentation selection, employ techniques impossible for use in a flight test (e.g., phosphor thermography or temperature-sensitive paint), and in general reveal any unanticipated issues. Juliano et al. conducted low-noise and conventional tests in the BAM6QT at Purdue University.^{34,35,36} Borg et al. studied transition on the leading edges and due to crossflow in the same facility.^{37,38,39} Holden et al. duplicated flight Reynolds number in the LENS I tunnel.^{13,40} Berger et al. made global heat flux measurements on smooth-walled and tripped models in NASA Langley Research Center's 20-Inch Mach 6 Tunnel.²⁶

Stability analyses for the HIFiRE-5 configuration were conducted by Choudhari et al.,⁴¹ Gosse et al.,⁴² and Li et al.⁴³ The HIFiRE-5 poses a particular challenge due to the presence of the highly inflected boundary-layer profile near the vehicle centerline, as well as stationary and traveling crossflow instabilities farther outboard.

4.1.1. Instrumentation

The primary aerothermal instrumentation for HIFiRE-5 consisted of Medtherm Corporation coaxial thermocouples. Type T (copper-constantan) thermocouples were installed in aluminum portions of the aeroshell and Type E (chromel-constantan) were installed in the steel portions. The Medtherm coaxial thermocouples were finished flush with the vehicle surface. These thermocouples were dual-junction thermocouples with one junction at the cone external surface, and the other on the back face. Kulite XCEL-100-15A pressure transducers measured local static pressures at a 200 Hz sampling rate. Four Kulite XTEL-190M-10D differential pressure transducers were connected to taps 180 degrees apart on the vehicle to aid in attitude determination and were also sampled at 200 Hz. Ten Kulite XCEL-100-5A transducers were sampled at up to 60 kHz to measure high-frequency pressure fluctuations. Six Vatell HFM-8 E/L gauges provided direct heat transfer measurements.

The 0 to 90° quadrant of the test article was the primary instrumented surface (Figure 4-1). It contained thermocouple rays at $\varphi = 0, 45$, and 90 degrees. In addition, three x -stations in this quadrant, $x = 400, 600$, and 800 mm, were instrumented with thermocouples at closely spaced angular locations. The other quadrant on the smooth side of the test article, 0 to -90° (or, equivalently, 360 to 270°), served as a secondary instrumented surface to provide a symmetry check of the primary instrumentation quadrant.

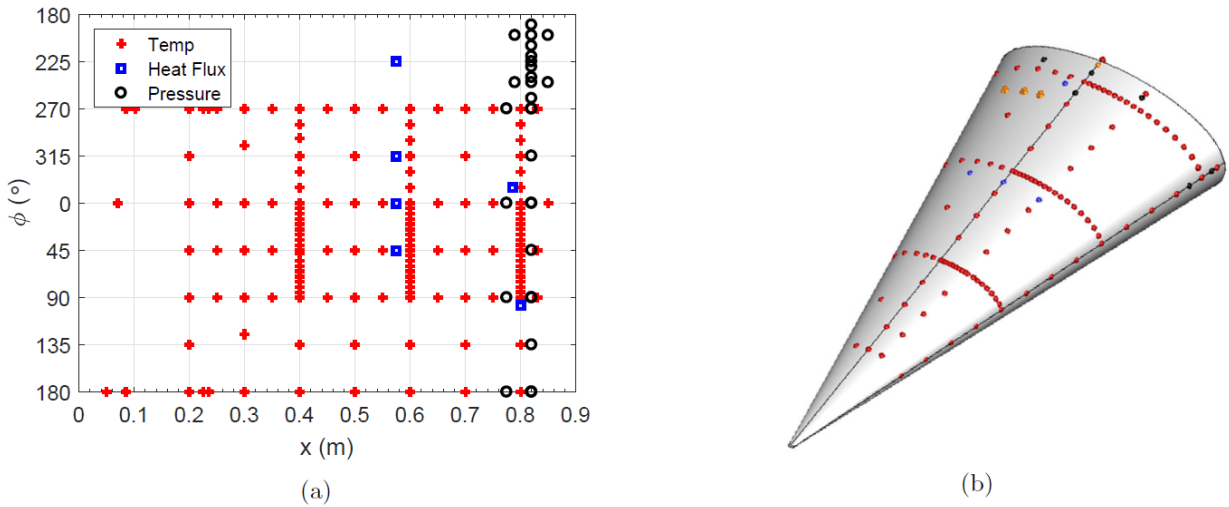


Figure 4-1 Layout of thermocouples, heat-flux gauges, and pressure transducers on HIFiRE-5b flight vehicle.

4.2. Data Reduction Methodology

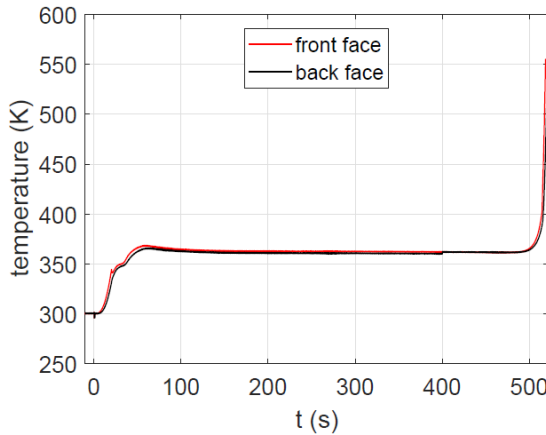
4.2.1. Calculation of Heat Flux from Thermocouple Data

Heat flux was calculated from the front- and back-face thermocouple temperatures by solving the transient 1-D heat equation. The FORTRAN QCALC subroutine was translated to Matlab for this purpose. QCALC assumes one-dimensional heat transfer and uses a second-order Euler explicit finite difference approximation to solve for the temperature distribution through the vehicle shell; heat flux is obtained from a second- order approximation to the derivative of the temperature profile at the outer surface.⁴⁴ The code provides the options of solving in Cartesian, cylindrical, or spherical coordinates and applying a constant or time-varying back-face temperature or the adiabatic boundary condition. For the HIFiRE-5 data reduction, the cylindrical-geometry equation was used with the local radius of curvature, wall thickness, and material properties. The front- and back-face thermocouples provided the boundary conditions.

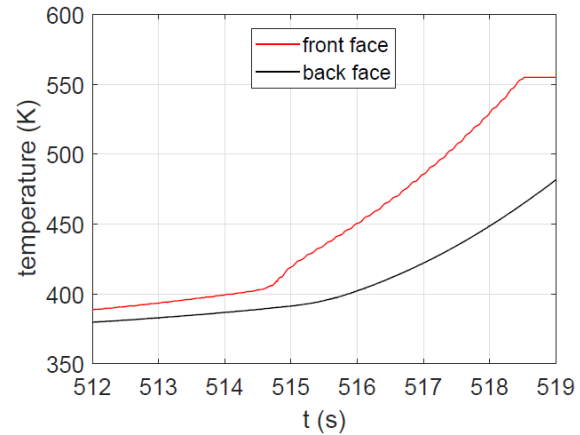
Figure 4-2 shows representative temperature histories for the pair of thermocouples at $x = 600$ mm, $\phi = 90^{\circ}$; Figure 4-3 shows the heat flux calculated from them. A 0.01-s moving average was applied to the thermocouple outputs to reduce noise prior to calculating heat flux (and generating Figure 4-2). The large surface temperature increases during ascent and descent are readily apparent; the rate of temperature change at high altitude is much lower, as expected. The nonzero heat flux during high-altitude flight can be at least partially attributed to axial heat conduction through the model shell, belying the assumption of strictly one-dimensional heat flux. Several thermocouple voltages drifted during flight, which is another contributor. All back-face thermocouples were shifted at $t = 400$ s to equal the front-face temperature at that location, thereby ensuring that the heat flux is identically zero shortly before reentry. The shift was in all cases less than 11.5 K; in the Figure 4-2 case, it was 1.4 K. The spike in the back-face heat flux at $t = 400$ s arises from the temperature shift described above. The front-face thermocouple output voltage saturated at $t = 518.5$ s, leading to a false indication of

decreasing heat flux for the brief remainder of the flight. The distinct change in the slope of the temperature history in Figure 4-2b indicates transition at $t = 514.6$ s, even without the reduction of temperature to heat flux.

Positive back-face heat flux indicates heat flux into the wall from within the vehicle. The positive (albeit small) back-face heat flux in Figure 4-3b is surprising. This behavior was typically observed for thermocouples near the leading edges. Therefore, it appears to be another error arising from the assumption of one-dimensional heat flux-spanwise temperature gradients lower the surface temperature along the leading edges, slightly reducing the wall-normal temperature gradient from which heat flux is calculated.

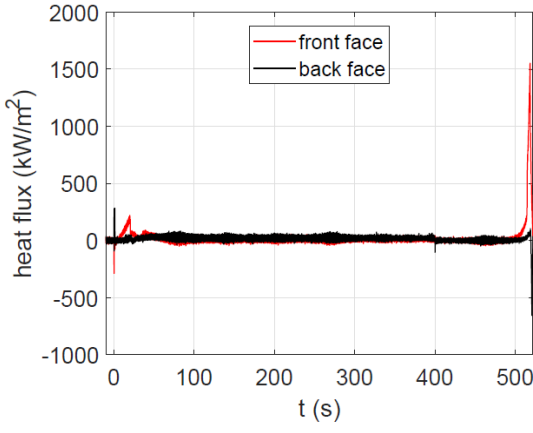


(a) Entire flight.

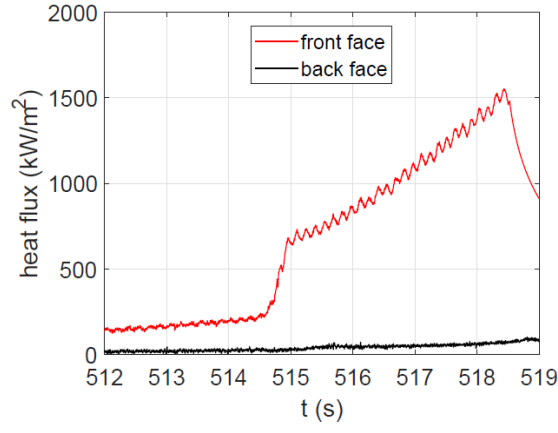


(b) Descent only.

Figure 4-2 Front- and back-face thermocouple temperature measurements. $x = 600$ mm, $\phi = 90^\circ$.



(a) Entire flight.



(b) Descent only.

Figure 4-3 Heat flux calculated from thermocouple data. $x = 600$ mm, $\phi = 90^\circ$.

4.2.2. Transition Assessment

Boundary-layer transition was determined by manual inspection of the heat-flux time traces. The dependence of heat flux on vehicle angle of attack and yaw, plus the noise in the signal, limited the accuracy with which an algorithm could automatically identify transition. For most sensors, three different transition times were identified to the nearest 0.1 s.

- The first sign of transition onset was regarded as the earliest departure from the laminar heating rate and denoted by an upward-pointing magenta triangle. This is regarded as ‘partial’ transition onset because it depends on vehicle attitude.²⁵
- Full transition onset is taken to be the final time at which the laminar heating rate was observed (magenta diamond).
- The end of transition was identified as the time when the heating rate remained close to the predicted turbulent rate (downward-pointing magenta triangle).

Transition time was tabulated; freestream unit Reynolds number and other relevant parameters were obtained by cross-referencing the trajectory and atmospheric data for that time. A consistent set of transition times is used for each form of data presentation.

4.2.3. Non-dimensionalization

To facilitate comparison of flight-test, ground-test, and computational results, the surface heat fluxes were converted to Stanton number:

$$St = \frac{\dot{q}''}{\rho_\infty u_\infty c_p (T_0 - T_{wall})} \quad (4.1)$$

Note that the Stanton number is defined using freestream stagnation temperature, rather than a recovery temperature, for convenience. The Stanton number was in turn scaled by $\sqrt{Re_x}$ a product which is constant for a self-similar laminar boundary layer. Although this scaling is strictly valid only for self-similar boundary layers, $St \cdot \sqrt{Re_x}$ was found to be approximately constant under laminar flow on HIFiRE-5b during descent, even near the vehicle centerline. This scaling made identification of transition onset easier, because the threshold is constant, rather than a function of time or freestream Reynolds number. Figure 4-4 shows the heat flux from Figure 4-11j ($x = 0.400$ m, $\varphi = 45^\circ$), non-dimensionalized and scaled. The results themselves are discussed below.

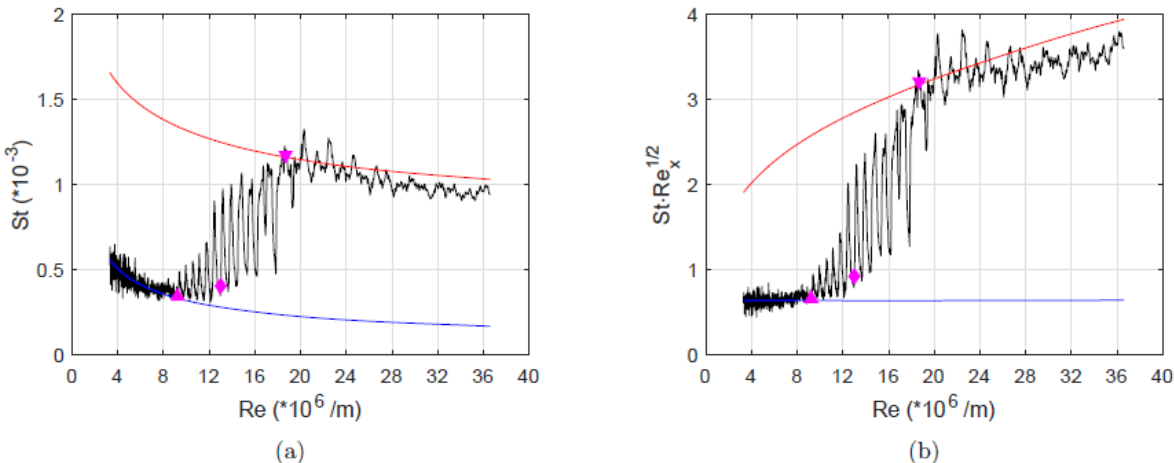


Figure 4-4 Heat transfer non-dimensionalization and $\sqrt{Re_x}$ scaling for sensor at $x = 0.40$ m, $\phi = 45^\circ$.

4.3. Heat Flux and Transition Results

4.3.1. Presentation Format

The HIFiRE-5b flight test yielded abundant data from the thermocouples. For this reason, two different formats were selected for the presentation of temperature, heat-flux, and boundary-layer transition results. Time histories of heat flux detected by a pair of thermocouples allow close examination of the heating and boundary-layer state on a point-by-point basis. These line plots are complemented by color-coded scatter plots containing the data from 128 pairs of thermocouples at a single instant in time which enable a broader picture of the overall temperature, heat flux, and boundary-layer state.

4.3.2. Streamwise Transition Variation

As a starting point for interpretation of the flight data, representative heat-transfer measurements at up-stream and downstream locations on the major and minor axes illustrate major features of the transition behavior. Measured heat transfer was compared to empirical correlations for laminar and turbulent surface heat flux on a circular cone at zero angle of attack as a function of cone half-angle. These correlations were derived from prior wind tunnel tests.¹⁷ The predicted heating is approximate and intended primarily to illustrate trends.

Figure 4-5 presents heat transfer on the leading edge (i.e., major axis or $\phi = 90^\circ$) during descent at $x = 0.40$ and 0.80 m. The solid black lines are the heat flux calculated from the temperatures measured by the coaxial thermocouples. The blue and red lines correspond to the laminar and turbulent empirical predictions, respectively. The magenta symbols mark transition as described in Section 4.2.2, above. Near the leading edges, transition was found to be relatively insensitive to attitude variations. Therefore, the ‘partial’ transition onset and ‘full’ transition onset symbols are coincident.

For these two examples, the laminar heating rate is observed to follow the trend of the empirical fit, but exceed it by $\approx 50\%$. Unsurprisingly, the time rate of change of heat flux rises sharply under transitional flow; the turbulent dq''/dt is less than the transitional rate, but larger than the laminar rate. The higher-than-predicted heating rates cannot be explained by the assumption of 1-D heat flux. Spanwise conduction would lower the leading edge temperatures, resulting in an erroneously low heat flux. The most likely explanation is the admitted limitation of the empirical prediction.

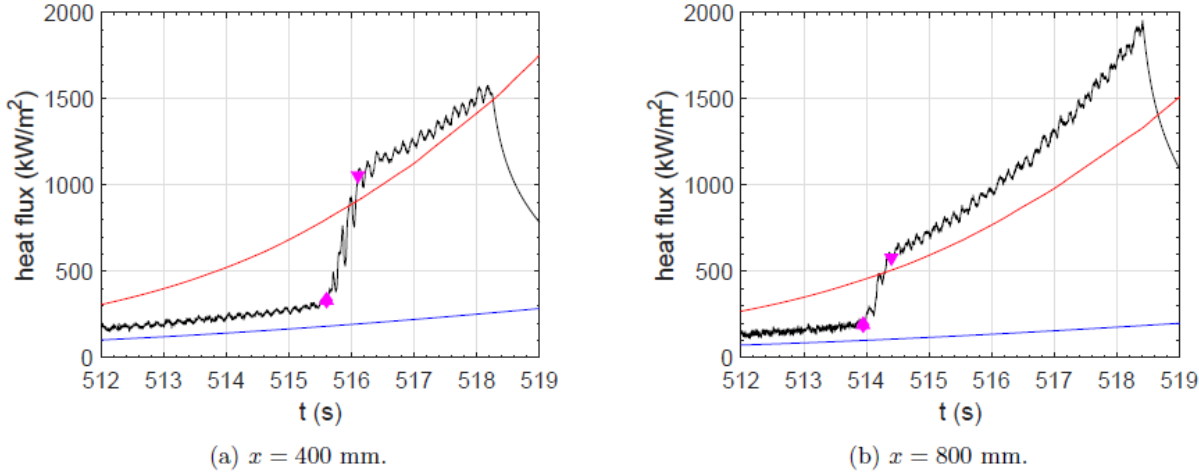


Figure 4-5 Heat transfer on the leading edge ($\phi = 90^\circ$).

Table 4-1 compares the flow conditions at the time of transition for two thermocouple pairs shown in Figure 4-5. The freestream Reynolds number at transition differs substantially for these two sensors, but Re_x at transition differ by less than 8%. Significantly, this behavior is different than that observed for the HIFIRE-5a flight test - in that experiment, all the $\phi = 90$ and 270° thermocouples detected a turbulent boundary layer at nearly the same time (and, therefore, Re). This observation indicated that leading-edge transition on HIFIRE-5a was induced by roughness that became critical at a particular flow condition. Since this transition “flashing” phenomenon was not observed on the HIFIRE-5b leading edge, it is presumed that transition in this case was not tripped by roughness. An examination of leading-edge transition drawing on all the relevant thermocouples is presented below.

Table 4-1 Leading-edge transition onset.

x (m)	t (s)	Re ($\cdot 10^6$ /m)	$Re_{x_{tr}}$ ($\cdot 10^6$)
0.40	515.6	12.0	4.81
0.80	514.0	6.50	5.20

Figure 4-6 is analogous to Figure 4-5, but presents heat transfer on the centerline (i.e., minor axis or $\phi = 0^\circ$). A brief amount of time elapses between the first sign of transition onset and

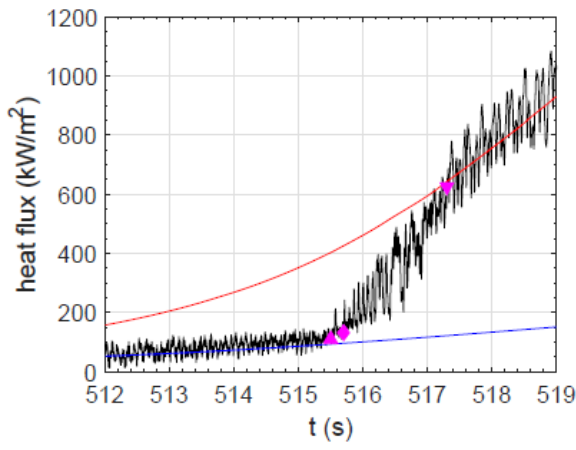
the last vestige of fully laminar flow, indicating that centerline transition is slightly more sensitive to angle-of-attack and yaw variation than leading-edge transition. Transition was observed to occur slightly earlier (lower Re and $Re_{x_{tr}}$) than along the leading edges (Table 4-2).

Table 4-2 Centerline transition onset

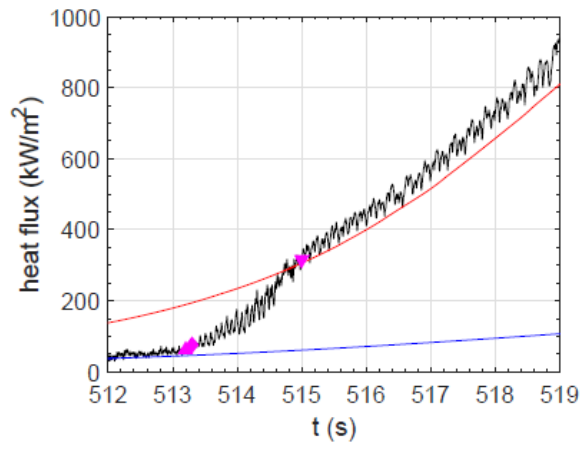
x (m)	t (s)	Re ($\cdot 10^6$ /m)	$Re_{x_{tr}}$ ($\cdot 10^6$)
0.40	515.7	11.6	4.63
0.80	513.3	5.00	4.00

Figure 4-7 contains streamwise distributions of the earliest transition onset location with angular coordinate as a parameter. The Reynolds number based on transition location (Figure 4-6b) is observed to remain nearly constant for $x > 0.3$ m along each of these rays. The larger $Re_{x_{tr}}$ observed near the nosetip may be due to the vehicle's modest nose bluntness or perhaps the higher nosetip temperatures. Good agreement is observed between each pair of symmetric rays: 0/180, 45/315, and 90/270°.

Figure 4-8 shows the streamwise transition profiles for the four most densely instrumented rays (0, 45, 90, and 270°). The earliest transition onset (blue line and symbols), full transition onset (green), and the end of transition (red) are displayed. Except along the $\varphi = 45^\circ$ ray, full transition onset closely follows the first signs of transition onset. This is interpreted as an insensitivity of transition to small angle of attack and yaw variations at these azimuths. See below for discussion of this behavior at additional azimuths. Transition is more rapid along the leading edges than elsewhere: Re_x at the end of transition is approximately 20% higher than at the onset for $\varphi = 90$ and 270°, but almost 50% higher elsewhere.

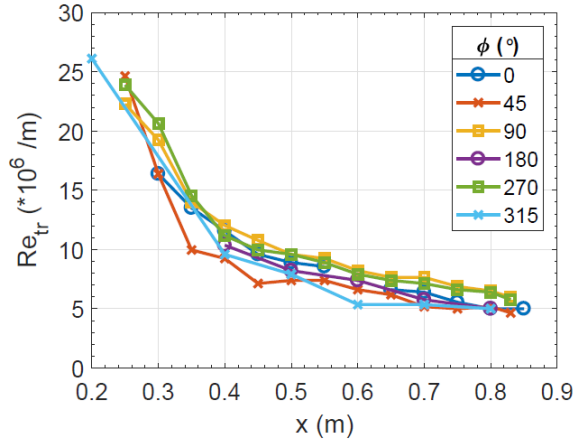


(a) $x = 400$ mm.

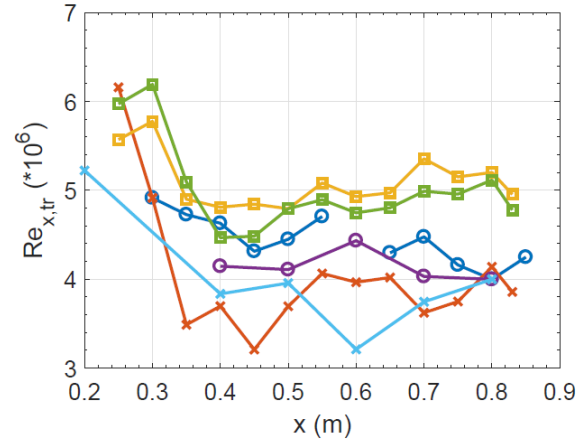


(b) $x = 800$ mm.

Figure 4-6 Heat transfer on the centerline ($\phi = 0^\circ$).



(a) Unit Re at transition.



(b) x -based Re at transition.

Figure 4-7 Streamwise profiles of earliest transition onset. The legend is common to both subfigures.

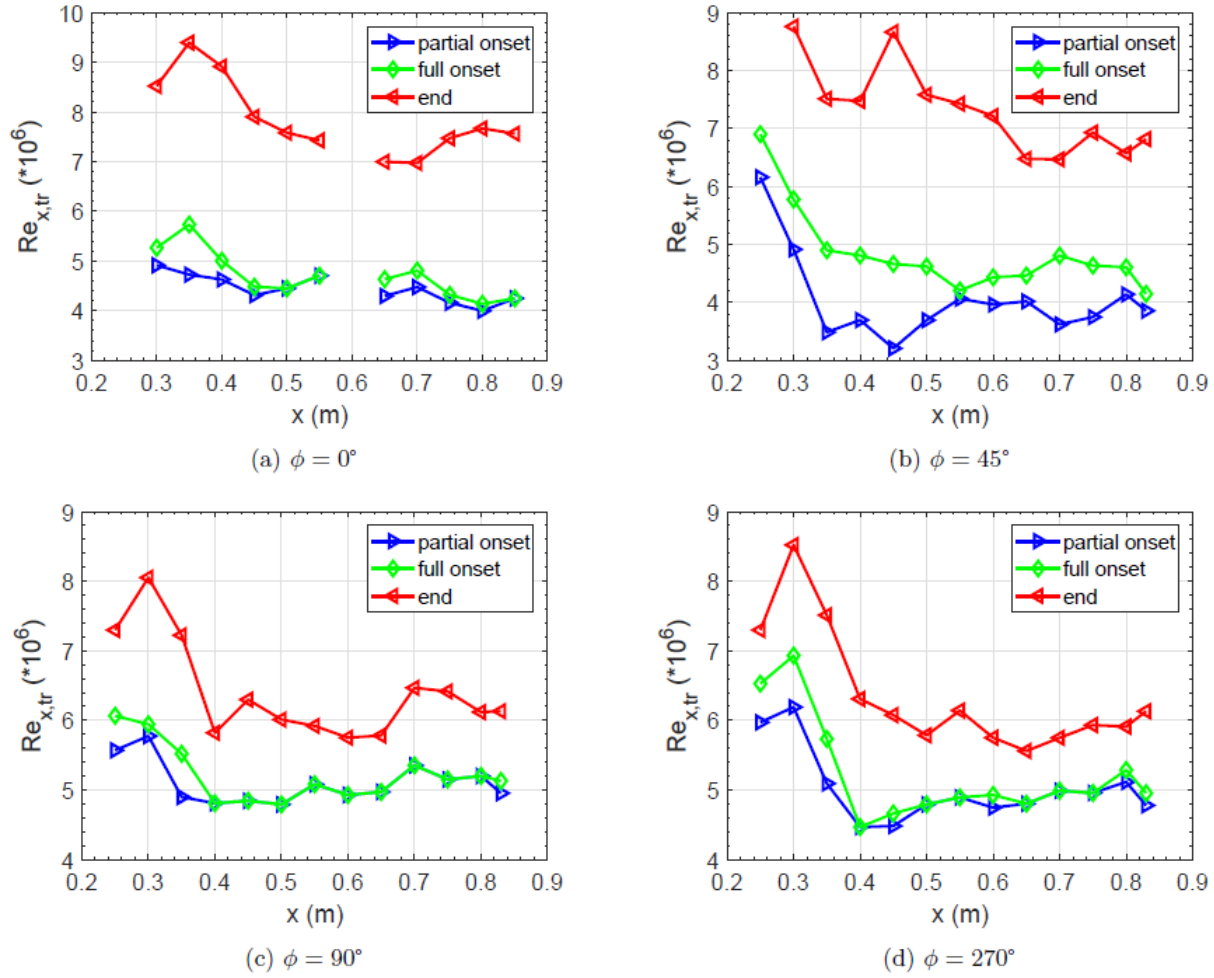


Figure 4-8 Streamwise profiles of transition location.

4.3.3. Spanwise Variation of Heat Flux and Transition

Figure 4-9 contains spanwise profiles of the earliest transition onset location. Figure 4-9a shows the freestream unit Reynolds number at transition onset for the three most densely instrumented axial stations ($x = 400$, 600 , and 800 mm). The three-lobed transition front is apparent; transition is earliest at $\phi \approx 0$ to 10 , 30 to 50 , and 90° . Linear stability analysis suggests that each transition locus arises from a different mechanism: traveling instability near the centerline, where the boundary-layer velocity profile has an inflection point, crossflow instability between the planes of symmetry, and second-mode waves at the leading edges.⁶ Quiet-tunnel ground-test results corroborate the shape of the transition front, except the leading-edge transition is not encountered.^{19,30} This difference is thought to arise from the relatively small stagnation- to wall-temperature ratio that occurs in flight. This mismatched parameter caused a similar discrepancy between HIFIRE-1 flight- and ground-test results.^{29,45,46}

Figure 4-9b shows spanwise profiles of the Reynolds number based on transition location. The profiles are observed to collapse significantly. The azimuth exhibiting earliest crossflow-

induced transition moves closer to the centerline for the farther aft axial stations, from about 45° at 400 mm to 35° at 800 mm.

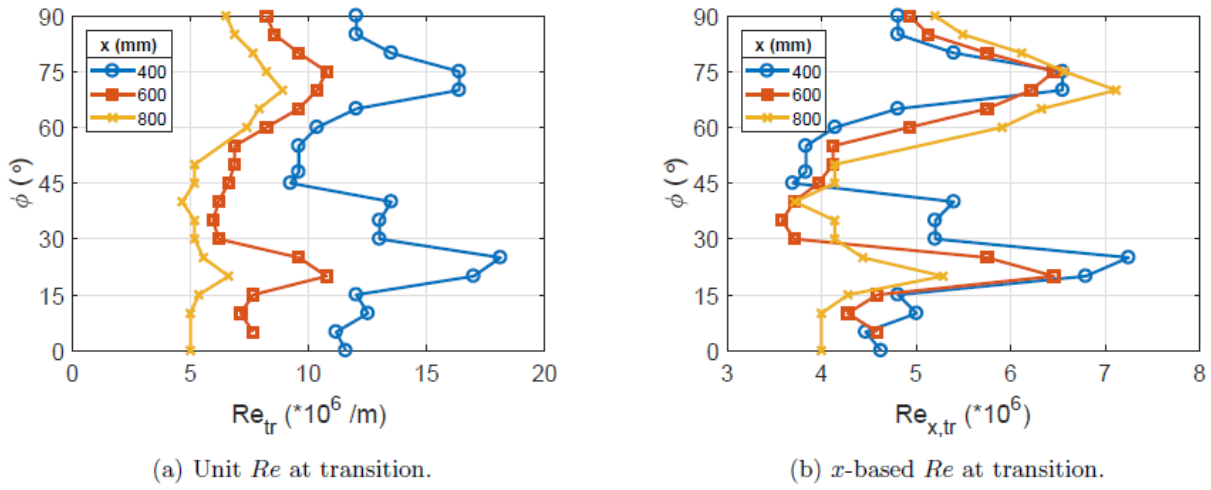


Figure 4-9 Spanwise profiles of earliest transition onset.

Figure 4-10 shows the spanwise transition profiles for each axial station separately. The earliest transition onset (blue line and symbols), full transition onset (green), and the end of transition (red) are displayed. The distance between the blue and green lines is indicative of the sensitivity of transition to the vehicle's attitude. For azimuths greater than about 75° , the transitional boundary layer did not return to laminar as the attitude changed. Similar behavior was observed at the vehicle centerline. The sensors a mere 5° away from the centerline exhibited much greater variation, indicative of the sensitivity of the flow field in this region to these small changes in angle of attack and yaw. See section 5 for further discussion based on ground-test results from infrared thermography. The difference between partial and full transition onset is smallest at the farthest downstream axial station. A possible explanation for this behavior is that the transitional hot streaks are broader farther downstream and, therefore, the varying attitude does not move the sensor away from them. It is also observed that Re_x at the end of transition and the extent of transitional flow do not vary greatly for each axial station.

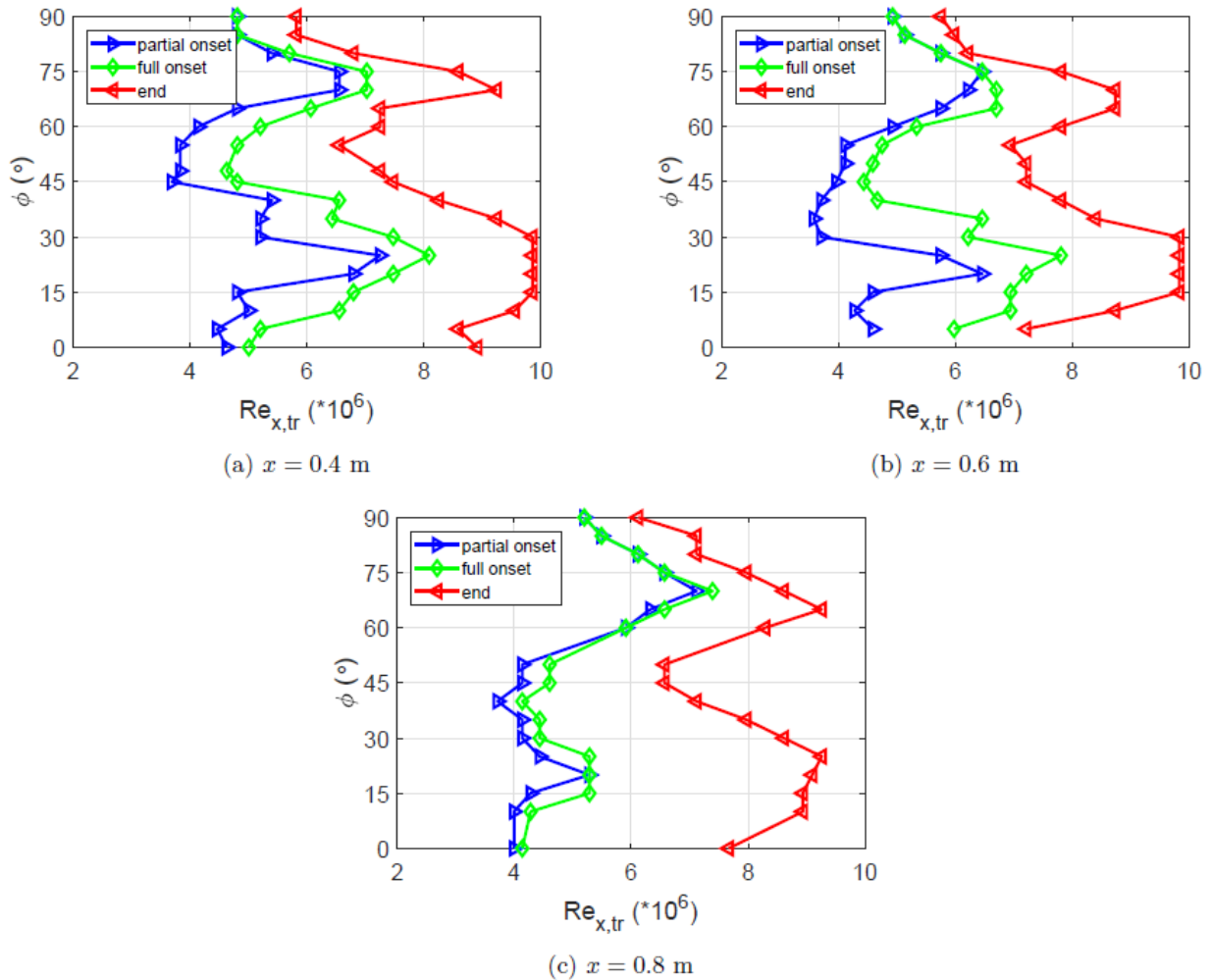


Figure 4-10 Spanwise profiles of transition location.

The $x = 0.4$ m axial station illustrates the effect of vehicle attitude on transition. The $x = 0.4$ m axial station was HIFiRE-5b's most densely instrumented, with sensors spaced azimuthally in 5° increments (the $\phi = 50^\circ$ sensor was repositioned to $\phi = 48^\circ$ to obviate a clash with a seam in the flight vehicle). The vehicle's semi-major axis is 127 mm at this station, so the average spanwise spacing between sensors was about 7 mm. The heat-flux time histories for all 19 sensors between $\phi = 0$ and 90° , inclusive, are shown in Figure 4-11. Although the $\phi = 40^\circ$ sensor data (Figure 4-11i) appear anomalous, transition at this station was determined as for the other sensors. Near the beginning of transition, the sensors at $\phi = 0, 5, 10$, and 25 to 60° all exhibit large heat-flux variations. These fluctuations are most likely due to the sensitivity of the configuration to yaw.^{6, 13, 45} Ground test and CFD demonstrate that the near-centerline region exhibits streamwise streaks of higher and lower heating. These streaks arise from boundary-layer flows created by the spanwise pressure gradient. The frequency of flight-vehicle heat-flux oscillations at $\phi = 0^\circ$ (Figure 4-11a) is double that of other nearby sensors and the vehicle spin rate. This is due to the passage of the near-centerline heating streaks over the sensor multiple times per payload revolution.³⁸ In addition, these streaks break down at

different times, leading to large excursions between fully laminar and fully turbulent heating, until the entire region is engulfed by turbulent flow.

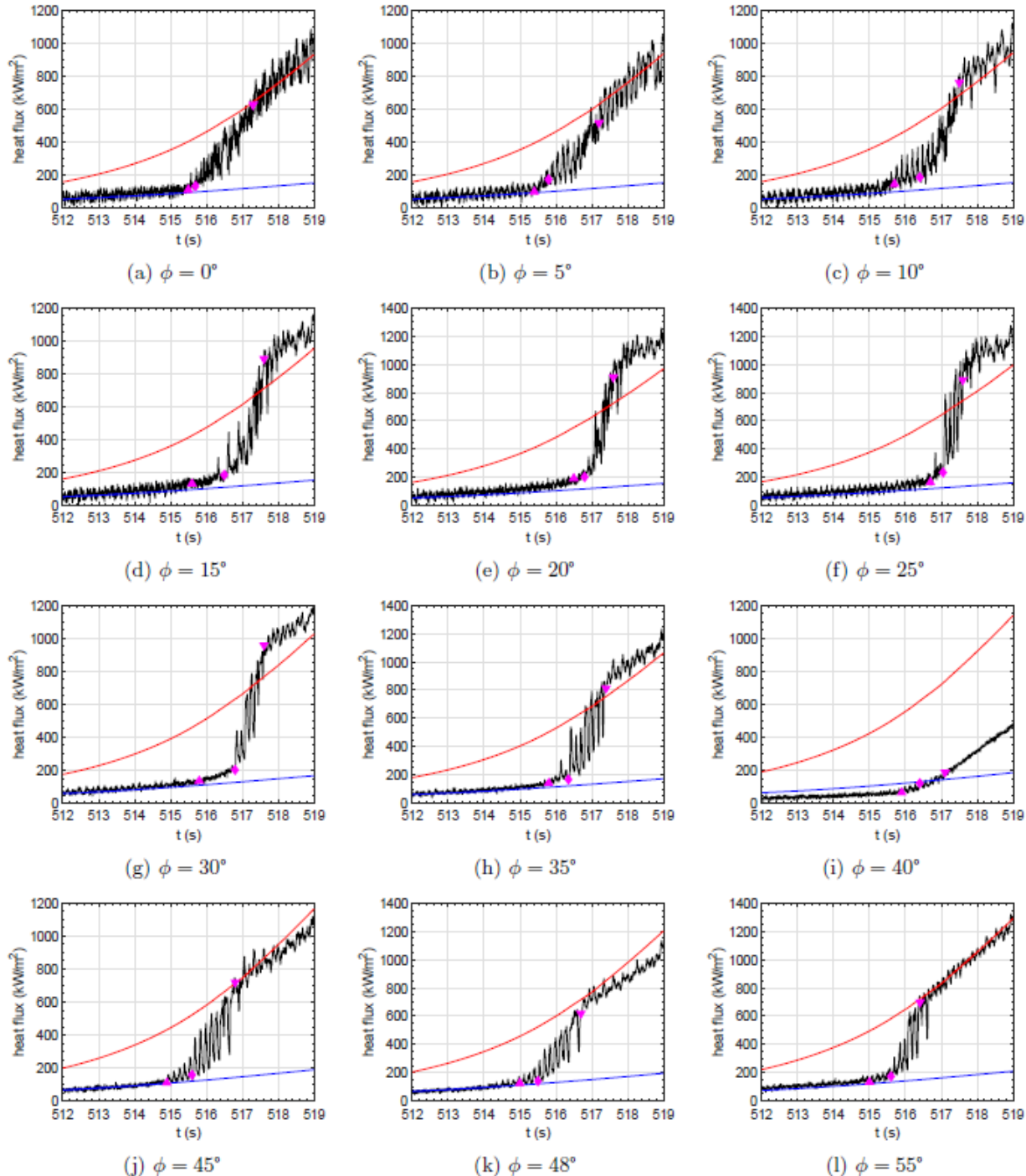


Figure 4-11 Heat-flux history, $x = 0.4$ m.

Comparison with computational simulations indicates that the hot streaks from 25 to 60° azimuth are due to stationary crossflow vortices.⁶ The crossflow vortices create a transition

process similar to that observed near the centerline. Immediately preceding transition, streaks of high and low heating meander over the sensors. These streaks break down at different times depending on the payload orientation, leading the large excursions between laminar and turbulent heating, prior to fully turbulent flow. Farther outboard, at azimuths larger than 65° , the amplitude of the heat-flux variations is somewhat smaller compared to the difference between laminar and turbulent heating rates. For this reason, it is concluded that these variations are not due to spatial hot streaks meandering over the vehicle's surface, but rather the influence of yaw on the heat flux.

4.3.4. Comparison to CFD Results

Laminar and turbulent mean-flow calculations were carried out for a range of conditions that bounded the flight conditions.³³ Specifically, the calculations spanned the full range of angle of attack, yaw angle, Mach number, and Reynolds number. The computed surface pressure were compared to values measured in flight to obtain a best estimate of vehicle attitude and flow conditions.² In Figure 4-12, the computed laminar and turbulent heat fluxes are compared to the flight-test results. Heat flux has been normalized to Stanton number as described in Section 4.2. The transition locations have not been reassessed.

By accounting for the vehicle's varying attitude, the calculated laminar and turbulent heating correctly predicts the fluctuations observed in flight. The turbulent heating calculation at $\varphi = 30^\circ$ (Figure 4-12b) is particularly excellent. The turbulent heat flux calculated from the flight-test data is slightly high ($\approx 10\%$) along the centerline, accurate at $\varphi = 30^\circ$, about 10% low at $\varphi = 60^\circ$, and about 20% low along the leading edge. This is consistent with the error expected from neglecting three-dimensional heat conduction.⁹ It is also noteworthy that the calculations correctly predict the higher frequency of fluctuations observed at $\varphi = 0^\circ$. This lends credence to the explanation given above, informed by the CFD, that finely spaced near-centerline hot streaks are their cause.

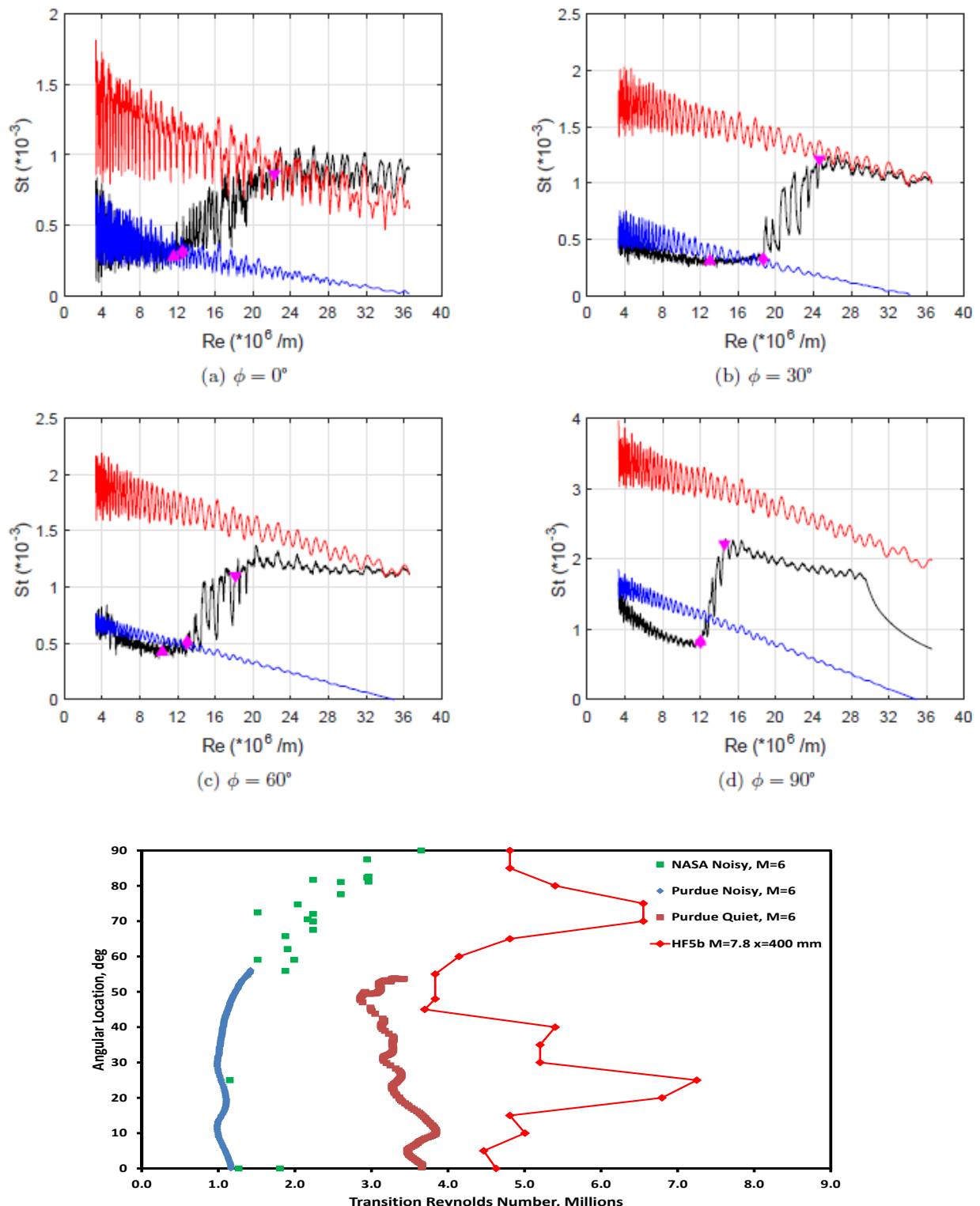


Figure 4-12 Comparison of experimental and computational heat flux, $x = 0.4$ m.

4.3.5. ‘Contour’ Plots

Plotting heat flux versus time does not offer an easily grasped picture of the overall heating on the HIFiRE-5b. To this end, overall ‘contour’ plots of the surface temperature, heat flux, and boundary-layer state were constructed by assigning the pertinent value from each thermocouple pair a pixel at its corresponding location. Thus, the areas of elevated temperature, higher heating, and the transition front (in particular) can be more easily visualized. The downside to this presentation is that each figure contains data from only a single instant in time.

Figure 4-13 shows the surface temperature on the HIFiRE-5b during its descent, as the freestream unit Reynolds number climbs from 5.0×10^6 to 20.0

$\times 10^6/\text{m}$ ($t = 513.19$ to 517.02 s). For clarity, only data from sensors on the more densely instrumented portion of the vehicle from $\varphi = -90$ (270) to $+90^\circ$ are shown. The sensors at $x = 200$ mm stand out as indicating especially high temperature; note that they are installed in the stainless steel joiner, rather than the aluminum frustum. Stainless steel has a lower thermal diffusivity than aluminum, which contributes to the relatively high indicated temperature. These thermocouples were Type E to more nearly match the thermal properties of stainless steel, whereas Type T thermocouples were installed in the aluminum frustum.

Figure 4-14 shows heat-flux distribution at the same times as in Figure 4-13. At $Re = 5.0 \times 10^6/\text{m}$, (Figure 4-14a), the overall low heating indicates an almost fully-laminar boundary layer. When Re has increased to $6.0 \times 10^6/\text{m}$ (Figure 4-14b), the increased heating rate near the $\varphi = 45^\circ$ ray is perceptible for $x \geq 800$ mm. By $Re = 8.0 \times 10^6/\text{m}$ (Figure 4-14c), increased heating is apparent along the leading edges, indicating transition onset at $x \approx 600$ mm. The small asymmetry in leading-edge transition is suspected to arise from nonzero yaw at this instant.² The leading-edge heating rates are very nearly equal in Figure 4-14d–h. As the freestream Re increases, transition moves steadily forward and heat flux — both laminar and turbulent — increases.

In order to simplify the presentation of boundary-layer transition results, the heat flux maps were converted to maps of the boundary-layer state. In Figure 4-15, blue symbols indicate sensors that have not yet departed from laminar heating (i.e., before “partial” transition onset) and red symbols show where transition onset has occurred. The steady advance of boundary-layer transition upstream and outward along the $\varphi = 0, \pm 45$ (45/315), and ± 90 (90/270°) rays is clear.

4.4. Conclusions

The successful HIFiRE-5b hypersonic flight test provided a wealth of surface temperature data, from which heat flux was calculated and boundary-layer transition was derived. A three-lobed transition front was observed, with transition onset farthest forward near the centerline, along the leading edges, and part way in between. Three different instability mechanisms are suspected as the causes of boundary layer transition: inviscid instability near the centerline, where the boundary-layer velocity profile has an inflection point, second-mode waves at the leading edges, and crossflow instability in between.

Transition along each ray was observed to correlate reasonably well with constant Re_x , but only for $x > 300$ mm, presumably due to the vehicle’s blunt nosetip and non-similar boundary layers.

Unlike HIFiRE- 5a, transition along the leading edges advanced steadily as Re increased, rather than flashing forward rapidly. For this reason, the roughness-induced transition suspected on HIFiRE-5a does not appear to be present.

Three different transition times were identified for most sensors: the first departure from laminar heating, the final departure from laminar heating, and the end of transition. A single distinct transition onset for each thermocouple pair could not, in general, be assigned due to transition's dependence on vehicle attitude. Flow near the leading edges was least sensitive to attitude variations. The sensors at azimuths from 25 to 60° indicated presence of hot streaks that were very sensitive to angle of attack and yaw; they are presumed to be evidence of stationary crossflow vortices.

Initial comparison of computational and flight-test heat flux shows excellent agreement. Additional results, based on a more comprehensive comparison, will be reported in the future.

Construction of the “contour” plots of temperature, heat flux, and boundary-layer state provides a useful means of comprehending the overall flow field at one instance in time. They facilitate comparison with computational and ground-test data obtained with infrared thermography or temperature-sensitive paint. Overall, the qualitative agreement with preceding ground-test results are good, with the exception of transition along the leading edges, which was observed in flight, but not low-enthalpy quiet-tunnel tests.

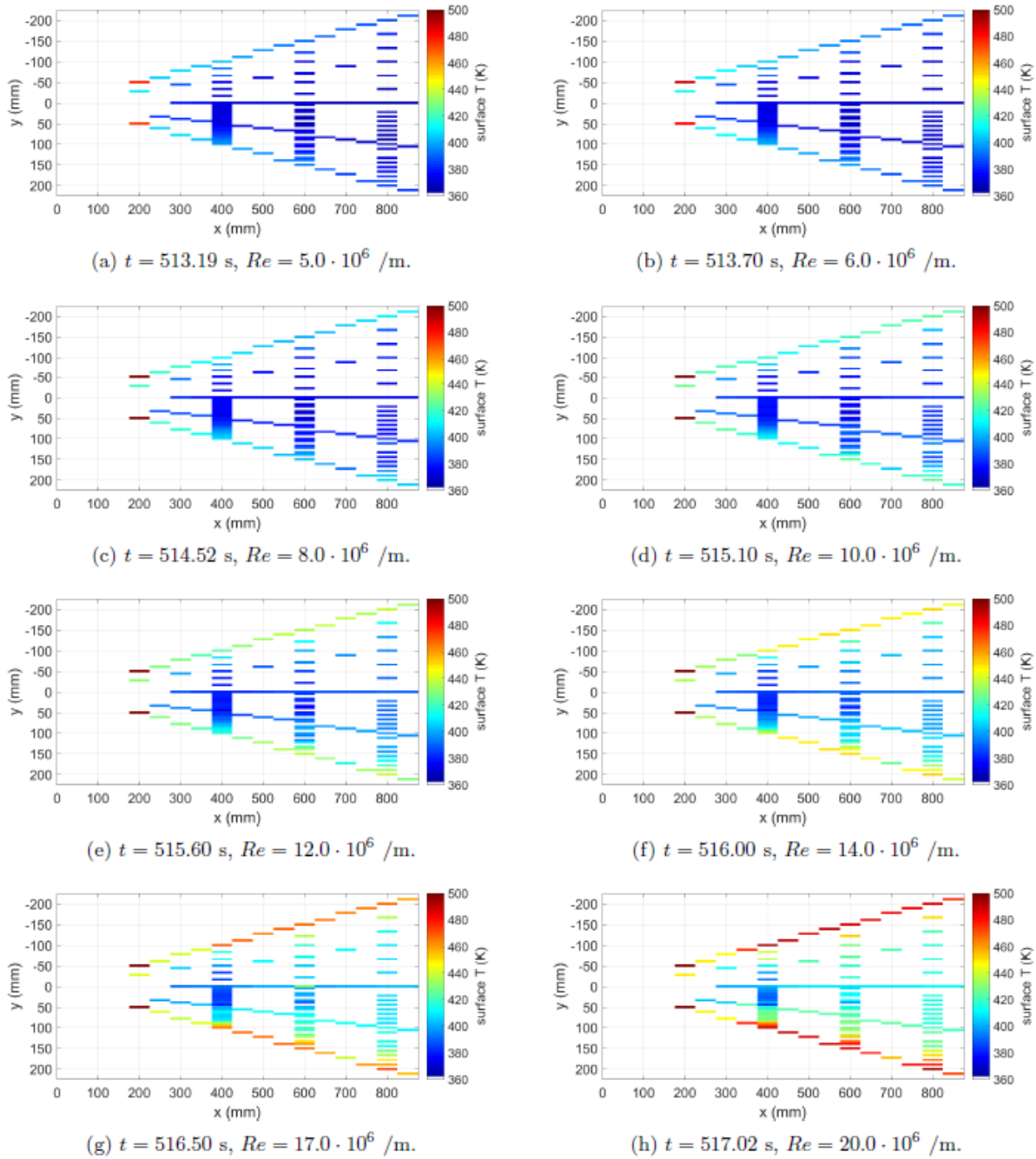


Figure 4-13 Surface temperature. $M = 7.7\text{--}7.9$.

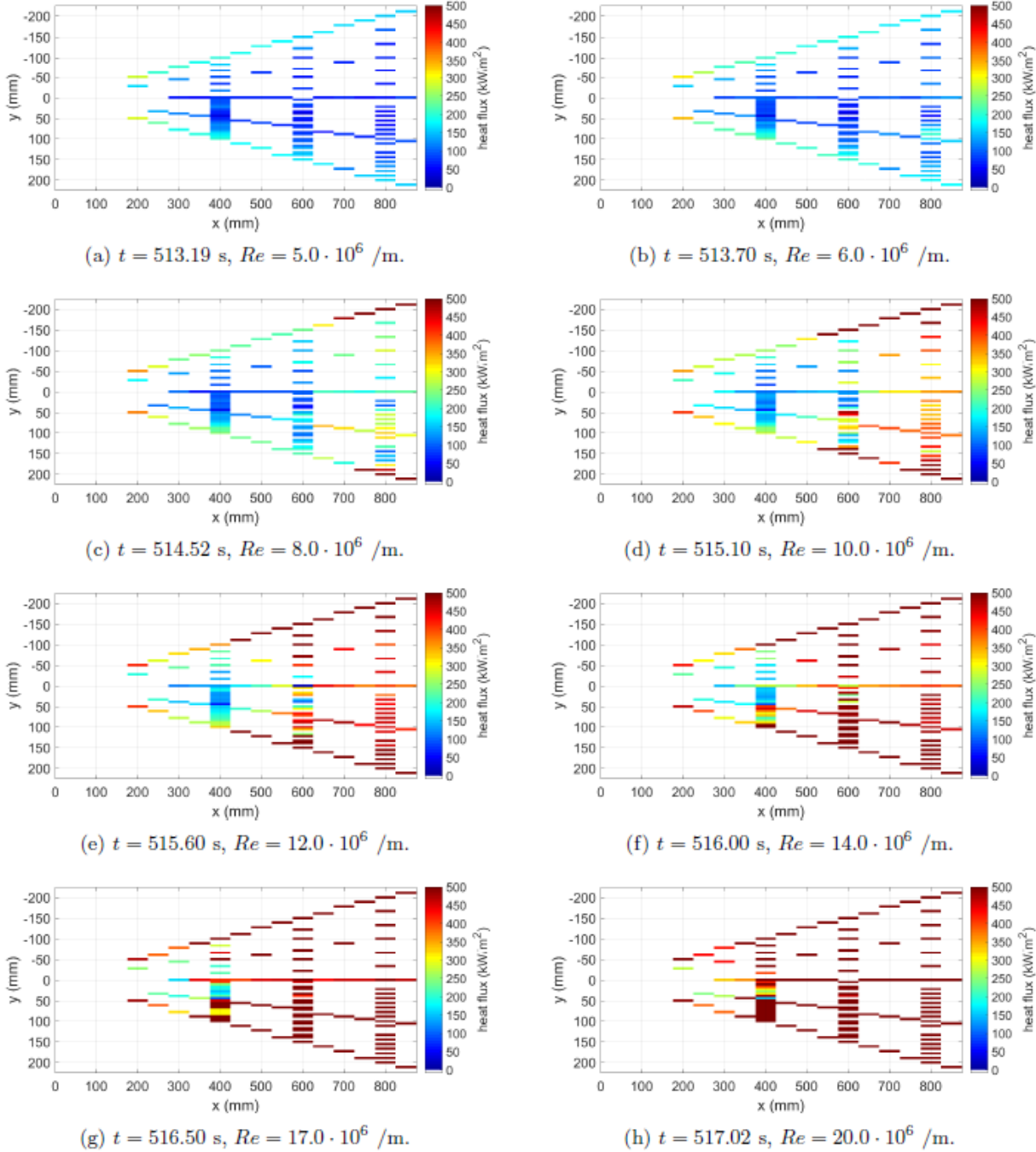
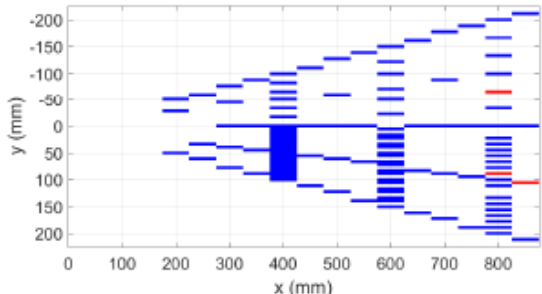
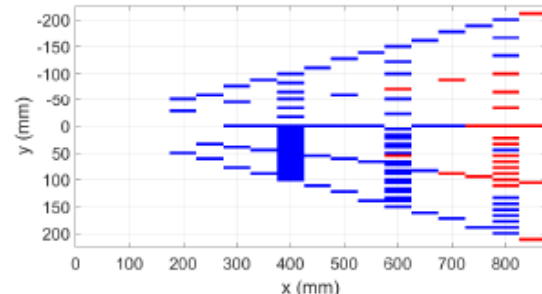


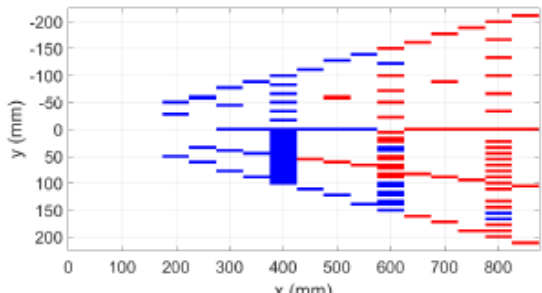
Figure 4-14 Global heat-flux distribution. $M = 7.7\text{--}7.9$.



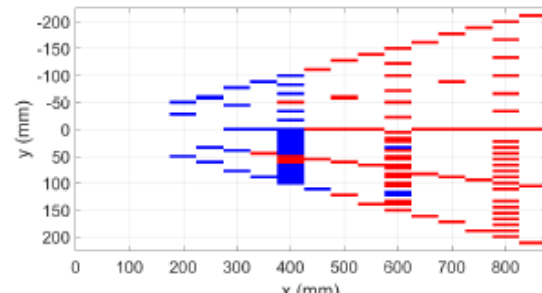
(a) $t = 513.19$ s, $Re = 5.0 \cdot 10^6$ /m.



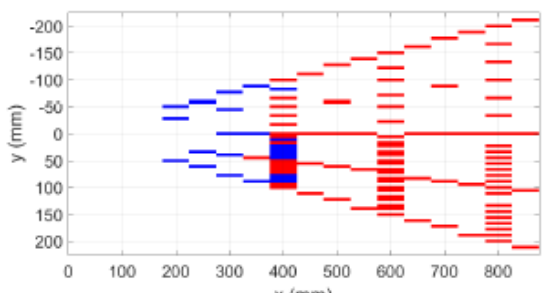
(b) $t = 513.70$ s, $Re = 6.0 \cdot 10^6$ /m.



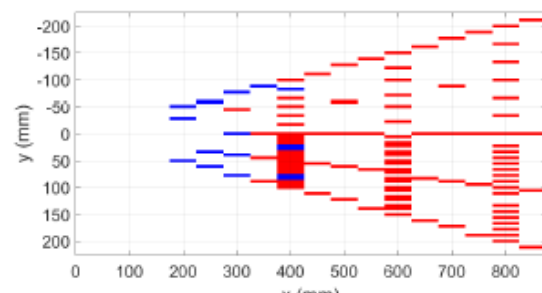
(c) $t = 514.52$ s, $Re = 8.0 \cdot 10^6$ /m.



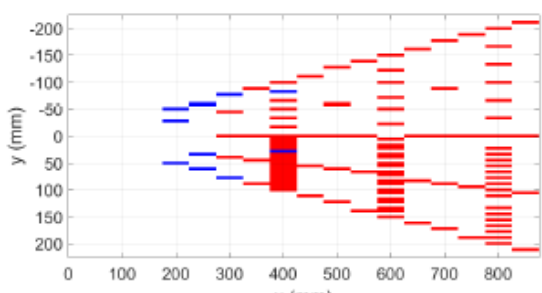
(d) $t = 515.10$ s, $Re = 10.0 \cdot 10^6$ /m.



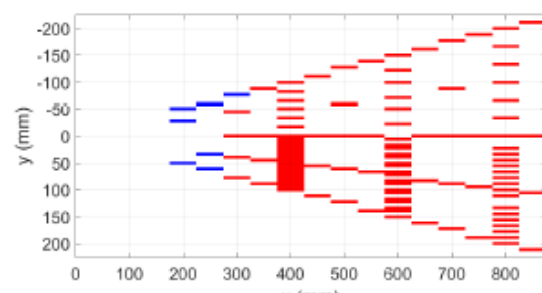
(e) $t = 515.60$ s, $Re = 12.0 \cdot 10^6$ /m.



(f) $t = 516.00$ s, $Re = 14.0 \cdot 10^6$ /m.



(g) $t = 516.50$ s, $Re = 17.0 \cdot 10^6$ /m.



(h) $t = 517.02$ s, $Re = 20.0 \cdot 10^6$ /m.

Figure 4-15 Boundary-layer state. Prior to transition onset = blue, after transition onset = red. $M = 7.7\text{--}7.9$.

5. HIFiRE-5 at Angle of Attack and Yaw

5.1. Experimental Overview

Previous ground tests on the HIFiRE-5 geometry revealed a number of interesting features as well as several limitations of both the experimental methods and model.^{47,48} For noisy and quiet flows, stationary crossflow vortices were readily detected with oil flow visualization. However, TSP did not show any vortices in noisy flow, and only revealed vortices in quiet flow for a subset of the Reynolds numbers for which they were detected with the oil flow.³⁸ In an attempt to study traveling crossflow waves in both conventional “noisy” and quiet freestream environments, previous experiments were performed on the HIFiRE-5 elliptic cone geometry in Purdue University’s BAM6QT and Texas A&M University’s ACE hypersonic wind tunnels. Traveling crossflow waves and transition were clearly measured in the quiet freestream environment. Since the traveling mode is conventionally thought to dominate crossflow transition in noisy environments, traveling waves were also expected in noisy flow. However, there was no evidence of traveling crossflow waves with a noisy freestream, even though the spectra of the surface pressure signals showed an expected progression from laminar to turbulent as the Reynolds number was increased.⁴⁸ It was thought that perhaps the very noisy freestream environment of the BAM6QT when run noisy caused transition apart from the traveling crossflow mode. Thus, the model was also tested in ACE at similar freestream temperatures and pressures, but with lower noise levels. Again, although transition was observed, the traveling crossflow instability was not.⁴⁷

The model used in these past experiments was not originally designed for surface instrumentation. Pressure sensors were mounted flush with the model surface in only one grouping near the back of the model with no feasible way of adding more instrumentation farther forward on the model. The results of these experiments motivate the current work.

In an attempt to obviate some of the experimental difficulties and answer some of the outstanding questions raised by the previous work, a new HIFiRE-5 model was designed and used for the work presented in this paper. The new model design satisfied two primary objectives. First, the new model accommodated IR heating measurements. The IR method alleviates roughness and steps induced by temperature-sensitive paint, and it was hoped the method might provide higher heat-transfer sensitivity over TSP. TSP could only image crossflow at relatively high Reynolds numbers. If stationary crossflow vortices were present under noisy flow, their amplitudes were below the TSP detection limit, particularly because the boundary layer transitioned at much lower Reynolds numbers for noisy flow than for quiet flow. It was hoped that the IR method would provide quantitative heat transfer measurements of stationary crossflow under noisy conditions, to support the qualitative oil-flow imaging. Secondly, the new model contained streamwise-distributed arrays of pressure sensors well upstream of the one measuring station available on the previous model. The streamwise-distributed sensors permit quantitative measurements of the evolution of crossflow instabilities at a variety of streamwise stations. It was hoped that both the IR and distributed pressure measurements would illuminate the evolution of instabilities leading to transition under noisy and quiet flow. Reference 49 presented preliminary results from the first tunnel entry with the new model. The current work details recent experiments that were free from some of the problems experienced during the first

test campaign with the new model. Additionally, results are presented with the model at three non-zero angles of attack, 1° , 2° , and 4° .

The new model, shown in Figure 5-1, maintains the same outer mold line as the previous model. It is a 38.1% scale model of the flight vehicle, is 328.1 mm long, and has a base semimajor axis of 82.3 mm. The half-angle of the elliptic cone in the minor axis plane is 7.00° , and 13.80° in the major axis (x - z plane). The nosetip cross-section in the minor axis plane is a 0.95 mm radius circular arc, tangent to the cone ray describing the minor axis, and retains a 2:1 elliptical cross-section to the tip.



Figure 5-1 Photograph of model.

The model is made of solid 15-5PH H-1100 stainless steel from the nose to $x = 150.3$ mm. The RMS surface finish of the steel is $0.4 \mu\text{m}$ ($16 \mu\text{in}$). Downstream of $x = 150.3$ mm, the model is a shell made of PEEK, a high emissivity, high temperature plastic. The surface-normal thickness of the PEEK is 10.0 mm, except along the leading edges where it is thicker. The use of a shell, rather than a solid model, facilitates the installation of surface-flush pressure sensors in many locations and much farther forward than in the previous model. The instrumented shell has forty-four holes for instrumentation. Since the shell has a high emissivity and low thermal conductivity, it is also well-suited for IR thermography. The use of IR thermography was inspired by previous successes in imaging crossflow vortices in hypersonic wind tunnels.^{45,50,51}

Due to poor machining practice, the model manufacturer overcut portions of the stainless steel nose. The overcut was backfilled with solder and then re-machined. Unfortunately, this resulted in some portions of the nose with discrete roughness patches and/or steps. On the top, instrumented side of the model at $x \approx 50$ mm, there are several divots that are $10\text{--}15 \mu\text{m}$ deep and about 0.5 mm wide. Sample surface-profile traces of a few of the divots can be seen in Figure 5-2. Computations determined that inviscid streamlines that lie on top of the pressure sensors pass within about 1 mm of these divots. The impact of this roughness near the leading edge is unknown. The bottom half of the model does not have such divots on the leading edge, but a small scratch was discovered on the leading edge of the PEEK on the bottom half of the model.

This scratch had an obvious effect on heating rates for the bottom of the model, increasing them substantially for some conditions. Data from this region affected by this scratch are essentially unused.

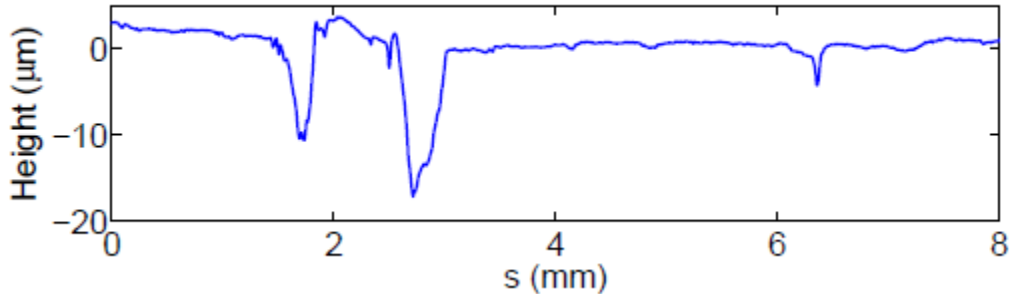


Figure 5-2 Leading edge near $x = 50$ mm

All data were obtained in the BAM6QT at Purdue University. In an attempt to determine the effect of freestream noise on crossflow instability modes, the current experiments were performed with both quiet and noisy freestreams. Quiet flow was realized for freestream Reynolds numbers (Re) up to $12.9 \times 10^6 / m$. The Purdue tunnel achieves quiet noise levels by maintaining a laminar boundary layer on the tunnel walls.⁵² A laminar boundary layer is maintained by removing the nozzle boundary layer just upstream of the throat via a bleed suction system. A new, laminar boundary layer begins near the nozzle throat. The boundary layer is kept laminar by maintaining a highly-polished nozzle wall to reduce roughness effects. The divergence of the nozzle is very gradual to mitigate the centrifugal Görtler instability on the tunnel wall.

For the current experiments, twenty pressure sensors were used. Table 5-1 lists the locations of the sensors relative to the nosetip. Here, x and z are the streamwise and spanwise coordinates, respectively, with the origin at the model nose. Figure 5-3 shows a sketch of the model and sensor locations. Seven groups of three sensors were located 25.4 mm apart along a line inclined 5° with respect to the centerline. This is the approximate angle between an inviscid streamline and the centerline.⁴³ Sensor holes that did not have sensors installed were plugged with nylon rods that were flush with the model surface.

Table 5-1 Instrumentation locations and notation

Sensor	x (mm)	z (mm)	Sensor	x (mm)	z (mm)
1	163.6	26.5	12	244.8	32.0
-	-	-	13	264.8	35.3
3	168.9	25.3	14	267.6	35.3
4	188.9	28.7	15	270.1	34.2
5	191.7	28.7	16	290.1	37.6
6	194.2	27.5	17	292.9	37.6
7	214.2	30.9	18	295.4	36.4
8	217.0	30.9	19	315.4	39.8
9	219.5	29.8	20	318.2	39.8
10	239.5	33.1	21	320.7	38.6
11	242.3	33.1			

Kulite XCQ-062-15A and XCE-062-15A pressure transducers with A screens were mounted flush with the model surface to detect traveling crossflow waves. The Kulite sensors are mechanically stopped at about 100 kPa so that they can survive exposure to high pressures but still maintain the sensitivity of a 100 kPa full-scale sensor. These sensors typically have flat frequency response up to about 30–40% of their roughly 270–285 kHz resonant frequency.⁵³

In addition to the pressure transducers, the PEEK shell of the model was imaged with a Xenics Onca IR camera. The camera is a mid-wave, 14-bit camera which is sensitive to IR radiation from 3.7–4.8 μm . The sensing array is 640 x 512 pixels. Images were acquired at about 50 Hz.

Using a subroutine called QCALC, IR data were reduced to heat flux by solving the transient one-dimensional heat equation on a pixel-by-pixel basis. QCALC uses second order Euler-explicit finite differences to solve for the temperature distribution through the model. Heat flux is calculated from a second-order approximation of the derivative of the temperature profile at the surface.⁴⁴ The measured surface temperature was used as one boundary condition. An adiabatic backface temperature was used as the other boundary condition. A constant initial temperature was assumed through the PEEK. The ratio of the wall temperature to the adiabatic wall temperature (T_w/T_{aw}) is approximately 0.8. The thermal conductivity, density, and specific heat of PEEK were obtained from the manufacturer and are 0.29 W/(m·K), 1300 kg/m³, and 1026 J/(kg·K), respectively. The size of the model precluded an precise measurement of its emissivity. A skilled researcher estimated the emissivity to be 0.88–0.93, depending on how diffuse the reflection from the model is. A future project is to procure a smaller sample of PEEK for a much more accurate determination of the actual model emissivity. For the results presented here, the emissivity was taken to be 0.91.

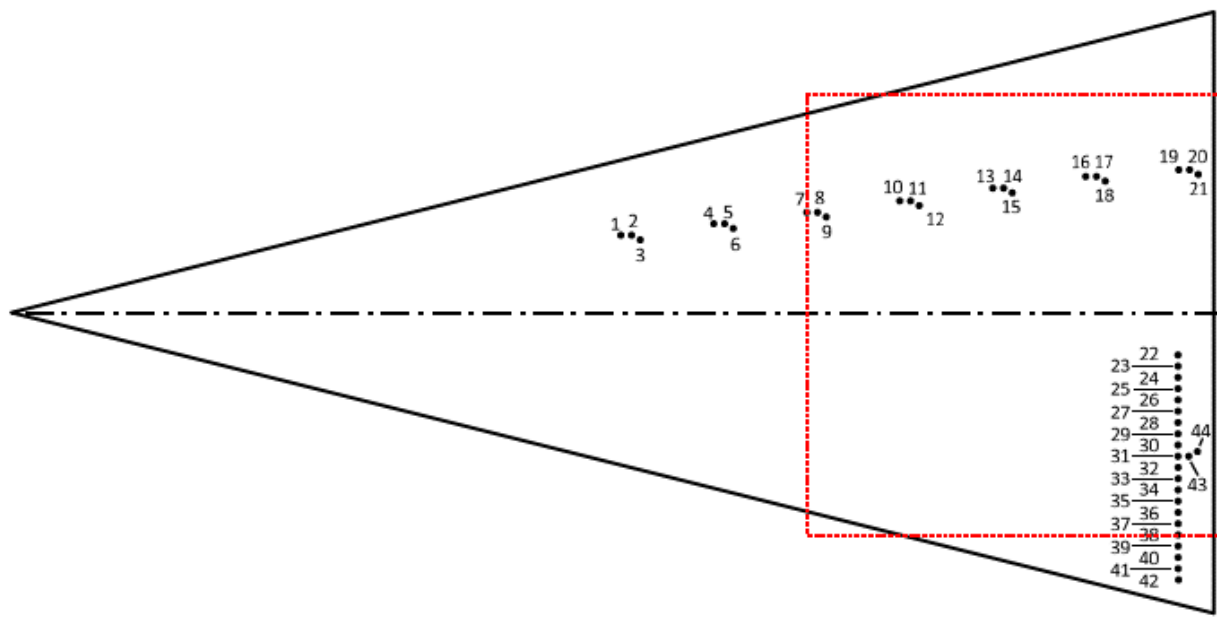


Figure 5-3 Schematic of pressure-sensor locations. The dashed red line denotes approximate field of view of IR camera.

5.2. Quiet Flow

5.2.1. 0° Angle of Attack

The model was first mounted in the tunnel at 0° angle of attack (α). A series of 18 runs at different initial pressures comprised a sweep of freestream Reynolds numbers with a fine gradation. This allowed the growth and breakdown of traveling crossflow waves to be studied in detail. Global heat flux measurements and pressure sensor measurements are presented below under quiet flow.

Global heat flux measurements for freestream Reynolds numbers from $6.5 - 12.9 \times 10^6 / m$ can be seen in Figure 5-4. The contour limits vary for each figure to highlight the salient heating features on the model surface. Streamwise streaks of increased heating are seen for all Re. It should be noted that previous work utilizing TSP technique did not reveal the presence of stationary crossflow vortices until the freestream Re was greater than $7.2 \times 10^6 / m$.³⁸ In the present work, for all but the lowest Re, it appears that the boundary layer along one or more of the streaks transitions. Transition is evidenced by a sudden increase in heat flux along a streak. As Re increases, more streaks transition farther forward, and the maximum heat flux levels also increase. This is an expected trend as the boundary layer thins and becomes more unstable.

A threshold heat flux of 2.5 kW/m^2 is selected as a value representative of transition for $\alpha = 0^\circ$. When the heat flux reaches this value at any given pressure sensor, spectral broadening is also generally observed in the spectrum for that sensor. Transition locations are extracted from the heat flux contours of the 4 highest Re in Figure 5-4 and are presented as dimensional transition locations in Figure 5-5a.

Three distinct transition regions are observed: I) the near-centerline region from $0\text{--}\pm7$ mm, II) slightly outboard of this from $\pm7\text{--}\pm19$ mm, and III) a broad acreage region with significant crossflow from $\pm19\text{--}\pm45$ mm. These regions have been marked by black horizontal lines in Figure 5-5. The boundary layer in Region I has large spanwise gradients and takes the form of a mushroom-like structure, being very thick on the centerline and experiencing significant localized thinning just outboard of the centerline (see, for example, Figure 7 of Ref. 31). Laminar heating rates under the thinned region are locally higher than locations immediately adjacent to the thinned region. Thus, with no instrumentation in this region, a conclusive classification of the boundary layer state cannot be made. However, the heat transfer along the streaks increases suddenly, moves upstream with increased freestream Re, and appears to broaden, transversely contaminating the centerline. Thus, it seems likely that the sharp increase in heat flux along the high-heat-flux streak in Region I does indicate transition. Region II includes one predominant heating streak that seems distinct from the stationary crossflow vortices in Region 3. This streak is likely due to a local thinning of the boundary layer, or highly-elongated streamwise vortex emanating from the nosetip. Transition of this streak is observed to move upstream with increasing freestream Re. The transition front in Region III is similar to that observed in low-speed stationary crossflow instability experiments,^{54,55} being notably jagged and occurring at different streamwise locations over the span of Region III. This transition front, due also to transition of stationary crossflow vortices, broadens and moves upstream with increasing freestream Reynolds number.

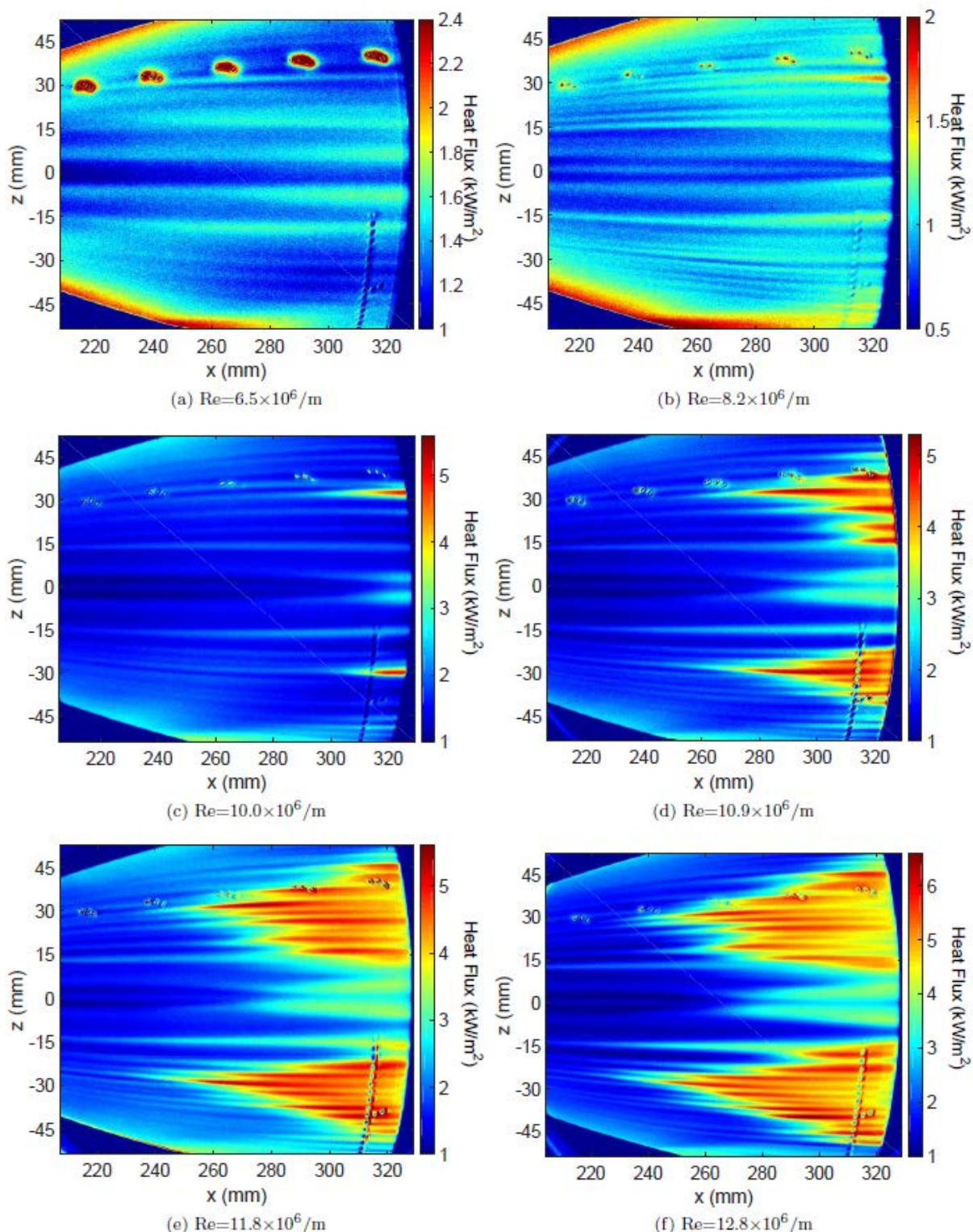


Figure 5-4 Heat flux for increasing Re, quiet flow

Boundary-layer transition is presented as transition Reynolds numbers (Re_{tr}) in Figure 5-5b, where Re_{tr} is found by multiplying the freestream unit Re and the streamwise transition location.

Transition locations, and thus Re_{tr} values, were not completely symmetric across the centerline. In Region I, Re_{tr} shows excellent agreement for the three lowest freestream Re with $Re_{tr} \approx 3.2\text{--}3.3 \times 10^6$ on both halves of the model. The agreement for the highest freestream Re is not as good, with $Re_{tr} \approx 3.4\text{--}3.5 \times 10^6$. Juliano et al.³⁶ report centerline Re_{tr} values of 2.8–3.1 for the previous model using temperature-sensitive paint. The discrepancy here likely falls within the uncertainty of estimating transition by simply using a threshold heat flux value. In Region II, transition was observed at $Re_{tr} \approx 2.9\text{--}3.0 \times 10^6$ on the bottom half of the model and $Re_{tr} \approx 3.1\text{--}3.3 \times 10^6$ on the top half of the model. In Region III, good agreement was seen for all freestream Re with Re_{tr} varying with z . On both halves of the model, Re_{tr} ranged from 2.8–3.7 $\times 10^6$. These results are tabulated in Table 5-2. There does not appear to be a freestream Reynolds number effect on transition, with the possible exception of the delayed transition observed in Region 1 for the highest freestream Re that was tested. Planned future tests with pressure instrumentation on and near the centerline may help determine whether transition is actually delayed or if this effect is due to the arbitrary threshold heat flux value not being truly representative of transition. Additionally, it appears that a conservative estimate of the lowest Re_{tr} for this model in quiet flow at $\alpha = 0^\circ$ is 2.8×10^6 .

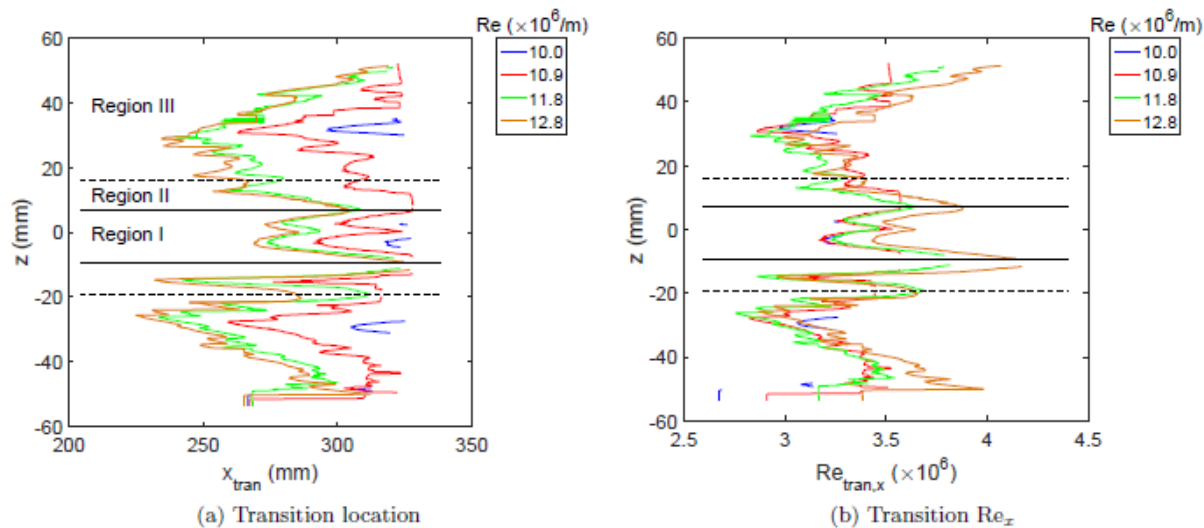


Figure 5-5 Transition Reynolds numbers

Table 5-2 Re_{tr} for $\square = 0^\circ$

Region	Model Half	$Re_{tr} (\times 10^6)$
1	Top	3.2–3.3
	Bottom	3.2–3.3
2	Top	3.1–3.3
	Bottom	2.9–3.0
3	Top	2.8–3.7
	Bottom	2.8–3.7

The signals from the pressure sensors are used to measure traveling instabilities in the boundary layer and also to determine state of the boundary layer. Figure 5-6 presents a sample of such data. Figure 5-6a shows PSDs for sensors 1, 4, 7, 10, 13, 16, and 19 at a fixed freestream unit Reynolds number of $10.8 \times 10^6 / m$. These 7 sensors are the most upstream sensors in each of the 7 sensor groups. The legend labels the spectra with sensor Reynolds numbers, based on the freestream unit Re and the streamwise location of each sensor. For $Re_x = 1.8 \times 10^6$, the spectrum reflects a laminar, unperturbed boundary layer. As Re_x increases, a peak in the spectra is seen to develop and grow near 55 kHz. This is attributed to the traveling crossflow instability. Additionally, the spectra exhibit significant broadening, particularly for $Re_x > 2.6 \times 10^6$. The broadness of the spectra and less significant 55 kHz peak for $Re_x = 3.1$ and 3.4×10^6 suggest that the boundary layer is transitional or turbulent. This spectral growth demonstrates that the boundary layer progresses from fully laminar to nearly fully turbulent between sensors 1 and 19, and that the traveling crossflow instability is present and growing over much of this path.

Figure 5-6b presents PSDs for sensor 13 for freestream unit Reynolds numbers ranging from $6.9 - 12.9 \times 10^6 / m$. The legend labels the spectra with sensor Reynolds numbers, based on the freestream unit Reynolds number and the streamwise location of sensor 13. As observed in Figure 5-6a, as Re_x increases, the spectra indicate that the boundary layer progresses from a nearly-unperturbed laminar state to a nearly-fully-turbulent state. The growth of the prominent traveling crossflow instability centered on 50 kHz is again evident.

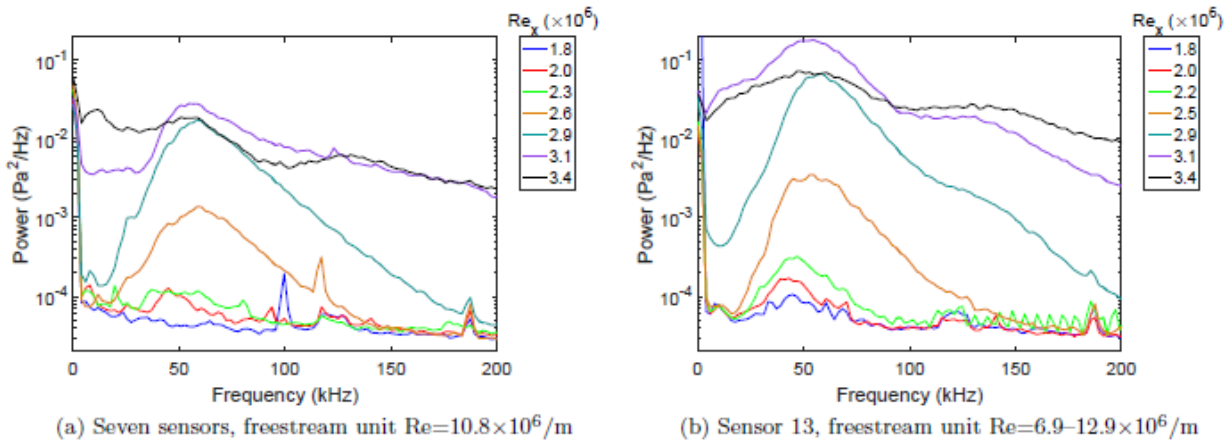


Figure 5-6 PSDs for $\square = 0^\circ$, quiet flow

Comparing Figure 5-6a and b, the spectra for equivalent Re_x are very similar. This suggests that the growth and breakdown of the traveling crossflow instability is insensitive to the freestream unit Reynolds number. Additionally, examining the evolution of the traveling crossflow instability at one location for varying freestream conditions may be a reasonable surrogate for examining the spatial development of the instability for fixed freestream conditions. Lastly, the good comparison implies that the traveling crossflow instability evolves in a similar fashion over much of the streamwise extent of the elliptic cone.

Having the sensors located in groups of three, the wave angle and phase speed of the traveling crossflow instability can be determined using the method described in detail in Reference 47. Figure 5-7 presents the wave angles and phase speeds of the traveling crossflow instability as a

function of frequency for several Reynolds numbers at sensor group 3. Wave properties are able to be calculated for a relatively small range of freestream Re , about $1.6 \times 10^6/m$. For lower Re , traveling crossflow waves are not of measurable amplitude. For higher Re , transition onset introduces nonlinear effects and precludes the accurate determination of wave properties.

Measured wave angles for traveling crossflow frequencies near the 50 kHz spectral peak vary from approximately 77° – 81° , increasing with increased freestream Re . These oblique wave angles are similar to the wave angles measured in Reference 47 near the downstream end of the model used in the previous experiments. Measured phase speeds for traveling crossflow frequencies near the 50 kHz spectral peak vary from approximately 110–170 m/s, decreasing with increasing freestream Re . The measured phase speed from Reference 20 near the downstream end of the cone was approximately 225 m/s.

Figure 5-8 presents the wave angles and phase speeds of traveling crossflow waves at all of the sensor groups and freestream Reynolds numbers for which they could be meaningfully calculated. Both wave properties are plotted as a function of Re_x , which is determined using the streamwise location of the middle sensor of each sensor group. Only two sensors were installed in sensor group 1, which precludes the determination of wave properties at that location. Reasonable wave properties cannot be determined for sensor group 7. The reason for this behavior is currently unknown. For each data point, the frequency for which the wave properties are selected is the center of the peak in coherence between the most upstream and middle sensors of the sensor group, and is always between 45 and 60 kHz. Although the data do not collapse perfectly, it is clear that the wave angle increases and the phase speed decreases with increasing Re_x . The data for sensor groups 2, 3, and 5 appear quite self-consistent, showing good agreement in wave angle and phase speed for similar Re_x values. The data from sensor groups 4 and 6 exhibit some significant discrepancies. The disagreement in the data from different sensor groups may be due to the relative locations of the sensor groups to particular stationary crossflow vortices. When the stationary vortices grow large enough, they distort the boundary layer. The effect of such distortions on the properties of traveling crossflow waves is unknown, and may vary from sensor group to sensor group since a line passing through all 7 sensor groups would also intersect several stationary crossflow vortices. The effect of sensor proximity to stationary crossflow vortices is discussed in Section 5.2.2. Across all Re and sensor groups, the wave angles are between 68° and 83° . The phase velocities vary from 90–350 m/s, but are mainly clustered between 140–250 m/s. Generally, traveling crossflow waves are of measurable amplitude and growing such that linear wave properties can be calculated for $Re_x \approx 1.9$ – 2.5×10^6 . This Re_x range is 68–90% of the conservative Re_{tr} discussed in Section III.A.1. Thus, the onset of nonlinear effects that preclude the calculation of wave properties seems to indicate imminent transition.

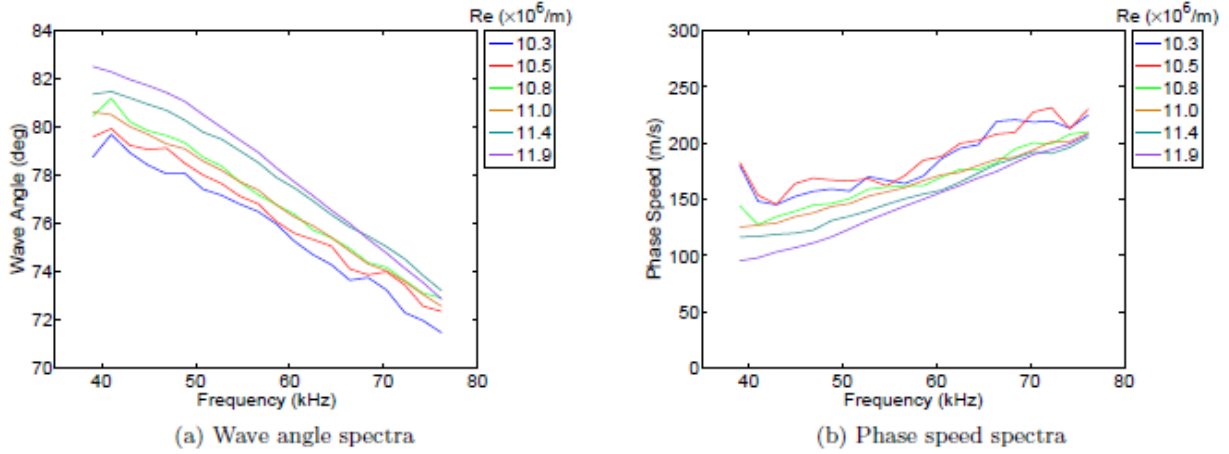


Figure 5-7 Wave properties for various Re at sensor group 3

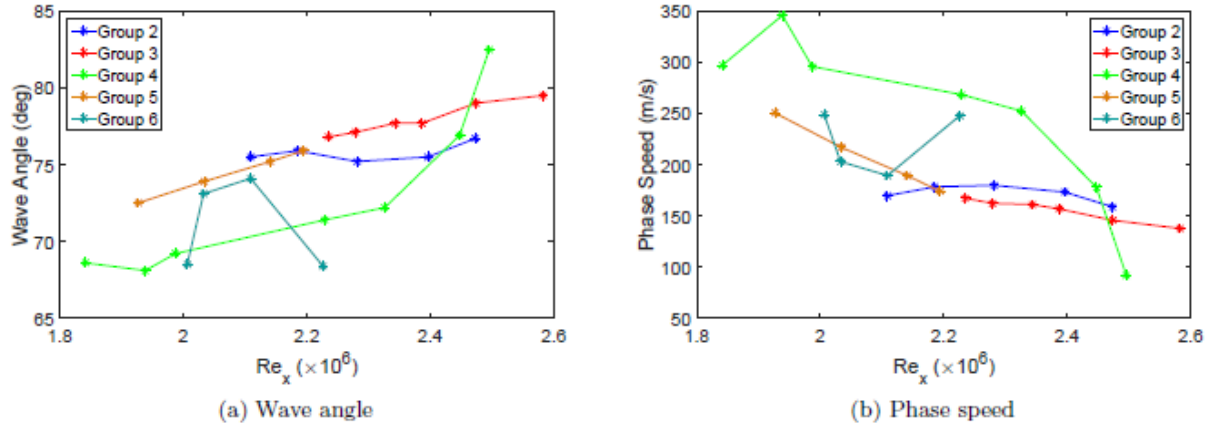


Figure 5-8 Wave properties at sensor groups 2-6

5.2.2. Effect of Stationary Crossflow on Traveling Vortices

The effect of stationary crossflow vortices on traveling crossflow waves is unknown. By examining pressure and heat-flux data simultaneously, some understanding can perhaps be gleaned. In each of the seven groups of three pressure sensors, the two most upstream sensors are located at the same spanwise station. The most downstream sensor is located inboard of the upstream sensors by 1.2 mm. This is on the order of 30–40% of the wavelength of the stationary crossflow vortices measured in the previous work.⁴⁹ Figure 5-9 shows heat flux values near sensors 13, 14, and 15 (sensor group 5), as well as PSDs of the signals from those sensors for freestream unit Reynolds numbers of 7.5 to $12.5 \times 10^6/\text{m}$ ($\text{Re}_x = 2.0$ to 3.3). For the two lowest freestream Re cases, the PSDs for all three sensors are similar. There are some differences in the amplitudes of spectra, but the peak frequency of the traveling crossflow instability and the general shape of the spectra show good agreement. The streak of elevated heat flux, presumably the trough between 2 stationary crossflow vortices that passes over the sensor group, remains laminar. The adjacent streak located near $z=30$ mm also remains laminar.

For $Re=10.7\times10^6/m$, the peak frequencies still match well for all three sensors. The spectrum for sensor 15 exhibits a kink at approximately 110 kHz that is not evident for sensors 13 or 14. The heat flux map shows that the streak over the sensor group remains laminar, but the adjacent streak transitions near $z=265$ mm. In this case, sensor 15 is closer to a transitional streak than the other sensors and also shows a difference in the spectral shape. As Re is further increased to $11.3\times10^6/m$, the streak that passes over the sensors transitions at or just downstream of the sensors. The adjacent streak transitions at a streamwise station upstream of the sensor group. Sensor 15 is thus in closer proximity to a turbulent streak than the upstream sensors. The spectra at this Re show significant differences. The spectra for sensors 13 and 14 are very similar, while the spectrum for sensor 15 has a higher peak frequency, higher power for low frequencies, and a modified behavior at higher frequencies. As Re is further increased to $11.8\times10^6/m$, the spectra for sensors 13 and 14 remain very similar, while the spectrum for sensor 15 has lower power levels for 0–110 kHz, higher for 110 to 200 kHz, a higher peak frequency, and two spectral peaks of similar magnitude. The streak passing over the sensors now transitions immediately upstream of the sensors. For $Re=12.5\times10^6/m$, the spectra for all three sensors look very similar and reflect a nearly fully turbulent boundary layer. Separate streaks appear to pass over sensors 13/14 and 15, and both transition well upstream of the sensors.

When transition is well downstream of the pressure sensors, the position of the sensors relative to a particular stationary crossflow vortex does not appear to have a significant effect on the traveling crossflow instability. However, when only one of the sensors is closer to a transitional or turbulent vortex, that vortex seems to modify the traveling crossflow instability. The exact nature of the interaction between stationary and traveling crossflow instability modes and the effect on transition is unknown.

5.3. Angle of Attack

5.3.1. Background

In an effort to determine the effect of angle of attack on stationary and traveling crossflow waves, the model was also inclined at 1° , 2° , and 4° into the flow. All data presented for positive α is thus for the windward surface of the model. The effect of such a positive model inclination is to increase the shock strength along the model centerline, thus reducing the pressure gradient between the leading edge and centerline. Reducing the pressure gradient reduces the crossflow and should serve to make the boundary layer less unstable to the crossflow instability.

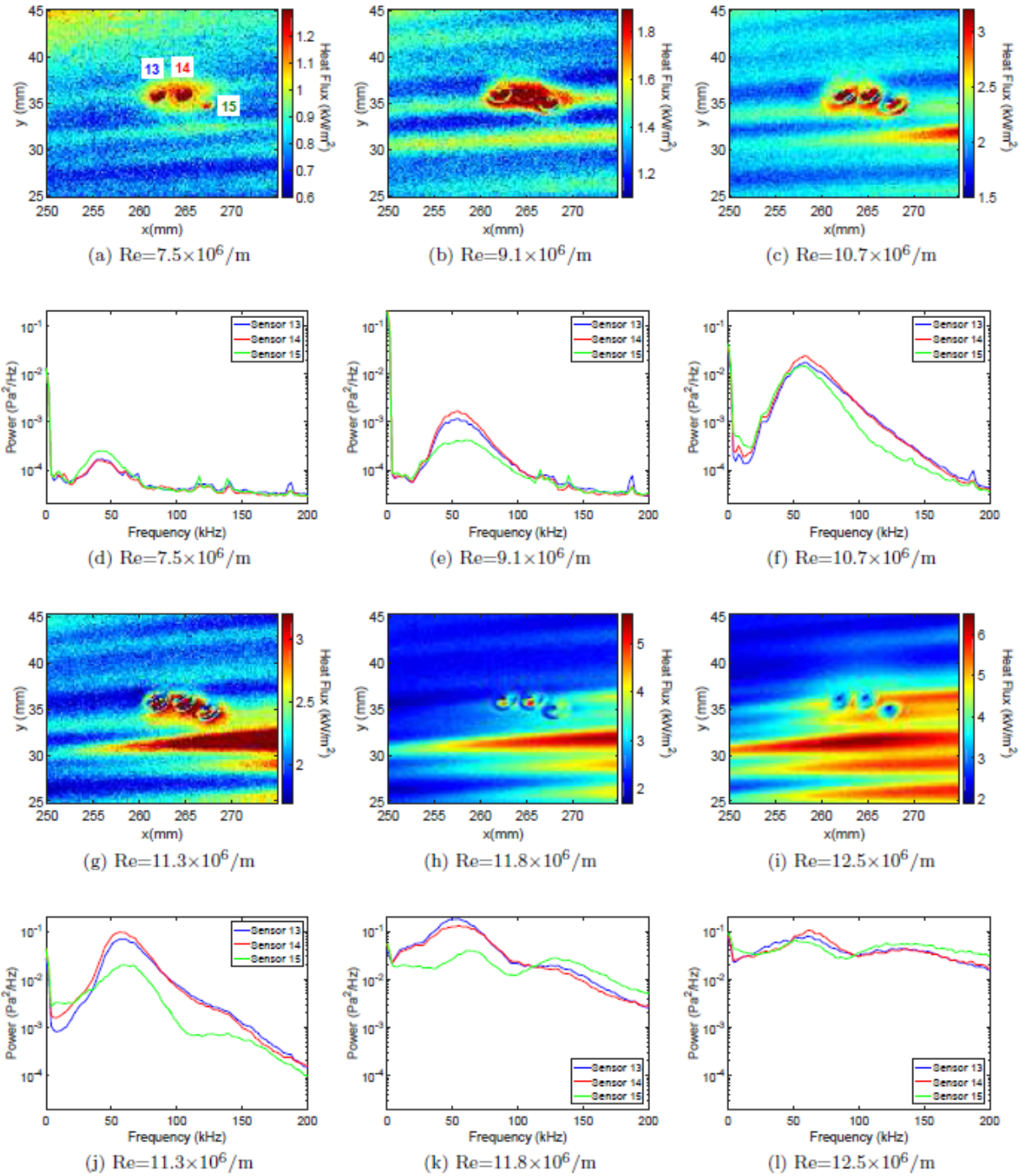


Figure 5-9 Heat flux for increasing Re, quiet flow

5.3.2. Global Heat Flux Measurements

Global heat flux contours are presented in Figure 5-10 for all four α tested at $Re \approx 12.9 \times 10^6$ m. The heat flux contours look similar for $\alpha=0^\circ$ and 1° . As α increases from 1° to 2° , the streaks of

increased heat flux due to transition along the stationary crossflow vortices are observed to move downstream. The spanwise extent of the turbulent region is also reduced. However, the amplitude of the heat flux along the stationary crossflow vortices is highest for the 2° case. This is likely due to the boundary layer being thinned there relative to the 0° case. For $\alpha=4^\circ$, no crossflow transition is observed. Faint vortices are still visible near the downstream end of the model. This behavior is congruent with the notion that the boundary layer at positive α is less unstable to the crossflow instability. This finding has implications for the flight test of HIFiRE-5. If the flight test article flies at positive α , crossflow transition may be moved downstream or may not occur for trajectory points for which it otherwise would have been expected. For negative α , transition may be moved upstream of what is expected for $\alpha=0^\circ$.

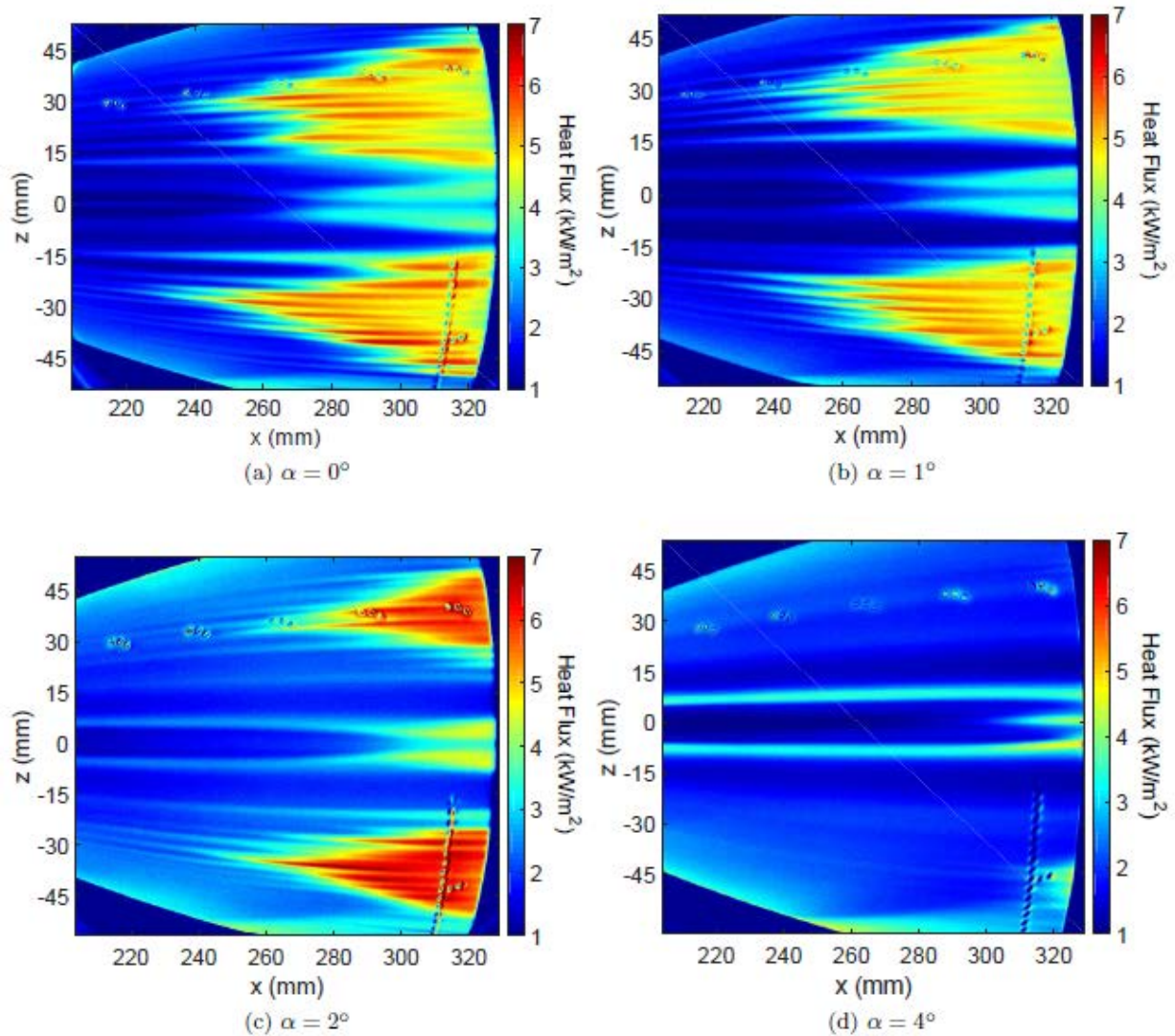


Figure 5-10 Heat flux for changing angle of attack, quiet flow, $Re \sim 12.8 \times 10^6 / m$

The centerline transition is also appears to be stabilized with increasing α . This is probably also due to the decreased spanwise pressure gradient that occurs at higher α on the windward surface. The centerline boundary layer transition is dominated by the strongly inflected boundary layer in

this region. This inflection is due to the convergence of flow from the higher-pressure sides of the model toward the lower-pressure centerline. As the spanwise pressure gradient decreases, the strength of this inflection likely also decreases. It appears that for $\alpha = 4^\circ$, only a small section of the centerline is turbulent. The two prominent streaks on either side of the centerline are probably regions of local high laminar heating, created by the nonuniform spanwise pressure gradient near the nosetip.

Using threshold values, Re_{tr} is again extracted from the heat flux data and is plotted Figure 5-11. Directly comparing transition locations determined from threshold values for varying α is a somewhat specious task. The threshold value used for each α varies since even the laminar heat flux values are higher for positive α due to the thinner boundary layer. The threshold value for $\alpha = 0^\circ$ and 1° was again 2.5 kW/m^2 . Threshold values of 3.1 and 3.8 kW/m^2 were used for $\alpha = 2^\circ$ and 4° , respectively.

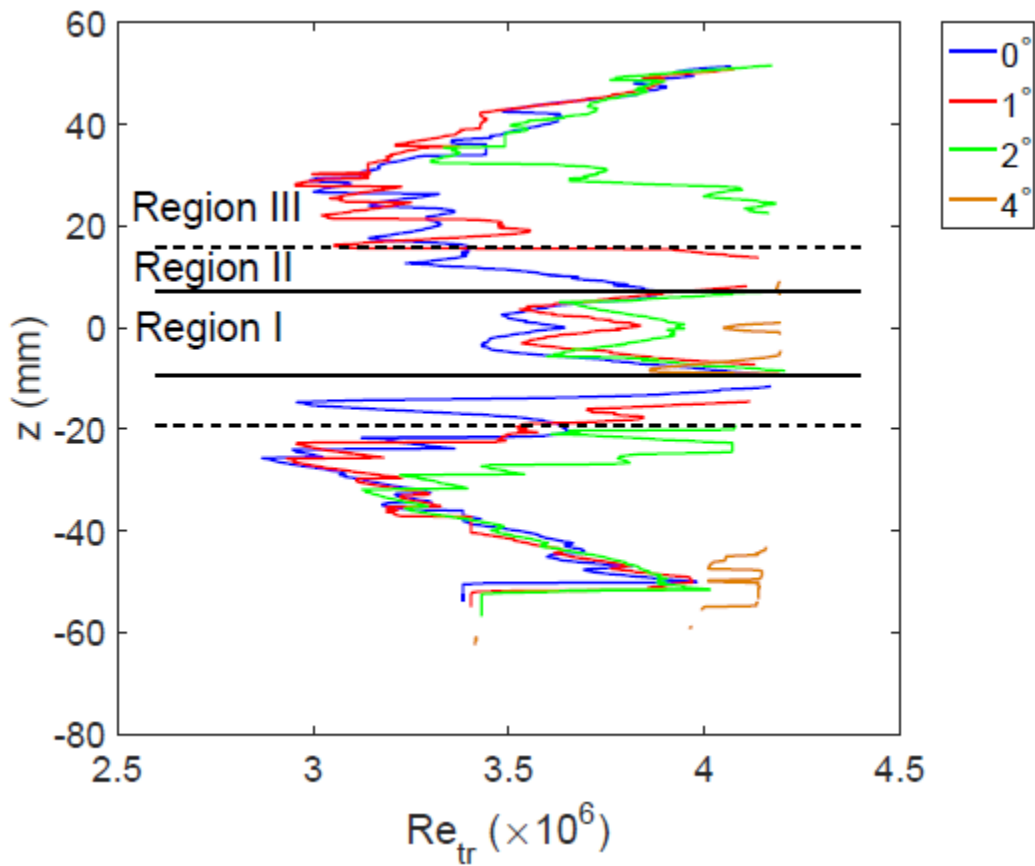


Figure 5-11 Transition locations for changing angle of attack, quiet flow, $Re \sim 12.8 \times 10^6/\text{m}$

As in Figure 5-5, boundary-layer transition is divided into three regions. Transition locations in Region I do not collapse neatly, but transition of the near-centerline streaks is observed to take place over a small range of Re_{tr} , approximately 0.2×10^6 for $\alpha = 0^\circ, 1^\circ$, and 2° . This range is likely within the uncertainty of using a varying threshold value to determine the location of transition. Region I transition for $\alpha = 4^\circ$ exhibits a qualitative difference when compared to the lower

α cases. At this angle, the two near-centerline streaks are much more pronounced than at lower α . The lower streak may transition, but the upper streak appears to remain laminar. Additionally, a narrow streak of turbulence on the centerline is observed. Evidently, at this higher inclination, the nature of centerline transition has been altered.

Transition in Region II is observed only for $\alpha = 0^\circ$ and 1° and appears to be farthest forward for $\alpha = 0^\circ$. The transition front in Region III for $\alpha = 0^\circ$ and 1° is nearly the same with the earliest transition occurring for $Re_{tr} = 2.9 \times 10^6$. For $\alpha = 2^\circ$, transition is delayed, with the earliest transition occurring at $Re_{tr} = 3.2 \times 10^6$. Although the lowest Re_{tr} increased by only 10%, it is evident that crossflow transition is significantly delayed at some spanwise locations. Inboard of $z = \pm 32$ mm, Re_{tr} is observed to increase by approximately $0.7\text{--}0.9 \times 10^6$, or by a maximum of about 30%. Outboard of $z = \pm 32$ mm, Re_{tr} is nearly identical to that observed for $\alpha = 0$ and 1° . When α is further increased to 4° , crossflow transition is delayed to $Re_{tr} > 4.2 \times 10^6$. On the bottom half of the model, the boundary layer may transition just downstream of the plugs installed in the instrumentation holes, as evidenced by increased heat flux there. If the increased heat flux is due to transition, it seems likely that it is either caused by or enhanced by the sensor plugs. Evidently, positively pitching the model by 2 degrees delays transition of stationary crossflow vortices by 0–30%, with the most significant delay occurring closer to the centerline. Increasing the model's pitch by another 2 degrees moves the transition of stationary crossflow vortices past the downstream end of the model.

Figure 5-12 shows spectra at $Re = 12.9 \times 10^6/m$ for sensor 10 and $\alpha = 0\text{--}4^\circ$. Sensor 10 is the most upstream sensor in the second sensor group from the left in Figure 5-10a–d. The broadening of the spectrum for $\alpha = 0^\circ$ indicates that the boundary layer is transitional. The peak due to the traveling crossflow instability is still evident. As α is increased to 1° , power levels across the spectrum are observed to increase, suggesting that boundary layer transition is more advanced. This is unexpected and may not be directly due to the change in α . Perhaps the 1° change in pitch also moved sensor 10 closer to a transitional stationary crossflow vortex. As α increases to 2° , the spectrum looks increasingly laminar as the broadband PSD amplitudes decrease, as well as the amplitude of the peak due to the traveling crossflow instability. For $\alpha = 4^\circ$, the spectrum appears laminar with a distinct peak due, again, to the traveling crossflow instability. In this case, the power levels are significantly reduced across the entire frequency span. The magnitude of the spectral peak for $\alpha = 4^\circ$ is over two orders of magnitude lower than for $\alpha = 0^\circ$. This behavior is further verification that positive α has a stabilizing influence on the traveling crossflow instability.

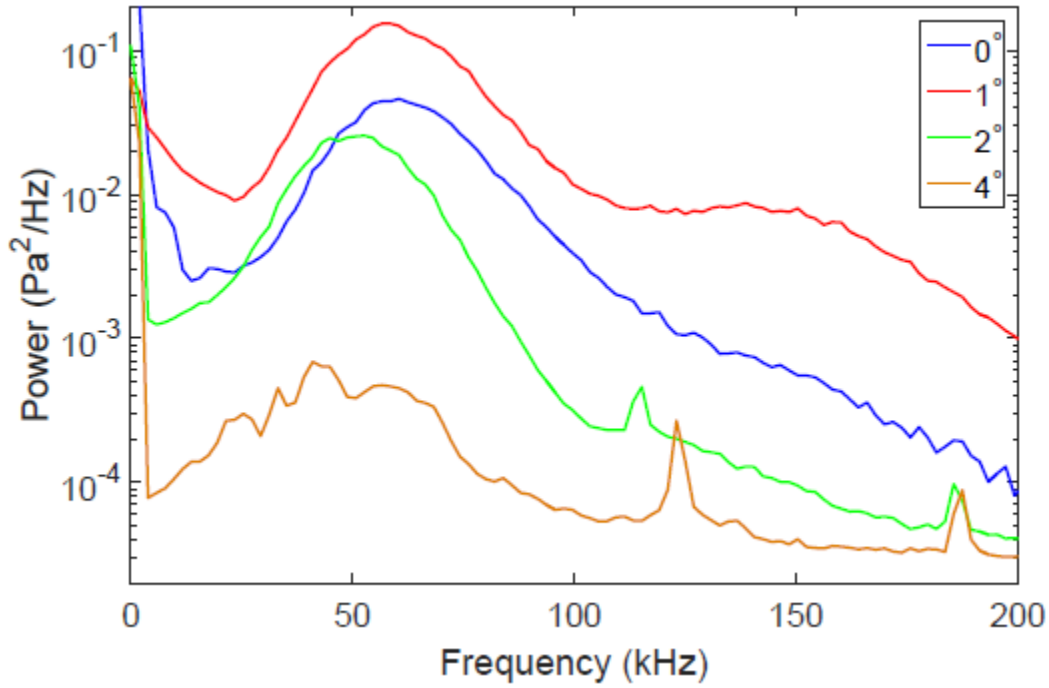


Figure 5-12 PSD for sensor 10 at $\alpha=0^\circ, 1^\circ, 2^\circ$, and 4° . $Re=12.9\times10^6/m$.

There are no freestream conditions for which traveling crossflow waves properties can be determined at all four α for one sensor group. However, there are some Reynolds number and sensor group combinations for which traveling crossflow wave properties can be compared for multiple values of α . One such combination is for $Re=8.6\times10^6/m$ at sensor group 4. Wave properties for these conditions and $\alpha=0^\circ, 1^\circ$, and 2° are shown in Figure 5-13. For 50 kHz traveling crossflow waves, the wave angle varies from 68° to 72° . There is no apparent systematic dependence on α . The phase speed varies from 235 to 300 m/s, and likewise, shows no systematic dependence on α . The $\alpha = 2^\circ$ curves exhibit more variation than for the smaller α . This is attributed to the reduced amplitude of the traveling crossflow waves and lower signal-to-noise ratio (SNR) at this α since the boundary layer is less unstable to the crossflow instability.

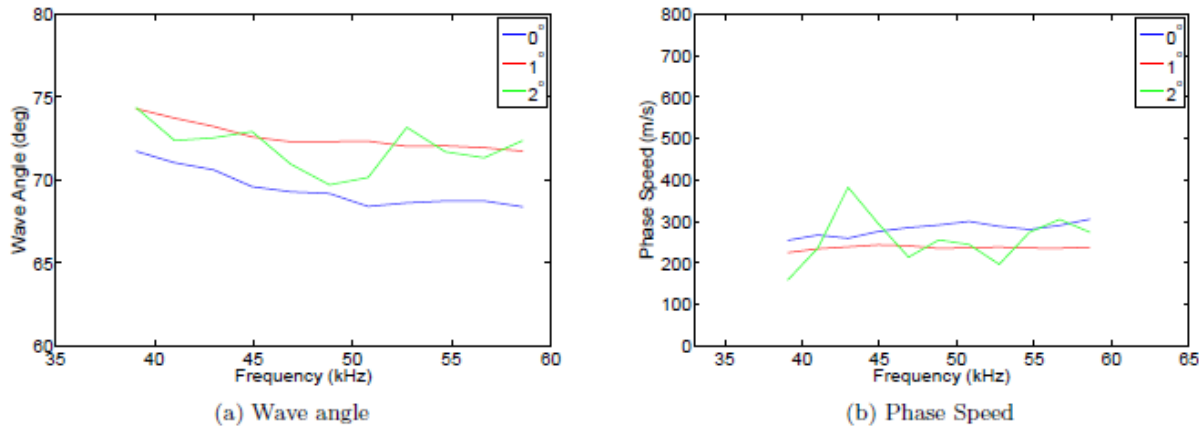


Figure 5-13 Wave angle and phase speeds for $\alpha=0^\circ$, 1° , and 2° . $Re=8.6\times10^6/m$, sensor group 4

The growth of traveling crossflow waves can be quantified by calculating the RMS amplitudes of disturbances from 17 to 80 kHz. Figure 5-14 shows the amplitudes of traveling crossflow waves for one sensor from each sensor group at all four α tested and for a variety of freestream unit Re . The amplitudes are presented as the natural logarithm of the RMS pressure normalized by the RMS pressure at the most upstream sensor.

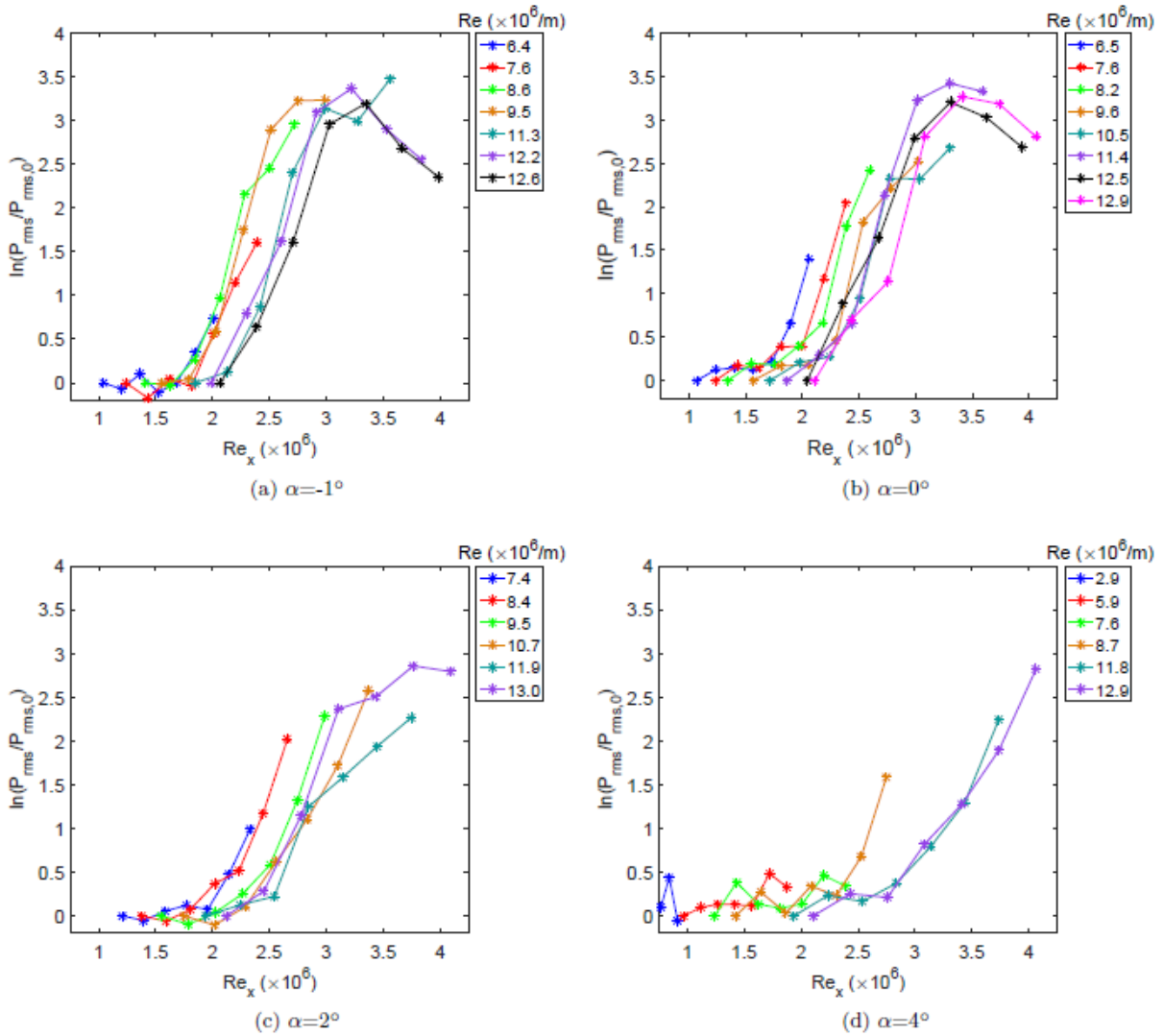


Figure 5-14 □N vs. Re_x for various □

This quantity is essentially a change in N-factor and quantifies the spatial growth of the traveling crossflow waves. All amplitudes are plotted as a function of Re_x . The initial amplitude invariance for small values of Re_x is likely because the amplitudes of the traveling crossflow waves are actually lower than the electronic noise floor of the measurement system. Growth is thus first observed when the traveling wave amplitudes have grown larger than the noise floor.

Several important features and trends are observed. The value of Re_x for which significant amplitude growth is observed increases with increasing α . This value is approximately $1.7, 1.9, 2.0$, and 2.5×10^6 for $\alpha = 0^\circ, 1^\circ, 2^\circ$, and 4° , respectively. For large enough values of Re_x , the amplitude ratio plateaus or even decreases. The value of Re_x corresponding to the peak wave amplitude is approximately 3.2 for $\alpha = 0^\circ$ and 1° and increases to 3.7 or greater for $\alpha = 2^\circ$. No peak is observed for $\alpha = 4^\circ$. Maximum amplitude ratios of

$\Delta N \approx 3.25$ are observed for $\alpha=0$ and 1° , while the maximum ratio is approximately 3 for the other pitch angles that were tested. The amplitude growth observed for $\alpha=0^\circ$ is very similar to what was predicted computationally in Ref. 34. Although there is some spread in the data, there does not appear to be a significant freestream unit Re effect, which suggests that the boundary layer in this region is self-similar and unaffected by the blunt nose.

Growth rates of the traveling crossflow instability can be calculated from the RMS pressure amplitudes. The growth rate between adjacent sensors is assumed to be constant and the growth is assumed to be exponential. Following the method of Roediger et. al,⁵⁶³⁵ the growth rate between two sensors located at x_j and x_{j+1} with amplitudes A_j and A_{j+1} is estimated as:

$$-\alpha_i = \frac{\ln(A_{j+1}/A_j)}{x_{j+1} - x_j}$$

Figure 5-15 shows growth rates as a function of Re_x for all four α and over a freestream unit Reynolds number sweep. Here, Re_x was determined by using the streamwise station equidistant to each sensor as the length term. Although there is considerable scatter, for a fixed α , the growth rate appears to vary similarly with Re_x , regardless of the freestream unit Re. That is, there does not seem to be a significant dependence on the freestream unit Re. For $\alpha=0$ and 1° , growth rates peak at approximately 45 to 60/m for $Re_x = 2.2$ to 2.8×10^6 and then decrease. For $\alpha=2^\circ$, growth rates peak at about 40/m for $Re_x = 2.7$ to 2.8×10^6 . For $\alpha=4^\circ$, no peak in the growth rates is observed, but a maximum value of approximately 40/m is achieved. The trends in the growth rates again demonstrate the stabilizing influence of increasing the pitch angle.

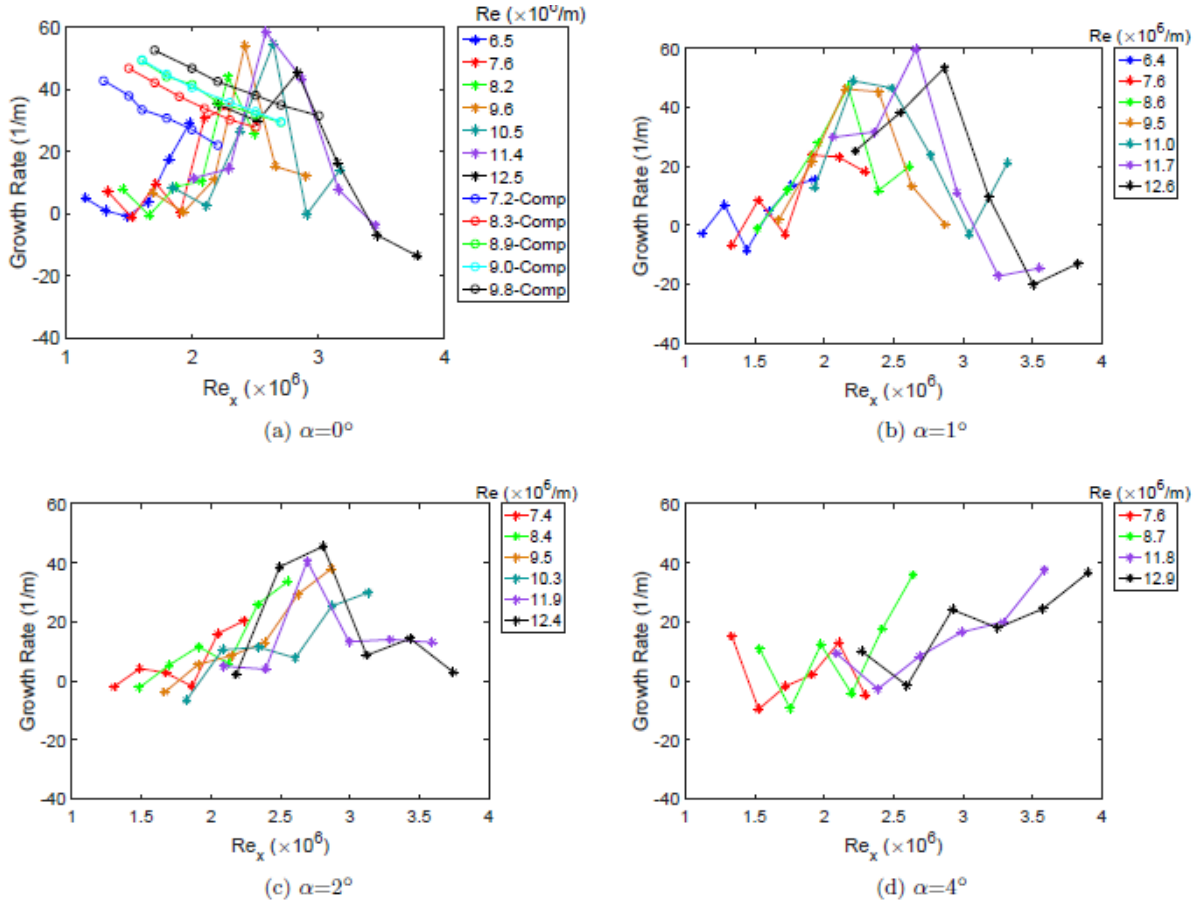


Figure 5-15 Growth rates

A limited number of computed growth rates are plotted with the experimental data in Figure 5-15c for freestream unit Reynolds numbers ranging from 7.2 to $9.8 \times 10^6/m$. Non-dimensional growth rates were extracted from Reference³⁴ and were recast in dimensional form with additional information from the author. These growth rates are for traveling crossflow waves with a frequency of 55 kHz and were found using LST, maximizing the growth rates with respect to the spanwise wavelength along an inviscid streamline that passed near one of the downstream model sensors. Computational data are only for $Re_x = 1.3$ to 3.0 . For $Re_x < 2 \times 10^6$, there is very poor agreement between the experiment and the computations. This is not surprising, however. For these low Re_x values, the traveling crossflow waves were below or near the noise floor of the sensors. It is only for $Re_x > 2 \times 10^6$ that the experimental growth rates depart from near-zero values. For $Re_x = 2.0$ to 3.0×10^6 , the computed growth rates fall roughly within the scatter of the experimental data. However, the computations do not exhibit the same trend and do show a significant effect of the freestream Reynolds number. It should be noted that the pressure sensors on the model do not lie along an inviscid streamline, as do the computations. It seems unlikely that this small difference could account for what appears would be significantly different trends in the growth rates for larger values of Re_x . The cause of the discrepancy is unknown. It is hoped that future computations can help resolve this question.

5.4. Noisy Flow

5.4.1. Zero angle of attack

Previous work at $\alpha=0^\circ$ measured transition of the boundary layer on the elliptic cone in noisy flow. However, no traveling crossflow was observed. Additionally, IR thermography did not detect any stationary crossflow vortices.²³ Additional earlier work with oil flow visualization on the previous model did reveal stationary crossflow vortices in noisy flow.²²

Global heat flux contours are shown in Figure 5-16 for freestream unit Reynolds numbers ranging from $1.2 - 11.6 \times 10^6/\text{m}$. Transition onset on the model centerline appears to take place upstream of the region imaged by the camera for $\text{Re} > 1.2 \times 10^6/\text{m}$, when transition onset is taken to be the streamwise station where the heat flux begins to rise. This finding is congruent with the earlier work of Juliano et. al.³³ This upstream centerline transition also precludes a comparison with tests performed in the NASA Langley Research Center's 20-inch Mach-6 Tunnel.³⁶ Two prominent streaks of high heat flux are observed near ± 8 mm. These streaks are likely transitional or turbulent for $\text{Re} \geq 2.9 \times 10^6/\text{m}$. As Re increases, these streaks merge with the more outboard transition fronts. For only the lowest Re , no transition is seen in the off-centerline regions of the model. For all other Re , boundary layer transition is observed in the regions expected to be dominated by the crossflow instability. As the freestream unit Reynolds number increases, the transition front is observed to move upstream and broaden. In no instance are stationary crossflow vortices observed.

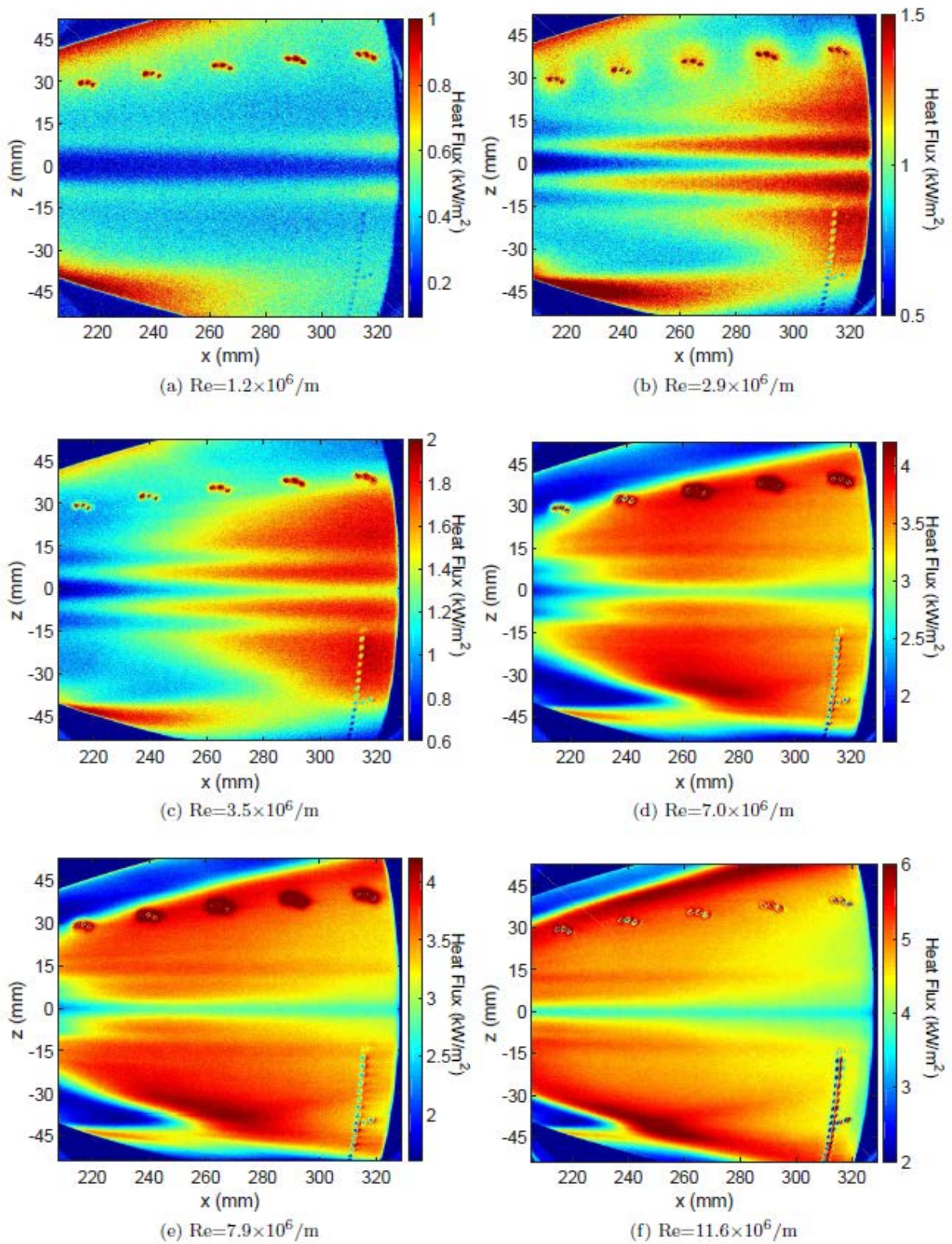


Figure 5-16 Heat flux for increasing Re, noisy flow

Figure 5-17 shows PSDs of pressure data in noisy flow. Figure 5-17a presents PSDs for a freestream unit Reynolds number of $7.0 \times 10^6/\text{m}$ for sensors 1, 4, 7, 13, and 19. The spectrum for sensor 1 at a freestream unit Re of $1.1 \times 10^6/\text{m}$ is also shown as a black dashed line and is included for reference as a known laminar spectrum. For $\text{Re}_x = 7.0 \times 10^6/\text{m}$, it appears that the boundary layer moves from transitional at $\text{Re}_x = 1.1 \times 10^6$ (sensor group 1) to nearly fully turbulent for $\text{Re}_x = 1.9$ and 2.2×10^6 (sensors groups 6 and 7). There is no evidence of the traveling crossflow instability in the spectra. Figure 5-17b displays PSDs for sensor 4 (sensor group 2) for freestream Reynolds numbers ranging from 1.2 to $11.6 \times 10^6/\text{m}$. The spectra indicate that the boundary layer transitions from fully laminar at $\text{Re}_x = 0.2 \times 10^6$ to nearly fully turbulent for $\text{Re}_x = 1.8$ to 2.2×10^6 . Neither the constant freestream Re or constant sensor data show any evidence of the traveling crossflow instability for any sensor at any Reynolds number. The primary instability mechanism remains unknown.

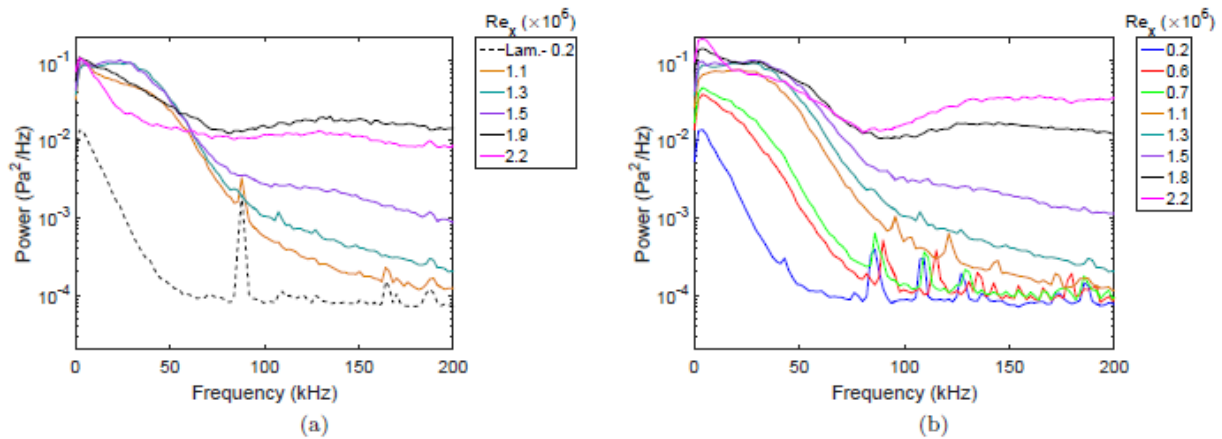


Figure 5-17 PSDs for a) constant $\text{Re}=7.0 \times 10^6/\text{m}$ and b) constant sensor number 4

Re_x could only be matched for 5 conditions for the noisy-tunnel data in Figure 5-17. It appears that the boundary layer disturbance spectra develop very similarly whether the freestream Re or the sensor location is fixed. In both cases, transition onset may be taken to be $\text{Re}_x \approx 1.1 \times 10^6$. This is the lowest value of Re_x for which the spectra do not relax back to the electronic noise levels at high frequencies. For quiet flow, Re_{tr} as determined by the pressure spectra was approximately 2.6×10^6 . Thus, reducing the freestream noise levels increased Re_{tr} in the instrumented region by a factor of 2.4.

5.4.2. Non-zero Angle of Attack

It was hoped that testing in noisy flow at non-zero angle of attack might help identify the primary instability mechanism under noisy flow. In addition to the 0° condition, the model was also tested for a limited range of Re at 1° , 2° , and 4° .

Figure 5-18a-d present global heat flux contours for $\text{Re} = 7.9 \times 10^6/\text{m}$ for $\alpha = 0^\circ$, 1° , 2° , and 4° , respectively. Figure 5-18e shows centerline heat flux profiles normalized by the mean heat flux. Figure 5-18f presents spanwise heat flux profiles at $x = 213$ mm. The heat flux contours for $\alpha = 0^\circ$ and 1° look very similar, with most of the model acreage being turbulent. The relatively lower heat fluxes observed along the centerline are likely due to the thick boundary layer caused

by the fluid driven by the crossflow pressure gradient. For $\alpha = 2^\circ$, transition appears to be the most upstream on the centerline, and spreads transversely downstream. The maximum heat flux also increases, due to the thinner boundary layer relative to the lower α cases. The off-centerline (Region III) transition front is observed to move downstream. For $\alpha = 4^\circ$, centerline transition remains upstream of the viewing area. The maximum heat flux increases again as the boundary layer thins further. Off-centerline transition moves even farther downstream. The spanwise heat flux profiles demonstrate the observations both on the centerline and away from it. As α increases, the heat flux near $z=0$ also increases. Conversely, the heat flux from $z = \pm 15$ to ± 30 mm decreases with increasing α . Although stationary crossflow vortices are not observed for in any of these images, the movement of the off-centerline transition front is instructive. Since this transition is in the region of the model expected to be dominated by the crossflow instability, and because transition is delayed with decreased crossflow (i.e. increased α), it may be surmised that this off-centerline transition is at least related to the crossflow instability, if not directly due to its breakdown.

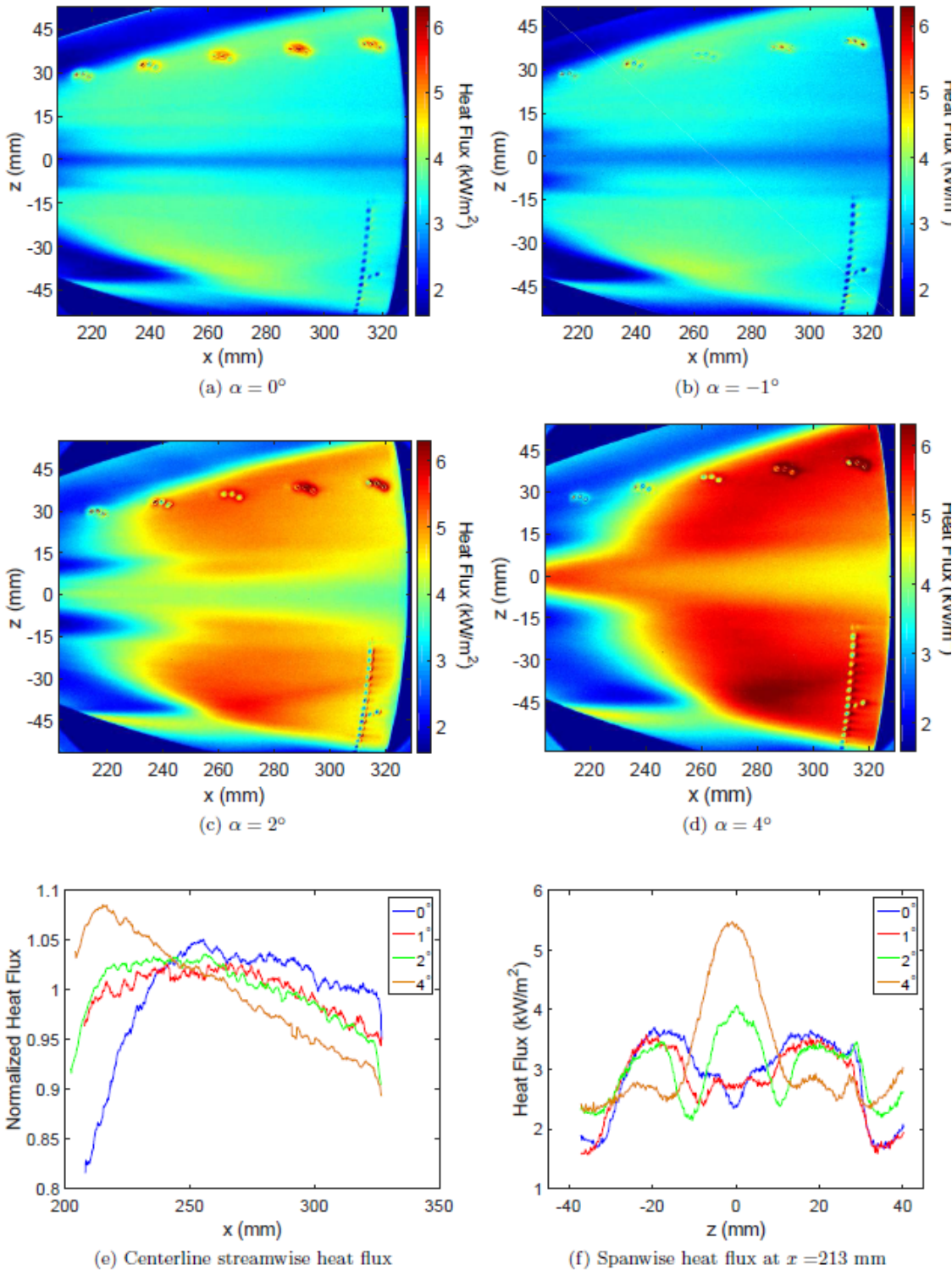


Figure 5-18 Heat flux for changing angle of attack, noisy flow, $\text{Re}=7.9\times10^6/\text{m}$

It may be reasonable to assume that the boundary layer along the model centerline has transitioned to full turbulence where the heat flux begins to drop. For $\alpha = 0^\circ$, transition is

complete by approximately 250 mm. For $\alpha = 1^\circ$ and 2° , the peak heat flux is not as well defined. In each case, the heat flux plateaus for a considerable distance. The beginning of the plateaus is approximately $x=240$ and 230 mm, respectively. For $\alpha = 4^\circ$, the peak moves upstream to about 215 mm. This forward progression of the end of transition implies that transition onset along the centerline also moves upstream with increasing α .

Figure 5-19a shows PSDs for sensor 9 and $Re = 7.9 \times 10^6/m$ for $\alpha = 0^\circ, 1^\circ, 2^\circ$, and 4° . Sensor 9 is the most downstream sensor of the most upstream sensor group visible in Figure 5-18. For $\alpha = 0^\circ$, the boundary layer at sensor 9 is almost fully turbulent. The spectrum for $\alpha = 1^\circ$ looks nearly the same. For $\alpha = 2^\circ$ and 4° , the power levels for 0–50 kHz increase somewhat and decrease for frequencies from 50 to 200 kHz. Although it appears that the boundary layer may be transitional and laminar for $\alpha = 2^\circ$ and 4° , respectively, the root mean square pressure amplitude for all non-zero α is greater than that for $\alpha = 0^\circ$. This may be due to the fact that as α increases, so does the static pressure. Figure 5-19b shows the same data, however the pressure histories were normalized by the measured mean static pressure in an attempt to remove the effect of the α -induced increased pressure. This normalization collapses the spectra for positive α in the 0 to 50 kHz range. The spectrum for $\alpha = 0^\circ$ has a higher power for all frequencies. This behavior is further evidence that reducing the crossflow stabilizes the boundary layer, even though none of the spectra indicate the presence of the traveling crossflow instability. This is consistent with past observations for $\alpha = 0^\circ$, which did not display a crossflow peak under noisy conditions.

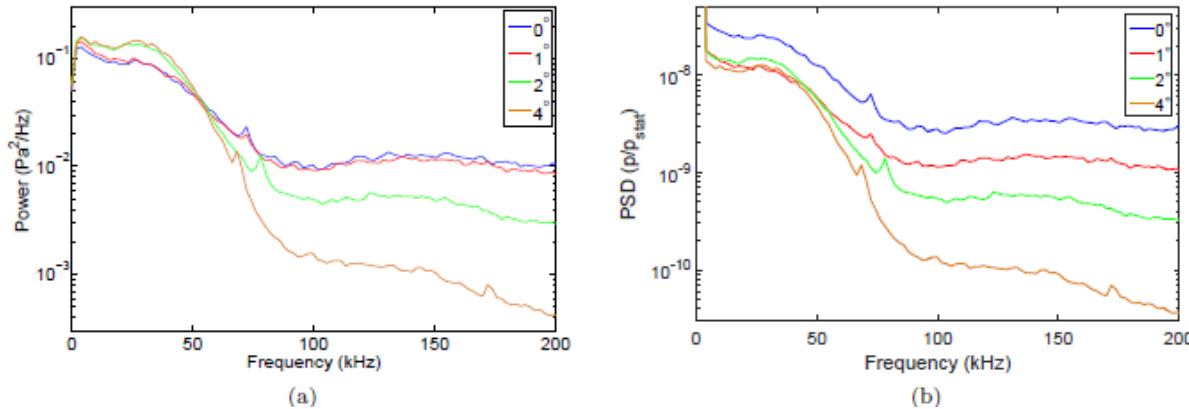


Figure 5-19 PSD for sensor 9 and $\alpha = 0^\circ, 1^\circ, 2^\circ$, and 4° . $Re = 7.9 \times 10^6/m$. (a) Dimensional (b) Non-dimensional

5.5. Summary and Conclusions

A 38.1% scale model of the 2:1 elliptic cone HIFiRE-5 geometry is tested in both the quiet and noisy flows of the BAM6QT at 0° , 1° , 2° , and 4° angles of attack. IR thermography is used to detect stationary crossflow vortices and transition. Pressure sensors that are flush with the model surface are used to detect traveling crossflow waves and transition. For quiet flow and $\alpha = 0^\circ$, transition in the crossflow-dominated region of the model is found to be described by Re_{tr} and was a function of z only, ranging from 2.8 to 3.7×10^6 . Thus, $Re_{tr} = 2.8 \times 10^6$ is taken as a conservative estimate of transition for this model with $\alpha = 0^\circ$ in the quiet flow of this facility. Traveling crossflow instability waves are measured over much of the instrumented portion of the model. Wave properties can be determined for $Re_x \approx 1.9$ to 2.5×10^6 , 68 to 90% of Re_{tr} in Region III. The wave angle is found to increase with increasing Re_x while the phase speed decreases. Varying the freestream Reynolds number and considering a constant streamwise station is found to be a reasonable surrogate for examining the spatial development of traveling crossflow waves for a constant freestream Reynolds number. When stationary crossflow vortices are fully laminar, there appears to be little dependence of traveling crossflow waves on the proximity to a particular stationary vortex. When a nearby stationary vortex becomes transitional or turbulent, the spectrum from the closest sensor changes significantly both qualitatively and in the frequency of the spectral peak. Evidently, a transitional or turbulent vortex modifies the traveling crossflow instability.

In quiet flow, pitching the model has several important effects. Both stationary and traveling crossflow instabilities are suppressed, particularly at $\alpha = 4^\circ$ condition. In Region III, as α is increased from 0° to 2° , Re_{tr} for $|z| < 32$ mm is increased by 30%. Outboard of $z = \pm 32$ mm, there is no observed delay in transition. Neither the wave angle nor the phase speed of traveling crossflow waves exhibit a dependency on α . Changes in N factor for traveling crossflow, calculated from RMS pressures, are approximately 3.5 for $\alpha = 0^\circ$ and 1° , and approximately 3 for $\alpha = 2^\circ$ and 4° . This yields growth maximum growth rates of approximately 60, 60, 45, and $40/m$ for $\alpha = 0^\circ$, 1° , 2° , and 4° , respectively. Little to no dependence on the freestream Reynolds number is observed, suggesting the flow over the instrumented portion of the cone is self-similar and unaffected by the nose bluntness. Computations for $\alpha = 0^\circ$ show reasonable agreement with growth rates for values of Re_x where traveling crossflow waves were measured. However, the computational and experimental trends in growth rate show significant disagreement. The cause of the disagreement is currently unknown.

In noisy flow for $\alpha = 0^\circ$, IR measurements show a broad off-centerline transition front in the region of the model where transition was expected to be dominated by the crossflow instability. However, there is no evidence of stationary crossflow vortices. Concurrent pressure measurements show the boundary layer transitioning from laminar to turbulent as the freestream Reynolds number increases, but there is no evidence of the traveling crossflow instability. When the model is set at $\alpha = 1^\circ - 4^\circ$, off-centerline transition is observed to move downstream. Stationary crossflow vortices are not observed. PSDs of pressure data show the suppression of traveling crossflow waves with increasing α . The downstream movement of off-centerline transition with decreased crossflow (i.e. increased α) suggests that transition in noisy flow may still be influenced by the crossflow instability, even if no crossflow instability is observed.

6. HIFiRE-5b Post Flight Testing

All data were obtained in the Boeing/AFOSR Mach-6 Quiet Tunnel (BAM6QT) at Purdue University. At the time these experiments were performed, the maximum unit Reynolds number (Re) for which quiet flow could be realized was approximately $9.7 \times 10^6/m$.

Previous ground tests on the HIFiRE-5 geometry revealed a number of interesting features as well as several limitations of both the experimental methods and model.^{47,48} For noisy and quiet flows, stationary crossflow vortices were readily detected with oil flow visualization. However, TSP did not show any vortices in noisy flow, and only revealed vortices in quiet flow for a subset of the Reynolds numbers for which they were detected with the oil flow.³⁸ In an attempt to study traveling crossflow waves in both conventional “noisy” and quiet freestream environments, previous experiments were performed on the HIFiRE-5 elliptic cone geometry in Purdue University’s BAM6QT and Texas A&M University’s ACE hypersonic wind tunnels. Traveling crossflow waves and transition were clearly measured in the quiet freestream environment. Since the traveling mode is conventionally thought to dominate crossflow transition in noisy environments, traveling waves were also expected in noisy flow. However, there was no evidence of traveling crossflow waves with a noisy freestream, even though the spectra of the surface pressure signals showed an expected progression from laminar to turbulent as the Reynolds number was increased.³⁸ It was thought that perhaps the very noisy freestream environment of the BAM6QT when run noisy caused transition apart from the traveling crossflow mode. Thus, the model was also tested in ACE at similar freestream temperatures and pressures, but with lower noise levels. Again, although transition was observed, the traveling crossflow instability was not.⁴⁷

The model is made of solid 15-5PH H-1100 stainless steel from the nose to $x = 150.3$ mm. The root-mean-square (RMS) surface finish of the steel is $0.4 \mu\text{m}$ ($16\mu\text{in}$). Downstream of $x = 150.3$ mm, the model is a shell made of unfilled PEEK, a high emissivity, high temperature plastic. The surface-normal thickness of the PEEK is 10.0 mm, except along the leading edges where it is thicker. Since the shell has a high emissivity and low thermal conductivity, it is well-suited for IR thermography. The use of a shell, rather than a solid model, also facilitates the installation of surface-flush pressure sensors in many locations. The instrumented shell has 28 sensor holes in the region of the model where the crossflow instability is expected to be significant. For the experiments reported here, 26 of the holes were populated with pressure transducers. Sensor holes that did not have sensors installed were plugged with nylon rods that were flush with the model surface. There are 7 groups of 3 closely-spaced sensors in one quadrant of the model. These groups lie 25.4 mm apart along what is a surface streamline for the model when angle-of-attack and yaw are 0° . The close spacing of the sensors in each group allows the phase speed and wave angle of traveling crossflow waves to be determined at that location. Near the most downstream sensor group, there are four additional sensors located at the same streamwise station. These sensors are used to examine the spanwise coherence of traveling crossflow waves. Ten additional pressure sensors were installed in two spanwise arrays near the model centerline. These sensors are used to examine the flow under and near the bulging boundary layer along the model centerline.

Kulite XCQ-062-15A and XCE-062-15A pressure transducers with A screens were mounted flush with the model surface in the crossflow-dominated region of the model to detect traveling

crossflow waves. The Kulite sensors are mechanically stopped at about 100 kPa so that they can survive exposure to high pressures but still maintain the sensitivity of a 100 kPa full-scale sensor. These sensors typically have flat frequency response up to about 30 to 40% of their roughly 270 to 285 kHz resonant frequency.²⁷ PCB Piezotronics 132A31 sensors were installed in the near-centerline instrumentation holes.

Table 6-1 lists the locations of the sensors relative to the nosetip. Here, x and z are the streamwise and spanwise coordinates, respectively, with the origin at the model nose. Figure 6-1 shows a sketch of the model and sensor locations.

Table 6-1 Instrumentation Locations

Sensor	x (mm)	z (mm)	Sensor	x (mm)	z (mm)	Sensor	x (mm)	z (mm)
K1	176.8	30.2	K13	269.5	37.1	K25	320.5	44.0
K2	179.2	30.2	K14	271.9	37.1	K26	315.8	-39.8
K3	181.6	29.6	K15	274.2	36.5	PCB1	230.0	7.8
K4	200.0	32.1	K16	292.6	38.5	PCB2	230.0	3.9
K5	202.4	32.1	K17	295.0	38.5	PCB3	230.0	0.0
K6	204.7	31.5	K18	297.3	37.9	PCB4	230.0	-3.9
K7	223.1	33.9	K19	315.8	39.8	PCB5	230.0	-7.8
K8	225.5	33.9	K20	318.2	39.8	PCB6	270.0	7.8
K9	227.8	33.3	K21	320.5	39.2	PCB7	270.0	3.9
K10	246.3	35.5	K22	320.5	34.4	PCB8	270.0	0.0
K11	248.7	35.5	K23	320.5	36.8	PCB9	270.0	-3.9
K12	251.0	35.0	K24	320.5	41.6	PCB10	270.0	-7.8

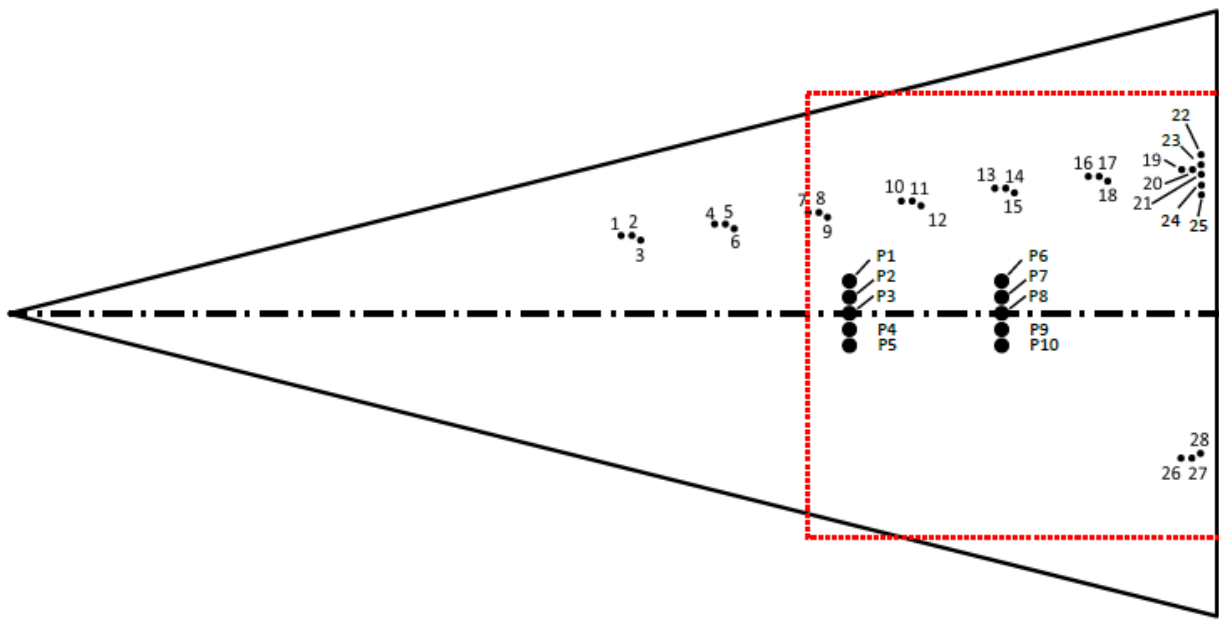


Figure 6-1 Schematic of pressure-sensor locations. The dashed red line denotes approximate field of view of IR camera.

In addition to the pressure transducers, the PEEK shell of the model was imaged with a Xenics Onca IR camera. The camera is a mid-wave, 14-bit camera which is sensitive to IR radiation from 3.7 to 4.8 μm . The sensing array is 640 x 512 pixels. Images were acquired at about 50 Hz.

Using a subroutine called QCALC, IR data were reduced to heat flux by solving the transient one-dimensional heat equation on a pixel-by-pixel basis. QCALC uses second order Euler-explicit finite differences to solve for the temperature distribution through the model. Heat flux is calculated from a second-order approximation of the derivative of the temperature profile at the surface.⁴⁴ The measured surface temperature was used as one boundary condition. An adiabatic backface temperature was used as the other boundary condition. A constant initial temperature was assumed through the PEEK. The thermal conductivity, density, and specific heat of PEEK were obtained from the manufacturer and are 0.29 W/(m·K), 1300 kg/m³, and 1026 J/(kg·K), respectively. The size of the model precluded a precise measurement of its emissivity. A skilled researcher estimated the emissivity to be 0.88 to 0.93, depending on how diffuse the reflection from the model is. A future project is to procure a smaller sample of PEEK for a much more accurate determination of the actual model emissivity. For the results presented here, the emissivity was taken to be 0.91. Heat fluxes are presented as scaled Stanton numbers of the form:

$$St = \frac{\dot{q}''}{\rho_\infty U_\infty c_p (T_0 - T_w)} \sqrt{Re_x}$$

Based on previous experiments with the HIFiRE-5 geometry in the BAM6QT, it is known that crossflow transition in quiet flow with the model oriented at $(\alpha, \beta) = (0^\circ, 0^\circ)$ is only observed for

Re greater than $10.0 \times 10^6/m$. The maximum Re providing quiet flow during the experiments reported in this paper was about $9.6 \times 10^6/m$. With respect to non-zero α , all but one of the attitudes tested had the instrumented side of the model on the lee side. It was thought that these orientations would serve to weaken the shock along the minor axis, thus increasing crossflow and destabilizing the boundary layer. Had the model been tested at positive α , the boundary layer would have been more stable to crossflow, and no transition would have been observed. The various combinations of α and β that were tested are shown in Table 6-2. Negative values of α indicate that the instrumented side of the model is leeward with respect to the angle of attack.

Table 6-2 Model Attitudes Tested

		α (°)			
		-2	-1	0	2
β (°)	2	x		x	
	1			x	
	0	x	x	x	
	-1			x	
	-2	x		x	x

Positive values of β indicate that the heavily-instrumented quadrant of the model is windward with respect to the angle of yaw. The arrows in Figure 6-2 depict the direction of the non-streamwise component of the freestream velocity with respect to the model. The direction is shown looking upstream at the back of the model. The highly-instrumented quadrant of the model is marked in red.

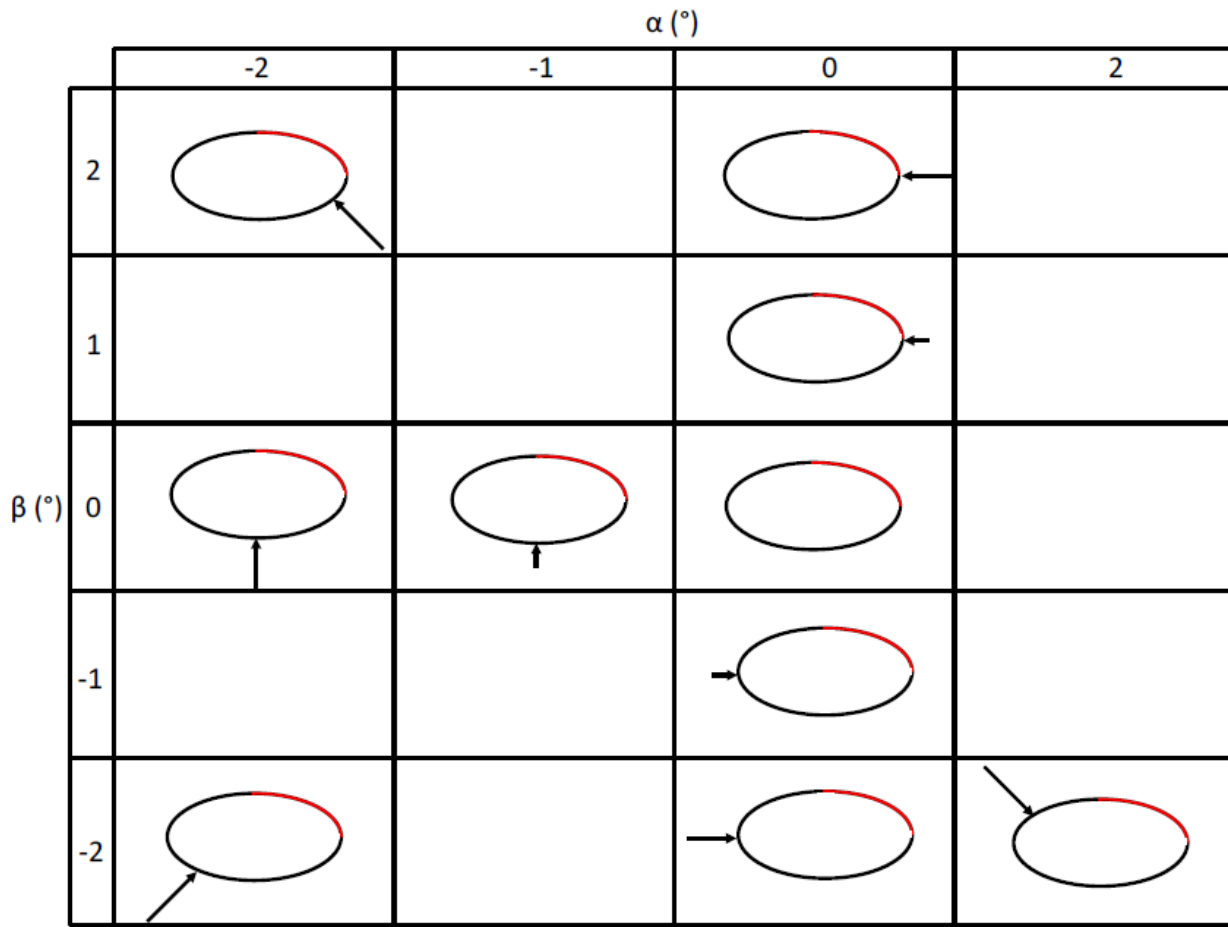


Figure 6-2 Model orientation, looking upstream at the back of the model. Instrumented quadrant is shown in red. The arrows depict the direction of the component of the freestream velocity perpendicular to the model longitudinal axis.

For all of the data presented, T_w/T_0 was approximately 0.7, where T_w is the wall temperature and T_0 is the stagnation temperature. The Mach number for quiet conditions is 6.0. This reduces to about 5.8 for noisy conditions. Comparisons are made to flight data. However, T_w/T_0 for flight was approximately 0.1, and the Mach number was 7.7 to 7.9. These differences notwithstanding, it is of interest to compare trends in transition. Additional analysis of transition on the flight vehicle is included in Reference 3.

In order to examine the effect of α on boundary-layer transition, β was held at 0° while α was set to 0° , -1° , and -2° . Surface heat transfer contours are shown in Figure 6-3. In all cases, enhanced heat fluxes are seen for $z < -35$ mm. After these experiments were completed, it was determined that the lead wires for an array of hot film sensors on the nozzle wall generate a disturbance that impinges on the lower portion of the model. Thus, data for $z < -35$ mm are ignored.

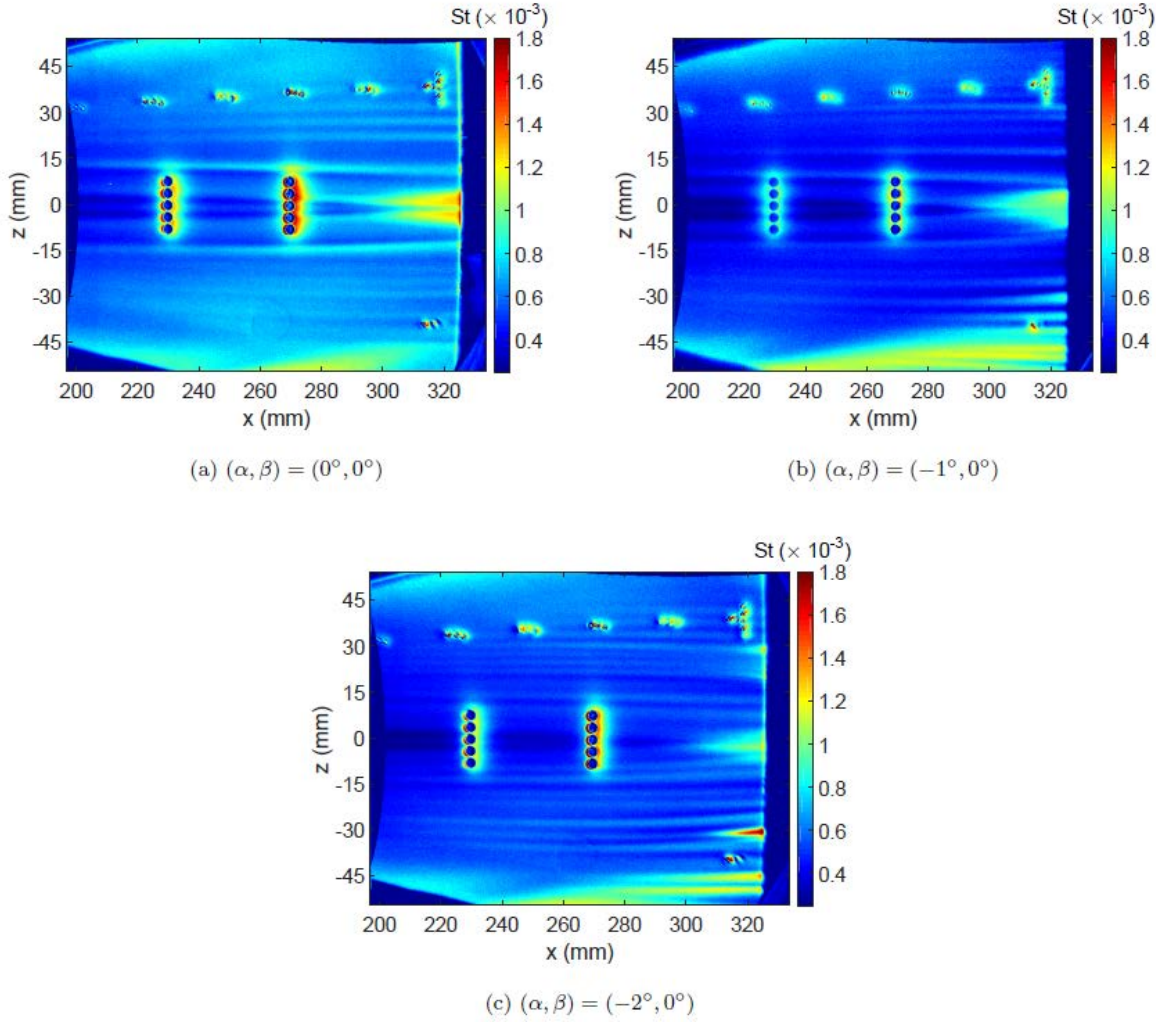


Figure 6-3 □sweep, quiet flow. $\text{Re}=9.6 \times 10^6/\text{m}$

For $(\alpha, \beta) = (0^\circ, 0^\circ)$, several interesting features are observed. Boundary layer transition is not seen in the crossflow-dominated portion of the model. Several streamwise-oriented streaks are visible. These are due to stationary crossflow vortices. Transition is observed near the model centerline near $x=290$ mm. Additionally, two prominent streaks, located just outboard of the PCB arrays near $x = \pm 13$ mm, are observed. These streaks are thought to be due to a localized thinning of the boundary layer outboard of the thick, lofted boundary layer along the model centerline. The boundary layer along the centerline is highly thickened due to the inflow of fluid driven by the spanwise pressure gradient (see Figure 5.1 of Reference 11 and Figure 6 of Reference 6). As α is decreased to -1° , the boundary layer along one stationary crossflow vortex at $z = -30$ mm may transition. The boundary layer near the centerline still transitions near the back of the cone, but the transition location has moved downstream. The near-centerline streaks are considerably less prominent. For $\alpha=-2^\circ$, the crossflow vortex near $z = -30$ mm is clearly turbulent. The crossflow vortex near $z = 30$ mm may also be transitional near the back of the cone. Near-centerline transition is again observed, but has moved even farther downstream. The near-centerline streaks are almost indistinguishable from the crossflow vortices farther outboard.

Evidently, the increased crossflow induced by the reduced angle of attack serves to alter the lofted centerline boundary layer in such a way that the streaks are diminished. Perhaps the near-centerline vortices are lifted farther from the surface by the increased mass flux toward the centerline.

A simple threshold method was used to estimate the location of transition on the model. Transition Reynolds numbers (Re_{tr}), where the streamwise transition location is used as the length parameter, are shown in Figure 6-4. The spanwise ordinate has been replaced by ϕ , the azimuthal angle around the cone. Using the same notation as what has been used to present the flight data,¹ $\phi = 0^\circ$ is the model centerline, while $\phi = 90^\circ$ and 270° correspond to the top and bottom leading edges of the model, respectively.

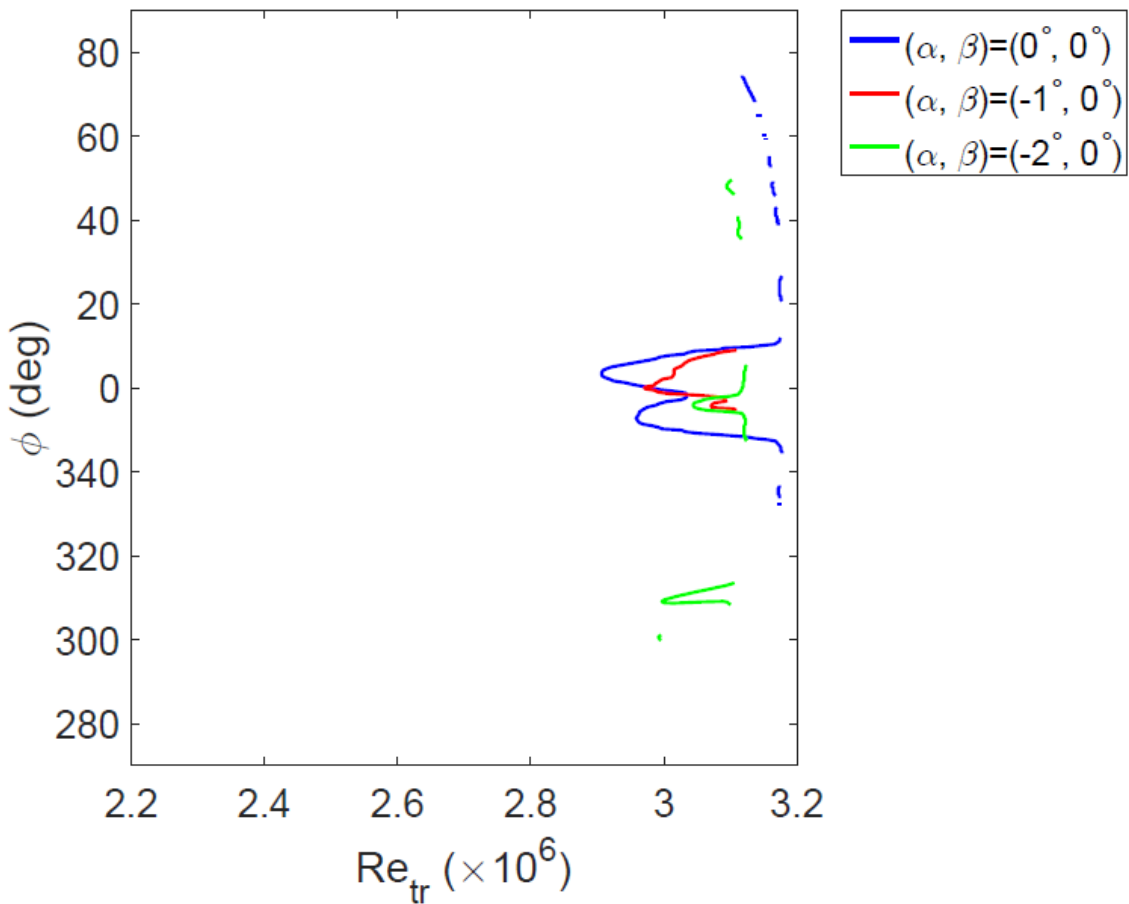


Figure 6-4 Re_{tr} for \square sweep, quiet flow, $Re=9.6\times 10^6/m$

It is clear from Figure 6-4 that decreased α moves crossflow transition upstream and moves near-centerline transition downstream. The enhanced crossflow transition is explained by the fact that the shock along the model centerline is weakened as α is reduced. This serves to increase the spanwise pressure gradient, leading to greater crossflow and a more unstable boundary layer. The exact instability mechanism(s) near the centerline are unknown. Thus, it is unknown why

decreased α leads to a slight delay of transition in that region, with the minimum Retr increasing by about 3% from $2.9\text{--}3.0 \times 10^6$. Flight centerline transition occurred at $Re_x=4.5 \times 10^6$, approximately 50% greater than the $(\alpha, \beta) = (0^\circ, 0^\circ)$ quiet-tunnel data shown here.¹ This difference may be due to the significantly colder wall in flight than in the ground test, especially if the boundary layer near the centerline is unstable to the second mode. In quiet flow, boundary layer transition in the near-centerline region is fairly insensitive to changes in α . It is likely that transition in the crossflow region is also fairly insensitive to changes in α , but this cannot be concluded from these data clear crossflow transition was not observed for $\alpha=0^\circ$ or -1° . Transition for the HIFiRE-5b flight vehicle was also relatively insensitive to α .¹

Similar measurements were also made in noisy flow in order to see if the same trend with α would be observed. Heat flux contours with noisy flow are shown in Figure 6-5. In this case, the freestream Re was reduced to $Re=3.1 \times 10^6/\text{m}$ in order for transition to be observed on the imaged portion of the model. For a noisy run at $Re=9.6 \times 10^6/\text{m}$, all but the most outboard regions of the model would have been fully turbulent. Several interesting features are evident. As α decreases, the spanwise extent of the off-centerline turbulent region decreases. Additionally, two streaks of higher heat flux are seen just outboard of the centerline for $\alpha=0^\circ$. When α decreases to -1° , the streaks become less pronounced. For $\alpha=-2^\circ$, they are no longer visible.

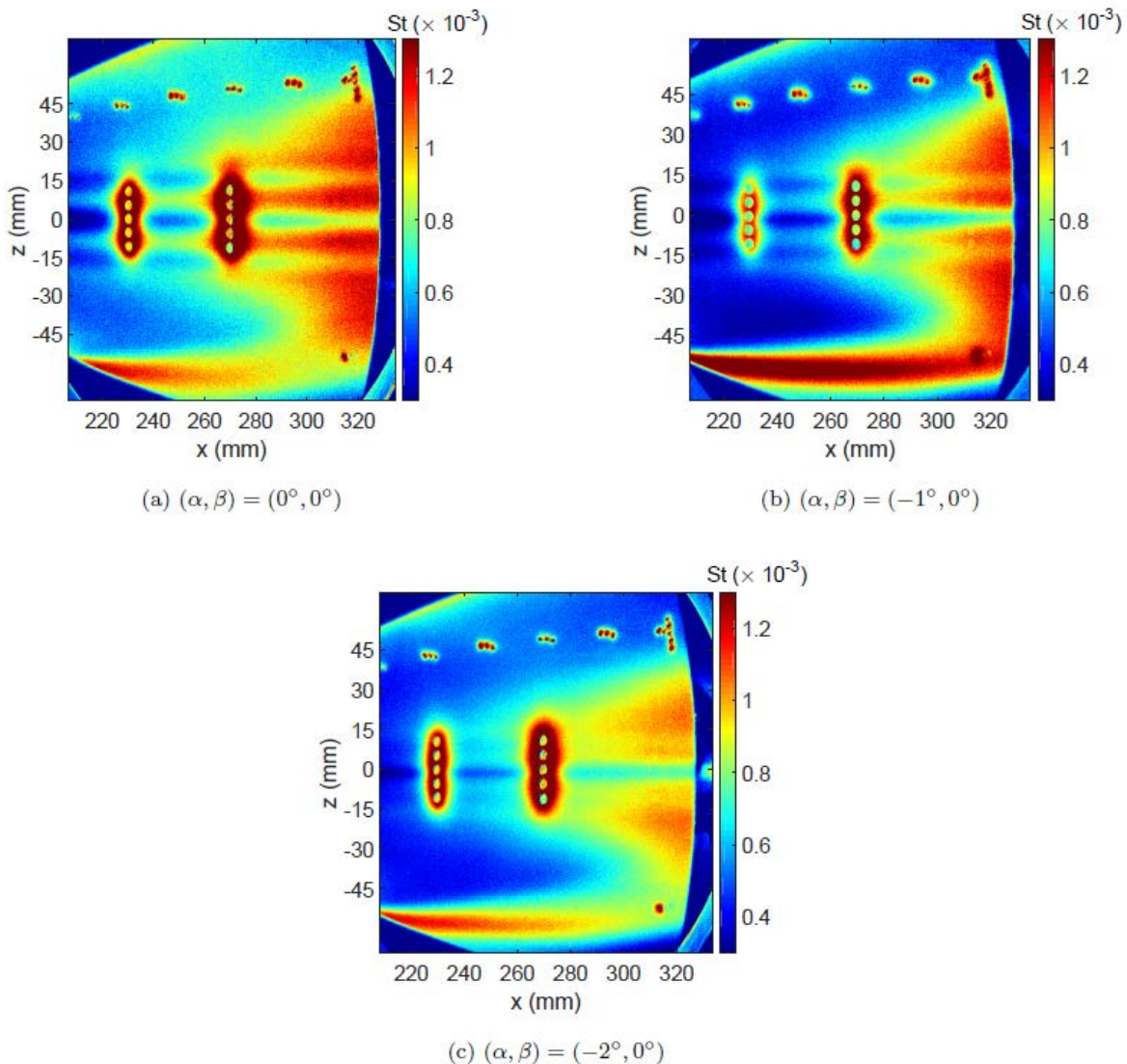


Figure 6-5 □sweep, noisy flow. $\text{Re}=3.1\times 10^6/\text{m}$

A threshold value was again used to extract approximate transition locations. This procedure for the noisy tunnel runs is made more challenging due to the fact that transition occurs at locations very near the PCB arrays. The PCB sensors serve to heat the PEEK model, resulting in a non-physical apparent high heat flux around the sensors. Nevertheless, transition Reynolds numbers are shown in Figure 6-6 for reference. An inboard and, perhaps downstream, movement of the transition front in the crossflow region is observed as α is reduced. This is the opposite trend of what was expected and what was observed in quiet flow. This is also unexpected based on previous noisy-flow results for positive values of α .⁵ A more robust transition-location criterion will need to be developed to ascertain if transition in noisy flow is truly delayed by reducing α to negative values. For the α sweep in quiet flow, Re_{tr} was always greater than 2.9×10^6 . In the noisy flow α sweep, Re_{tr} ranged from 0.7 to 1.0×10^6 , a reduction of at least 66%.

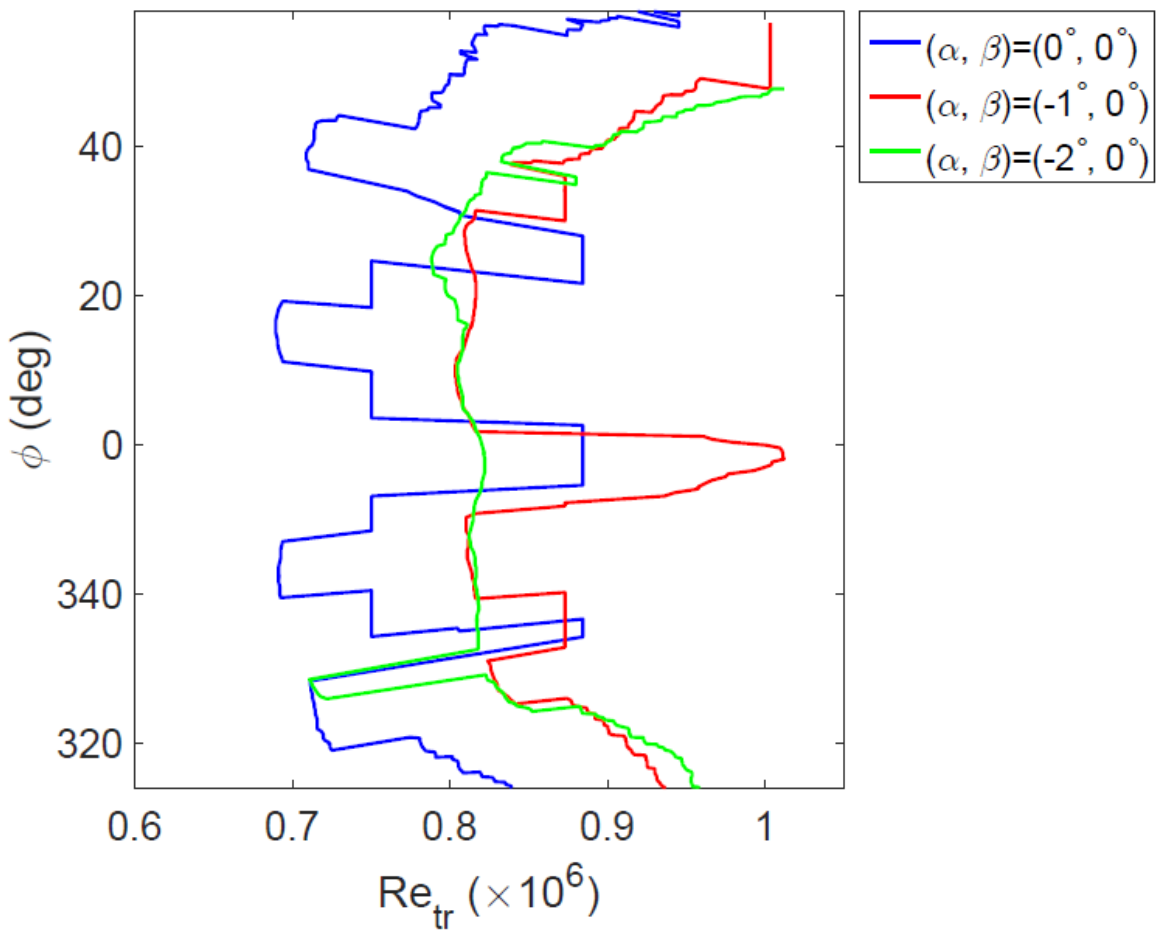


Figure 6-6 Transition Re for \square sweep, noisy flow, $Re=3.1\times 10^6/m$

The model was also oriented so that the angle of attack was held constant at $\alpha=0^\circ$, while the angle of yaw was swept from $\beta=2^\circ$ to -2° . Heat flux contours with quiet flow are shown in Figure 6-7 for $Re=9.6\times 10^6/m$. Several interesting trends are observed as the model is moved through the range of β . As previously discussed, for $(\alpha, \beta) = (0^\circ, 0^\circ)$, the boundary layer along the cone centerline is highly thickened and has been described as mushroom-like for large enough Re . This feature is manifested as two streamwise streaks of low heat flux just outboard of the centerline that appear to transition near $x=290$ mm in Figure 6-7c. For non-zero values of β , it was anticipated that this thickening feature would still exist, but that it would be translated to different locations on the model as the spanwise pressure gradient was altered. In Figure 6-7, the thickened part of the boundary layer is observed to shift to the lee side of the cone. For example, for $\beta=2^\circ$ and 1° (Figure 6-7a and b), the streamwise streaks of low heat flux are observed outboard of the PCB array and centered on the two lowest PCB sensors, respectively. Similar behavior is observed for negative values of β , with the streaks of low heat flux being shifted onto the sensor side (lee side) of the model. The streaks of low heat flux shift approximately 35 mm at the back of the cone for a 4° change in β . A qualitatively similar translation of the boundary layer bulge was seen in computations for flight conditions.³³ Additionally, of the two turbulent streaks associated with transition near the low heat flux streaks, the most windward streak is generally

observed to transition farther upstream than the most leeward streak. This is most readily seen in Figure 6-8a, where transition Reynolds numbers are shown for transition related to the low heat flux streaks. Transition related to crossflow has been manually removed for clarity. The lowest value of Re_{tr} varies by a small amount, ranging from 2.8 to 3.0×10^6 . Evidently, the yaw angle serves mainly to alter the azimuthal location of transition in the boundary layer bulge regions without significantly changing the stability there.

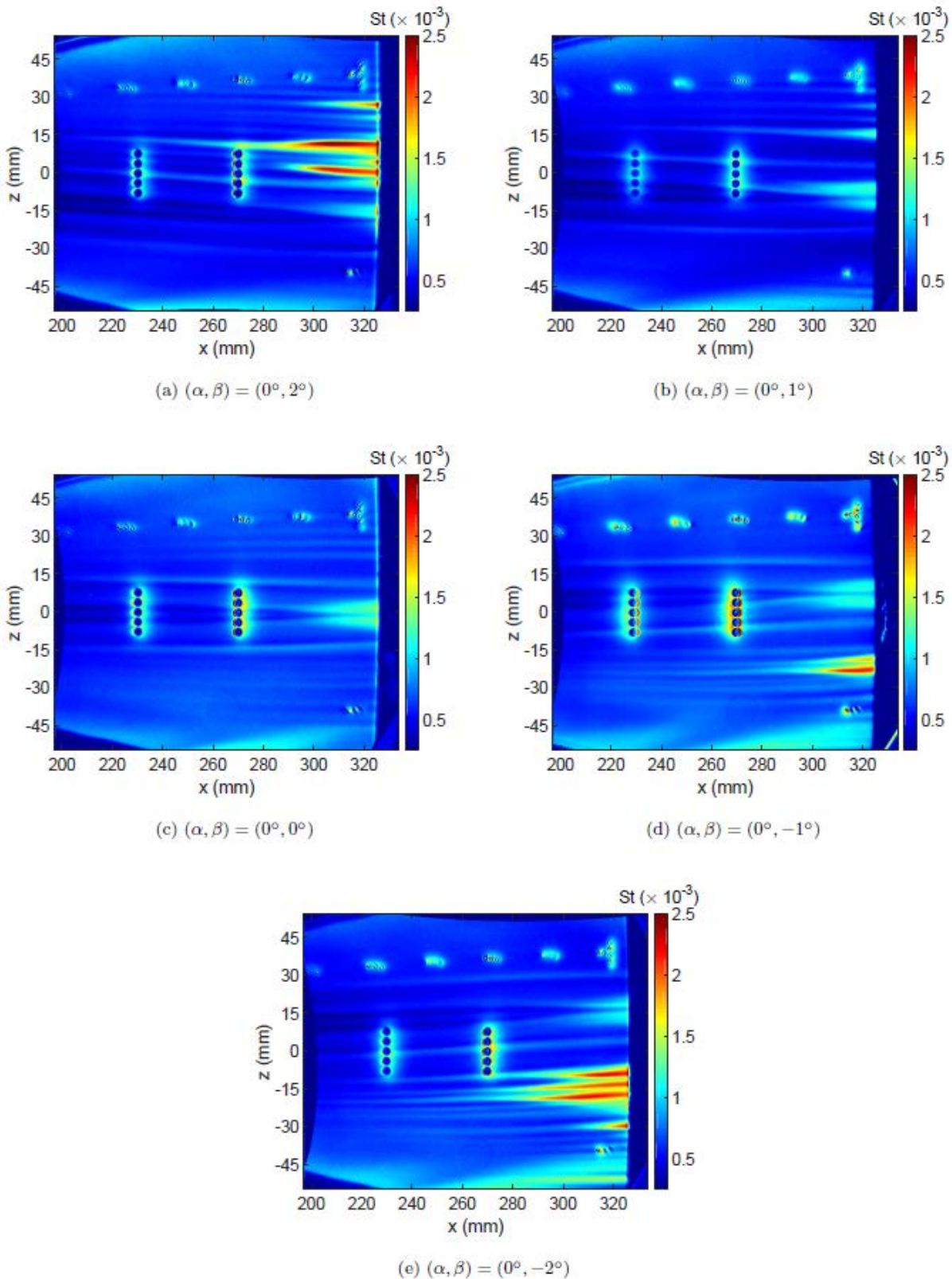
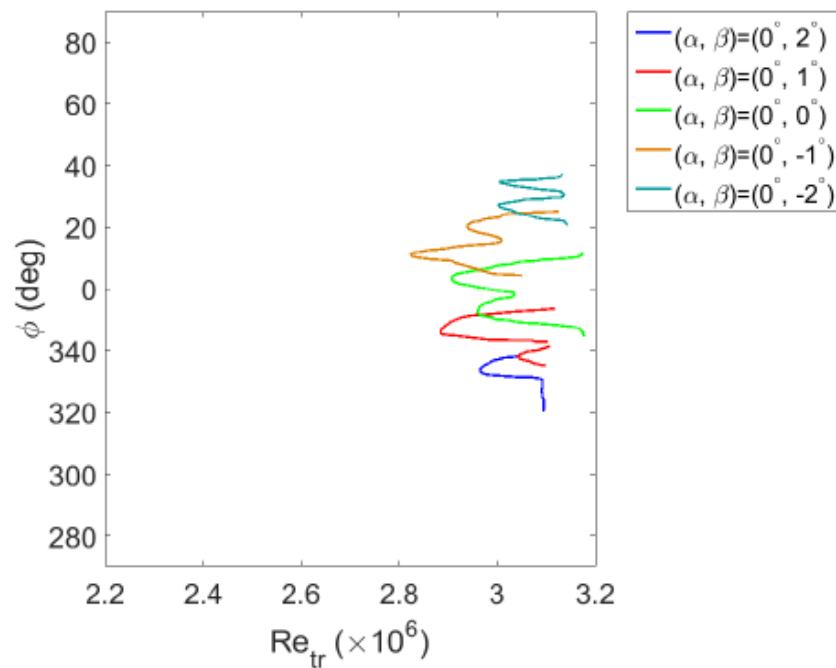
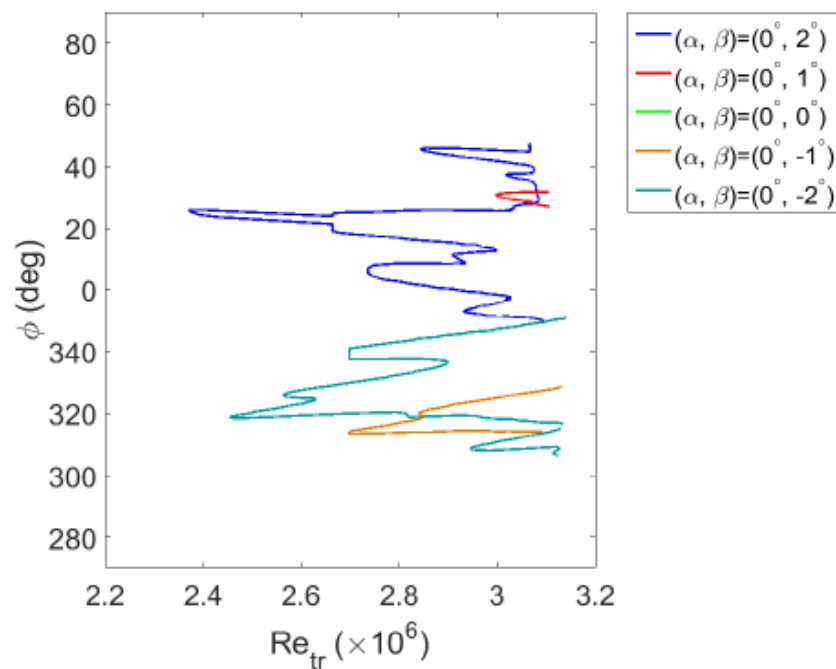


Figure 6-7 \square sweep, quiet flow, $Re=9.6\times 10^6/m$



(a) Low heat flux streaks



(b) Crossflow

Figure 6-8 Transition Reynolds number for \square sweep, quiet flow, $Re=9.6\times10^6/m$

Transition due to the crossflow instability is significantly affected by the yaw angle in quiet flow. As previously discussed, no crossflow transition is observed for $(\alpha, \beta) = (0^\circ, 0^\circ)$. This means that Re_{tr} is greater than 3.2×10^6 . Crossflow transition is observed on the wind side along one or two stationary crossflow vortices for $\beta = \pm 1^\circ$. For $\beta = \pm 2^\circ$, more laminar stationary vortices are observed as well as transition along several of them. Figure 6-8b shows Re_{tr} for crossflow transition. When compared to the $\beta = 0^\circ$ orientation, a yaw angle of only 2° is sufficient to reduce the minimum Re_{tr} from greater than 3.2×10^6 to 2.4×10^6 , a decrease of more than 25%. The minimum crossflow Re_{tr} is increased by 20% when changing β from 1° to 2° . In all cases, the windward side is destabilized with respect to both the lee side and the $\beta = 0^\circ$ orientation. This is likely due to the increased pressure on the windward leading edge giving rise to increased crossflow. This is the same trend that is seen in the HIFIRe-5b flight data. For the flight vehicle, crossflow transition Reynolds numbers were as low as 3.9×10^6 for $\beta = 0.9^\circ$ and were increased to 6.6×10^6 for $\beta = -0.6^\circ$ at the $\varphi = 45^\circ$ location.¹ For regions outboard of the low heat flux streaks on the lee side, the presence of stationary crossflow vortices is greatly diminished.

The model was also swept through the range of yaw angles in noisy flow for $Re = 3.1 \times 10^6/m$. Heat flux contours are shown in Figure 6-9. Meaningful transition locations could not be extracted using the threshold method due to the proximity of transition to the non-physical high heating rates near the PCB sensors. For $(\alpha, \beta) = (0^\circ, 0^\circ)$, near-centerline transition is seen as two streaks of elevated heat flux near $z = \pm 8$ mm. This transition phenomenon is adjacent to the thick, lofted centerline boundary layer. As the model is yawed, these streaks shift away from the centerline onto the lee side of the model, as is observed in quiet flow. In all cases, it appears that the streaks transition upstream of the area of the model imaged by the IR camera. In the regions of the model dominated by the crossflow instability in quiet flow, the transition front is observed to shift inboard and move upstream on the windward half of the model when compared to the $(\alpha, \beta) = (0^\circ, 0^\circ)$ case. On the lee side, the transition front is significantly reduced in spanwise extent. Interestingly, the most upstream transition location on the lee side appears to be at a similar location to that on the wind side. The trends are similar to those observed in quiet flow. However, the $(\alpha, \beta) = (0^\circ, 0^\circ)$ case for quiet flow did not transition in the crossflow region, so a comparison cannot be made of the crossflow transition relative to the $(\alpha, \beta) = (0^\circ, 0^\circ)$ orientation. The similar trends suggest that the crossflow instability mechanism may be the primary instability away from the area of the model dominated by the lofted boundary layer despite the fact that stationary crossflow vortices are not observed in any of the heat flux plots.

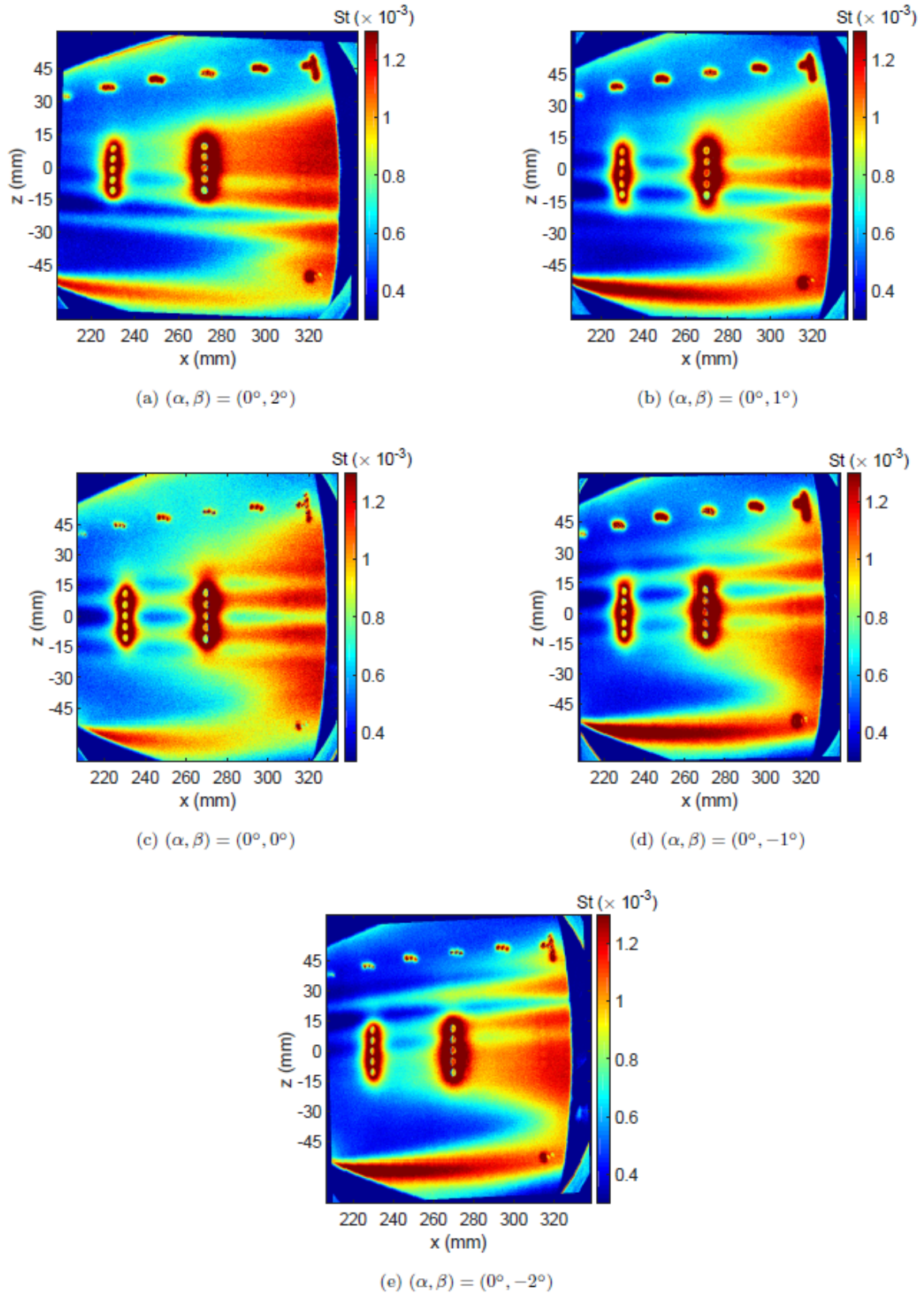


Figure 6-9 □sweep, noisy flow, $\text{Re}=3.1 \times 10^6/\text{m}$

Although varying angle-of-attack and yaw independently is a useful exercise to examine the trends in transition, the HIFiRE-5b flight test article was rarely oriented with a pure α or β . Both angle-of-attack and yaw were generally less than $\pm 2^\circ$ during the primary descent experimental window.¹ The orientation of the flight vehicle was determined using the same method reported in Reference 10. The HIFiRE-5 model was thus tested for combinations of angle-of-attack and yaw that would envelope the maximum flight angles: $(\alpha, \beta) = (-2^\circ, 2^\circ)$, $(-2^\circ, -2^\circ)$, and $(2^\circ, 2^\circ)$. Due to time constraints, the model was not tested at the $(\alpha, \beta) = (2^\circ, -2^\circ)$ orientation. Heat flux contours in quiet flow for $Re=9.6\times 10^6/m$ are shown in Figure 6-10. Re_{tr} based on the threshold value are shown in Figure 6-11. Several interesting transition features are again seen. Comparing Figure 6-10a and b to Figure 6-7a and e, respectively, demonstrates the additional effect that pitching the model to $\alpha=-2^\circ$ has when the model is yawed to $\beta=-2^\circ$ and 2° . In each case, the addition of the angle-of-attack serves to slightly increase the spanwise extent of transition. However, the minimum value of Re_{tr} for crossflow transition changes very little from the $(\alpha, \beta) = (0^\circ, \pm 2^\circ)$ orientations. The minimum Re_{tr} for $(\alpha, \beta) = (0^\circ, \pm 2^\circ)$ is 2.4×10^6 (see Figure 6-8b), and for $(\alpha, \beta) = (\pm 2^\circ, 2^\circ)$ the minimum Re_{tr} increases only 4% to 2.5×10^6 . This change is within the uncertainty of the transition location as it is estimated in this work. As expected, the yaw angle has the dominant effect on transition; the addition of a negative angle-of-attack serves mainly to alter the spanwise location of transition, but not the minimum value of Re_{tr} across the crossflow region.

When β is fixed at 2° , the effect of angle-of-attack is demonstrated by comparing Figure 6-10a and c and the Re_{tr} values shown in Figure 6-11. Increasing α from -2° to 2° moves crossflow transition outboard and increases the minimum value of Re_{tr} approximately 17%, suggesting a stabilizing effect of increased α , as expected. It also appears that the spanwise wavelength of the stationary crossflow vortices decreases. Planned future work includes a quantitative comparison of stationary crossflow wavelengths.

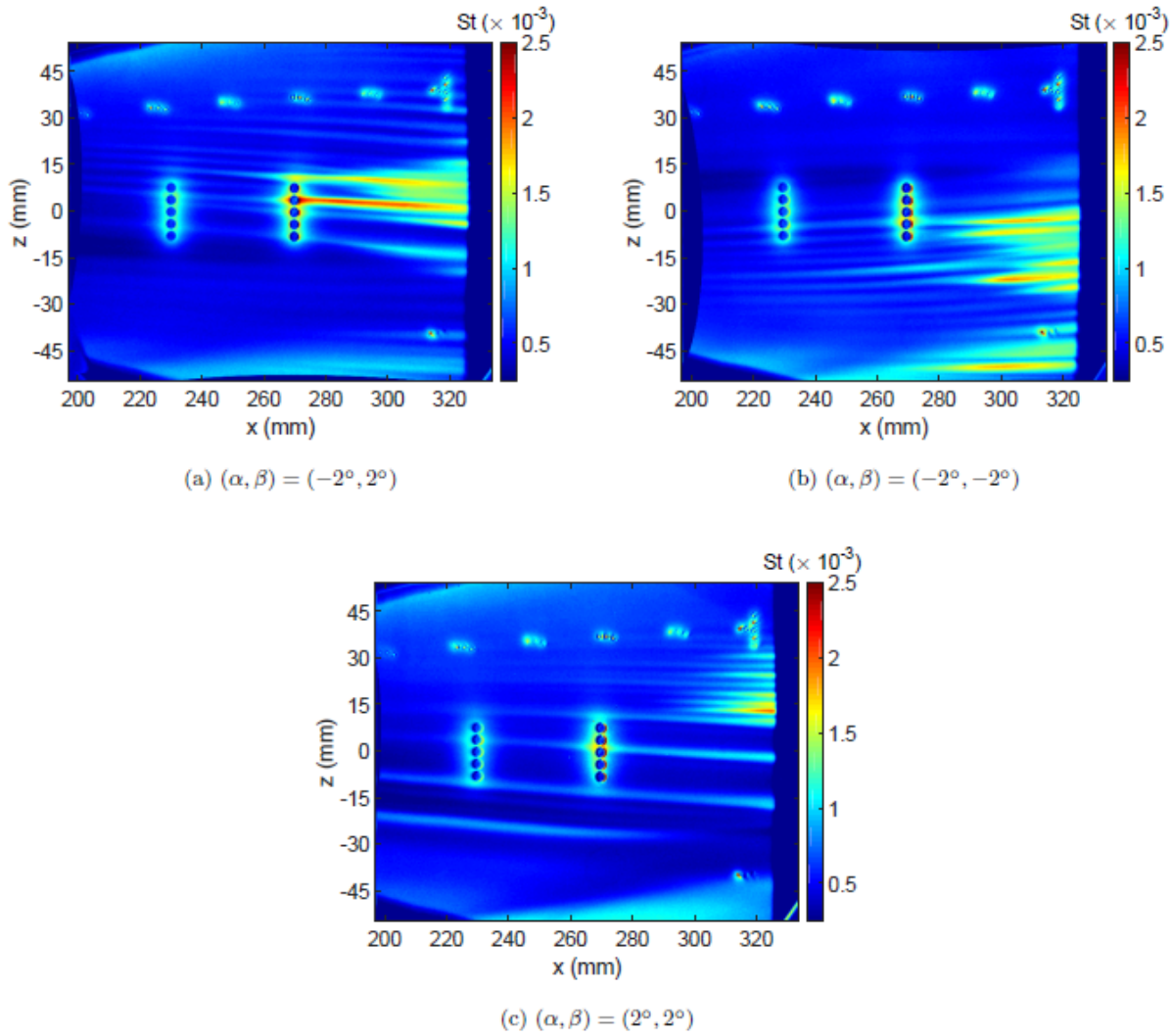


Figure 6-10 Heat flux for mixed (\square/\square combinations, quiet flow

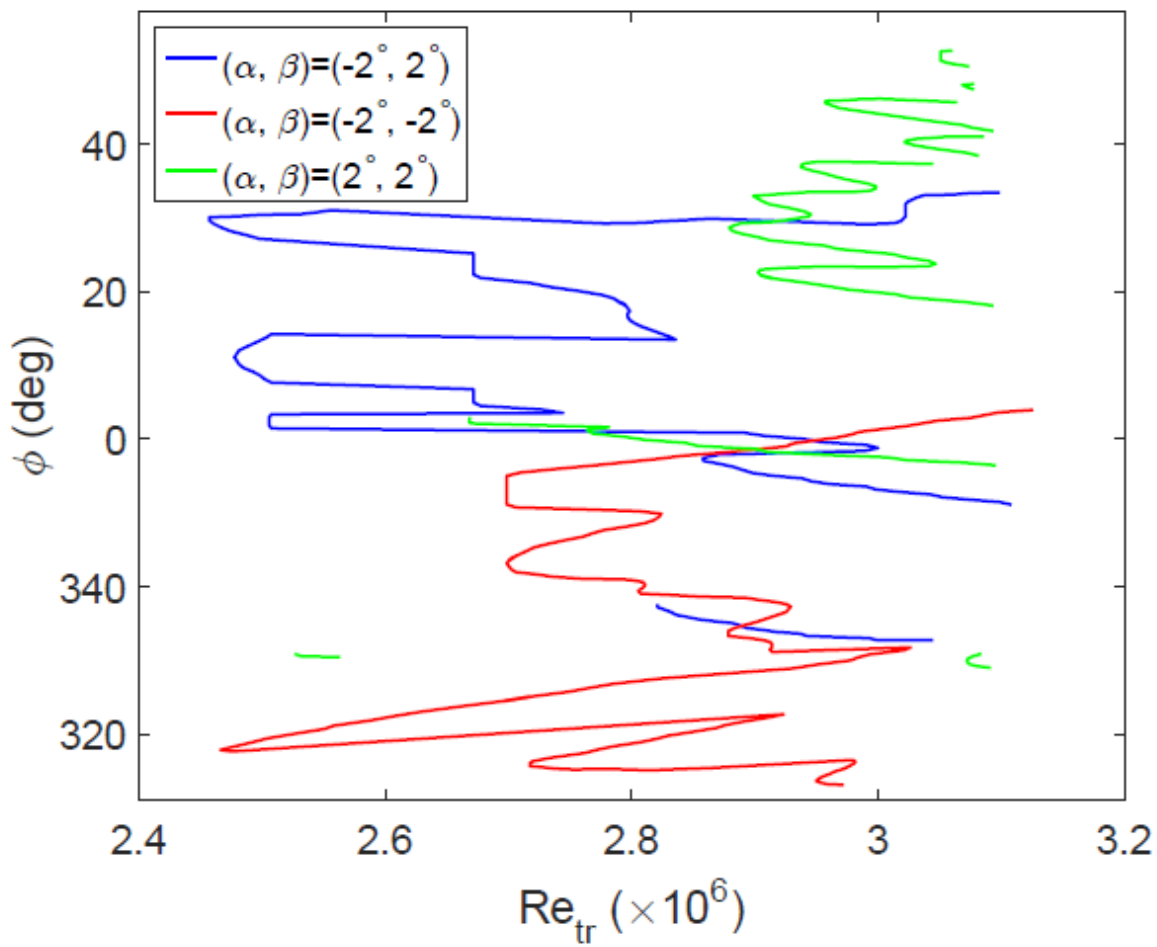


Figure 6-11 Transition Re for mixed (////) pairs, quiet flow

The model was also tested in noisy flow at $Re=3.1\times 10^6/m$ for the same combinations of α and β that were tested in quiet flow. Heat fluxes are shown in Figure 6-12. The extraction of transition locations was again precluded by the proximity of transition to the PCB sensors. Nevertheless, qualitative trends can still be observed. As in quiet flow, holding α fixed at -2° and testing at $\beta=\pm 2^\circ$ (Figure 6-12a and b) moved transition downstream on the lee side (with respect to yaw) when compared to the $(\alpha, \beta) = (-2^\circ, 0^\circ)$ orientation (shown again in Figure 6-12d for comparison). Transition on the windward side (with respect to yaw) was moved inboard, but does not appear to have moved upstream. This surprising behavior is in contrast to what was observed in quiet flow. The cause for this discrepancy is unknown. Additionally, the transition front is observed to shift toward the lee side (with respect to yaw) of the cone, as was observed in quiet flow. Comparing Figure 6-12a and c demonstrates the effect of changing the angle-of-attack from -2° to 2° when the model is yawed at $\beta=2^\circ$. The 4° swing in angle-of-attack shifts the near-centerline transition front toward the wind side (with respect to yaw). This effect is expected due to the reduction in the spanwise pressure gradient. The change in α also moves transition upstream on the lee side (with respect to yaw), but appears to have little effect on the streamwise location of transition on the wind side (with respect to yaw). The effect of α on the

yawed model in noisy flow appears to be more significant than in quiet flow for the Reynolds numbers tested in these experiments.

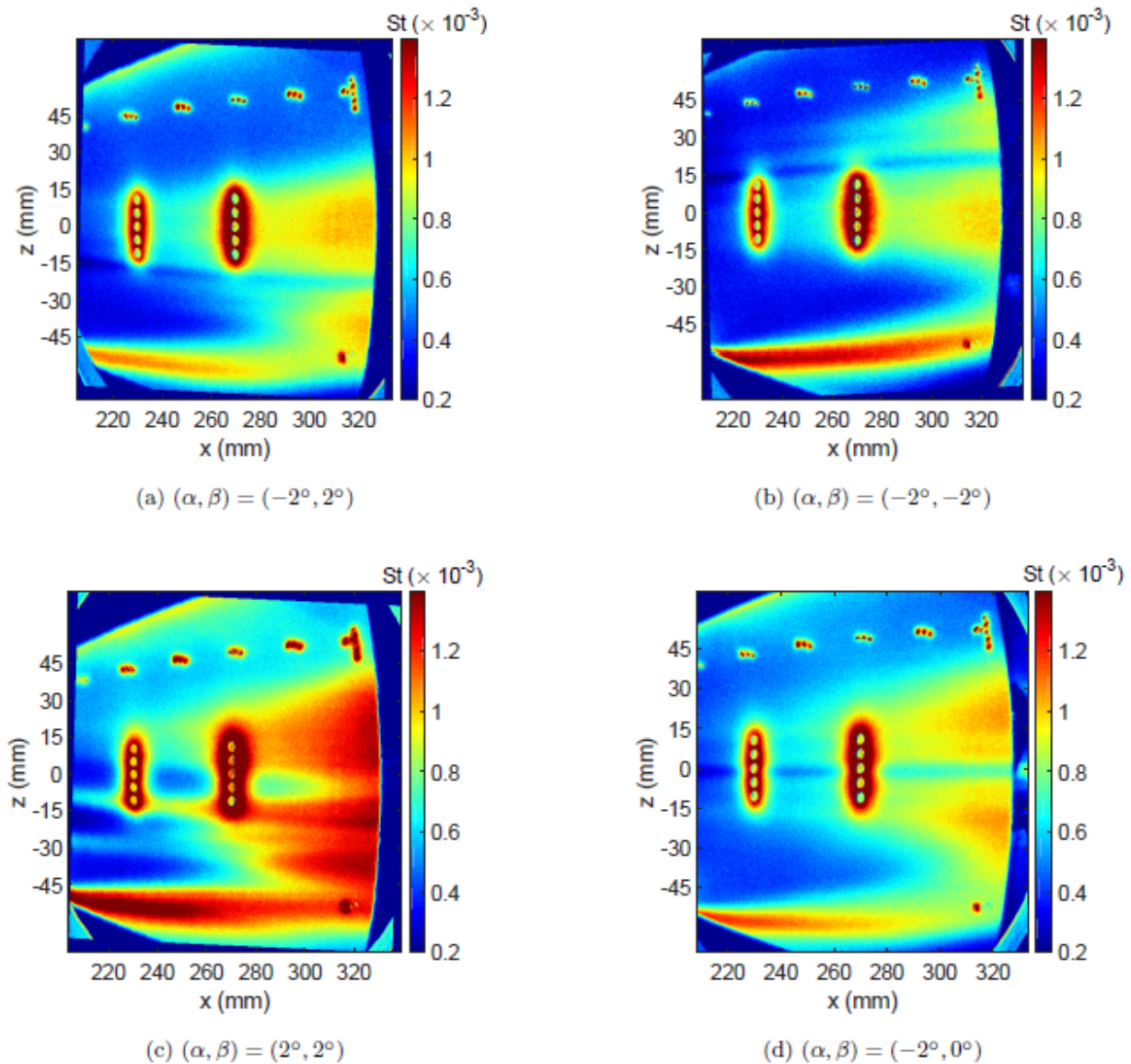


Figure 6-12 Mixed (□□□□) Combinations, noisy flow

Whether in quiet or noisy flow, it is clear that transition is much more sensitive to yaw than angle-of-attack. This observation appears due in part, at least, to the relative sensitivity of the spanwise pressure gradient to yaw and angle-of-attack. This sensitivity was characterized by calculating the spanwise pressure differential between the leading edge and centerline, as calculated with a Newtonian approximation. In this analysis, a one-degree change in angle-of-attack creates approximately a 10% change in the pressure differential. A one degree change in yaw however, creates approximately a 20% change in the pressure differential. Therefore, it appears to be a reasonable that crossflow instabilities would be more sensitive to yaw changes.

A preliminary analysis of the effect of model orientation on the traveling crossflow instability is presented below. Only Kulite sensor K19 is considered. Figure 6-13 shows power spectral densities (PSDs) for sensor K19 in quiet flow for the various model orientations. Figure 6-13a shows the effect of α on traveling crossflow. Since reducing α to progressively negative angles weakens the shock strength along the centerline and increases the spanwise pressure gradient, it was thought that traveling crossflow waves would have higher amplitudes for more negative values of α . This is not the trend observed in Figure 6-13. Rather, the traveling crossflow peak for $(\alpha, \beta) = (0^\circ, 0^\circ)$ clearly has the highest PSD amplitude. Several factors may contribute to this unexpected trend. Reference 48 reports that the PSD amplitudes of traveling crossflow waves for nominally identical freestream conditions varied by an order of magnitude in one wind tunnel entry. It is possible that the effect of varying α from 0° to -2° on traveling crossflow wave amplitudes falls within experimental variability. Additionally, by altering the spanwise pressure gradient, the locations of individual stationary vortices as well as the region of the model unstable to crossflow are likely shifted on the model surface, which could affect the PSD amplitudes.

Figure 6-13b shows PSDs for sensor K19 as β is swept from 2° to -2° and α is fixed at 0° . No clear trend is observed as β is reduced from 2° to 1° to 0° . However, when sensor K19 is on the lee side of the cone, the PSD amplitudes clearly decrease over most of the spectrum. For $\beta=-2^\circ$, the peak due to traveling crossflow is nearly gone. The reduction in PSD amplitude with decreasing yaw angle does not necessarily indicate that the lee side of the cone is less unstable to the crossflow instability. Orienting the model with a yaw angle does appear to alter the stability of the boundary layer, but also serves to displace some gross boundary layer features. For example, for $(\alpha, \beta) = (0^\circ, -2^\circ)$, it is clear that the highly-thickened portion of the boundary layer has been displaced toward the Kulite pressure transducers (see Figure 6-7 e). The low PSD amplitude for traveling crossflow at this orientation may simply be due to an outboard displacement of the region of the lee side of the model unstable to crossflow.

Figure 6-13c shows PSDs for the mixed angle-of-attack/yaw model orientations. For the two orientations with the same yaw angle, $(\alpha, \beta) = (-2^\circ, 2^\circ)$ and $(\alpha, \beta) = (2^\circ, 2^\circ)$, the PSD amplitudes are similar and fall within the expected scatter for runs at the same nominal condition. The PSD for $(\alpha, \beta) = (-2^\circ, -2^\circ)$ shows a greatly diminished traveling crossflow instability. This may again be due to the outboard displacement of a crossflow-unstable region or may indicate that this orientation greatly stabilizes the lee side (with respect to yaw) to the crossflow instability.

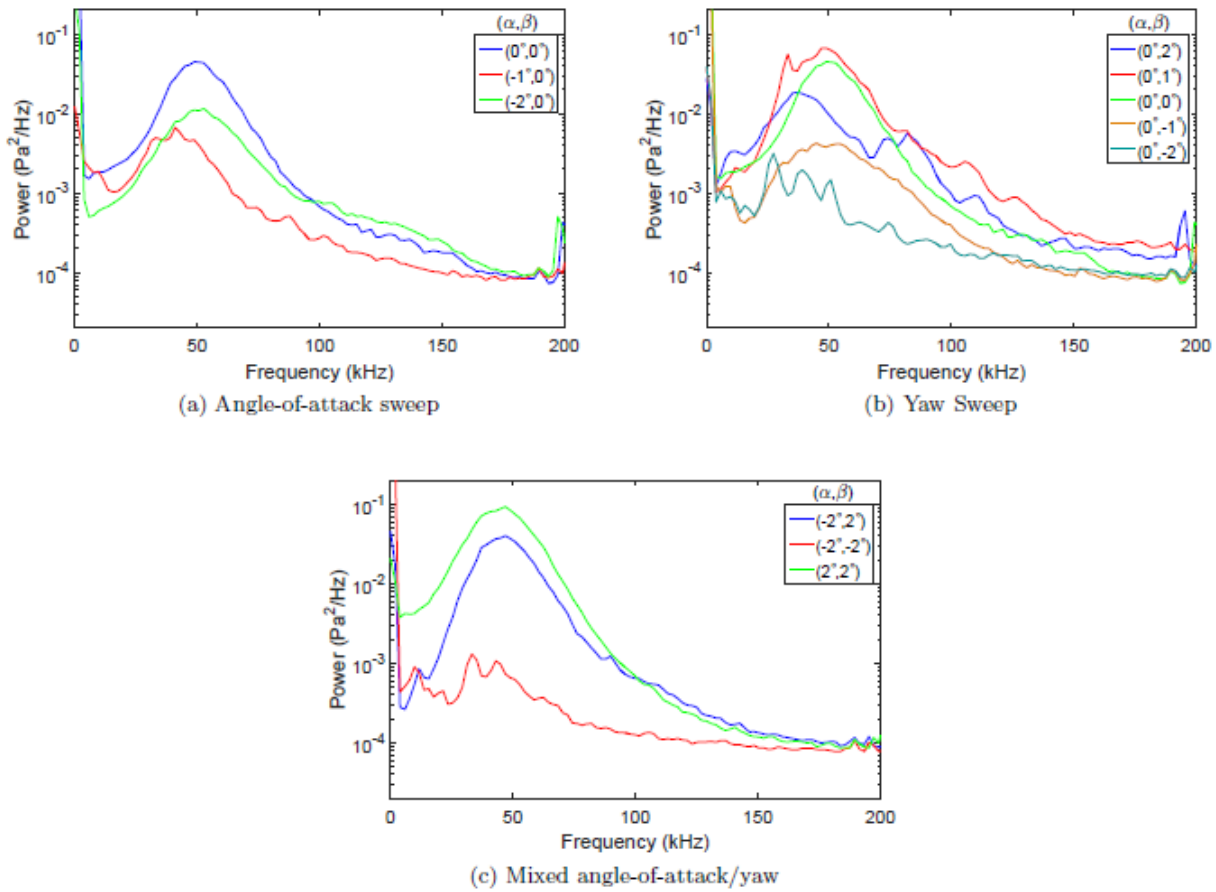


Figure 6-13 PSDs for sensor K19, quiet flow, $\text{Re}=9.6 \times 10^6/\text{m}$

6.1. PCB Sensors

The two spanwise arrays of PCB sensors were primarily installed near the model centerline to investigate stability in the region under and near the thickened centerline boundary layer. Since most of the model orientations reported in the present work include some yaw angle, the lofted boundary layer region is displaced in span by various amounts from run to run. The PCB sensors thus yield little information about the stability of the lofted boundary layer for most of the conditions tested. When the model is oriented at $(\alpha, \beta) = (0^\circ, 0^\circ)$ or purely pitched, the model centerline is a symmetry plane, and the PCB arrays are well-positioned to make measurements near the lofted centerline boundary layer. For the work reported here, the off-centerline PCB sensors show no evidence of instabilities. Thus, data from those sensors are not included here.

The two centerline sensors, PCB3 and PCB8, do show some interesting features for noisy flow. Figure 6-14 shows PSDs for PCB3 and PCB8 for $(\alpha, \beta) = (0^\circ, 0^\circ)$, $(\alpha, \beta) = (-1^\circ, 0^\circ)$, and $(\alpha, \beta) = (-2^\circ, 0^\circ)$. Here, the solid lines correspond to PCB3 and the dashed lines correspond to PCB8. When the model is uninclined, a sharp, low-amplitude peak can be seen near 70 kHz for both PCB3 and PCB8. This frequency of the peak is very similar to that observed on a different model of the same shape, at the PCB8 location, for a similar Reynolds number.³⁵ The PSD amplitude for PCB8 is nearly identical to that for PCB3, though there is some evidence of spectral

broadening for PCB8. This peak is still present but is substantially diminished when the model is pitched to $\alpha=-1^\circ$, and all but disappears for $\alpha=-2^\circ$. This corroborates the observed downstream movement of near-centerline transition with decreasing α observed in the heat flux data (Figure 6-3 and Figure 6-4). The 70 kHz disturbance may be the second mode instability. However, other earlier experiments that focused more on centerline transition were unable to conclude that such disturbances were the second mode.³⁵ Future experiments with $\beta=0^\circ$ and at higher freestream Reynolds numbers are planned to study the stability and transition of the lofted centerline boundary layer in more detail.

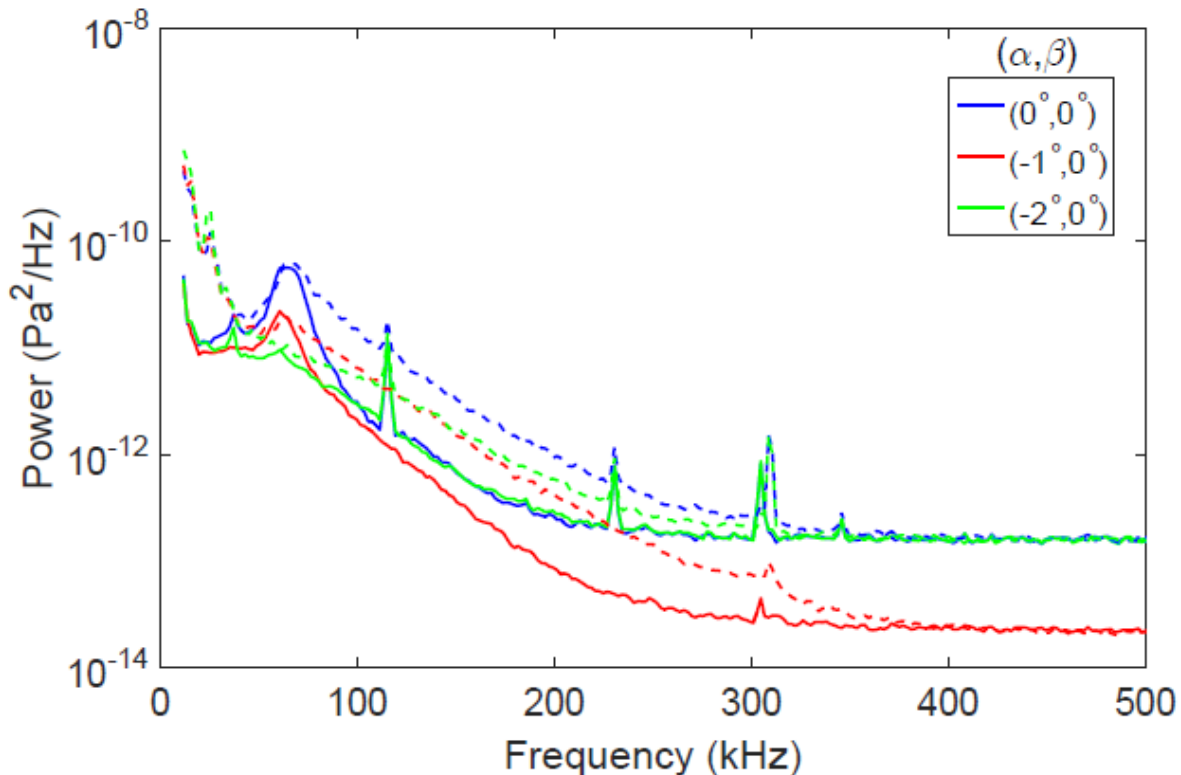


Figure 6-14 PSDs for sensor PCB3 (solid) and PCB8 (dashed), \square/\diagup sweep, noisy flow

The apparent change in the high-frequency noise floor for the three tunnel runs shown here is likely due to an experimental oversight. It was noted that when the PCB sensors are powered, they appreciably heat the PEEK shell of the model. This heating effect is manifested as non-physical high heat fluxes in the near-sensor regions for all of the heat fluxes shown. In order to minimize the time the PCB sensors could heat the model, the sensors were only powered on immediately prior to running the tunnel. After turning on the power, the PCB conditioning electronics take approximately 60 seconds to provide a stable output. It was only after this steady state was reached that the tunnel was operated and data were recorded. In the cases where the noise floor appears to shift, it is thought that the steady state had not quite been reached. Future experiments will establish a more rigorous wait time after powering the sensors on before operating the wind tunnel to hopefully eliminate such shifts in the spectra.

6.2. Preliminary Evidence of Secondary Instability of Stationary Crossflow Vortices

Although the PCB sensors are not located at a position that is particularly useful in examining the lofted boundary layer region of the model, there are additional 3 model orientations for which high-frequency disturbances are evident in the PCB data. For quiet flow and $(\alpha, \beta) = (0^\circ, 2^\circ)$, $(-2^\circ, 2^\circ)$, and $(-2^\circ, -2^\circ)$, the lofted boundary layer is displaced outboard of the PCB arrays. The crossflow-dominated region of the model is also displaced such that some of the PCB sensors are within it, as seen in Figure 6-7a, Figure 6-10a, and Figure 6-10b. Figure 6-15 shows PSDs for the PCB sensors and model orientations of interest, as well as the corresponding heat flux data to highlight the location of the sensors with respect to stationary crossflow vortices and transition. For all the data presented here, a streak of higher heat flux is observed to pass over the sensor of interest, with transition of that streak occurring on the model but downstream of the sensor. Thus, these sensors are positioned such that they are relatively close to transition of a stationary crossflow vortex. For all the cases shown, high-frequency disturbances ranging from 150–300 kHz are observed. It may be that these high-frequency disturbances are secondary instabilities of the stationary crossflow vortices. These frequencies are similar to those observed by Edelman et al.⁵⁷ on a 7° half-angle cone at 6° angle-of-attack in quiet flow. The authors suggest that their high-frequency disturbances are secondary instabilities of stationary crossflow. Their measurements were also very sensitive to the sensor location relative to a particular stationary vortex. As such, it should not be surprising that only some of the PCB sensors here measured the high-frequency disturbances. It may be that adjacent sensors were not positioned properly relative to a stationary vortex to measure a secondary instability.

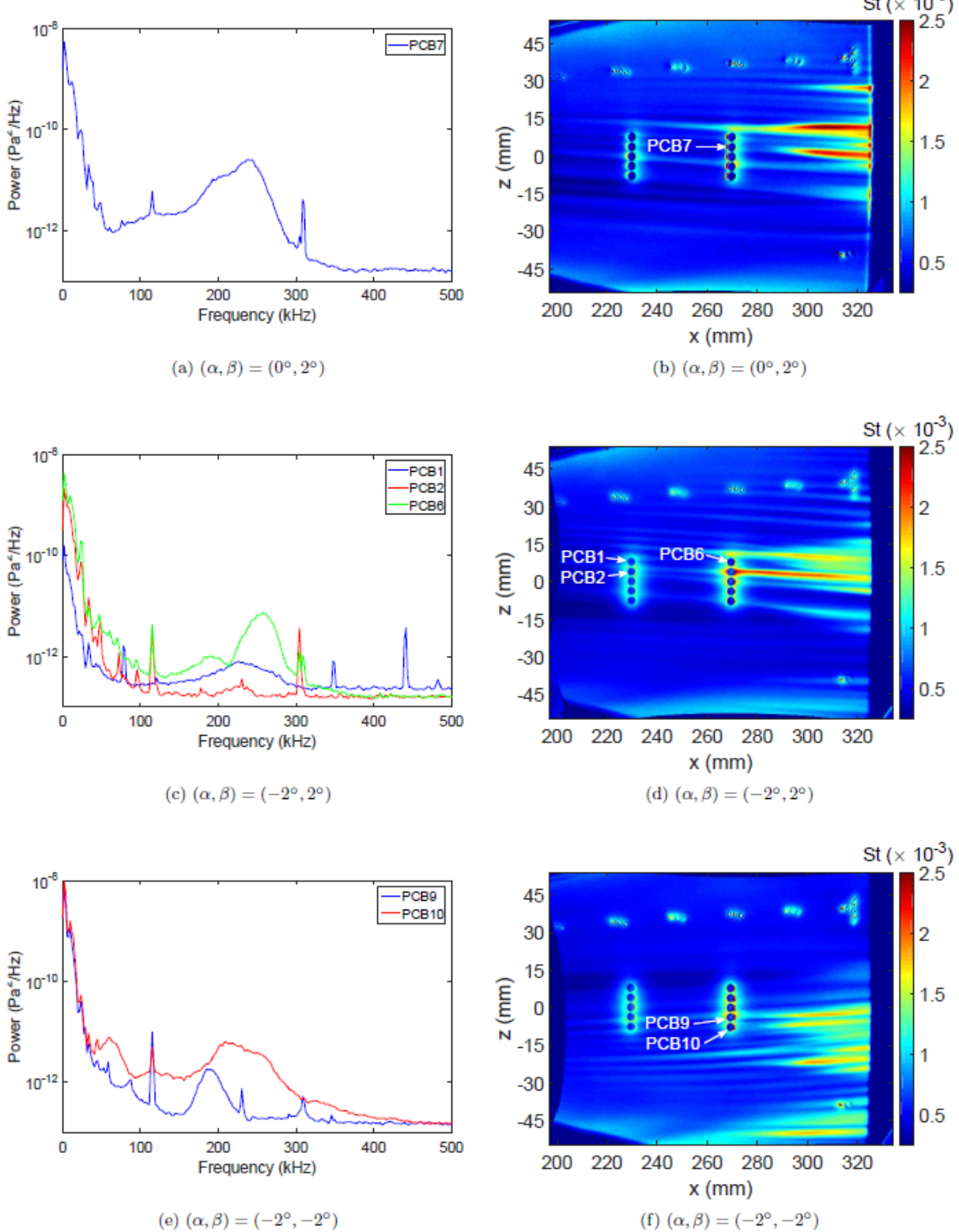


Figure 6-15 PSDs of PCBs possibly showing secondary instability

6.3. Summary and Conclusions

A 38.1% scale model of the HIFiRE-5 flight vehicle was tested in quiet and noisy flow at flight-like orientations. Several key observations and conclusions follow below.

In both quiet and noisy flow, inclining the model to larger negative values of α served to increase Re_{tr} in the near-centerline region while decreasing it in the crossflow region.

Transition Reynolds numbers dropped by greater than 66% when comparing transition in noisy flow to quiet.

The purely yawed model showed greater destabilization in the crossflow region on the wind side of the model, as was observed in flight. In quiet flow, a 2° yaw angle decreased the minimum Re_{tr} for crossflow transition by 20% and >25% compared to the 1° and 0° yaw orientation, respectively.

Transition was found to be much more sensitive to yaw angle than angle-of-attack, as was observed on the flight vehicle.

Angle-of-attack was found to have a greater effect on transition when the model was also yawed when compared to the $\beta=0^\circ$ orientation. In quiet flow, the minimum crossflow Re_{tr} across the span increased by >17% when α was changed from -2° to 2° with $\beta=2^\circ$.

For $\alpha=-2^\circ$, yawing the model in quiet flow reduced Re_{tr} on the windward side of the cone (with respect to yaw) compared to the $\beta=0^\circ$ orientation. For noisy flow with $\alpha=-2^\circ$, yawing the model gave wind-side (with respect to yaw) transition at a similar streamwise location when compared to the $\beta=0^\circ$ orientation. Furthermore, for $\beta=0^\circ$ in quiet flow, inclining the model to more negative values of α moved crossflow transition upstream. In noisy flow, it appears that the opposite trend may have been observed. The cause for these discrepancies between transition trends in quiet and noisy flows is unknown.

For $-2^\circ \leq \alpha \leq 0^\circ$, α had a negligible effect on traveling crossflow amplitudes

For the purely yawed cone, positive values of β had a negligible effect on traveling crossflow amplitudes. For $\beta=-2^\circ$, the traveling crossflow waves nearly vanished. This may just be due to the outboard displacement of the crossflow-unstable region on the lee side of the model.

PCB sensors on the model centerline appear to have measured a centerline instability that was stabilized with decreasing (more negative) values of α .

High-frequency disturbances were measured by the PCBs when the crossflow-unstable region had been moved over their location. These disturbances may be secondary instabilities of stationary crossflow vortices.

These preliminary ground tests demonstrate many of the same transition features observed in the HIFiRE- 5b flight experiment. A more quantitative comparison to flight data will be made if future testing can occur at higher freestream Reynolds numbers.

7. PSE Analysis of Crossflow Instability on HIFiRE-5b Flight Test

7.1. Computational Methods

The current study uses computationally calculated flows coupled with stability theory (LST, LPSE) to examine the development and expected characteristics of the transition seen during the HIFiRE 5b flight and associated ground tests. For both geometries considered; structured, hexahedral, multi-block grids were created using Pointwise glyph scripting. The computational model was assumed to be completely smooth (no modeled surface roughness) with a perfectly 2:1 elliptical tip that inscribed a circular segment along the minor axis. The nose was represented by projecting a square mesh onto the blunted ellipse and subsequently smoothing the projected shape to blend smoothly with a conical grid placed on the frustum. Only one symmetry plane along the minor-axis plane was included to reduce computational expense, but also to allow for the addition of angle of attack in the simulations while using the same grid. Wall-normal spacing in terms of $y+$ was less than 1 everywhere on the surface of the cone, except very near the stagnation point, where the boundary layer is extremely thin.

The US3D7 flow solver with 2nd-Order Steger-Warming fluxes was used to solve for the basic states. In keeping with laminar-flow stability studies, no turbulence models were needed, as the base-state flow is necessarily considered to be laminar everywhere. Because the mean flow solution is intended as the base state for stability calculations, the flow was solved as a steady-state flow. Boundary conditions for the model surfaces were modeled as no-slip, isothermal, uniform-temperature walls.

The LASTRAC3d^{58,59,60} stability suite was used to solve the LST/PSE stability equations. An in-house Fortran script converted the US3D unstructured cell-centered solution to LASTRAC3d formatted meanflow file without interpolation, however, as is suggested in the LASTRAC3d manual⁵⁹ the solution was projected to the wall-normal direction while calculating the wall-normal distance.

LST/PSE were performed by integrating along inviscid streamlines for the crossflow instabilities. Using these marching paths approximates the true vortex path stationary crossflow is thought to develop along. Similar to the findings of Choudhari et al.¹¹ it was found that moving from LST to LPSE produced an overall ΔN of around positive 1 count for most stationary crossflow modes for these flow conditions. A sample comparison of LST and LPSE for crossflow development can be seen in Figure 7-1 and Figure 7-2.

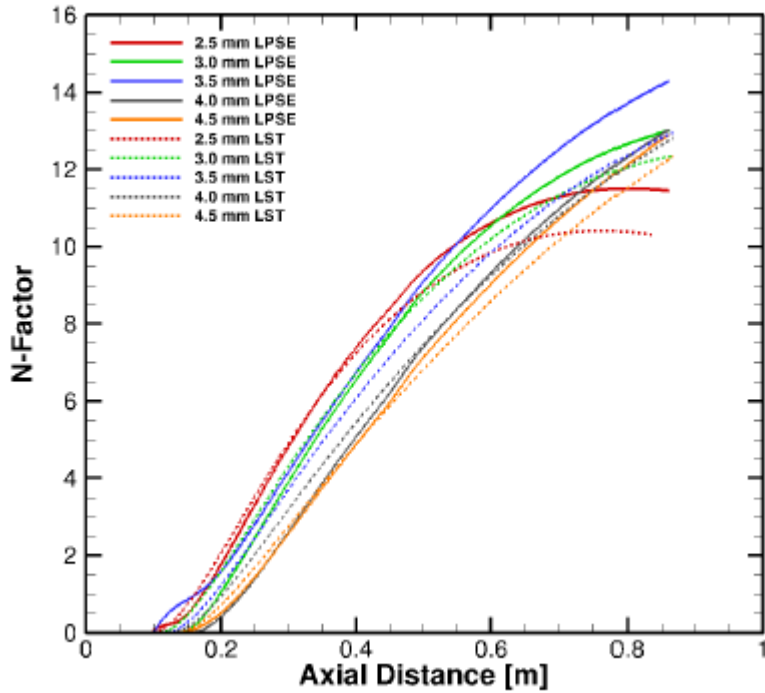


Figure 7-1 LST vs. LPSE Stationary Crossflow N-Factors

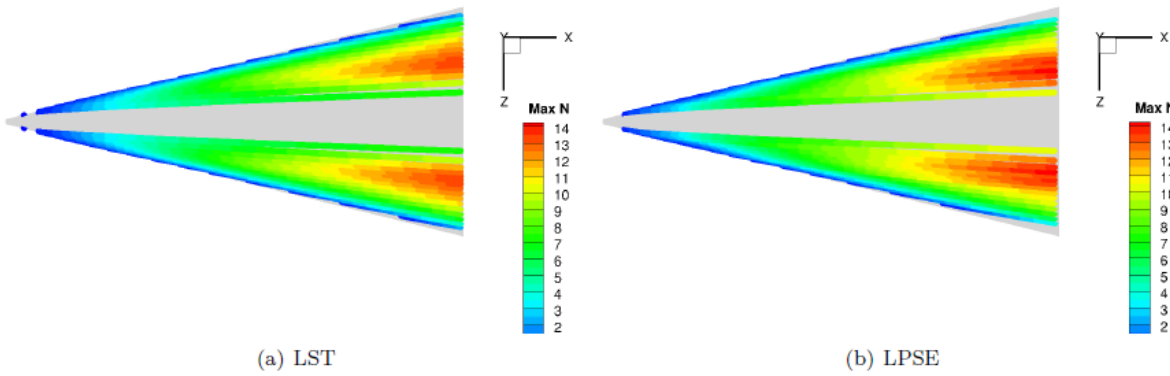


Figure 7-2 Full Scale HIFiRE5 $t = 514.8$ s, $0^\circ \square 0^\circ \square$ Stationary Crossflow N-Factors

Examination of infrared thermography from recent wind-tunnel experiments provided direction for the crossflow analysis. Under quiet flow, there is clear evidence of stationary crossflow streaking on the model.⁵ It also appears that the transition breakdown appears to follow the saw-tooth, spatially fixed pattern traditionally associated with breakdown driven by stationary crossflow. The images also qualitatively appear to show that the azimuthal wavenumber is not a constant. In other words, the number of vortices that appear at a given streamwise station is increasing as one moves further back along the cone. Until further experimental data reduction is completed, it has not been determined how the wavelength varies with axial distance. For this reason, the first analyses of crossflow modes focused on stationary waves with a constant spanwise wavelength. For discussion on the qualitative differences that would result in the changing of these assumptions see Choudhari et al.¹¹

Second mode instabilities are expected to be most relevant near the attachment lines. Second mode instabilities in these areas were calculated by integrating single modes (frequency) along a ray of constant azimuthal angle. Second modes were assumed to be two-dimensional ($\beta_R = 0$). When calculating 2nd mode instabilities, the ΔN between LST and LPSE methodologies are smaller than for crossflow instabilities.

After examining the initial solutions, it was determined that the resolution in the axial direction could be redistributed to better resolve the roll-over shapes near the centerline, and the points were redistributed to create Flight Grid A. Flight grids B and C are created by uniform coarsening of A in all three i-j-k directions. Grid resolution details are summarized in Table 7-1. In Table 7-1, “i” and “j” represent the sides of the nose cap, “k” represents wall-normal points, and “axial” represents points along a given azimuthal ray. Because the grid is multi-block structured, along the frustum of the cone the number of azimuthal points was necessarily $2i + j$. A similar process was followed for the wind-tunnel conditions. Grid independence was judged by calculating the stationary crossflow stability characteristics on each grid topologies. Solution convergence was judged by using the stationary crossflow N-Factors. At any given location the maximum change in N-Factor is on the order of 0.5 counts, but in most locations, the change is smaller. Contours of these N-Factors can be seen in Figure 7-3. Solutions reported for in flight cases are as calculated on the initial grid shown below, wind-tunnel results are taken from Wind-Tunnel A. Future studies are expected to be calculated using Flight Grid A and Wind Tunnel Grid B to take advantage of the increased resolution near the centerline.

Table 7-1 Grid Resolution Figures

Configuration	“i”	“j”	“k”	“axial”	Total Pts.	Approx. Pts. in B.L.
Initial Grid	55	73	373	1793	123,885,982	150
Flight Grid A	109	145	373	933	132,222,532	150
Flight Grid B	87	115	299	747	67,540,512	120
Flight Grid C	71	93	240	597	32,255,520	96
Wind Tunnel A	53	69	353	2301	143,435,196	150
Wind Tunnel B	83	111	299	645	56,175,522	120

7.2. Flow Conditions

The first set of computational flow conditions are representative of in-flight conditions experienced during the descent portion of the flight at a time 514.83 s from launch. The freestream conditions at this time stamp were near the lowest Reynolds number that produces a detectable transition front around the entire circumference of the model, i.e. most azimuthal rays appear neither completely turbulent nor completely laminar. In addition, the yaw angle (β) at this time was nearly zero, which allows for a symmetry plane to be included in the grid. Experimental investigations^{1,5} have found that yaw angle exerts a strong influence on crossflow transition, and to some extent on centerline transition. The effect of yaw angle on derived N-factors will be discussed in detail in section 7.3.2. As a first step only $\beta = 0^\circ$ cases have been completed and examined in this paper. It was also found^{1,5} that leading edge transition is less sensitive to payload orientation. Calculations were performed for angle of attack (α) at two conditions: 0° as a reference condition and -1° , which is within the uncertainty of the measured flight AoA. Full flow conditions for the computation and current Best Estimated Trajectory (BET) are found in Table 7-2. The best estimate³ of flight angle of attack at t=514.83s is -1.2° . Wall conditions were taken as isothermal with $T_w = 373.15$ K which represents an average over the acreage

of the test vehicle.¹ Although the nosetip of the flight vehicle was at much higher temperatures, this was not expected to affect the stability results significantly. Previous tests⁶¹ and computations⁶² showed little effect of a hot nosetip on boundary layer stability.

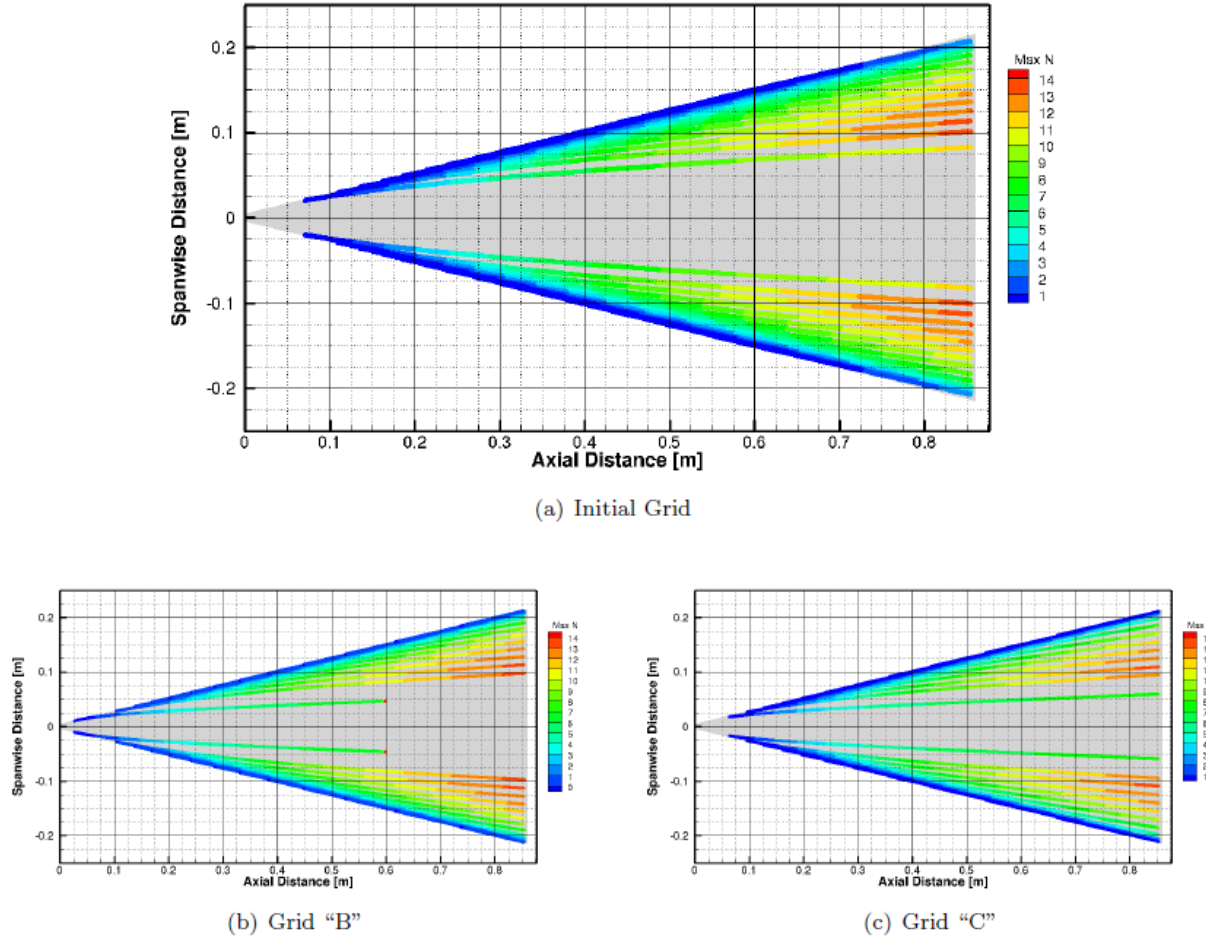


Figure 7-3 Full Scale HIFiRE5 $t = 514.83$ s, $0^\circ \square 0^\circ \square$, Stationary Crossflow N-Factors (LST)

Table 7-2 Nominal in-flight flow parameters

Case	Unit Reynolds Number ($\times 10^6/\text{m}$)	Unit Reynolds Number ($\times 10^6/\text{in}$)	ρ_∞ (kg/m^3)	P_∞ (Pa)	T_∞ (K)	M_∞	T_w (K)	T_w/T_0
Computational	8.89	0.225	0.055	3379	216	7.81	373.15	0.131
Current BET $t=514.83$	9.00	0.229	0.055	3435	215.6	7.80	-	-

A second set of flow conditions was modeled to be representative of recently tested wind-tunnel conditions as experienced in the BAM6QT. These conditions represent the highest Reynolds number at which quiet flow could be maintained in the BAM6QT at the time of the ground tests. For details on this test, see Borg and Kimmel.⁵ At these conditions, infrared thermography indicates strong crossflow growth, however at 0° angle of attack, no boundary-layer transition is observed in the regions dominated by the crossflow instability, although centerline transition is observed. However, once the

model is given a slight AoA such that the observed side is slightly leeward (destabilizing to crossflow), boundary-layer transition becomes visible near the back of the cone in the crossflow-dominated region. This implies that the model at 0° angle of attack is very near the threshold for crossflow-induced transition. Full flow conditions are found in Table 7-3

Table 7-3 Nominal Flow Parameters - Wind Tunnel (BAM6QT)

Case	Unit Reynolds Number ($\times 10^6/\text{m}$)	Reynolds Number ($\times 10^6/\text{in}$)	ρ_∞ (kg/m^3)	P_∞ (Pa)	T_∞ (K)	M_∞	T_w (K)	T_w/T_0
Nominal	9.78	0.248	0.038	57.0	52.2	6.0	300	0.7

The mean flow features calculated for the in-flight conditions, as seen in Figure 7-4, are, as expected, similar to those calculated for wind tunnel tests. Along the minor axis, a collection of low momentum fluid resulting from opposing crossflow vectors appears. Predominantly in wind-tunnel cases, current CFD solutions and previous computations^{11, 63} showed several small secondary lobes of increased boundary thickness that appear to the sides of this main collection of low momentum fluid, visible in Figure 7-5 near the centerline on the back of the cone, and inset in Figure 7-6. These flow features are strikingly visible when looking at several surface conditions e.g. wall heat transfer or shear stress. Stability characteristics are also influenced by these secondary roll-overs. It is worth noting that these features appear in several independently-calculated studies of this geometry^{11,63} and appear to be relatively insensitive to grid changes in this study between Wind Tunnel Grids A & B. For this reason, they are thought to be physical mean flow features and not instability growth due numerical error. However, a study by Dinzl and Candler⁶⁴ showed that the solution in this area is sensitive to grid resolution and solver dissipation. Dinzl and Candler⁶⁴ also note that the main shock-generated vortex generates vortical structures separate from crossflow instability development and thus should be considered a meanflow feature, although the two phenomena are difficult to separate especially downstream on the cone. Porter et al.³³ report a similar phenomena occurring for in-flight conditions. Work is underway to identify the specific causes of this change in the mean flow features.

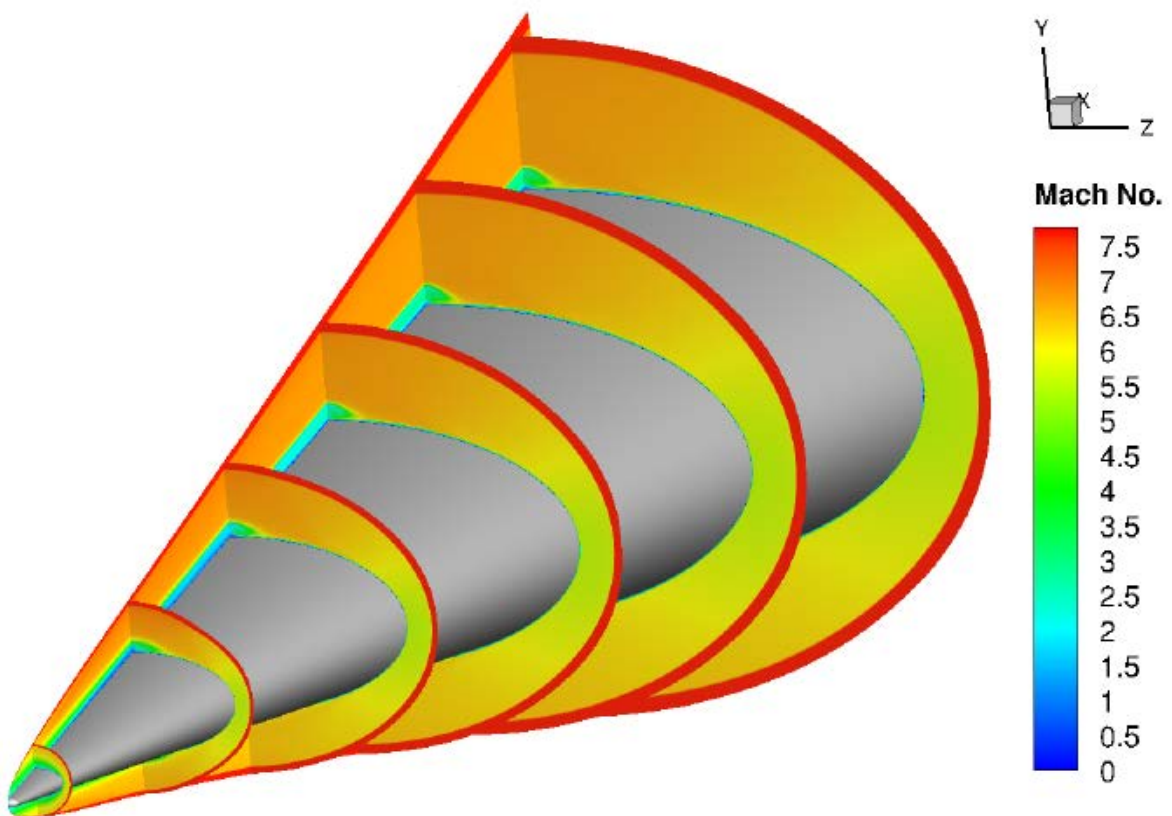


Figure 7-4 Contours of Mach Numbers, In-Flight Conditions, $1^\circ \square 0^\circ \square$

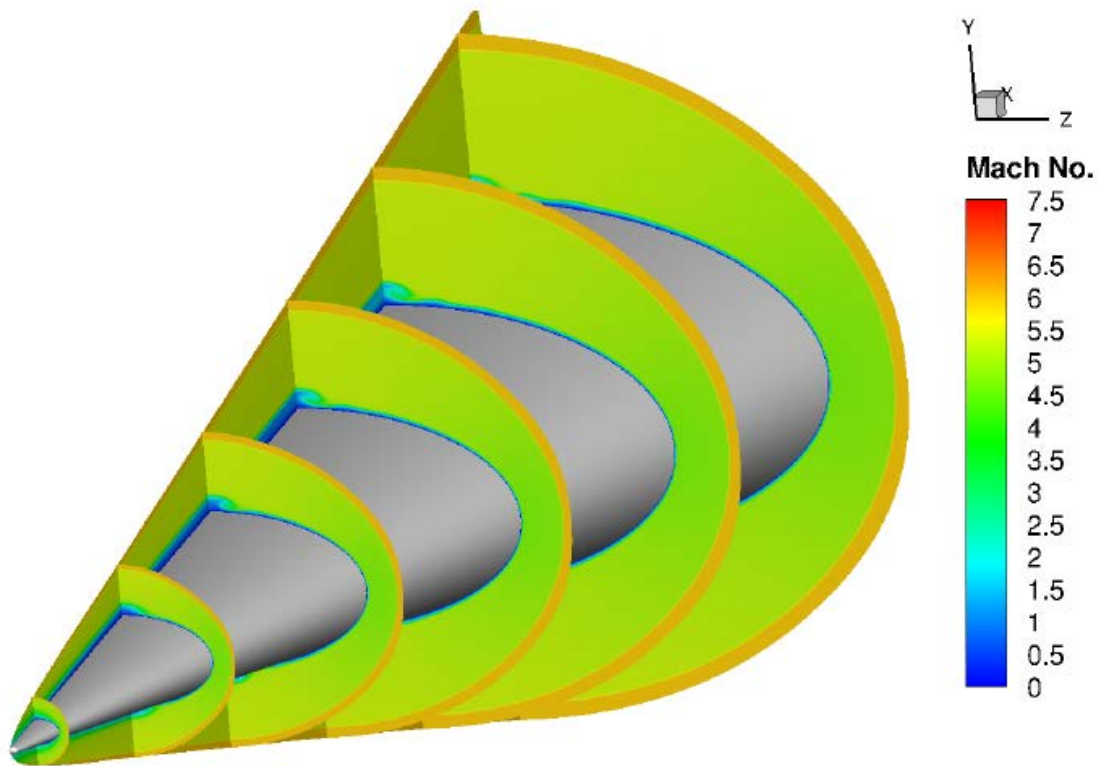


Figure 7-5 Contours of Mach Numbers, BAM6QT Conditions, $0^\circ \square 0^\circ \square$

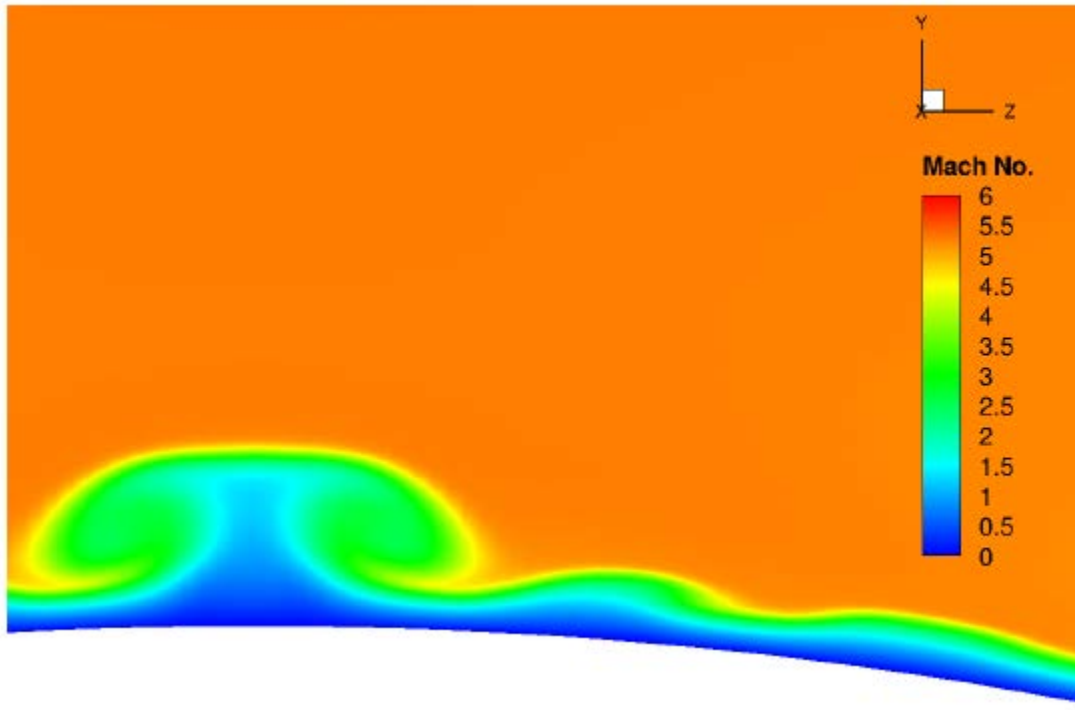


Figure 7-6 Contours of Mach Numbers, Wind Tunnel Conditions, $0^\circ \square 0^\circ \square$

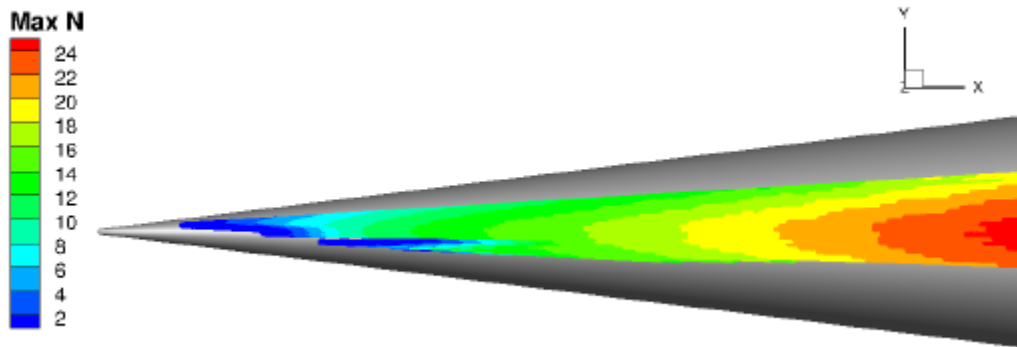


Figure 7-7 Second Mode N-Factor Envelope, Flight Conditions, $1^\circ \square 0^\circ \square$

7.3. Stability Characteristics

7.3.1. Second Mode

N-Factor results shown for second mode instabilities are calculated using LST. For second mode, LST N-Factors are not expected to deviate much from those calculated from LPSE. Given the relatively high Mach numbers and that the wall temperature at these conditions results in a relatively strongly cooled wall, first mode instabilities are not expected to play a strong role in the transition process. Therefore along the attachment lines, second mode is expected to be the dominant transition mechanism for in-flight conditions. Consistent with results reported in Choudhari et al.¹¹ there exists a

region of high second mode growth along the attachment line. For the flight conditions examined in this study the Maximum N-Factor for any frequency is about 24 with $Re = 8.9 \times 10^6/m$, for comparison Choudhari et al. report a maximum N of approximately 36 with $Re = 18.5 \times 10^6/m$. Figure 7-7 shows leading edge N-factors.

By comparing the experimental transition locations with the calculated N-Factors one can find a correlating transition N for the HIFiRE 5 geometry for use in an amplitude-based method e.g. the e^N method. For second mode instabilities, this method has worked reasonably well for predicting the transition location when the nose tip is reasonably sharp. For the in-flight cases, the transition N was estimated by simply examining the transition locations given by Juliano et al.³ and setting the transition N threshold to produce a similar contour. For this case it appears that the best correlating transition is around $N = 18$. This is somewhat higher than what was found for the axisymmetric transition at $M \approx 5.3$ HIFiRE-1 flights, which correlated well with a transitional N of about 14.⁶²

In Figure 7-8, the flow expected to remain laminar is shown in blue, while transitional and turbulent flow is shown in red. By examining Figure 7-8 one can see that with this envelope set, transition is predicted in a narrow band surrounding the attachment line that appears to widen as one moves further back along the cone, consistent with the outboard lobe observed in the flight experiment.³ This leading edge transitional lobe was not observed in quiet tunnel ground tests, due to a combination of factors. First, the wind tunnel tests had a higher T_w/T_0 ratio than the flight experiments, which is stabilizing to second mode instabilities. Second, the quiet Reynolds number in the wind tunnel was limited, precluding examination of leading-edge transition under quiet flow. Leading-edge transition occurred under noisy-flow conditions in several tests, but was different in nature than that observed in flight. In most noisy wind tunnel tests, leading edge transition was the most downstream point in the transitional front, and appeared to be due to contamination from acreage transition. The only known ground tests, noisy or quiet, where a distinct leading edge transition lobe was observed was in tests performed at CUBRC¹³ where T_w/T_0 more closely approximated flight conditions. In this sense, the HIFiRE-5b leading edge transition behavior is somewhat analogous to the attachment line transition on HIFiRE-1 at angle of attack.²⁹

For the wind-tunnel cases examined, the maximum N-Factor for any given second mode frequency was about $N = 6$, seen in Figure 7-9. Assuming that the BAM6QT operating quietly has similar freestream noise levels to those experienced in flight (i.e. the transition N-Factor is the same for both cases) one would not expect to see second mode transition appear on the model, which is consistent with the experimental observations.⁵

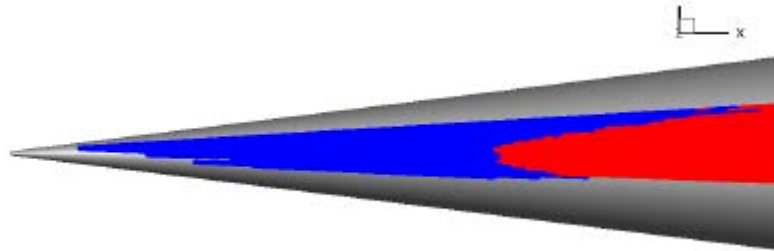


Figure 7-8 Flight Conditions, 1° □ 0° □ Estimated Second Mode Transition Location

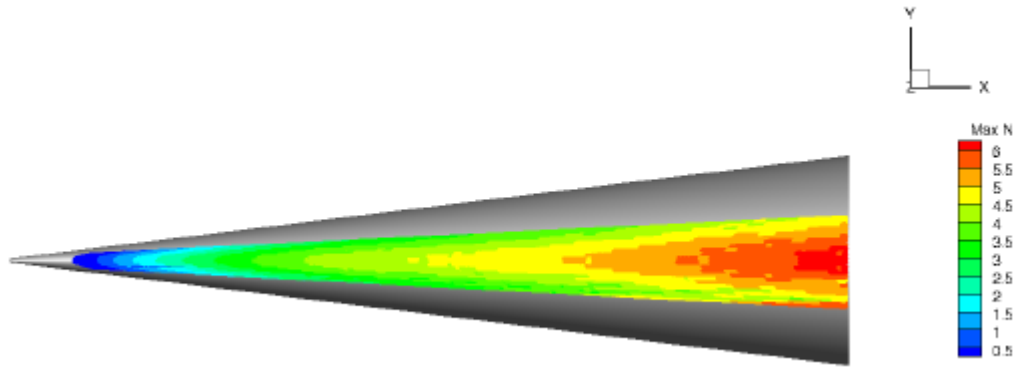


Figure 7-9 Second Mode N-Factor Envelope, Wind-Tunnel Conditions, $0^\circ \square 0^\circ \square$

7.3.2. Stationary Crossflow

The N-Factors calculated for stationary crossflow were calculated using LPSE methods. Stationary crossflow instabilities experience relatively strong growth over much of the HIFiRE-5b acreage, as seen in Figure 7-10. For both sets of flow conditions the most unstable wavelength is around 3.5 mm, commensurate with the similar boundary layer thicknesses computed for both cases. As seen in Figure 7-11 and Figure 7-12 the maximum stationary crossflow N-Factor is around 14 for the lee side of the flight vehicle and 10 for the wind tunnel model respectively.

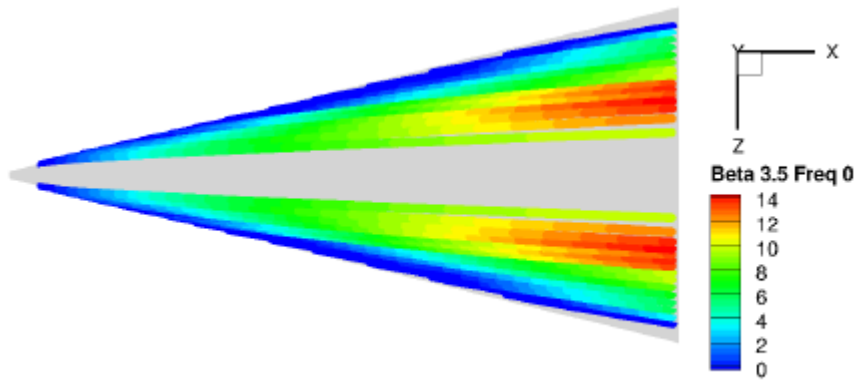


Figure 7-10 Flight Conditions, $0^\circ \square 0^\circ \square$ Stationary Crossflow N-Factors

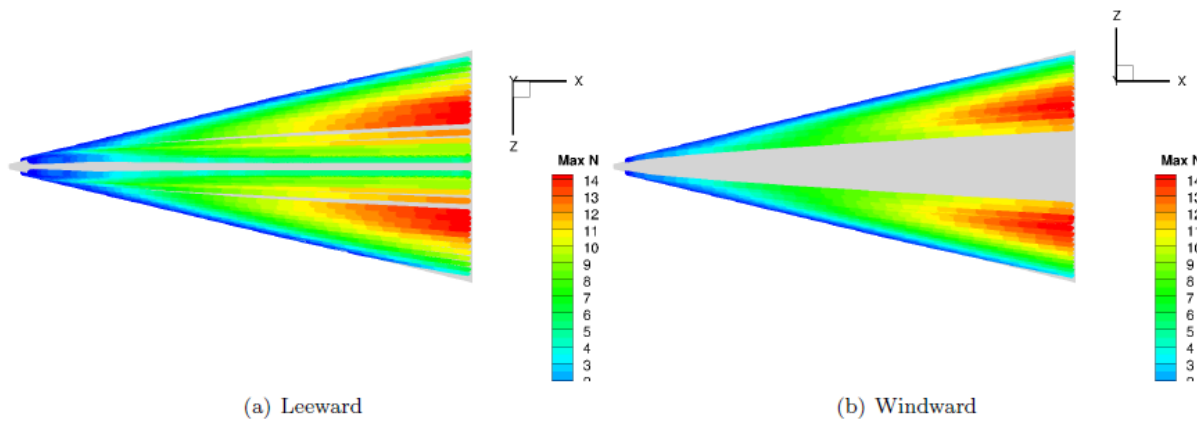


Figure 7-11 Flight Conditions, 1° 0° Stationary Crossflow N-Factors

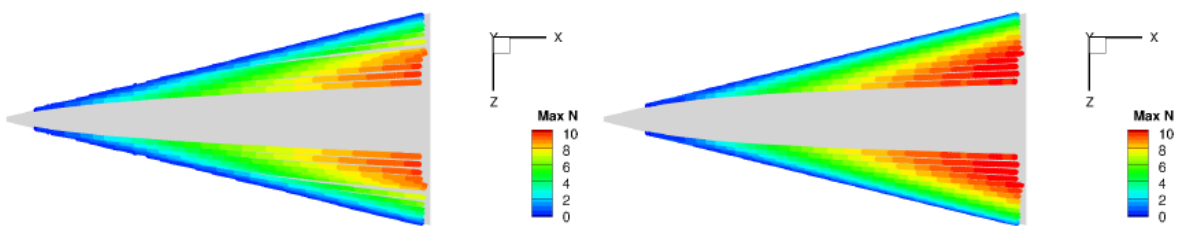


Figure 7-12 Wind-Tunnel Conditions, Stationary Crossflow N-Factors

In low-speed flows it is believed that transition due to crossflow is not directly caused by the crossflow vortices themselves, but rather by a secondary instability that arises in the meanflow after being distorted by the stationary waves.^{65,66} By extension if transition in hypersonic flows are caused by this same mechanism, this precludes the use of a simple e^N amplitude method correlated with the primary instability.⁶⁷ Calculations of secondary instabilities and comparisons with experimental results in high-speed flows are ongoing with promising results,^{68,69} but knowledge in this area is still incomplete. Rather than a general case method to predict transition, these N-Factor correlations are therefore intended to provide a measure of the relative strength of crossflow growth when moving between scales of geometry and between flight and wind-tunnel facilities. For this reason, transition estimates made using a simple threshold N-Factor method based on the primary instability, as done here, should be considered preliminary.

N-Factors for acreage transition due to crossflow were difficult to assess, because the crossflow transition proved very sensitive to yaw angle. Crossflow transition, both in flight and in the wind tunnel, was destabilized when that side of the payload was yawed into the wind, and stabilized when that side was yawed away from the wind. The slight, time-varying yaw angles encountered in flight thus created multiple transition events at a given transducer. The crossflow transition process at a given transducer began at an early time when that transducer was yawed into the wind, and completed at a later time when the Reynolds number was high enough to produce turbulent flow over the transducer when it was yawed away from the wind. Between these times, the heat transfer oscillated between laminar and turbulent, depending on the payload orientation. Currently, only a beginning and end of

transition have been extracted from flight data. N-factor values derived from these data thus represent a lower bound.

With these caveats in mind, one may compare the experimental transition to computational N-Factors to find a correlating transitional N. Figure 7-13 shows a transition front for stationary crossflow based on $N = 10$, for the most unstable wavelength, in this case 3.5 mm. As before, the flow expected to remain laminar is shown in blue, while transitional and turbulent flow is shown in red. The shape and location of this transition front is similar to the flight crossflow transition front shown in Figure 7-14(a). Examination of the crossflow N-Factors as well as Figure 7-11 and Figure 7-14 show that the expected location of maximum crossflow development corresponds well with the observed "middle lobe" of the transition front.

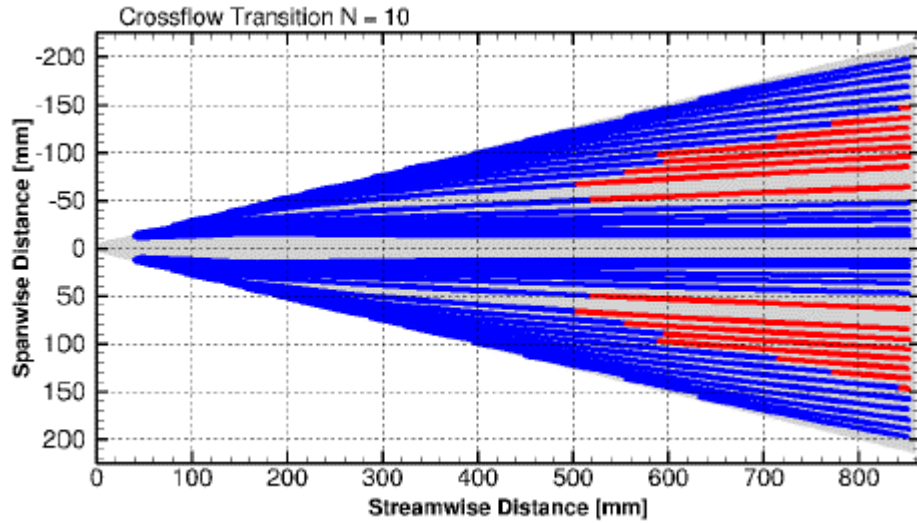


Figure 7-13 Flight Conditions, $1^\circ \square 0^\circ \square$ Preliminary Estimated Transition Locations - Stationary Crossflow Only

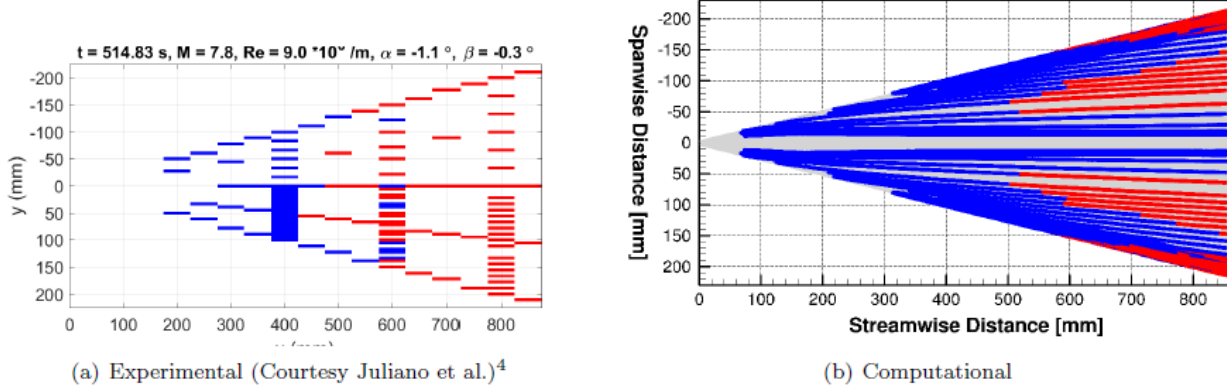


Figure 7-14 Flight Conditions, $1^\circ \square 0^\circ \square$ Preliminary Estimated Transition Locations

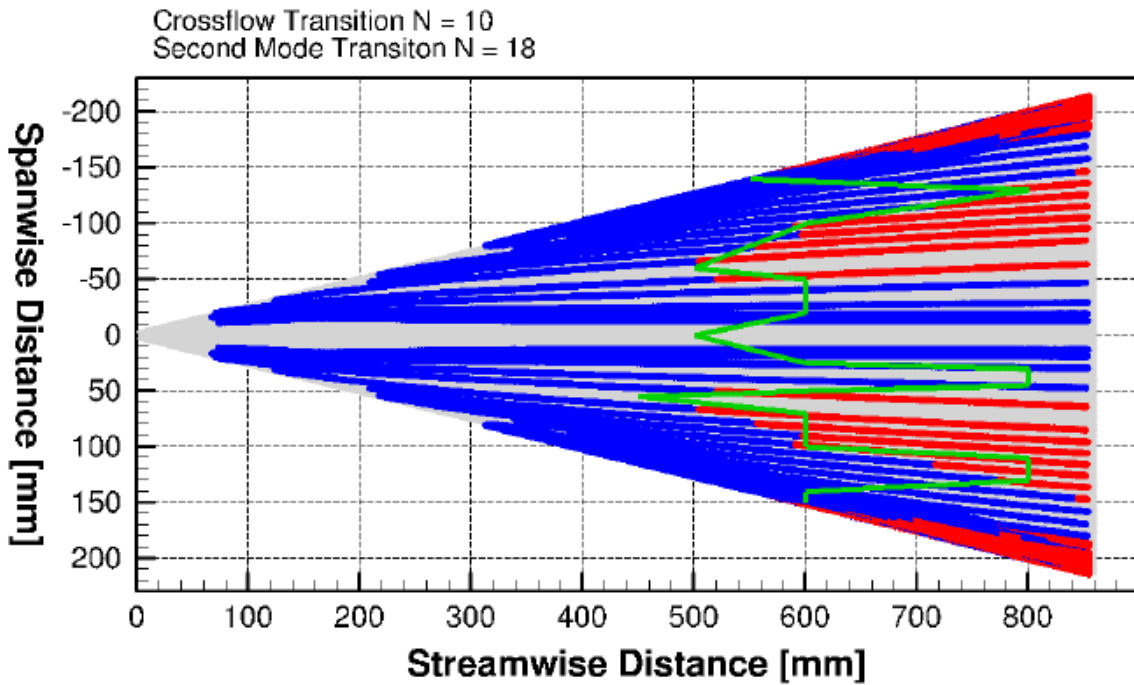


Figure 7-15 Flight Conditions, $1^\circ \alpha, 0^\circ \beta$ Preliminary Estimated Transition Locations, Experimental in Green

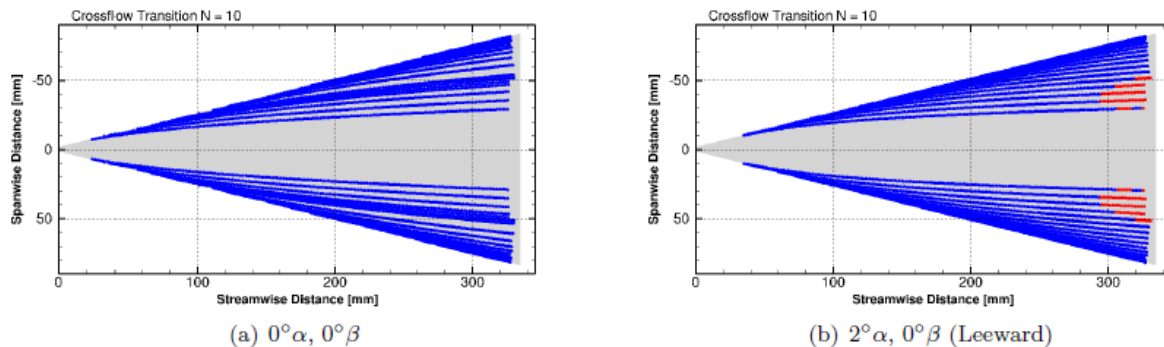


Figure 7-16 Wind-Tunnel Conditions, Preliminary Estimated Transition Locations

The preliminary crossflow transition locations can be combined with the second mode transition locations to produce an overall transition front. Figure 7-14 and Figure 7-15 compare the measured and predicted transition fronts. Most notably, the computed transition front is multi-lobed, similar to the front observed in flight. Although the N-Factor correlations used to derive the Figure 7-14 transition fronts are ad-hoc, it is clear that the stability-based prediction captures the qualitative behavior of the transition front, and by extension, the physical processes leading to transition in the flight case.

Extrapolating the threshold N to the wind-tunnel results produces good agreement as well. As stated previously, for 0° AoA in the wind tunnel tests, no clear transition was observed. However, for 2° AoA isolated transitional spots were observed near the back of the cone. Applying the same threshold to the wind-tunnel conditions produces results consistent with these observations as can be seen in Figure

7-16. For this case at least, N=10 appears to be a satisfactory correlating value for crossflow transition under these conditions.

Analysis of crossflow transition is an ongoing effort. Examination of secondary instabilities, as well as nonlinear effects are expected to produce more accurate results with regards to the transition location.

7.3.3. Centerline

Centerline transition was not examined computationally as part of this study. The rapid changes in the spanwise direction suggests that the assumption of spanwise-invariant flow that goes into LST calculations would render such results invalid. However, recent studies^{70,71} suggest that LST may be able to recover qualitatively accurate growth rates for centerline modes. Choudhari et al.¹¹ as well as Paredes et al.⁷⁰ provide discussion on possible transitional modes in this area.

7.4. Summary and Conclusions

Baseflows for the HIFiRE-5b were calculated using the US3D flow solver. Initial stability analyses of these flows using LASTRAC3d was performed. Calculations were performed for a flight time of $t = 514.83$ s. Nominal conditions at this time were $Re = 9 \times 10^6/m$ and $M = 7.8$ and AoA = 1°.

Complementary calculations were carried out for the HIFiRE-5b model in the Purdue University Mach 6 quiet wind tunnel. Nominal conditions for the wind tunnel test were $Re = 9.8 \times 10^6/m$ and $M = 6$.

Results showed two distinct regions on HIFiRE-5b that were unstable to different types of disturbances. This behavior was observed on both the flight vehicle and in the wind tunnel. The leading edge of the vehicle was unstable to traveling second mode disturbances, but stable to crossflow. Stationary crossflow instability dominated the acreage of the vehicle. Centerline instability was not examined computationally.

Both the flight vehicle and the wind tunnel case exhibited transitional lobes on their centerline and acreage, additionally the flight vehicle exhibited a third lobe on the leading edges. Although instabilities were not measured in flight, the existence of these transitional lobes, coincident with their predicted regions of high amplification, suggests that LST/PSE successfully captured the relevant physics of the transition process. The similarity between the flight and quiet wind tunnel transition patterns also suggests that, at least for this case, the quiet wind tunnel transition processes for acreage and centerline are similar to flight. Leading edge flight transition was correlated by an N-factor of about 18. An equivalent leading edge N-factor for the wind tunnel could not be determined, since leading edge transition did not occur under quiet flow in the wind tunnel. N-factors for acreage transition due to crossflow were more difficult to assess. This is because the crossflow transition proved very sensitive to yaw angle. Currently, only a beginning and end of transition have been extracted from the flight data. An N-factor of 10 for stationary crossflow correlated the beginning of transition. Due to the transition movement with payload orientation, this N-factor value represents a lower bound.

Future stability calculations will expand the range of payload orientations to include yaw angle. Flight heat transfer will be examined in more detail to attempt to extract transition fronts as a function of payload attitude as well as Reynolds number. These efforts will produce a significantly refined definition of N-factor for positive and negative yaw angles. In addition, centerline transition will be evaluated and compared to flight and ground test in an effort to determine transition N-factors for this region.

The full effects of changing the parameters of the experiment when moving to wind-tunnel conditions are being studied. The relative effect of changing individual parameters is not fully understood at this time, and it would likely be beneficial to future wind tunnel tests to better understand these changes e.g. the quantitative effect of matching or not matching T_w/T_0 .

Further examination of the crossflow instability is needed to be able to accurately predict crossflow induced transition. Examination of both non-linear effects and the effects of secondary instabilities is on-going. In addition examination of instabilities related to the centerline flow structure are needed to resolve transitional effects in this area.

8. Analysis of Windward Side Hypersonic Boundary Layer Transition on Blunted Cones at Angle of Attack

8.1. Background

A key factor in the design of a hypersonic vehicle is a reasonable method of predicting the boundary layer transition to turbulence. A PSE-based e^N method using a constant N-factor has performed remarkably well in correlating wind tunnel transition on cones with small bluntness at zero angle of attack.⁷² However, the addition of even a small amount of geometrical complexity in the form of AoA creates rather complex changes in the transition behavior on cones. As a point of reference, consider the windward meridian of a cone at AoA. This is also a practical consideration, due to the increased heating on the cone attachment line.

Although, as noted by Stetson,⁷³ the behavior of windward-side transition on cones at AoA in hypersonic flow can vary widely among different data sets, some general trends are consistent. For sharp cones, as AoA increases, windward transition moves downstream.^{73, 74, 75} Blunt cones showed a more complex trend. Stetson⁷³ observed windward transition on blunt cones to move downstream for small AoA, up to some maximum displacement. The angle of attack producing the maximum downstream displacement varied with nose bluntness. At higher AoAs, transition moved upstream as AoA increased.

Some variations in the behavior of blunt cone windward transition at AoA have been observed. Stetson and Rushton⁷⁴ saw only monotonic upstream movement of windward transition for two bluntnesses on an 8° cone at $M = 5.5$. Holden⁷⁶ saw downstream movement of the windward transition front on a sharp and 6% blunt cones, but upstream movement for a 21% blunt cone at $M = 11$ and 13. Tests of the HIFiRE-1 blunt cone at CUBRC6–8 at $M = 6.6$ and 7.2 showed little movement of the windward transition front for 1° AoA, and upstream movement at 2° and 5° AoA. Tests of HIFiRE-1 at NASA LaRC9 showed slight downstream movement of the windward transition front at AoA = 3° and 5°. Juliano et al.⁴⁶ showed no movement of the windward transition front (within transducer resolution) with increasing angle of attack for AoA $\leq 6^\circ$, and downstream movement for higher AoAs.

Although a constant N-factor of $N = 5.5$ worked well to correlate transition for HIFiRE-1 at zero AoA, it was less successful for correlating windward transition at AoA. 1 N -factor calculations using PSE on the windward centerline of HIFiRE-1 for NASA LaRC test conditions showed N-factors exceeding 8 for AoA of both 3° and 5°. However, the windward boundary layers remained laminar in the wind tunnel at both AoAs. This behavior was difficult to reconcile with the good correlation obtained for AoA = 0°.

For zero AoA conditions Lei and Zhong⁷⁷ showed that increases in nose bluntness consistently delayed the onset of second mode instabilities. For non-zero AoA cases, Alba⁷² applied an axisymmetric PSE analysis to the windward centerline flowfield derived from a 3D basic state calculation, since tools accounting for three-dimensionality were unavailable to him at the time, and this was noted as a source of uncertainty. Several other possible complicating factors might explain the difficulty in adapting a constant N-factor prediction method to the windward side of cones at AoA. A partial list of complications includes changes in edge Mach number, edge unit Reynolds number, dominant instability frequency, dependence of initial amplitude upon frequency, and entropy swallowing lengths.

Given the very complex behavior of cone attachment line transition at AoA, and the limited success in correlating it, a systematic investigation is suggested, starting with non-axisymmetric PSE analysis and attempting to reduce uncertainties cited by Alba et al. moving towards implementing three-dimensional formulations and analyzing flow away from the windward meridian. Recently, in preparation for a series of tests on cones at AoA, Jewell and Kimmel⁷⁸ performed zero-degree AoA, axisymmetric computations using stability theory to predict the transition on cones with differing nose radii at Stetson's⁷³ conditions. Jewell and Kimmel showed that the calculated 2nd mode *N*-Factor at the observed experimental transition location decreases rapidly when transition is within the entropy swallowing distance. The current paper continues this effort by extending the LST/PSE analysis to the windward meridian of cones at AoA. In addition, the mean flow field on the attachment line is carefully examined in an attempt to provide heuristic explanations of the windward stability behavior.

8.2. Reference Experiment

8.2.1. Model Geometry

A 7° half-angle, spherically blunted, circular cone with a base radius of 2 inches (50.8 mm) and interchangeable nose-tip pieces has been fabricated for a planned experiment in the AFRL High Reynolds Number Facility and AFRL Ludweig Tube. The available values of nose radius and bluntness ratio are tabulated in Table 8-1. For a perfectly sharp cone, the geometry would result in a cone length of 16.3 inches (413.7 mm).

Table 8-1 Cone Geometry Parameters

Bluntness %	Nose Radius (mm)	Nose Radius (in)	Total Length (mm)	Total Length (in)
"sharp" (0.35)	0.18	0.007	413.7	16.3
1.0	0.508	0.02	410.1	16.1
3.0	1.524	0.06	402.8	15.9
5.0	2.54	0.10	395.4	15.6
10.0	5.08	0.20	377.1	14.8
20.0	10.16	0.40	340.5	13.4
30.0	15.24	0.60	303.9	12.0

Given the relatively short planned run times, the wall temperature has been assumed to be roughly ambient ($T_w = 300K$) and isothermal as the model is not expected to experience significant heating during course of a run. For the conditions planned, this gives a $T_w/T_{aw} = 0.57$ and $T_w/T_0 = 0.49$. Note that this cone, in order to better compare with recent experiments is planned for a 7° half-angle cone, as opposed to the 8° half-angle used in the original Stetson⁷³ experimental series.

8.2.2. Freestream Conditions

Flow conditions used for the study model those found in the AFRL High Reynolds Number Facility. The facility is a blowdown tunnel equipped with a constant-geometry, axisymmetric nozzle having an exit diameter of 12.3 inches, resulting in a test core with an approximately 10 inch diameter. The nozzle is operated with nominal stagnation pressures ranging from 700 to 2100 psia (4.8 MPa - 14.5 MPa), and a nominal stagnation temperature of 1100° R (611 K). These conditions result in unit Reynolds numbers that range from roughly $30 \times 10^6/m$ to $90 \times 10^6/m$. Full conditions that result from this operating range are listed in Table 8-2.

Available details on the flow parameters in the wind tunnel can be found in Fiore and Law.⁷⁹ The nozzle can be assumed to produce conventional (non-quiet) acoustic noise levels, justifying the choice of a relatively low second mode transition N-factor ($N = 4$) for analysis.

Table 8-2 Nominal Flow Parameters - AFRL High Reynolds Number Facility

P_0 (psia)	Unit Reynolds Number ($\times 10^6/m$)	ρ_∞ (kg/m ³)	P_∞ (Pa)	T_∞ (K)	U_∞ (m/s)	M_∞
700	30.4	0.154	3388.8	76.75	1036.19	5.90
1400	60.9	0.308	6777.5	76.75	1036.19	5.90
2100	91.3	0.461	10166.3	76.75	1036.19	5.90

8.3. Methods

8.3.1. Computational Grid

Multi-block topology grids used for the study were created using Pointwise glyph scripts. Computationally, the model was assumed to be smooth (no modeled surface roughness) with a perfectly spherical tip. The nose was represented by projecting a square mesh onto the spherical nose tip, similar to the cartoon of Figure 8-1, and subsequently smoothing the projected shape to blend smoothly with a conical grid placed on the frustum. A symmetry plane was included to reduce computational expense. Wall-normal spacing in terms of $y+$ was less than 1 everywhere on the surface, except very near the stagnation point, where the boundary layer is extremely thin.

Due to the changing nose radii, and changing overall cone length, the total number of grid points in each grid, but the average is approximately 50 million points. The grid topology can be found in Table 8-3.

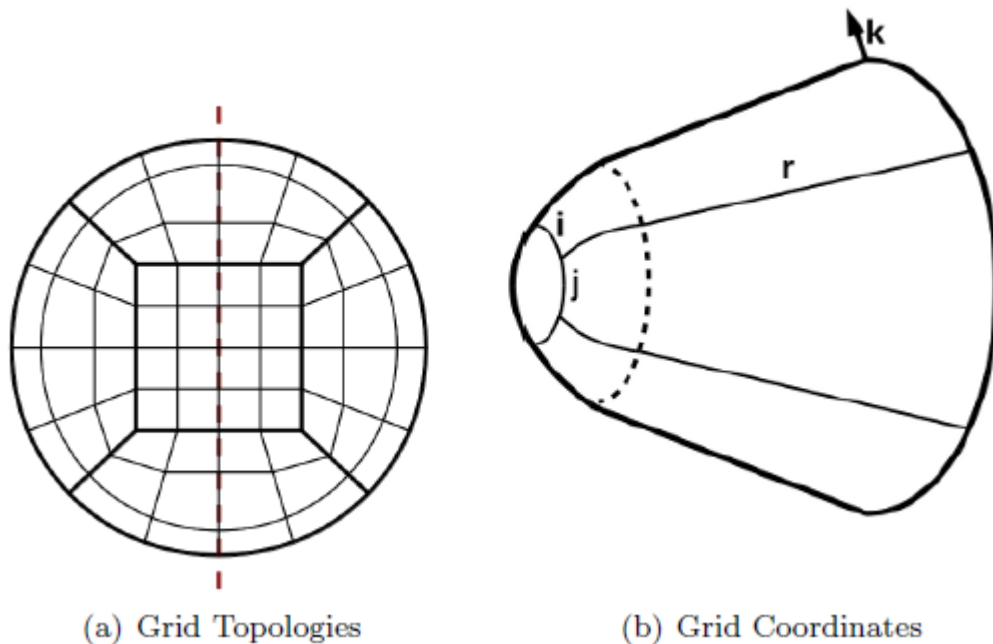


Figure 8-1 Cartoon of grid topology

Table 8-3 Grid resolution figures

Configuration	"i" Pnts.	"j" Pnts.	"k" Pnts.	"r" Pnts.
Sharp (0.35% Blunt)	51	67	353	869
1% Blunt	59	77	353	857
3% Blunt	59	77	353	839
5% Blunt	59	77	353	821
5% Blunt (Medium)	47	63	283	643
5% Blunt (Coarse)	39	51	227	515
10% Blunt	59	77	353	773
20% Blunt	59	77	353	673
30% Blunt	87	115	353	643

8.3.2. Computational Methods

The US3D14 flow solver with 2nd-Order Steger-Warming fluxes was used to solve for the basic states. In keeping with laminar-flow stability studies, no turbulence models were needed, as the base-state flow is necessarily considered to be laminar everywhere. In general, a balance between taking a time step large enough to facilitate reasonable convergence while maintaining numerical stability was striven for. A maximum timestep on the order of 1.0e-8 seconds was used, accordingly in the smallest cells near the nose the maximum CFL is on the order of 100.

The LASTRAC^{58,59} stability suite was used to solve the LST/PSE stability equations. An in-house Fortran script converted the US3D unstructured cell-centered solution to LASTRAC3d⁶⁰ formatted meanflow file without interpolation.

Because the meanflow in the vicinity of the windward ray has relatively few rapid changes in the azimuthal direction, assuming azimuthal homogeneity (i.e. PSE and LST) can be used to compute 2nd mode growth rates. As seen in Figure 8-2, because there is zero curvature in the axial direction and small non-parallel effects due to the high Reynolds numbers, PSE and LST show reasonable agreement for these cases.

It was also found that inclusion of corrections for spanwise non-uniformity as implemented in the LASTRAC3d formulation resulted in minimal changes in stability behavior, even along the shoulder of the cone where spanwise non-uniformity is stronger than along the windward plane.

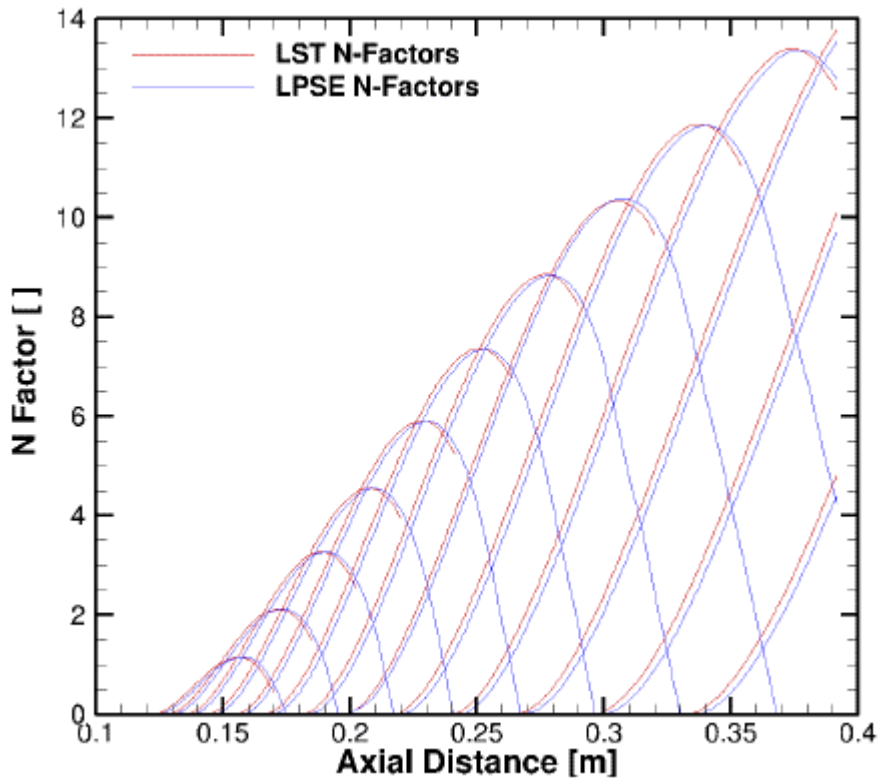


Figure 8-2 Comparison of PSE and LST N-Factors, 5% Bluntness, 5 AoA, Re = 30 M/m

8.3.3. Crossflow Instabilities

As has been noted in literature^{64, 80} the crossflow instability can be seeded even due to grid-to-grid roughness. This leads to distortion of the base state, and if the instability reaches an amplitude great enough to affect the stability analyses, may preclude meaningful results in the areas that are affected.

The question arises as to whether or not this is a physical mechanism, or some feature due to the numerics. If one computes the stationary N-Factors for the configuration using meanflows containing these vortices, assuming that the distortion arising from the vortices does not totally divorce the computed results from reality, as seen in Figure 8-3 the maximum N-Factor reaches above 30. This corresponds to an amplification ratio above 1×10^{13} . It is therefore not surprising that stationary crossflow vortices are present in the Navier-Stokes calculations.

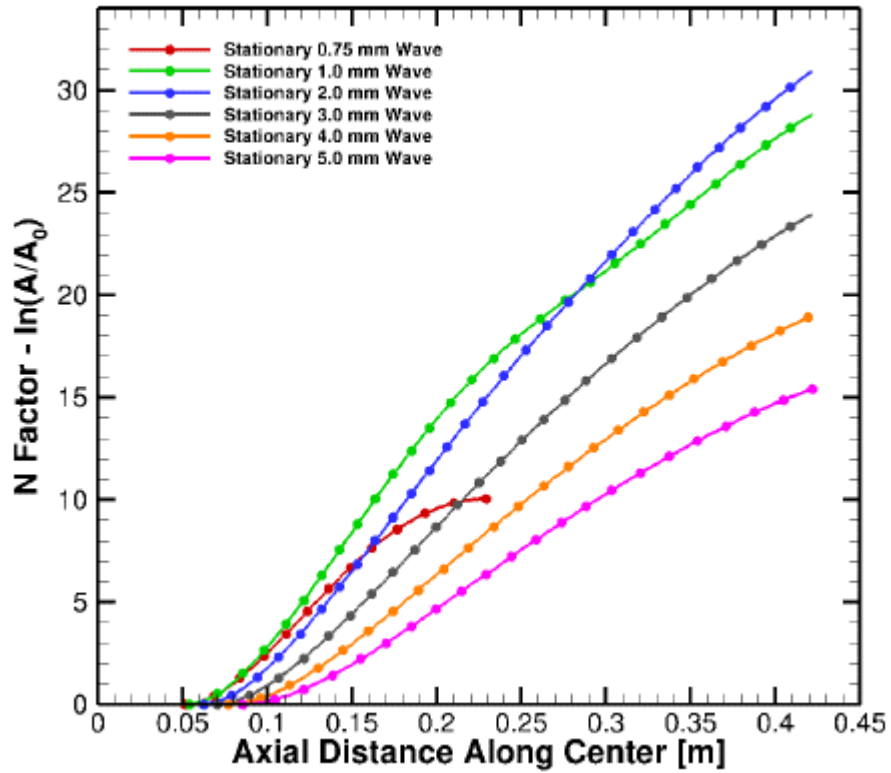


Figure 8-3 Sample Crossflow N-Factors Along 90 Ray, 5% Bluntness, 5 AoA, Re = 60 M/m

This effect can be lessened by careful smoothing of the surface grid, or alternatively by coarsening of the mesh (and thus increasing the dissipation) as suggested by Dinzl and Candler.⁶⁴ For this study, it was found the appearance of these crossflow vortices could be reduced to a level that did not impact the windward meridian second mode analysis, as discussed in the next section. However, somewhat counter-intuitively but confirmed in literature, increased grid resolution causes the appearance of these undesired flow distortions to become higher in wavenumber and higher in amplitude.

Grid convergence was judged by calculating the desired solution functional, the windward 2nd mode stability characteristics. To test the effects of the nose-seeded instability waves six different nose configurations were calculated seen in Figure 8-4(a). For this portion of the study, the grid configurations were tested using a bluntness ratio of 5%, Re = 60 M/m, and AoA = 5°. The second mode stability behavior converges well, as in Figure 8-4(b).

Given the number of cases examined, full grid convergence studies were not done for each configuration. However, a sample case (5% bluntness, 5°, Re = 30M/m) can be seen in Figure 8-5. The changes in the N-Factor for a given frequency were found to be acceptable.

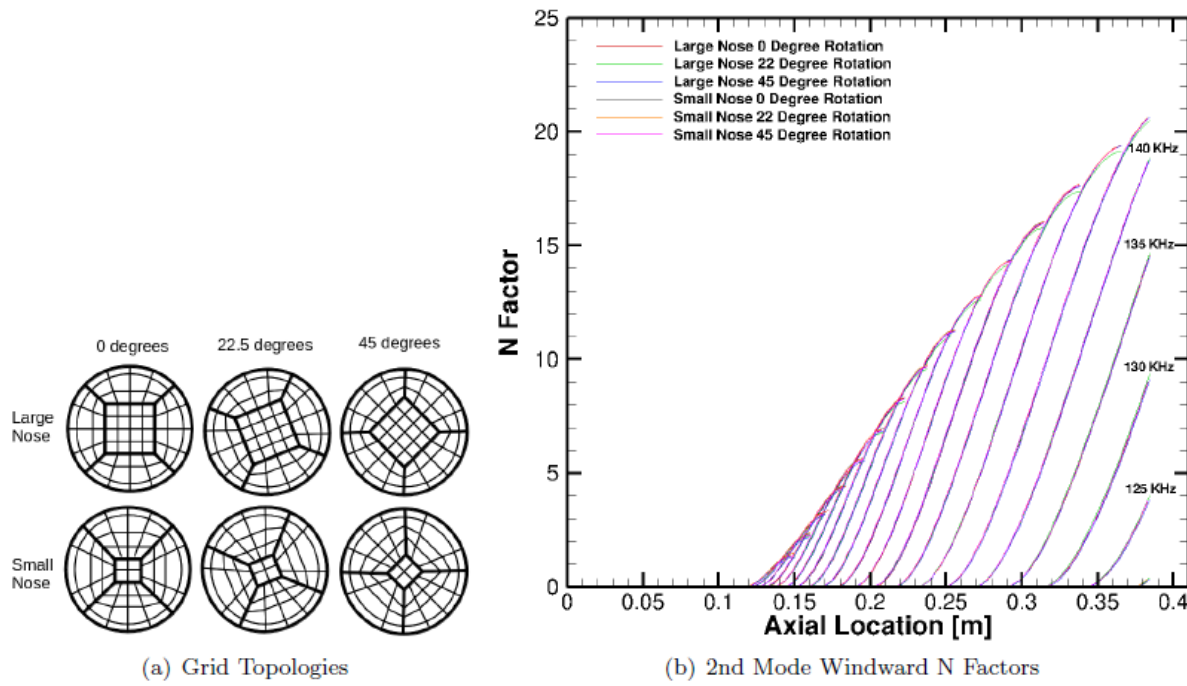


Figure 8-4 2nd Mode Windward N-Factors 5% Bluntness, 5 AoA, Re = 30 M/m

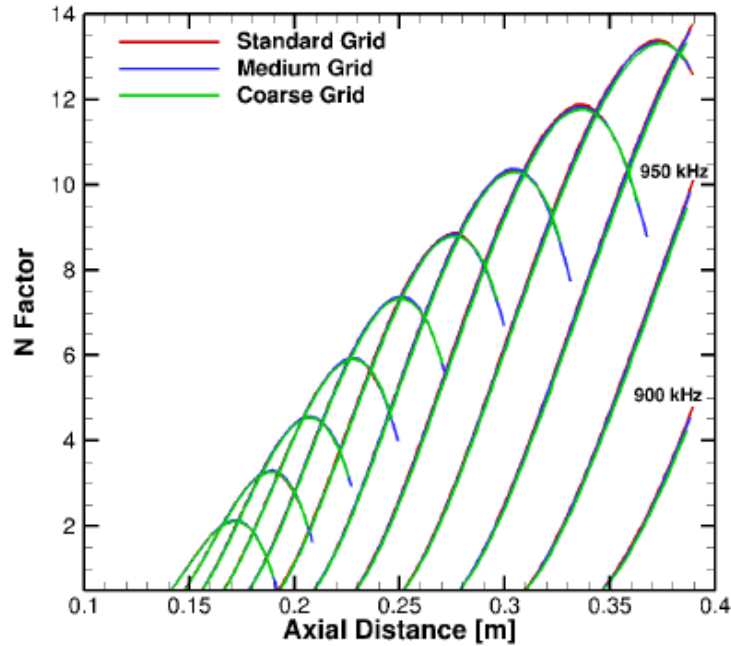


Figure 8-5 2nd Mode Windward N-Factors 5% Bluntness, 5 AoA, Re = 30 M/m

8.3.4. Overexpansion

As has been experienced in previous studies^{81, 82} certain combination of flow conditions may result in an overexpansion of the flow moving around the shoulder of the nose tip onto the frustum. In cases

where this situation occurs on conical geometries, the resulting expansion and compression waves reflect from both the shock surface and from slip lines in the flow, causing an inflection in the shape of the shock. As the angle of attack increases, this effect becomes more and more prominent.

8.4. Entropy Swallowing

The entropy swallowing location for a blunted cone is physically defined according to Stetson⁸³ as the location where the fluid at the edge of the boundary layer has passed through a nearly conical shock, and hence the edge conditions are close to those that would be experienced on a perfectly sharp cone. As Stetson noted, the entropy swallowing length is somewhat ill-defined. However, when a consistent method is applied, entropy swallowing is a useful metric to describe the extent of the entropy layer effects on a body. Stetson and others^{73, 74, 84, 85} developed methods to estimate entropy swallowing distances at 0 AoA. In order to understand the behavior of cones at non-zero AoA it is useful to develop an estimation of entropy swallowing distance on yawed cones.

Zakkay and Krause⁸⁴ used analytical solutions for conical flows to find the following closed expression for entropy swallowing distance based on comparing the mass flow rate through the bow shock to the mass flow rate through the boundary layer on an axisymmetric cone at zero AoA.

$$\frac{X_{sw}}{R_n} = \left[\frac{3}{2} \frac{(R/\gamma)^{1/2}}{\lambda p_c} \frac{\rho_\infty^2 U_\infty^2}{3M_c + M_s} \frac{\bar{y}^4 R_n}{f^2(\eta) \sin^2 \theta_{cone}} \right]^{1/3} \quad 8-1$$

Following Rotta²⁴ equation (8.1) can be rearranged to the form

$$X_{sw} = C_{sw} Re'^{(1/3)} R_n^{(4/3)} \quad 8-2$$

Where

$$C_{sw} = \left[\frac{3}{2} \frac{p_\infty}{p_c} \frac{M_\infty}{3M_c + M_s} \frac{\bar{y}^4}{f^2(\eta) \sin^2 \theta_{cone}} \right]^{1/3} \quad 8-3$$

where $C_{sw} = C_{sw} (\theta_{cone}, M_\infty)$ is a constant based only on cone angle and freestream Mach number. Note that Re , R_n , and X_{sw} must use consistent units. Stetson⁸³ provides a convenient graphical representation of the coefficient for a range of cone angles, and a range of freestream Mach numbers. However, as is noted in Stetson,⁸³ because y used appears as a quartic term in the analytical expression: “*The swallowing distance is a somewhat ambiguous length, since it depends upon the chosen shock shape and definition of the boundary of the entropy layer, and the choice of boundary layer assumptions. Therefore one should not think of the swallowing length as a precise dimension.*”

Implicit in the development of these equations is the assumption of an axisymmetric flowfield. Commonly used geometric fits for shock shape e.g. Klaimon,⁸⁶ Billig⁸⁷ are also limited to axisymmetric configurations. However, an approximation for the windward plane can be found by using the above solution, Equation (8.1) but replacing the cone half angle (θ_{cone}) with the included angle along the windward plane (θ_{inc}) where

$$\theta_{inc} = \theta_{cone} + \alpha \quad 8-4$$

Note that this substitution was made in all steps of the calculation (e.g. θ_{inc} was used to calculate the Taylor-Maccoll parameters, shock angle, etc.)

Examining Equation (8.2) it is apparent that the swallowing distance scales by nose radius with a 4/3 power law, and with Reynolds number by a 1/3 power law. However, less obvious by inspection, the changing terms in Equation (8.3) result in a decrease of C_{sw} with increasing θ_{cone} for fixed freestream conditions (e.g. Figure 5 in Stetson⁸³). If the usage of θ_{inc} holds for cones at angle of attack, accordingly the swallowing distance along the windward plane decreases for a given cone with increasing α .

Rather than using analytical solutions, one can use a computational method to calculate entropy swallowing distances. Two approaches were taken to find the entropy swallowing lengths for cones at AoA. The first method is based on the same definitions used by Zakkay and Krause to derive their expression. In the second method, a swallowing criterion is defined and calculated directly.

Finding boundary layer thicknesses in hypersonic flows is often ambiguous in nature since there is often not an obvious choice for edge conditions. We may define our boundary layer thickness δ_h defined as the point farthest away from the wall where

$$\left| 1 - \frac{h_0(y) - (h_0)_w}{(h_0)_\infty - (h_0)_w} \right| > 0.1\% \quad 8-5$$

Doing so gives a convenient and consistent measure of boundary layer thickness.

In order to directly follow Zakkay and Krause, one can use a Taylor-Maccoll solution to determine the Mach number downstream of the sharp conical shock and at the surface. Then finding the point on the computed shock where the flow behind the shock results in a Mach number 95% of the surface Mach number when expanded to surface pressure, denotes the start of the “conical shock”. One can then draw an annulus between this point and the cone surface, and integrate between the two points to find the mass flow rate through this annulus (bow shock annulus). This mass flow rate represents the mass ingested through the bow shock. Using Equation (8.5) to find the BL edge, one can also integrate from the cone surface to the boundary layer edge. At the farthest upstream location where the mass flow through the boundary layer is equal to or greater than the mass flow through the bow shock annulus, the entropy layer is considered swallowed.

When applying this algorithm to axisymmetric flow, as done analytically, the choice of azimuthal angle is inconsequential. Due to the change in flow azimuthally for cones at angle of attack, the choice was made for the current study to find the conical shock location on the windward plane. The resulting annulus was drawn in a plane normal to the cone’s axis from the cone surface to the shock at this axial location, despite the difference in conditions as azimuthal angle changes. For the cases studied, this

method for the most part closely reproduced the curves given by evaluating the analytical expression, however cases at higher AoA showed some inconsistent trends. This method also proved to be very sensitive to the definition of boundary layer thickness, as the mass flux near the edge of the boundary layer is high. In addition as one moves either farther downstream or farther from the wall, the area included in the annulus increases more rapidly due to the larger local radius of the annulus.

A more robust and somewhat simpler method is after finding the point on the computed shock where the expanded flow behind the shock results in a Mach number 95% of the surface Mach number, find the relative (to the freestream) entropy at this point. One can then march down the cone using Equation (8.5) to find the boundary layer edge. At the point where the entropy at this boundary layer edge is \leq than 95% of the entropy found in the first step, the entropy layer is considered swallowed. A comparison of the analytical method and this computational method can be seen in Figure 8-6. It can be seen that the trends found by the analytical method and the computational methods largely agree, however the constants (C_{sw}) differ by a factor of 2. This is not unexpected, given that the swallowing distance is not easily defined, and is used only as a figure of merit for extracting trends. Note however, that by examining Figure 8-6 it appears that at 5° AoA, the windward swallowing distance scales somewhat more weakly with R_N than at 0° AoA.

This method also has the advantage of removing the ambiguity in choosing the angle of the slice chosen to be the annulus, as well allowing for the acknowledgment that entropy swallowing length varies with meridian of the cone when the flow is non-axisymmetric. This variation can be seen in Figure 8-6(b).

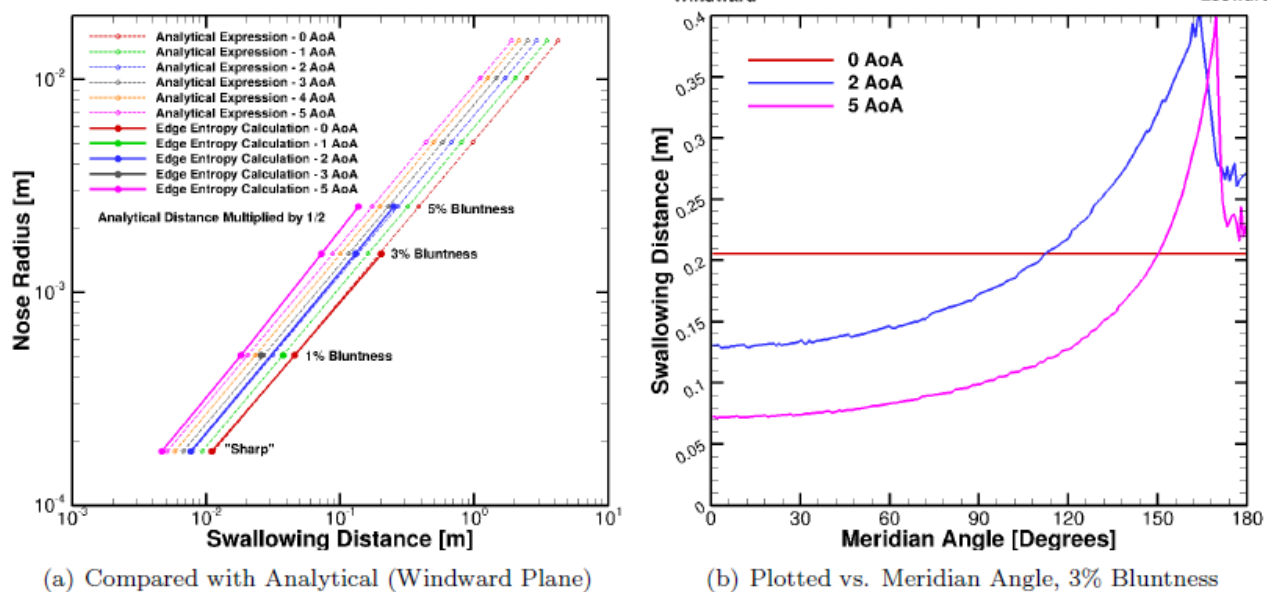


Figure 8-6 CFD Calculated Swallowing Distance

8.5. Stability Results

Once base states have been calculated, these can be used to calculate stability behavior. For this study, only second mode instabilities along the windward ray are considered.

It was observed by Juliano et al.⁸⁸ in an examination of HIFiRE-1 wind tunnel data that the effect of increasing nose bluntness was to decrease the pressure fluctuations observed at a given Reynolds number and a given station along a cone. Furthermore, Juliano et al. noted that the maximum pressure fluctuation amplitudes observed were similar for different bluntnesses. These results suggest that the effect of increasing nose bluntness is to delay amplification of second mode instabilities, rather than to increase the critical amplitude required for breakdown. The “ e^N method”, as commonly applied, is based upon the premise that once a disturbance has reached some critical amplitude, transition to turbulence follows. Because stability theory predicts only the amplification of disturbances, a critical aspect of the e^N method is selecting a correlating transition N-Factor. Note the choice of transition N-Factor is essentially equivalent to modeling the receptivity process to the freestream disturbance spectra. Good comparisons between computation and experiment were obtained for HIFiRE-1 wind tunnel data using a constant N-Factor of 4 for noisy wind tunnels. Recent work at higher Mach and Reynolds numbers^{78, 89, 90} have indicated that a higher N-factor may provide better correlations under these conditions and that the correlating N-Factor may depend on the particular frequency that provokes transition, due to differences in the initial disturbance spectrum. However, at this time variable N-Factor methods are not yet mature.

Second mode instabilities, are therefore assumed to be equally forced at all frequencies in a conventional hypersonic wind tunnel (equal initial disturbance amplitudes). At the farthest upstream location which the second mode envelope reaches the selected N-Factor, the resulting point is denoted as the estimated transition location. Tests of HIFiRE-1 at zero AoA indicated a correlating N-Factor of about 4 for noisy wind tunnels. Jewell and Kimme¹⁷⁸ showed correlating N-Factors of about 7-8 for sharp and slightly blunted cones at zero AoA in the AFRL High Reynolds Number Facility where Stetson's experiments were carried out. Therefore, N-Factors of 4 and 7 were chose for the current analysis. The results of this algorithm can be seen in Figure 8-7. The quantitative characteristics change with the choice of transition N-Factor, as would be expected. However, with the notable exception that the transition location crossover starts at a lower AoA with higher transition N-Factors, there is little qualitative change due to this choice in both the trends shown and the hypothesized explanation for the observed trends.

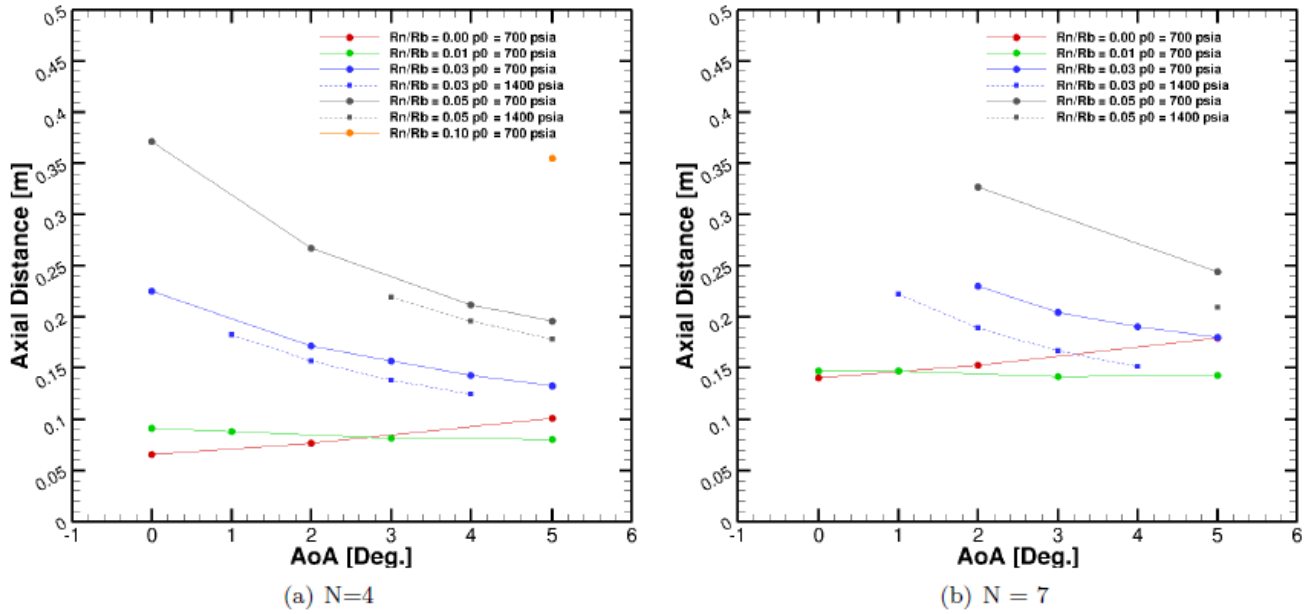


Figure 8-7 Computed 2nd Mode Transition Location (LST) Windward Plane

In general the results of this study are qualitatively similar to the experimental results available from Stetson⁷³ in that one would expect the windward transition to generally move downstream with angle of attack for sharp cases, and upstream for blunt cases. As can be seen in Figure 8-7, the case a 1% bluntness (a configuration not examined by Stetson) falls somewhere in-between and shows little movement along the windward plane with AoA changes. A discrepancy with the experimental results of Stetson is the magnitude of the transition front movement. If a constant N-Factor is used to predict transition location, the computational results predict larger amounts of movement than the experimental tests actually reported. In particular, for larger nose radii at low angle of attack the transition front is predicted downstream of the experimental results.

8.5.1. Effects of Entropy Swallowing on Transition

An obvious trend is that the discrepancy between experimental and computational results increases as the analytical prediction of swallowing distance increases. Additionally, comparison of the experimental results of Stetson with computational results by Jewell and Kimmel⁷⁸ suggests that the transition 2nd mode N-Factor is approximately constant only when experimental transition occurs outside of the entropy swallowing region. Calculating the swallowing length using the methods employed by Zakkay and Krause, the current conditions for larger bluntnesses (above 1%) predict transition inside the swallowing region, therefore this difference is not unexpected.

If one plots the CFD calculated entropy swallowing length along with the N-factors, as seen in Figure 8-8 and Figure 8-9 it becomes apparent that the first neutral point for second mode instabilities as calculated using stability theory, at both axisymmetric and at-angle of attack cases, appears to always be near this point for the cases examined. However, plotting the 1st neutral point location versus nose radius shows that the trend is closer to linear with nose radius rather than the 4/3 power law that would be suggested if the location of the 1st neutral point scaled directly with swallowing distance.

By following the envelope (maximum N-Factor at a given axial location) either on the raw plots like the one in Figure 8-8 or in the re-plotting given in Figure 8-10 it can be seen that while increasing bluntness moves the first neutral point rearward on the cone, the growth rates immediately after this point are also higher with increasing bluntness. This is supported by findings presented in both Stetson⁸³ and in Juliano et al.⁸⁸ stating that the dominant effect is likely delaying the amplification of second mode instabilities rather than increasing the critical amplitude. It is interesting to note that while the entropy layer thickness near the nose will increase with nose bluntness, the boundary layer thickness as defined in equation 7-5 stays largely the same. This means that, downstream of the swallowing distance, given disturbances amplify similarly, regardless of nose bluntness. For example the 1000 kHz modes shown in Figure 8-9 are quite similar, despite the change in entropy swallowing.

Some of these effects can be explained heuristically by examining contours of local Reynolds number, as in Figure 8-11. It is difficult to compare across angles of attack (e.g. 5% bluntness 0° AoA to 5% bluntness 5° AoA) since many of the flow properties along the windward plane are changing. However, by comparing across bluntnesses at the same angle of attack, one can see that at zero angle of attack the effects of nose-bluntness affects the local Reynolds number. There is a fairly mild overexpansion, and therefore the accompanying recovery is also mild. The overall effect is therefore largely a reduction in the local Reynolds number for much of the cone, and a recovery to flow similar to the sharp conditions.

However, for a cone at angle of attack the overexpansion in pressure along the windward plane, and the accompanying recovery downstream, becomes stronger. The resulting recovery increases the local Reynolds number to above that of the sharp cone, leading to overall stronger growth once the region of high Reynolds number is reached. This area starts at approximately the CFD entropy swallowing distance, which provides some insight into the changes in N-Factor envelopes. However it should be noted again as before that this measure is problematic because the overexpansion features due to the shock appear to scale linearly with nose radius in the cases examined, instead of the 4/3 power law with nose radius as would be implied by a linear scaling with swallowing distance.

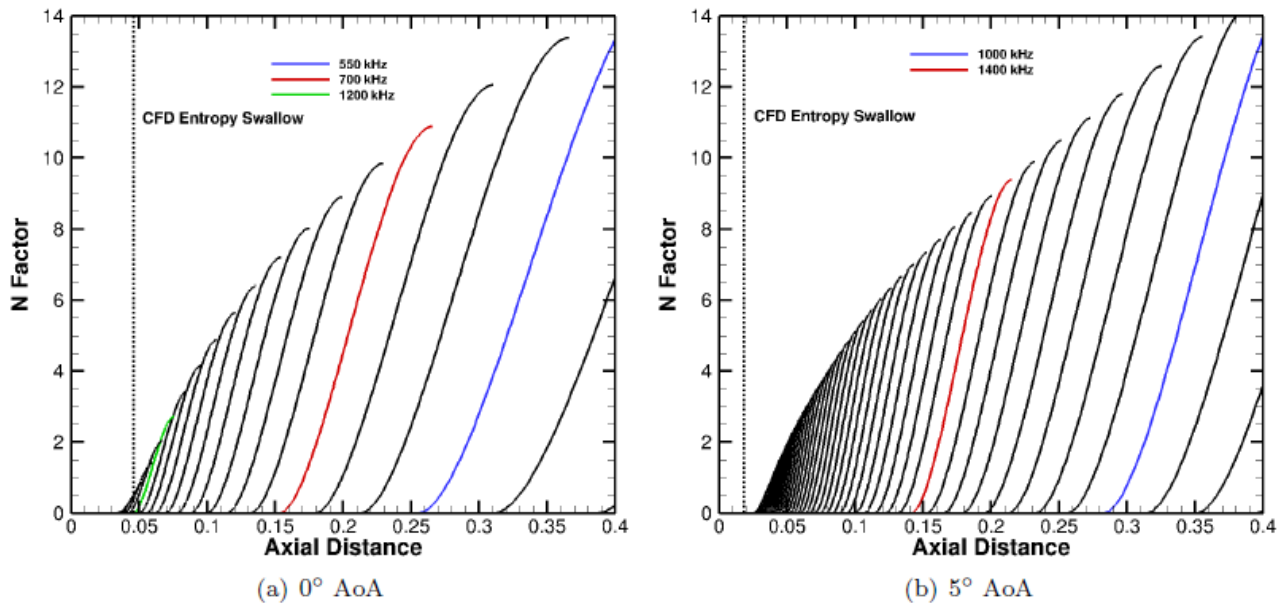


Figure 8-8 Windward 2nd Mode N-Factors, 1% Bluntness, $Re = 30$ M/m

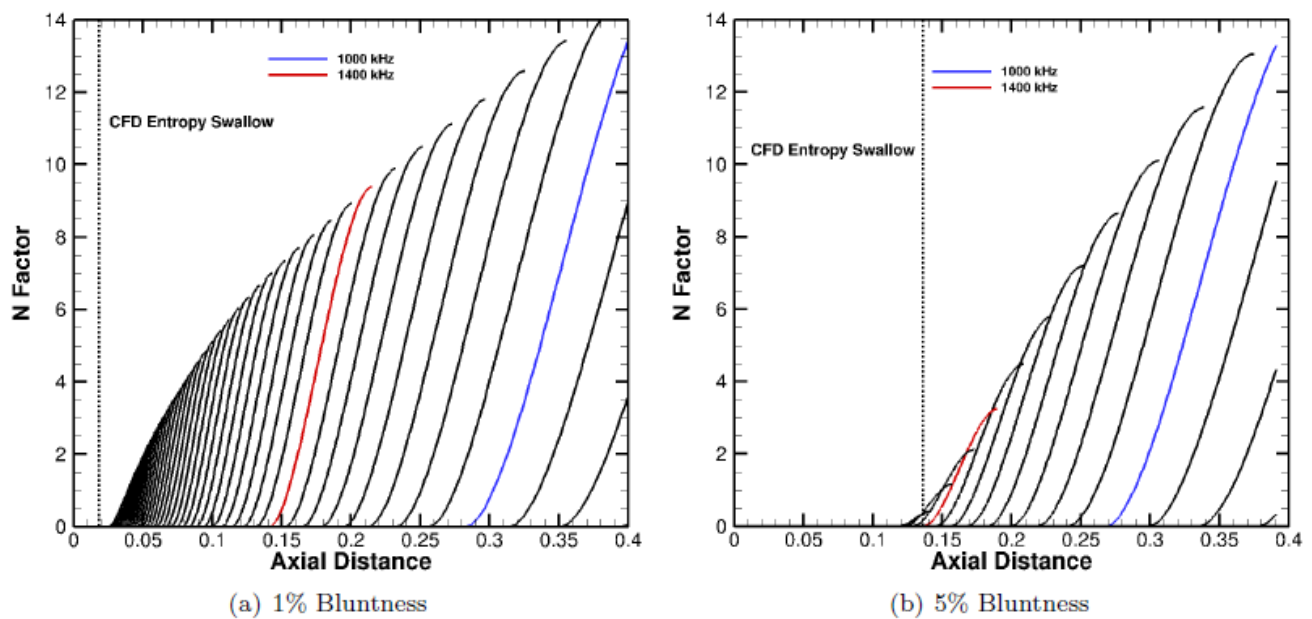


Figure 8-9 Windward 2nd Mode N-Factors, 5 AoA, $Re = 30$ M/m

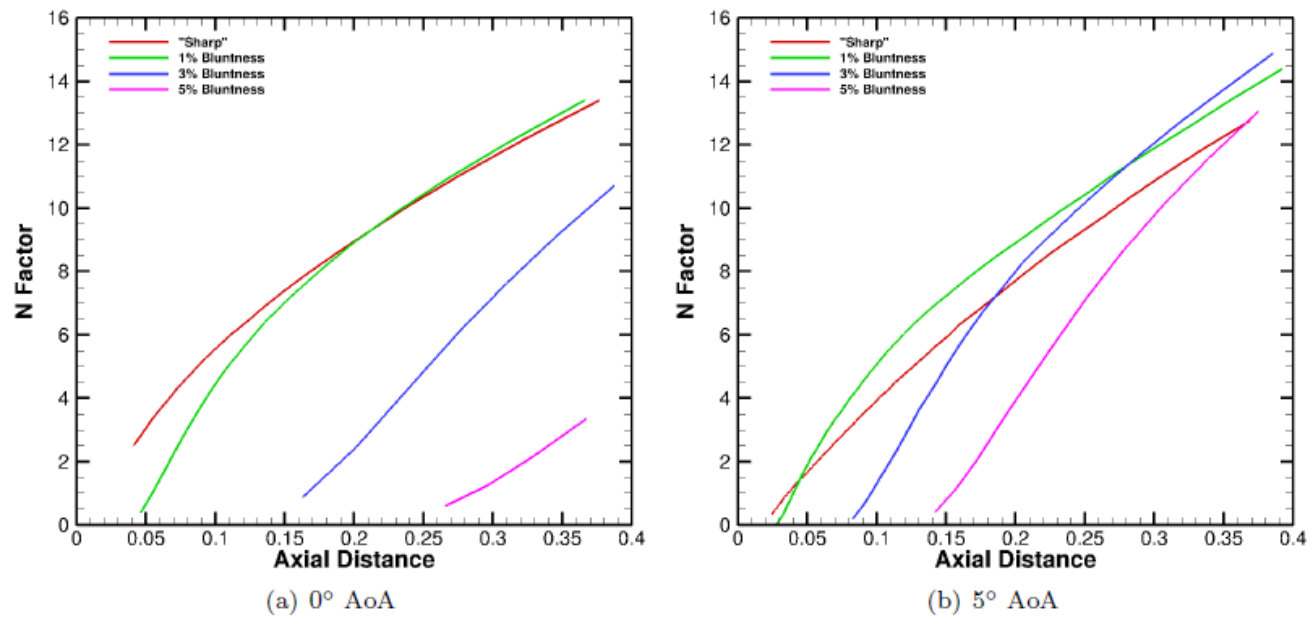


Figure 8-10 Windward 2nd Mode N-Factor Envelopes, $Re = 30 \text{ M/m}$

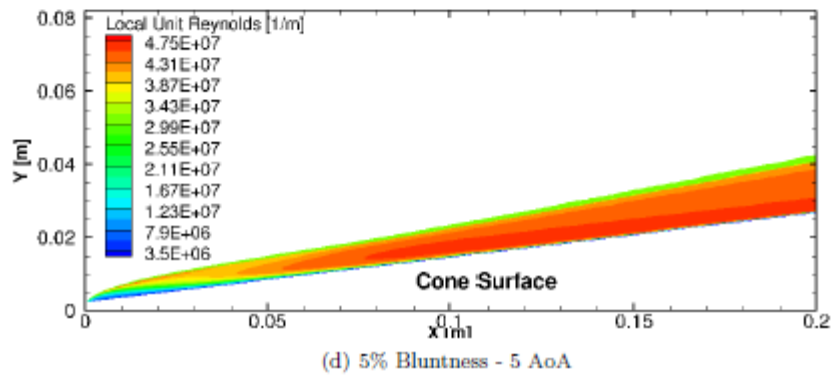
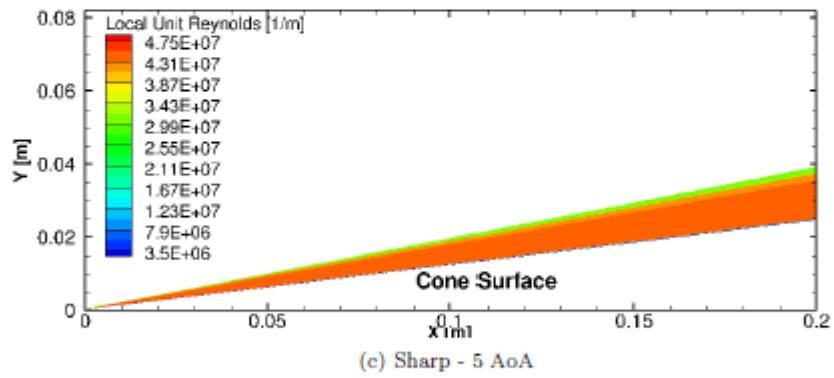
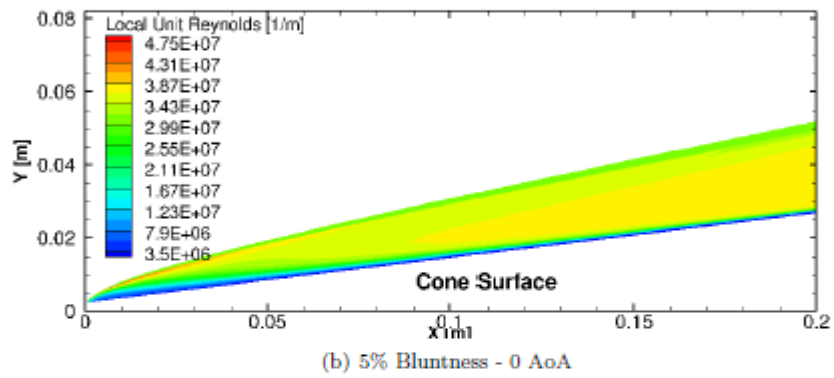
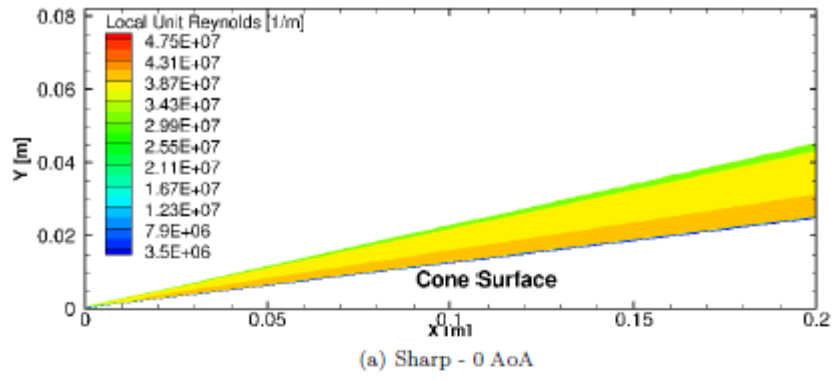


Figure 8-11 Contours of Unit Reynolds Number (Windward Plane)

By non-dimensionalizing the data using the method of Stetson, one can make a direct comparison of the current computations to Stetson's experimental data. Figure 8-12 non-dimensionalizes transition distance by the swallowing distance, and angle of attack by cone half angle. Overall, the trends with angle of attack seen by Stetson are captured using a constant N-Factor method, with the exception of the movement downstream when going from small angles of attack to zero angle of attack for larger bluntnesses. For $N = 7$ the non-dimensionalized transition movement does not match the magnitude, although note that the slope of the lines appear to be approximately correct, and that Stetson's data are taken for two different unit Reynolds number. Because the attachment line boundary layer thins significantly with increasing AoA, the range of unstable second mode frequencies also increases with AoA. This shift in disturbance frequencies implies that a differences in initial disturbance amplitudes between frequencies would be reflected in the transition location. Because of this a variable N-Factor method (better modeling of receptivity) might better recover changes in the absolute movement of the transition front. $N = 4$ was also plotted, as this allowed data for more configurations to be shown as $N = 4$ was reached more easily. As seen in Figure 8-13, many of the predicted $N=4$ transition locations are well within the swallowing distance. Jewell and Kimmel's⁷⁸ analysis of Stetson's zero AoA data showed that a constant N-factor method was not applicable in this region, where calculated N-factors at transition were often < 2 .

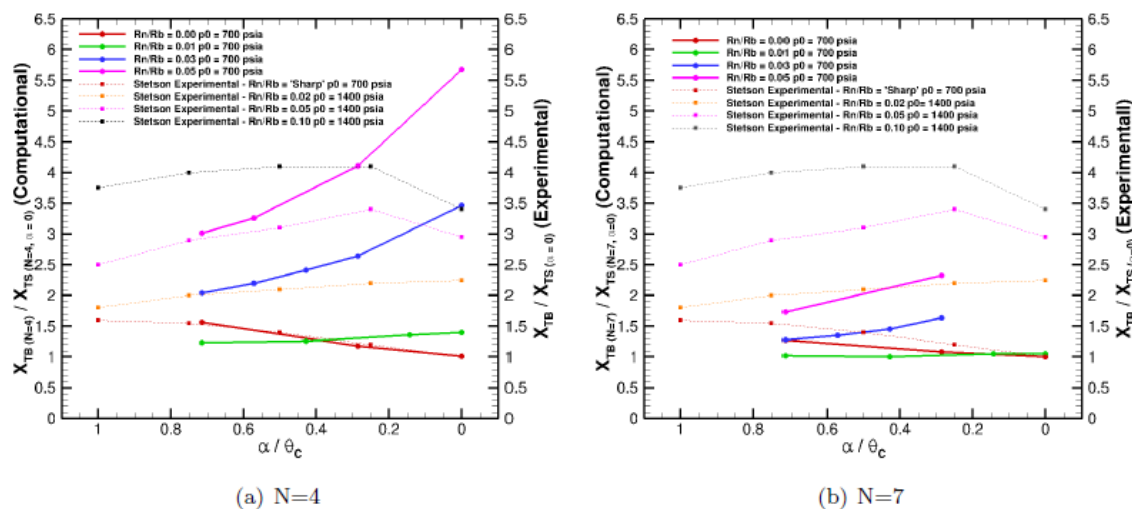


Figure 8-12 Non-Dimensional Transition (Style of Stetson)

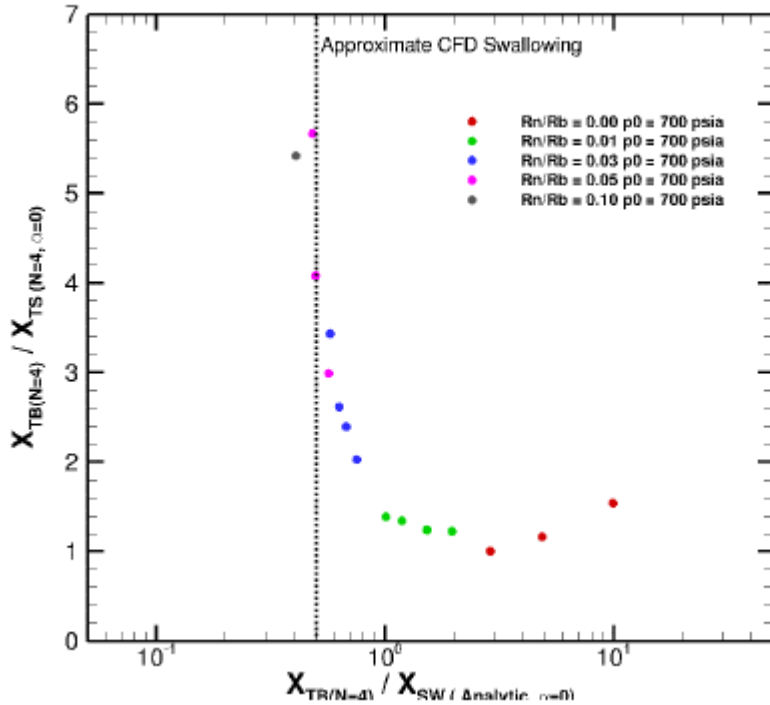


Figure 8-13 Swallowing Distance vs. Predicted Transition

Experimentally, there are cases where transition to turbulence occurs well within the entropy-swallowing distances. Both first- and second-mode N-Factor levels at these locations are well below what would be expected to lead to transition from modal growth. It is hoped that frequency and wave angle information from the upcoming experimental series will help to shed some light onto this issue.

8.6. Conclusions and Future Work

Computational simulations of seven-degree half-angle cones have been completed and analyzed with regards to second mode instabilities. It has been shown that computationally derived entropy swallowing distances confirm the trends shown by analytical methods, and both are a good figure of merit when considering bluntness effects on transition. Stability results suggest that the hypothesis that bluntness effects for the most part delay amplification of instabilities rather than increase the critical amplitude is correct. When the experimentally observed transition front is within the entropy swallowing distance, stability results suggest that second mode is not the responsible mode, and some other mechanism is likely causing transition to turbulence.

Future computational work has been started include characterization of the crossflow instabilities known to be present on the shoulders of yawed cones. A second area of investigation is the effect of wall-temperature ratios on the overall transition pattern.

List of Acronyms, Abbreviations, Symbols

A	= disturbance amplitude, dimensionless
A_1	= disturbance amplitude at lower neutral bound, dimensionless
c_p	= specific heat, J/(kg K)
f	= frequency, units as noted
h	= specific enthalpy, KJ/kg
i	= grid index
j	= grid index
k	= wall-normal grid index
M	= Mach number
N	= $\ln[A(f)/A_1(f)]$, dimensionless
P	= pressure, units as noted
p	= pressure, units as noted
\dot{q}''	= heat transfer rate, W/m ²
Pt	= peak-to-valley step height
R	= radius, units as noted
Re	= unit Reynolds number per meter
St	= Stanton number
T	= temperature, K
t	= time, units as noted
U	= total velocity, m/s
u	= velocity component along missile longitudinal axis, m/s
v	= velocity component perpendicular to missile axis in yaw plane, m/s
w	= velocity component perpendicular to missile axis in pitch plane, m/s
u^*	= friction velocity, $\sqrt{\tau_w/\rho}$, m/s
X	= streamwise coordinate
x	= streamwise coordinate, origin at model nose stagnation point, dimensions as noted
y	= spanwise coordinate, origin at model nose stagnation point, or coordinate normal to model wall, dimensions as noted
$y+$	= distance from model wall, yu^*/ν , non-dimensional
α	= angle of attack, degrees
β	= yaw angle, degrees
ϕ	= body-fixed missile azimuthal coordinate, degrees
θ	= cone halv-angle, degrees
η	= similarity variable, non-dimensional
γ	= ratio of specific heats, dimensionless
ν	= kinematic viscosity, m ² /s
ρ	= density, kg/m ³
τ	= skin friction, Pa

Subscripts

aw = adiabatic wall
B = blunt
CFD=computed pressure at sensor location
CL = centerline
F = measured at transducer
LE = leading edge
n = nose
S = sharp
sw = swallowing
T = transition
tr = transition
w = wall
0 = stagnation conditions
 ∞ = free stream, upstream of model bow shock

Acronyms

ACE	Actively-Controlled Expansion
AEDC	Arnold Engineering Development Complex
AFRL	Air Force Research Laboratory
AoA	angle of attack
BAM6QT	Boeing/AFOSR Mach 6 Quiet Wind Tunnel
CCW	counter-clockwise
CFD	computational fluid dynamics
CFL	Courant, Friedrichs, Lewy
CUBRC	Calspan / University of Buffalo Research Center
DPLR	Data Parallel-Line Relaxation
DRE	discrete roughness element
DSP	digital signal processor
FADS	flush air data sensing
GPS	global positioning system
HIFiRE	Hypersonic International Flight Research Experiments
HT	heat transfer (heat transfer gauge identifier)
IMU	inertial measurement unit
IR	infrared
LaRC	Langley Research Center
LENS	Large Enthalpy National Shock Tunnel
LPSE	linear parabolized stability equations
LST	linear stability theory
NASA	National Aeronautics and Space Administration
PCM	pulse-code modulation
PEEK	poly-ether ether ketone
PH	precipitation-hardened
PLBW	pressure, low bandwidth (pressure sensor identifier)
PSD	power spectral density

PSE	parabolized stability equation
Ra	arithmetic average roughness
RTV	room-temperature vulcanizing
RMS	root-mean-square
TLBW	temperature, low bandwidth (thermocouple identifier)
TSP	temperature-sensitive paint
TZM	titanium zirconium molybdenum
VKF	von Karman facility

References

- ¹ Kimmel, R. L., Adamczak, D. A., and DSTO AVD Brisbane Team, “HIFiRE-5b Flight Overview,” AIAA paper 2017-3131, June 2017.
- ² Jewell, J. S., Kimmel, R. L., Poggie, J., Porter, K. M., and Juliano, T. J., “Correlation of HIFiRE-5b Flight Data With Computed Pressure and Heat Transfer for Attitude Determination,” AIAA paper 2017-3133, June 2017.
- ³ Juliano, T. J., Poggie, J., Porter, K. M., Jewell, J. S., Kimmel, R. L., Adamczak, D. A., “HIFiRE-5b Heat Flux and Boundary-Layer Transition,” AIAA paper 2017-3134, June 2017.
- ⁴ Borg, M. P., and Kimmel, R. L., “Measurements of Crossflow Instability Modes for HIFiRE-5 at Angle of Attack,” AIAA paper 2017-1681, January 2017.
- ⁵ Borg, M. P. and Kimmel, R. L., “Ground Test Measurements of Boundary-Layer Instabilities and Transition for HIFiRE-5 at Flight-Relevant Attitudes,” AIAA paper 2017-3135, June 2017.
- ⁶ Tufts, M. W., Gosse, R., and Kimmel, R. L., “PSE Analysis of Crossflow Instability on HIFiRE 5b Flight Test,” AIAA paper 2017-3136, June 2017.
- ⁷ Tufts, M. W. and Kimmel, R. L., “Analysis of Windward Side Hypersonic Boundary Layer Transition on Blunted Cones at Angle of Attack, AIAA paper 2017-0764, January 2017.
- ⁸ Kimmel, R. L., Adamczak, D., Juliano, T. J., DSTO AVD Brisbane Team, “HIFiRE-5 Flight Test Preliminary Results,” AIAA paper 2013-0377, January 2013.
- ⁹ Juliano, T. J., Adamczak, D. and Kimmel, R. L., “HIFiRE-5 Flight Test Heating Analysis,” AIAA paper 2014-0076, January 2014.
- ¹⁰ Jewell, J. S., Miller, J. H., Kimmel, R. L., “Correlation of HIFiRE-5 Flight Data With Computed Pressure and Heat Transfer,” AIAA paper 2015-2019, June 2015.
- ¹¹ Choudhari, M., Chang, C.-L., Jentink, T., Li, F., Berger, K., Candler, G., and Kimmel, R., “Transition Analysis for the HIFiRE-5 Vehicle,” AIAA paper 2009-4056, June 2009.
- ¹² Gosse, R., Kimmel, R., and Johnson, H. B., “Study of Boundary-Layer Transition on Hypersonic International Flight Research Experimentation 5,” *AIAA Journal of Spacecraft and Rockets*, vol. 51, no. 1, January 2014.
- ¹³ Holden, M. S., Wadhams, T. P., MacLean, M., Mundy, E., “Review of Studies of Boundary Layer Transition in Hypersonic Flows Over Axisymmetric And Elliptic Cones Conducted in the CUBRC Shock Tunnels,” AIAA paper 2009-0782, January 2009.

¹⁴ Kimmel, R. L., Adamczak, D., Berger, K., and Choudhari, M., “HIFiRE-5 Flight Vehicle Design,” AIAA paper 2010-4985, June 2010

¹⁵ Palmerio, A. F.; Peres da Silva, J. P. C.; Turner, P.; Jung, W., “The development of the VSB-30 sounding rocket vehicle,” in 16th ESA Symposium on European Rocket and Balloon Programmes and Related Research, 2 - 5 June 2003. Ed.: Barbara Warmbein. ESA SP-530, Noordwijk: ESA Publications Division, 2003, p. 137 – 140.

¹⁶ “NASA Sounding Rocket Program Handbook,” 810-HB-SRP, Sounding Rockets Program Office, Suborbital & Special Orbital Projects Directorate, Goddard Space Flight Center, Wallops Island Flight Facility, June 2005.

¹⁷ Kimmel, R. L., and Poggie, J., “Transition on an Elliptic Cone at Mach 8,” American Society of Mechanical Engineers ASME FEDSM97-3111, June 1997.

¹⁸ Kimmel, R. L., and Poggie, J., “Three-Dimensional Hypersonic Boundary Layer Stability and Transition,” Air Force Research Laboratory Technical Report, WL-TR-97-3111, December 1997, Wright-Patterson Air Force Base, Ohio.

¹⁹ Kimmel, R. L., and Poggie, J., Schwoerke, S. N., “Laminar-Turbulent Transition in a Mach 8 Elliptic Cone Flow,” *AIAA Journal*, vol. 37, no. 9, Sep. 1999, pp. 1080-1087.

²⁰ Schmisseur, J. D., “Receptivity of the Boundary Layer on a Mach-4 Elliptic Cone to Laser-Generated Localized Freestream Perturbations,” Doctoral Dissertation, Purdue University Aerospace Sciences Laboratory, December 1997.

²¹ Holden, M., “Experimental Studies of Laminar, Transitional, and Turbulent Hypersonic Flows Over Elliptic Cones at Angle of Attack,” Air Force Office of Scientific Research Technical Report AFRL-SR-BL-TR-98-0142, Bolling Air Force Base, DC, 1998.

²² Schmisseur, J. D., Schneider, S. P., and Collicott, S. H., “Receptivity of the Mach 4 Boundary Layer on an Elliptic Cone to Laser-Generated Localized Freestream Perturbations,” AIAA paper 1998-0532, January 1998.

²³ Schmisseur, J. D., Schneider, S. P., and Collicott, S. H., “Response of the Mach 4 boundary layer on an elliptic cone to laser-generated freestream perturbations,” AIAA paper 1999-0410, January 1999.

²⁴ Lyttle, I. J., and Reed, H. L., “Use of Transition Correlations for Three-Dimensional Boundary Layers Within Hypersonic Flows,” AIAA-95-2293, June 1995.

²⁵ Löhle,S., Böhrk, H., Fuchs, U., Kraetzig, B., and Weihs, H., “Three-Dimensional Thermal Analysis of the HIFiRE-5 Ceramic Fin,” AIAA paper 2012-5920, September 2012.

²⁶ Berger, K. T., Rufer, S. J., Kimmel, R. and Adamczak, D., “Aerothermodynamic Characteristics of Boundary Layer Transition and Trip Effectiveness of the HIFiRE Flight 5 Vehicle,” AIAA paper 2009-4055, June 2009.

²⁷ Kimmel, R. L., Adamczak, D., Paull, A., Paull, R., Shannon, J., Pietsch, R., Frost, M., and Alesi, H., “HIFiRE-1 Ascent-Phase Boundary-Layer Transition,” *AIAA Journal of Spacecraft and Rockets*, vol. 52, no. 1, Jan-Feb 2015.

²⁸ Gosse, R., Kimmel, R., “CFD Study of Three-Dimensional Hypersonic Laminar Boundary Layer Transition on a Mach 8 Elliptic Cone,” AIAA paper 2009-4053, June 2009.

²⁹ Stanfield, S. A., Kimmel, R. L., and Adamczak, D., “HIFiRE-1 Data Analysis: Boundary Layer Transition Experiment During Reentry,” *AIAA Journal of Spacecraft and Rockets*, vol. 52, no. 3, May-June 2015, pp 637-649.

³⁰ Juliano, T. J., Adamczak, D., and Kimmel, R. L., “HIFiRE-5 Flight Test Results,” *Journal of Spacecraft and Rockets*, vol. 52, no. 3, 2015, pp. 650-663.

³¹ Karlgaard, C. D., Kutty, P., Schoenberger, M., Munk, M. N., Little, A., and Kuhl, C., “Mars Science Laboratory Entry Atmospheric Data System Trajectory and Atmosphere Reconstruction,” *Journal of Spacecraft and Rockets*, vol. 51, no. 4, 2014, pp. 1029-1047.

³² Karlgaard, C. D., Kutty, P., and Schoenberger, M., “Coupled Inertial Navigation and Flush Air Data Sensing Algorithm for Atmosphere Estimation,” AIAA paper, AIAA-2015-0526, January 2015.

³³ Porter, K. M., Poggie, J., and Kimmel, R. L., “Laminar and Turbulent Flow Calculations for the HIFiRE-5b Flight Test,” AIAA paper 2017-3132, June 2017.

³⁴ Juliano, T. J. and Schneider, S. P., “Instability and transition on the HIFiRE-5 in a Mach-6 quiet tunnel,” AIAA Paper 2010-5004, June 2010.

³⁵ Juliano, T J., *Instability and Transition on the HIFiRE-5 in a Mach-6 Quiet Tunnel*, PhD thesis, Purdue University School of Aeronautics & Astronautics, West Lafayette, IN, August 2010. Available from DTIC as ADA528752.

³⁶ Juliano, T. J., Borg, M. P., and Schneider, S. P., “Quiet tunnel measurements of HIFiRE-5 boundary-layer transition,” *AIAA Journal*, vol. 53, no. 4, pp 832–846, 2015.

³⁷ Borg, M., Kimmel, R. L., and Stanfield, S., “Instability and Transition for HIFiRE-5 in a Hypersonic Quiet Wind Tunnel,” 2011-3247, June 2011.

³⁸ Borg, M. P., Kimmel, R. L., Stanfield, S., “Crossflow Instability for HIFiRE-5 in a Quiet Hypersonic Wind Tunnel,” AIAA paper 2012-2821, June 2012.

³⁹ Borg, M. P., Kimmel, R. L., and Stanfield, S., “Traveling Crossflow Instability for HIFiRE-5 in a Quiet Hypersonic Wind Tunnel,” AIAA 2013-2737, June 2013.

⁴⁰ Holden, M. S., Wadhams, T. P., MacLean, M., Dufrene, A. Mundy, E. and Marineau E, “A Review of Basic Research and Development Programs Conducted in the LENS Facilities in Hypervelocity Flows” AIAA Paper 2012-0469, January 2012.

⁴¹ Choudhari, M., Chang, C.-L., Jentink, T., Li, F., Berger, K., Candler, G., and Kimmel, R., “Transition Analysis for the HIFiRE-5 Vehicle,” AIAA paper 2009-4056, June 2009.

⁴² Gosse, R., Kimmel, R. L., and Johnson, H. B., “CFD Study of the HIFiRE-5 Flight Experiment,” AIAA paper 2010-4854, June 2010.

⁴³ Li, F., Choudhari, M., Chang, C.-L., White, J., Kimmel, R., Adamczak, D., Borg, M., Stanfield, S., and Smith, M., “Stability Analysis for HIFiRE Experiments,” AIAA paper 2012-2961, June 2012.

⁴⁴ Boyd, C. F., and Howell, A., “Numerical Investigation of One-Dimensional Heat-Flux Calculations,” Naval Surface Warfare Center report NSWCDD/TR-94/114, 25 October 1994.

⁴⁵ Willems, S., Gühan, A., Juliano, T. J., and Schneider, S. P., “Laminar to turbulent transition on the HIFiRE-1 cone at Mach 7 and high angle of attack,” AIAA 2014-0428, January 2014.

⁴⁶ Juliano, T. J., Kimmel, R. L., Willems, S., Gühan, A., and Schneider, S. P., “HIFiRE-1 Surface Pressure Fluctuations from High Reynolds, High Angle Ground Test,” AIAA paper 2014-0429, January 2014.

⁴⁷ Borg, M. P., Kimmel, R. L., Hofferth, J. W., Bowersox, R. D., and Mai, C. L., “Freestream Effects on Boundary Layer Disturbances for HIFiRE-5,” Paper 2015-0278, AIAA, January 2015.

⁴⁸ Borg, M. P., and Kimmel, R. L., “Traveling Crossflow Instability for the HIFiRE-5 Elliptic Cone,” *AIAA Journal of Spacecraft and Rockets*, vol. 52, no. 3, May-June 2015, pp. 664-673.

⁴⁹ Borg, M.P., and Kimmel, R. L., “Simultaneous Infrared and Pressure Measurements of Crossflow Instability Modes for HIFiRE-5,” AIAA paper 2016-0354, January 2016.

⁵⁰ van den Kroonenberg, A., Radespiel, R., Candler, G., and Estorf, M., “Infrared measurements of boundary-layer transition on an inclined cone at Mach 6,” AIAA paper 2010-1063, January 2010.

⁵¹ Muñoz, F., Heitmann, D., and Radespiel, R., “Instability Modes in boundary layers of an inclined cone at Mach 6,” *Journal of Spacecraft and Rockets*, Vol. 51, No. 2, March-April 2014, pp. 442-454.

⁵² Schneider, S. P., “Design of a Mach-6 Quiet-flow Wind-Tunnel Nozzle Using the e**N Method for Transition Estimation,” AIAA 98-0547, January 1998.

⁵³ Beresh, S. J., Henfling, J., Spillers, R., and Pruett, B., “Measurements of Fluctuating Wall Pressures Beneath a Supersonic Turbulent Boundary Layer,” AIAA paper 2010-0305, January 2010.

⁵⁴ Saric, W. S. and Reed, H. L., “Supersonic Laminar flow control on swept wings using distributed roughness,” AIAA paper 2002-0147, Jan. 2002.

⁵⁵ Downs, R. S., Lovig, E. N., and White, E. B., “Experimental Investigation of the Crossflow Instability in Moderate Freestream Turbulence,” AIAA paper 2012-2824, June 2012.

⁵⁶ Roediger, T., Knauss, H., Kraemer, E., Heitmann, D., Radespiel, R., Smorodosky, B., Bountin, D., and Maslov, A., “Hypersonic instability waves measured on a flat plate at Mach 6,” Proceedings of the International Conference on Methods of Aerophysical Research, 2008.

⁵⁷ Edelman, J. B., Chynoweth, B. C., McKiernen, G. R., Sweeny, C. J., and Schneider, S. P., “Instability and Transition Measurements in the Boeing/AFOSR Mach-6 Quiet Tunnel,” AIAA Paper 2016-3343, AIAA, June 2016.

⁵⁸ Chang, C.-L., “The Langley Stability and Transition Analysis Code (LASTRAC): LST, Linear & Nonlinear PSE for 2-D, Axisymmetric, and Infinite Swept Wing Boundary Layers,” AIAA-2003-0974, 2003.

⁵⁹ Chang, C.-L., “The Langley Stability and Transition Analysis Code (LASTRAC) Version 1.2 User Manual,” June 2004.

⁶⁰ Chang, C.-L., “LASTRAC 3D: Transition Prediction in 3-D Boundary Layers,” AIAA-2004-2542, 2004.

⁶¹ Wadhams, T. P., Mundy, E., MacLean, M. G., and Holden, M. S., “Ground Test Studies of the HIFiRE-1 Transition Experiment Part1: Experimental Results,” *AIAA Journal of Spacecraft and Rockets*, vol. 45, no. 6, November-December 2008, pp. 1134-1148.

⁶² Li, F., Choudhari, M., Chang, C.-L., Kimmel, R., Adamczak, D., and Smith, M., “Transition Analysis for the HIFiRE-1 Flight Experiment,” AIAA paper 2011-3414, June 2011.

⁶³ Kocian, T. S., Moyes, A. J., Mullen, D., and Reed, H. L., “PSE and Spatial Biglobal Instability Analysis of Reduced Scale and Flight HIFiRE-5 Geometry,” AIAA-2017-0768, 2017.

⁶⁴ Dinzl, D. J. and Candler, G. V., “Analysis of Crossflow Instability on HIFiRE-5 using Direct Numerical Simulation,” AIAA paper 2015-0279, January 2015.

⁶⁵ Malik, M. R., Li, F., and Chang, C.-L., “Crossflow Disturbance in Three-Dimensional Boundary Layers: Nonlinear Development, Wave Interaction, and Secondary Instability,” *Journal of Fluid Mechanics*, vol. 268, 1994, pp. 1-36.

⁶⁶ White, E. B. and Saric, W. S., “Secondary Instability of Crossflow Vortices,” *Journal of Fluid Mechanics*, vol. 525, 2005, pp. 275-308.

⁶⁷ Saric, W. S., Reed, H. L., and White, E. B., “Stability and Transition of Three-Dimensional Boundary Layers,” *Annual Review of Fluid Mechanics*, vol. 35, No. 1, 2003, pp. 413-440.

⁶⁸ Li, F., Choudhari, M., Paredes, P., and Duan, L., “Secondary Instability of Stationary Crossflow Vortices in Mach 6 Boundary Layer over a Circular Cone,” Tech. Rep. NASA-TP-2015-218997, National Aeronautics and Space Administration, 2015.

⁶⁹ Moyes, A. J., Paredes, P., Kocian, T. S., , and Reed, H. L., “Secondary Instability Analysis of Crossflow on a Hypersonic Yawed Straight Circular Cone,” *Journal of Fluid Mechanics*, vol. 812, 2016, pp. 370-397.

⁷⁰ Paredes, P., Gosse, R., Theofilis, V., and Kimmel, R. L., “Linear Modal Instabilities of Hypersonic Flow Over an Elliptic Cone,” *Journal of Fluid Mechanics*, vol. 804, 2016, pp. 442-466.

⁷¹ He, W., Tendero, J. A., Paredes, P., and Theofilis, V., “Linear Instability in the Wake of an Elliptic Wing,” *Theoretical and Computational Fluid Dynamics*, 2016, pp. 1-22.

⁷² Alba, C. R., Johnson, H. B., Bartkowicz, M. D., Candler, G. V., and Berger, K. T. “Boundary-Layer Stability Calculations for the HiFiRE-1 Transition Experiment,” *AIAA Journal of Spacecraft and Rockets*, vol. 45, no. 6, November-December 2008, pp. 1125-1133.

⁷³ Stetson, K. F., “Mach 6 Experiments of Transition on a Cone at Angle of Attack,” *Journal of Spacecraft and Rockets*, vol. 19, no. 5, Sep.-Oct. 1982, pp. 397-403.

⁷⁴ Stetson, K. F., and Rushton, G. H., “Shock Tunnel Investigation of Boundary-Layer Transition at M=5.5,” *AIAA Journal*, vol. 5, no. 5, May 1967, pp. 899-906.

⁷⁵ DiCristina, V., “Three-Dimensional Boundary Layer Transition on a Sharp 8° Cone at Mach 10,” *AIAA Journal*, vol. 8, no. 5, May 1970, pp. 852-856.

⁷⁶ Holden, M., Bower, D., and Chadwick, K., “Measurements of Boundary Layer Transition on Cones at Angle of Attack for Mach Numbers from 11 to 13,” AIAA-95-2294, June 1995.

⁷⁷ Lei, J. and Zhong, X., “Linear Stability Analysis of Nose Bluntness Effects on Hypersonic Boundary Layer Transition,” *Journal of Spacecraft and Rockets*, vol. 49, no. 1, 2012.

⁷⁸ Jewell, J. S., and Kimmel, R. L., “Boundary Layer Stability Analysis for Stetson’s Mach 6 Blunt Cone Experiments,” AIAA paper 2016-¹⁵²0598, January 2016.
DISTRIBUTION STATEMENT A: Approved for public release. Distribution is unlimited.

⁷⁹ Fiore, A. W. and Law, C. H., "Aerodynamic Calibrations of the Aerospace Research Laboratories M = 6 High Reynolds Number Facility," ARL-TR-75-0028, 1975.

⁸⁰ Perez, E., Reed, H. L., and Kuehl, J. J., "Instabilities on a Hypersonic Yawed Cone," AIAA paper 2013-2879, 2013.

⁸¹ Traugott, S. C., "Some Features of Supersonic and Hypersonic Flow About Blunted Cones," *Journal of Aerospace Sciences*, vol. 29, no. 4, 1962, pp. 389-399.

⁸² Cleary, J. W., "An Experimental and Theoretical Investigation of the Pressure Distribution and Flow Fields of Blunted Cones at Hypersonic Mach Numbers," NACA TN D-2969, 1965.

⁸³ Stetson, K. F., "Nose Tip Bluntness Effects on Cone Frustum Boundary Layer Transition in Hypersonic Flow," AIAA paper 83-1763, July 1983.

⁸⁴ Zakkay, V. and Krause, E., "Boundary Conditions at the Outer Edge of the Boundary Layer on Blunted Conical Bodies," *AIAA Journal*, vol. 1, vo. 7, 1963, pp. 1671-1672.

⁸⁵ Rotta, N. R., "Effects of Nose Bluntness on the Boundary Layer Characteristics of Conical Bodies at Hypersonic Speeds," NYU-AA-66-66, 1966.

⁸⁶ Klaimon, J. H., "Bow Shock Correlation for Slightly Blunted Cones," *AIAA Journal*, vol. 1, no. 2, 1963, pp. 490-491.

⁸⁷ Billig, F. S., "Shock-Wave Shapes around Spherical- and Cylindrical-Nosed Bodies," *Journal of Spacecraft*, vol. 4, No. 6, 1967, pp. 822-823.

⁸⁸ Juliano, T. J., Kimmel, R. L., Willems, S., Gühan, A., and Wagnild, R. M., "HIFiRE-1 Boundary-Layer Transition: Ground Test Results and Stability Analysis," AIAA-2015-1736, 2015.

⁸⁹ Marineau, E. C., Moraru, G., Lewis, D. R., Norris, J. D., Lafferty, J. F., Wagnild, R. M., and Smith, J. A., "Mach 10 Boundary-Layer Transition Experiments on Sharp and Blunted Cones," AIAA paper 2014-3108, 2014.

⁹⁰ Jewell, J. S., "Boundary-Layer Transition on a Slender Cone in Hypervelocity Flow with Real Gas Effects," Ph.D. thesis, California Institute of Technology, May 2015.